The Dissertation Committee for Michael Barron Sigman, Jr. Certifies that this is the approved version of the following dissertation:

Solventless Synthesis, Characterization, and Self-Assembly of Colloidal Nanocrystals

Committee:

Brian A. Korgel, Supervisor

Roger T. Bonnecaze

Gyeong S. Hwang

Chih-Kang (Ken) Shih

Zhen Yao

Solventless Synthesis, Characterization, and Self-Assembly of Colloidal Nanocrystals

by

Michael Barron Sigman, Jr., B.Ch.E.

Dissertation

Presented to the Faculty of the Graduate School of
The University of Texas at Austin
in Partial Fulfillment
of the Requirements
for the Degree of

Doctor of Philosophy

The University of Texas at Austin
May, 2005

Dedication

To Stacey and Garrett

Acknowledgements

The most enjoyable aspect of graduate school has been the opportunity to learn and work with the numerous bright and hard working people here at the University of Texas. In particular, I wanted to thank my advisor, Dr. Brian A. Korgel, for the opportunity to study and research nanomaterials. I also thank Dr. Roger Bonnecaze, Dr. Gyeong Hwang, Dr. Ken Shih, and Dr. Zhen Yao for their thoughts and comments as members of my committee.

A significant portion of my research has involved the use of TEM and electron diffraction, and I thank Dr. Miguel Jose-Yacaman for his willingness to assist in this area. Dr. J.P. Zhou, Dr. Dwight Romanovicz, Dr. Yang-ming Sun, Dr. Vince Lynch, and Dr. John Mendenhall are all appreciated for their knowledge, training, and assistance with various instruments and aspects of my research.

I would like to thank the members of the Korgel group: Chris, Cindy, Lindsay, Tobias, Aaron, Ali, April, Felice, Doh, Tripp, Hsing-Yu, and Dayne, for all of their suggestions, assistance, and friendship over the years. Parag Shah, Fred Mikulec, Jose-Luis Elechiguerra, Michael Dickey, and many others are also deserving of thanks their help.

Finally, I want to thank my parents and family for their many years of love, guidance, and encouragement. I thank my son, Garrett, for tolerating all of the late nights away in the lab as well as for making me very proud. And most importantly, I thank my wife, Stacey, who agreed to join me on this journey and whose faith and love have never faltered.

Solventless Synthesis, Characterization, and Self-Assembly of Colloidal Nanocrystals

Publication No._____________

Michael Barron Sigman, Jr., Ph.D.
The University of Texas at Austin, 2005

Supervisor: Brian A. Korgel

New and general synthetic methods for materials confined to nanometer length scales are needed to provide both an experimental route for exploring material properties as a function of size and a viable means of production for commercial applications. A solventless synthesis technique was developed to produce metal sulfide and oxy-chloride nanocrystals including Cu_2S, Bi_2S_3, and $Pb_3O_2Cl_2$. A metal thiolate or metal chloride-octanoate serves as the molecular precursor for particle formation via thermolytic decomposition. Monodisperse Cu_2S nanoplatelets were synthesized with the c-axis of the hexagonal high chalcocite crystal structure oriented across the width of the disks and the {100} facets oriented along the edges. Preferred adsorption and increased surface reactivity of dodecanethiol on the more energetic {100} crystal facets results in the hexagonal prism morphology.

In comparison, Bi_2S_3 nanorods and nanowires with the orthorhombic bismuthinite crystal structure grow preferentially in the [001] direction. The aspect ratio depends on the choice of sulfur source. Nanowires were formed using dodecanethiol, while elemental sulfur results in shorter nanorods. Increased reaction temperature produced crossed networks of nanofabric with highly oriented growth resulting from the heterogeneous nucleation of wires 90^{o} from the surface of existing wires. $Pb_3O_2Cl_2$ nanobelts with the orthorhombic mendipite crystal structure were also produced. These belts are highly birefringent with a difference in the refractive index exceeding 0.48 with respect to the [010] and [100] crystallographic directions compared to the value of 0.07 for bulk mendipite.

Self-assembly methods are also needed to arrange nanocrystals into films suitable for incorporation into devices. A fundamental study of three-dimensional nanocrystal superlattice formation was performed by depositing metallic nanocrystals from different solvents. Nanocrystals drop cast from chloroform produced smooth films, while hexane resulted in mounds. Interparticle attraction is 20% higher in hexane contributing to the observed increase in growth of the films in the [111] superlattice direction. The combination of nanocrystal synthesis techniques with self-assembly methods offers the ability to produce materials with size and shape dependent properties that may then be utilized to improve the functionality of devices such as LEDs, photovoltaics, or surface sensitive sensors in the future.

Table of Contents

List of Figures

Chapter 1: Introduction

1.1 HISTORICAL BACKGROUND

"Citius, altius, fortius"* is the official Olympic motto, but it is also a suitable description for the ever increasing demands that are placed on the physical properties of materials in the continuous search to improve existing or create novel technology for commercial applications. This drive to improve performance requires the manipulation of materials at smaller and smaller length scales to achieve continual advancement. Recently, an ever increasing amount of research effort and money has focused on materials confined to nanometer dimensions in order to explore and utilize the unique properties that are exhibited during the transition from the macroscopic to the atomic level. Historically, this emphasis appears to be sudden, but it is interesting to look at some of the past uses of nanocrystals and the development of analytical techniques that initiated what Louis Brus described as "a recent burst of excitement focused on the experimental observation of the transformation from molecular to solid-state electronic properties."[1]

Biological systems first evolved mechanisms for producing and utilizing inorganic nanocrystals through biomineralization.[2] Magnetotactic bacteria contain spherical, single magnetic domain magnetite (Fe_3O_4) or greigite (Fe_3S_4) nanocrystals 45 nm in diameter that align forming chains up to 1200 nm in

---

* Latin for "Faster, higher, stronger."

length.[3] The resulting magnetic moment allows the bacteria to orient themselves with respect to the earth's magnetic field.[4] A variety of higher order organisms such as bees, migratory birds, and whales also demonstrate the ability to utilize the earth's magnetic field for navigation through mechanisms that may possibly incorporate nanocrystals. Specifically, rainbow trout and sockeye salmon have been shown to respond to magnetic fields via Fe_3O_4 nanocrystals that are associated with magnetically responsive nerves located in their nasal cavities.[5,6] Fe_3O_4 nanocrystals have been observed in human brain tissue including the hippocampus at an estimated concentration between 5 to 100 million single domain crystals per gram as well.[7] The hippocampus is an area of the brain that is responsible for basic navigation skills and has been shown to be sensitive to applied magnetic fields in individuals with epilepsy.[8,9]

Historically, nanocrystals have been used by different cultures, albeit unknowingly, to improve the physical properties of composite materials. For over 2000 years, nanocrystals have been incorporated into glass as a colorant.[10] The Lycurgus Cup is an example dating back to the Roman civilization in ~400 AD.[11] The glass of the cup contains nanocrystalline gold particles that results in a green color in reflected light and red when viewed in transmitted light.[12] Mesoamerican pottery and artwork dating between 700 and 900 AD contains paint pigments with nanocrystals of a variety of different minerals whose colors have shown reduced degradation over time relative to other pigments from similar time periods.[13] More recently, nanocrystalline carbon black has been used as a filler to improve the elastic modulus of rubber tires for over 100 years.[14]

The study of nanocrystals began almost 150 years ago as well. Michael Faraday is attributed with the first documented synthesis when he studied the color of colloidal solutions of metals in 1857. He explained the observed color of one of his gold solutions as "exceedingly fine particles, which becoming diffused, produce a beautiful ruby fluid … , but it soon changes to purple or violet."[15] Although Faraday's work initiated the study of colloidal solutions of nanocrystals, more detailed research was limited due to the lack of analytical techniques for imaging particles at such small length scales. During the late 19th and early 20th century, optical microscopy was at a relatively advanced stage of development, but the resolution is limited by the wavelength of light λ, as approximated using the Rayleigh criterion:

$$\delta = \frac{0.61\lambda}{\mu \sin \beta} \tag{1}$$

where δ is the smallest distance that can be resolved, μ is the refractive index of the medium, and β is the semi-angle of collection of the magnifying lens.[16] These conditions limit the resolution of high quality (far field) optical microscopes to ~300 nm. The limits imposed by the wavelength of light were bypassed when Knoll and Ruska successfully created the first electron microscope in 1932.[17,18] The de Broglie wavelength of an electron is inversely proportional to the square root of the accelerating voltage of the microscope offering the potential to resolve distances significantly less than the diameter of an atom (~ 4 pm for an electron accelerated at 100 keV).[16] The first electron microscopes did not exceed the resolution of existing optical microscopes, but by 1949 the construction had improved to the point that a variety of colloids with nanometer dimensions were able to be imaged.[19] Even today, the theoretical resolution limit for an electron microscope is far from being realized, but subsequent improvements in its operation, the development of the scanning electron microscope (SEM), and related analytical techniques such as electron diffraction, X-ray energy-dispersive spectrometry (EDS), and electron energy-loss spectrometry (EELS) have enabled materials to be imaged and examined at the atomic level. In 1982, Bennig and Rohrer developed the first scanning tunneling microscope (STM) initiating the development of scanning probe techniques as a second means of imaging and characterizing surfaces with atomic precision.[20] The combination of the electron microscope and scanning probe techniques provide the ability to "see" nanocrystals and are essential to the development of synthetic techniques for nanocrystal production. In addition, these analytical methods allow for the basic characterization that is necessary to further understand the effect of size, shape, and surface chemistry on the corresponding physical properties of nanocrystalline materials.

Although size effects had been of interest for many years with respect to colloidal systems,[21] significant interest in the physical properties of nanocrystals did not start until several research groups began to notice variations in their optical properties. In 1967, Berry observed a decrease in the absorption coefficient for AgI and AgBr nanocrystals relative to the bulk.[22,23] At the time, synthetic techniques suitable for producing stable nanocrystals were limited. Significant progress did not occur until the early 1980s when research groups led by Brus, Grätzel, and Henglein developed the necessary techniques while studying the photochemistry of soluble CdS and TiO_2 colloids.[24-29] These studies led to the first experimental observations of quantum size effects when the photoluminescence and absorption spectra of CdS and ZnS colloids were observed to blue shift with decreasing particle size.[30-33] The excitement generated by these experiments has contributed at least from a colloidal perspective to the rapid growth in nanotechnology research as quantified by an increase in U.S. government funding for nanotechnology R&D of over 800% between 1997 and 2004 ($116 M/yr to $961 M/yr).[34]

1.2 SIZE DEPENDENT PROPERTIES

The observed shift in the optical properties of nanocrystals confirmed what had been expected since the development of quantum mechanical theory. As the size of a material decreases, its properties shift from that of the bulk to that of an individual atom. One basic way to visualize this phenomenon is through the classical particle in a box problem. When a free particle is confined to oscillate within a one dimensional box of length a, with a potential energy of zero inside and infinity outside, then the movement of the particle may be described using the time independent Schrödinger equation:

$$\frac{\partial^2 \Psi(x)}{\partial x^2} = -\frac{2mE}{\hbar^2}\Psi(x) \tag{2}$$

where Ψ(x) is the wavefunction, m is the mass, and E is the energy of the particle. Using the boundary conditions that Ψ(x) = 0 at x = 0 and x = a, the equation has the following solution:

$$E_n = \frac{n^2\pi^2\hbar^2}{2ma^2} \quad \text{for n = 1, 2, 3 …} \tag{3}$$

Although the problem is greatly simplified, it reveals two important conclusions. First, the energy levels of confined particles shift from the continuous bands typically observed in bulk materials to discrete atomic-like values whose energy depend on the quantum number n. Second, the allowable energy levels increase as particle confinement increases with reduced box size. The schematic in Figure 1.1 illustrates the transition in energy levels for a semiconductor as it decreases in size from the macroscopic to the nanometer regime to a single molecule.

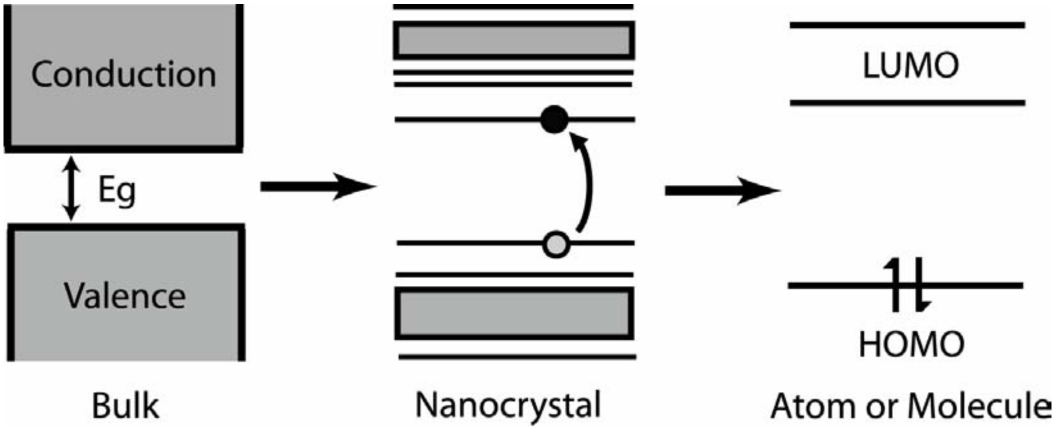

Figure 1.1: Schematic illustrating the variation in energy band structure with decreasing crystallite size for a semiconducting material. Eg is the band gap for a bulk semiconductor, LUMO is the lowest unoccupied molecular orbital, and HOMO is the highest occupied molecular orbital.

The size at which the transition from the continuous to the discrete begins to alter the optical and electronic properties of a material is the Bohr exciton radius a_b, as defined below:

$$a_b = \frac{4\pi\varepsilon\varepsilon_o\hbar^2}{m^* e^2} \tag{4}$$

where ε is the dielectric constant of the material, ε_o is the permittivity of free space, and m^* is the effective mass of the exciton. Nanocrystals smaller than this natural length scale of the electron-hole pair result in confinement of the exciton and exhibit properties unique compared to that of the bulk material.[35-37]

Size dependent confinement effects offer the ability to create materials with unique physical properties and to tune those properties based on crystallite size. These effects have been demonstrated experimentally for a variety of properties including chemical, optical, electrical, magnetic, thermal, and mechanical.[38-40] For example, the heat transport properties of nanowires and nanocrystal superlattices are size dependent.[41] When the dimensions of a nanocrystal is less in one or more dimensions than the phonon mean free path, heat transport is impeded due to phonon-boundary scattering and interfacial scattering.[42,43] Experimental results for individual nanowires ($r < 50$ nm) of Si and SnO_2 indicate a decrease in thermal conductivity of up to two orders in magnitude compared to the bulk.[44-46] These results are of interest because of the desire to make materials with high thermoelectric figures of merit ZT, which may be used to produce a variety of refrigeration and power generation devices. A reduction in thermal conductivity improves device performance as long as other often interdependent physical properties such as the electrical conductivity are not degraded as well. ZT values greater than 3 are necessary to commercialize devices that are competitive with current refrigeration and power generation processes,[47] but until recently the highest observed values were around 1. The use of nanocrystal and nanofilm superlattices have improved device performance with ZT ranging from 1.6 to 2.4 at room temperature.[48,49] This example illustrates how size confinement enables the development of materials with unique properties that may potentially alter the current state of technology in a variety of areas including LEDs,[50-53] photovoltaics,[54-58] drug delivery,[59,60] and nanoelectronics.[61-65]

In addition to confinement effects, reduced crystal size significantly increases the ratio of surface to interior atoms. A spherical particle 50 nm in diameter has ~6% of its total atoms at the surface versus 50% for a 3 nm diameter particle.[66] Atoms located at the surface of a particle have different properties due to dangling bonds and increased surface tension resulting from curvature. In terms of thermodynamics, the Gibbs-Thomson equation relates the chemical potential μ, of a particle of radius r, to surface tension γ:

$$\mu(r) = \mu(\infty) + \frac{2\gamma\Omega}{r} \qquad (5)$$

where $\mu(\infty)$ is the chemical potential of the bulk and Ω is the molecular volume of the solid. Experimentally, the effect of surface tension with respect to size is illustrated by the depression of crystal melting temperature. Goldstein et al. reported a melting point of 573 K for bare CdS nanocrystals ~1.5 nm in diameter.[67] This value is over 1100 K below the bulk melting temperature of 1678 K for CdS.

Increased surface to volume ratios also allow particle surfaces to be functionalized with a variety of surfactants that affect nanocrystal interaction with its surrounding environment. One example is the use of surface functionalization as a means of creating highly sensitive chemical sensors based on changes in a physical property, such as the conductance, of the nanocrystal.[68] In particular, nanowires have been incorporated into sensing devices that function similar to a field effect transistor.[69-71] Molecules that adsorb to the nanowire surface act as a chemical gate resulting in changes to the nanowire conductance. For example, Cui et al. used boron-doped Si nanowires to create sensitive pH sensors.[72] By functionalizing the surface with 3-aminopropyltriethoxysilane, the conductance of the wire varies with pH due to protonation and deprotonation of both the $-NH_2$ and SiOH groups on the wire surface. Alternatively, functionalizing the nanowire surfaces with streptavidin allowed them to be used as highly sensitive and specific sensors for biotin.

1.3 SHAPE DEPENDENT PROPERTIES

The coupling between size and nanocrystal shape also plays a major role in the properties of a material. Variation in the dimensionality controls the relative degree of confinement with respect to different directions altering the density of electronic states.[73] In terms of optical properties, nanorods emit linearly polarized light down the long axis of the rod relative to spherical nanocrystals that emit plane polarized light.[74] Pseudopotential calculations indicate that the change in polarization results from a shift in the highest occupied energy level of CdSe from the Se $4p_x,p_y$ to the Se $4p_z$ state as the crystal shape transforms from spherical to rod-like.[74] The photoluminescence of nanorods also shifts from higher to lower energy with increasing rod length indicating a variation in the band gap with respect to the degree of confinement in one direction.[75]

The orientation of a material's crystal lattice with respect to nanocrystal morphology also affects the resulting properties of the crystal. Particularly, materials with anisotropic crystal structures exhibit physical properties such as the refractive index, ferroelectric polarization, and electrical conductivity that are dependent on crystallographic orientation. Kuykendall et al. demonstrated that the photoluminescence of GaN nanowires of similar diameter shifts by 100 meV depending on the growth direction of the particular nanowire.[76] The effect of morphology on the moment of single magnetic domain nanocrystals is also of interest. Hexagonal Co nanodisks have been produced with the c-axis oriented across the short growth direction of the disk.[77] The typical crystallographic direction of the magnetic dipole moment is confined more strongly than the radial directions raising questions as to the resulting magnetic properties of this configuration.

Nanocrystal shape also affects surface structure by altering the prevalence of specific edge, corner, and kink sites located at energetically distinct atomic positions. The catalytic properties of nanocrystals are, therefore, specifically sensitive to shape. Narayanan and El-Sayed demonstrated that the catalytic activity of tetrahedral, cubic, and spherical Pt nanocrystals is proportional to the fraction of atoms located at the edges and corners of each type of particle for the electron-transfer reaction between hexacyanoferrate (III) and thiosulfate ions.[78,79] The tetrahedral particles with 35% of its atoms located at active surface sites exhibited rate constants over two times larger than that for the spherical particles with 13% and cubic particles with 4% of their atoms on active sites respectively.[80] Similar results were observed in the catalytic performance of spherical and cubic Pt nanocrystals used in the reduction of NO to N_2.[81]

1.4 COLLOIDAL ROUTE TO NANOCRYSTAL SYNTHESIS

In order to capitalize on the advantages of size and shape, a variety of techniques have been used to form nanocrystalline materials including chemical/physical vapor deposition,[82,83] laser ablation,[84,85] and reactive ion etching/lithographic techniques.[86] Primary disadvantages of these techniques are cost, broad particle size distributions, and low throughput. In contrast, a colloidal approach to generating nanostructured materials has proven to be useful for producing large quantities of these materials relatively cheaply with significant control over the resulting nanocrystal size and dispersity. Colloidal techniques typically involve the homogeneous nucleation and growth of nanocrystals from a supersaturated solution. The driving force for nucleation is due to a difference in Gibbs free energy ΔG, between the solute molecules in the liquid and crystalline phases:

$$\Delta G = -\frac{4\pi r^3}{3\nu}\Delta\mu + 4\pi r^2\gamma \qquad (6)$$

where ν is the molecular volume of the nucleated species and Δμ is the change in chemical potential.[21,87] ΔG consists of two terms: one corresponding to the difference in chemical potential between the two phases and the other to the surface energy necessary for the formation of curved surface area. For solute-crystal equilibrium, Δμ is defined as:

$$\Delta\mu = RT\ln\frac{c}{c_e} \qquad (7)$$

with c being the concentration of the solute and c_e the concentration of solute at equilibrium in solution. Values of ΔG greater than zero correspond to nonspontaneous processes indicating that an energetic barrier must be overcome for nucleation to occur. Figure 1.2 shows the variation of ΔG with crystal radius for a spherical particle. The radius r_c, corresponding to the maxima in ΔG is the critical radius for nucleation of a stable crystal:

$$r_c = \frac{2\nu\gamma}{RT\ln\frac{c}{c_e}} \qquad (8)$$

Nuclei with $r < r_c$ will dissolve back into solution, while crystals with $r > r_c$ have a thermodynamic driving force for continued growth as long as supersaturation conditions persist.

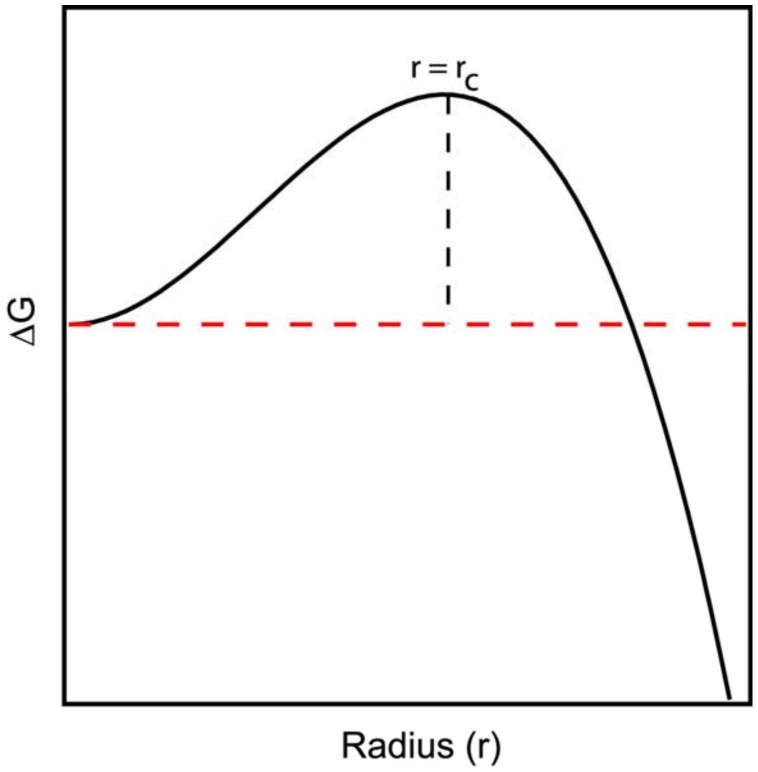

Figure 1.2: Schematic demonstrating the change in Gibbs free energy versus crystal radius.

In order to overcome the thermodynamic forces driving continued crystal growth, an arrested precipitation technique is used in which organic ligands are added that chemisorb to the crystal surface limiting continued molecular adsorption.[88] The capping ligands also protect nanocrystals from aggregation through steric repulsion.[89-92] In a good solvent, the organic ligands are well solvated extending out from the particle into the surrounding solvent. As two particles come into contact with one another, the ligands compress resulting in a repulsive force that is significantly greater than kT.[21] By at least 1984, organic ligands had been used to stabilize small molecular "clusters".[93] Fojtik et al. were the first to incorporate their use into the synthesis of true nanocrystals when they formed CdS crystals capped with $(NaPO_3)_6$ by injecting H_2S into an aqueous solution of $Cd(ClO_4)_2$.[32,94] By adjusting pH, CdS nanocrystals averaging 4 to 6 nm in diameter were produced. Due to the steric stabilization provided by the ligands, these nanocrystals were able to be removed from solution via evaporation and then redispersed without significant degradation of crystal quality. Steigerwald et al. improved on this technique by making CdSe nanocrystals via arrested precipitation in reverse micelles.[95] By varying the reverse micelle diameter, the nanocrystal diameter could be controlled between 1 and 10 nm with 25% standard deviation. Following nanocrystal formation, phenyl(trimethylsilyl) selenium was used to cap the nanocrystals making them soluble in organic solutions.

Murray et al. developed a general synthesis for II-VI CdE (E = S, Se, Te) semiconductor nanocrystals via the thermal decomposition of dimethylcadmium (Me_2Cd) and trioctylphosphine E (TOPE) in the presence of trioctylphosphine (TOP) and trioctylphospine oxide (TOPO) at 300°C.[96,97] Rapid injection of the precursor into hot solvent results in a relatively discrete nucleation period followed by slow growth via addition of monomer to existing nuclei as described by La Mer and Dinegar.[98] Following nucleation, slow nanocrystal growth consists of Ostwald ripening where a net mass transfer from smaller nanocrystals to larger ones results due to the higher solubility of crystals with increased surface curvature.[21] The size distribution of the particles ranged from 10 to 15%.[99] The gradual addition of methanol as an anti-solvent in a size selective precipitation procedure enabled the removal of larger particles resulting in a final size distribution of ± 5%.[96] Organically capped III-V semiconductors have also been produced using similar techniques in high boiling point solvents. For example, Mićić et al. produced 2.5 nm diameter InP by mixing a chloroindium oxalate complex with tris(trimethylsilyl)phospine [$(SiMe_3)P$] in a solution of TOP/TOPO at 270°C,[100] and Guzelian et al. formed InAs with sizes ranging from 2.5 to 6.0 nm in diameter via decomposition of $InCl_3$ and tris(trimethyl)arsine {$As[Si(CH_3)_3]$} in TOP at ~250°C.[101]

Colloidal synthesis techniques have also been developed to form metallic nanocrystals. In 1994, Brust et al. formed gold nanocrystals using a two phase liquid-liquid technique.[102,103] An aqueous solution of hydrogen tetrachloroaurate trihydrate was transferred to an organic toluene phase using tetraoctylammonium bromide as a phase transfer catalyst. Sodium borohydride was then added to reduce $AuCl_4^-$ to gold in the presence of a capping ligand, dodecanethiol. This technique was adapted by Korgel and Fitzmaurice to form silver nanocrystals using $AgNO_3$ as the source of Ag^+.[104] In addition, they demonstrated that the size distribution of the nanocrystals could be narrowed via the size selective precipitation technique used previously for semiconductor nanocrystals.

Size selective precipitation has proven to be a valuable technique for producing small quantities of a wide variety of monodisperse nanocrystals, but it is time intensive limiting its usefulness for large scale production. One of the major goals for new colloidal synthesis techniques is to eliminate this step forming monodisperse nanocrystals directly during the chemical synthesis. Katari et al. synthesized CdSe nanocrystals ranging in size from 1.0 to 3.3 nm with nearly monodisperse size distributions without a size selection step.[105] Their synthesis was similar to that developed by Murray et al. except that TOP was replaced with tributylphospine (TBP). The nucleation and growth of the nanocrystals were effectively separated by rapidly injecting the reactants at 350˚C and then lowering the temperature to 300˚C during a prolonged growth phase. Absorption and photoluminescence spectra were used to demonstrate that nanocrystal size increases with time while the size distribution narrows or "focuses" due to an increased rate of growth of the smaller crystals relative to the larger ones.[106,107] As monomer concentrations drop with increased particle growth, the crystals begin to "defocus" due to Ostwald ripening resulting in a broader size distribution. Variation in the concentration of reactants initially injected into hot solvent controlled nanocrystal size and determined the optimum time to reach a focused size distribution.[106] Subsequent work by the Hyeon group has utilized the separation of nucleation and growth phases to produce gram-sized batches of monodisperse Fe_2O_3, Fe_3O_4, CoO, and MnO nanocrystals via the thermal decomposition of a metal-oleate complex at 320˚C in a variety of solvents.[108]

Saunders et al. used small-angle X-ray scattering to further investigate the effect of nucleation and the subsequent growth kinetics on the size distribution of gold nanocrystals formed using the previously mentioned two phase synthesis.[88,102] Two cases were examined. The first separated the nucleation step from the growth phase by slowly adding reducing agent until the solution went clear with a light brown tint indicating that stable nuclei had just formed. The remainder of the reducing agent was then added at once to start the growth phase. The second case was for concurrent nucleation and growth, in which all of the reducing agent was added immediately. Interestingly, the initial growth kinetics had no effect on the resulting size distribution of the particles. Both cases experienced a reduction in size distribution over time with a final particle size that was dependent on the binding strength of the organic ligand used during particle growth.

1.5 ANISOTROPIC NANOCRYSTAL GROWTH

The formation of nonspherical nanocrystals has received significant interest in order to study the relationship between confinement and shape. A variety of non-colloidal techniques have been used to generate anisotropic nanocrystal growth including vapor deposition methods,[83,109-115] vapor-liquid-solid growth,[116,117] templated growth,[118] and self-assembly.[104] These techniques are advantageous with regard to forming nonspherical geometries because they utilize methods that either direct growth or occur at high temperatures (greater than the boiling point of most solvents) where kinetic growth is highly favored. In contrast, colloidal routes tend to result in more thermodynamically favorable faceted spherical crystals. Spheres are preferred because they minimize the surface to volume ratio resulting in a minimum total surface energy for the particle. Regardless of this limitation, the development of colloidal techniques for asymmetric nanocrystal formation has improved and is desirable in order to increase production and reduce synthesis cost.

Materials with highly anisotropic crystal structures have been shown to form nonspherical morphologies in solution due to variations in the kinetic rate of growth along different crystallographic axes. Examples include the formation of Se and Te nanowires in aqueous solutions via the reduction of selenious acid (H_2SeO_3) or orthotelluric acid (H_6TeO_6) with hydrazine (N_2H_4) at ~100°C.[119-121] The trigonal crystal structure of these materials form helical chains in the direction of the c-axis significantly favoring growth in that direction forming wire morphologies.[118] The resulting wires range in diameter from 10 to 100 nm and are microns in length. Systems exhibiting such highly anisotropic growth are not common. Typically, high levels of precursor supersaturation and the use of surfactants are necessary to enhance their growth.

The Alivisatos group demonstrated that the choice of capping ligand can significantly alter the resulting shape of nanocrystals formed in supersaturated solutions.[122,123] By selecting ligands that selectively bind more strongly to specific crystal facets, the rate of crystal growth in specific directions can be controlled. The ligand also reduces the surface energy of particular crystal facets stabilizing anisotropic shapes that would typically evolve into a more favorable spherical morphology. For example, spherical CdSe nanocrystals are produced by injecting dimethylcadmium [$Cd(CH_3)_2$] and elemental Se dissolved in tributylphosphine into TOPO at 300°C.[106] TOPO acts as the capping ligand stabilizing the spherical nanocrystals. The addition of hexyl-phosphonic acid, HPA ($C_6H_{15}PO_3$), as a second capping ligand results in an elongated nanorod morphology with the long axis of the rod directed along the c-axis of the CdSe wurtzite crystal structure.[123] Nanorods formed using a single injection were 3 nm in diameter with aspect ratios of ~5:1. The length of the nanorods was increased to greater than 100 nm by performing multiple injections of precursor during the course of the reaction.[124] In comparison, the shape control of Co nanocrystals has also been demonstrated. Spherical Co nanocrystals were produced by injecting a solution of di-cobalt octa-carbonyl [$Co_2(CO)_8$] into a pre-heated (182°C) solution of *o*-dichlorobenzene with oleic acid.[77] By adding TOPO or linear amines as a second capping ligand, Co nanodisks or platelets were formed.[122] In contrast to CdSe, the additional ligand stabilizes the (001) facets of the hexagonal Co crystal structure limiting growth along its c-axis.[77] In addition, the use of surfactants to control nanocrystal shape has been demonstrated for the GaP and TiO_2 nanocrystal systems.[125,126]

Surfactants have also been used to form more complex branched tetrapod structures of CdSe and CdTe.[127] High yields of CdTe tetrapods were formed by injecting Te powder dissolved in TOP into a solution of CdO, TOPO, and n-octadecylphosphonic acid ($C_{18}H_{39}O_3P$ or ODPA) at 320°C.[128] These structures are polytypic with the core consisting of a cubic (zinc blende) crystal structure terminated by four {111} facets that initiate the formation of four rod-like arms growing in the (0001) direction of the hexagonal (wurtzite) CdTe crystal structure.[128] The zinc blende structure of CdTe nucleates as the central core, but the presence of ODPA as a capping ligand stabilizes the surfaces of the wurtzite structure resulting in the growth of four arms of a different crystal structure.[128,129]

In addition to surfactant effects, Peng and coworkers examined the effect of precursor concentration on the growth of CdSe nanocrystals using a technique similar to that he helped develop in the Alivisatos group.[130-132] By increasing the concentration of injected precursor, they found that nanorods were produced under conditions that previously had produced spheres.[131] Increased supersaturation levels result in a higher chemical potential reaction environment favoring anisotropic growth.[132] A diffusion limited growth mechanism was proposed to explain the observed variation of CdSe nanocrystal shape from spherical to rice shaped to rods to branched nanorods with increasing precursor concentration.[130] These results illustrated that, although capping ligand chemistry is important, the level of precursor supersaturation is a critical factor in the resulting nanocrystal shape as well.

Joo et al. also noted the importance of concentration on the resulting morphology of CdS nanocrystals.[133] CdS nanocrystals were formed by reacting $CdCl_2$ and elemental sulfur in oleylamine at 140°C for 20 hours. Samples formed with excess molar ratios of S formed relatively monodisperse spherical nanocrystals, while samples formed with excess Cd resulted in nanorods and branched bipods and tripods. In addition to illustrating the effect of precursor concentration on nanocrystal shape, this technique also proved to be a high quality route for producing a variety of monodisperse metal sulfides including

PbS cubes, ZnS spheres, and MnS rods by simply varying the metal chloride used in the synthesis.[133]

The shape of materials with isotropic cubic crystal structures have been elongated using surfactants combined with nucleating seed particles. Au nanorods were produced in aqueous solution using a seed-mediated surfactant-directed technique.[134-137] Gold nanocrystals, 4 nm in diameter, are used to seed the subsequent formation of nanorods by reducing $HAuCl_4$ with ascorbic acid in the presence of the surfactant cetyltrimethylammonium bromide (CTAB).[135] Ascorbic acid is a weak reducing agent that does not nucleate crystals, but does enable their heterogeneous growth in the presence of a seed. This technique effectively separates the nucleation and growth phases of the rods allowing anisotropic growth in the presence of CTAB which binds more strongly to the {100} crystal facets resulting in growth in the [110] direction.[134] Ag nanorods have been formed using a similar seed-mediated technique. In this case, $AgNO_3$ is reduced by ethylene glycol in the presence of poly(vinyl pyrrolidone) as a capping ligand.[138-141]

A solution-liquid-solid growth mechanism has been used to form nanowires in solution using metallic liquid droplets as sites for nucleation and growth. This technique is similar to the vapor-liquid-solid mechanism, except that low melting point metals such as Bi, In, or Sn are used which form liquid droplets at temperatures suitable for use with high boiling point organic solvents.[118] The reactants for the particular nanowire synthesis dissolve within the metallic droplet until suitable supersaturation levels are reached and nucleation occurs. The Buhro group used this technique to form InP, InAs, GaAs, InN, and $Al_xGa_{1-x}As$ nanowires with diameters ranging from 3 to 100 nm.[142-146] A typical synthesis includes the addition of tri-*tert*-butyl indane and phoshine to a solution of 90 mol % toluene and 10 mol % phenylthiol at 111°C.[143] Metallic droplets form either through the thermal decomposition of $(t\text{-}Bu)_3In$ or by adding In nanocrystals directly to the solution.[142] Although this is a promising route for nanowire synthesis, wire quality tends to be low. The growth of wires from liquid metal droplets in supercritical fluids was demonstrated by the Korgel group to form Si, Ge, and GaAs.[147-150] Supercritical fluids enable the use of increased synthesis temperatures and pressures allowing the formation of high quality single crystalline wires over a broader range of synthesis conditions.[151]

1.6 SELF-ASSEMBLY OF NANOCRYSTAL SUPERLATTICES FROM SOLUTION

A variety of potential uses for nanocrystals, such as sensors, LEDs, photovoltaics, and electronics, require thin films of particles. One of the advantages of colloidal nanocrystals is the ability to form films of ordered particles (superlattices) by depositing them directly from solution onto a substrate. Small angle X-ray scattering (SAXS) has demonstrated that during solvent evaporation size monodisperse nanocrystals self-assemble into organized close packed structures via natural transport and thermodynamic processes.[89,152,153] The interparticle separation within the film is controlled by the length of the organic ligand used to cap the particles.[154,155] Therefore, the organization of nanocrystals into ordered mesoscopic structures enables the creation of novel materials whose collective properties are controllable not only by the choice of material but also by the spatial orientation of the particles within the superlattice. For example, the electrical and optical properties of metallic nanocrystal films have been shown to go through a metal-insulator transition based on interparticle spacing and the degree of superlattice order.[156-158]

Initial research regarding superlattice formation began in the 1930s with X-ray studies of ordered sub-micron sized amorphous silica particles that make up natural deposits of opal.[159] Researchers were particularly interested in the difference in color or 'fire' observed in specimens obtained from different areas of the world.[160] This phenomenon was found to result from the diffraction of light off of the surfaces of these three dimensional superlattices with the color exhibited by a particular opal depending on the size and packing of its constituent colloids. [161-163] Understanding of colloidal crystallization began with the study of hard spheres, idealized spheres without attractive or repulsive interparticle forces. With no energetic potential between the spheres, entropy governs the packing behavior. Numerous computational and experimental studies have been performed studying the nucleation and phase behavior of hard spheres from solution.[164-171] Frenkel described the entropic driving force for crystallization as the result of an increase in the microscopic disorder that exceeded the macroscopic "configurational" loss in entropy due to crystallization.[172,173] This increase in microscopic disorder was attributed to an increase in the free volume of the spheres at each lattice site within the crystal over that experienced in the dense liquid. These studies demonstrated that small differences in the driving force for crystallization of solutions of monodisperse hard spheres can result in ordered, self-assembled structures.

In 1989, the first examples of ordered nanocrystal superlattices were synthesized via heterogeneous nucleation at a solid or liquid interface. Schmid and Lehnert formed small ordered domains consisting of 20 nm diameter ($\sigma = \pm 10\%$) Au nanocrystals.[174,175] In the same year, Bentzon et al. used iron oxide particles 6.9 nm in diameter with a similar size distribution to form significantly larger hexagonal close packed superlattices.[176] Unlike hard spheres, a variety of forces including van der Waals, electrostatic, and magnetic contribute to the ordering of superlattices. In 1995, Ohara et al. demonstrated the size dependence of van der Waals attraction on the alignment of a polydisperse mixture of Au nanoparticles.[177] In these experiments, the attractive force between particles due to van der Waals interactions were dominant over the entropic packing factors that have been determined to govern packing in hard spheres. TEM images of superlattices showed larger particles in a hexagonal pattern surrounded by progressively smaller and smaller particles at the outer portions of the formation. Simulations were also performed to qualitatively describe this phenomena using the theory developed by Hamaker to determine the interparticle potentials.[178] Therefore, the magnitude of the attractive force between particles can be controlled to some extent via the size of the particles used to form the superlattice.

In addition to van der Waals forces, the organic capping ligands attached to the nanocrystal surface greatly affect the interactions between particles in solvent. As opposed to hard spheres which have an infinitely large repulsion upon contact, capped nanocrystals are more characteristic of “soft” spheres that experience a gradual increase in the steric repulsive force as ligands are compressed.[179] As solvent evaporates, supersaturation levels increase reducing this repulsive force to the point that heterogeneous nucleation occurs onto the substrate. Factors such as surface coverage, ligand orientation, and ligand length control the nature of this repulsion and the subsequent superlattice formation.

Luedtke and Landman performed molecular dynamics simulations of the preferred packing arrangements of capping ligands on Au nanoparticles organized into 3D superlattices.[155,180] They predicted that the superlattice packing could be changed from body centered cubic (bcc) to tetragonally distorted face centered cubic (t-fcc) to face centered cubic (fcc) depending on the degree of ligand bundling.[155] The different configurations were attributed to the orientational freedom of the ligands and were dependant on ligand length and temperature. These theoretical findings were confirmed by Whetten et al. who studied the phase behavior of Au nanoparticle superlattices of varying particle size and capping ligand length.[181] They used the dimensionless quantity $\chi = 2L/D_{core}$ (L equals ligand length and D_{core} is the diameter of the crystalline nanoparticle core) to summarize these results into a phase diagram. The transition from fcc to bcc structures occurs at $\chi = 0.73$ with a corresponding Au volume fraction of 22%. Hcp structures were not observed experimentally, but were noted to be expected at values of $\chi < 0.3$.

Interparticle spacing within the superlattice increases with ligand length, but it has been found to be less than twice the full length of the ligand indicating that they become entangled.[182,183] The interdigitation of ligands has been described as a means of particles "bonding" to one another resulting in correlation between the atomic crystal structure of the individual nanocrystals and the overall superlattice orientation.[184,185] Spherical nanoparticles (typically < 10 nm) are actually highly faceted exhibiting numerous shapes such as tetrahedron, truncated octahedron, decahedron, and icosahedron.[104,186,187] Ligand packing and alignment varies depending on which crystallographic planes are exposed on the surface of the nanocrystal.[188-190] For example, truncated octahedral shaped Ag nanoparticles were shown to align with the same exposed facets oriented towards one another (i.e. {111} planes align together and {100} planes align together).[184-186,191] Alignment between equivalent crystal facets maximizes van der Waals interactions due to increased surface exposure between neighboring nanocrystals.[155,179]

The effect of solvent conditions on the heterogeneous nucleation and growth of superlattices has also been studied. Korgel and Fitzmaurice described the formation of nanocrystal superlattices as wetting films which spread on the substrate as a function of the surface tensions between the solvent, substrate, and nanocrystals.[192] Nanocrystal film thickness was found to be dependent on solvent polarity. Superlattices formed from pure chloroform resulted in a monolayer of hexagonally ordered nanocrystals. The addition of a polar solvent (ethanol) increased van der Waals attraction which reduced the spreading of the nanocrystal film resulting in layered superlattice growth versus two dimensional monolayers.

The rate of solvent evaporation has been noted as having a significant effect on the corresponding order of the superlattice. Harfenist et al. formed 3D hexagonal superlattices made of silver particles.[193] Samples formed while adding additional solvent during the evaporation exhibited a greater degree of faceting and order than those formed without additional solvent. Lin et al. demonstrated that by adding excess dodecanethiol capping ligand to Au nanoparticles in toluene they could increase drying times and the corresponding order seen in the monolayer over a range of microns.[194] The less volatile dodecanethiol slowed the overall evaporation rate of the solvent droplet giving the particles longer to orient into an ordered array. The capping ligand is also attributed with having a lubricating effect during the settling of particles on the substrate.[155] This allows greater movement of the particle both on the substrate surface as well as between other particles.

Under appropriate conditions, homogeneous nucleation and growth of colloidal crystals has been initiated from solution. Compared to heterogeneous nucleation, this requires significantly higher levels of nanocrystal supersaturation within the solvent. In order to prevent heterogeneous nucleation from occurring first, slow methods of increasing supersaturation have been developed. Murray et al. accomplished this by gradually heating monodisperse CdSe nanocrystals in a solution that initially consisted of octane with ~10% octanol.[195] Octane boils off preferentially, increasing the concentration of the more polar octanol. Octanol acts as an antisolvent reducing nanocrystal solubility within the solution and initiating homogeneous nucleation. Faceted colloidal crystals with fcc packing formed measuring 5 to 50 μm in size. Talapin et al. formed colloidal crystals via the slow diffusion of an antisolvent (methanol) through a buffer solution (propan-2-ol) into a solution of CdSe nanocrystals in toluene.[196] Hexagonal platelets 100 μm in diameter and 20 μm in thickness formed over the course of two months.

1.7 DISSERTATION OVERVIEW

A novel solventless synthesis technique was developed forming several metal sulfide and oxy-chloride nanocrystals. This technique offers the advantage over other solvent based colloidal syntheses of limiting interparticle diffusion and collisions during nanocrystal growth. The effect of this technique on particle size distribution and nanocrystal shape is examined. The solventless synthesis of Cu_2S nanocrystals is discussed in Chapter 2. Monodisperse Cu_2S hexagonal platelets were formed via the thermolysis of a copper alkylthiolate precursor. The relationship between the Cu_2S hexagonal (high chalcocite) crystal structure and the resulting nanocrystal morphology is examined using HRTEM. A face-sensitive surface reactivity mechanism is proposed to explain the growth of these anisotropically shaped nanocrystals. Chapter 3 discusses the solventless synthesis of Bi_2S_3 nanorods and nanowires. The aspect ratio of the nanocrystals is controlled by the choice of sulfur source. The addition of sulfur through the thermal decomposition of thiol results in nanowire growth, while elemental sulfur results in shortened nanorods. Elevated reaction temperatures are shown to induce heterogeneous nucleation of nanowires that grow 90° from existing ones resulting in elaborate nanofabric structures.

In addition to the formation of metal sulfides, $Pb_3O_2Cl_2$ nanobelts were formed using the solventless synthesis technique. Chapter 4 covers the formation of these nanobelts which consist of mendipite with an orthorhombic crystal structure. HRTEM and electron diffraction were used to confirm that the belts grow in the [010] direction which coincides with the direction that chains of linked (OPb_4) tetrahedra occur within the natural crystal structure. Elongation of these chains is believed to cause the resulting belt-like morphology. The nanobelts are highly birefringent with a difference in refractive index between the allowable vibration directions for light being approximately an order of magnitude larger than that found for bulk mendipite.

The formation of three dimensional Au and Ag nanocrystal superlattices drop cast from various solvents is discussed in Chapter 5. SEM imaging was used to study the dependence of film morphology on the solvent used during deposition. Nanocrystals drop cast from hexane produced rough superlattice films consisting of mounds that formed via successive 2D nucleation. Superlattices formed using chloroform resulted in smoother films that grow through screw dislocations. Addition of ethanol as an antisolvent prior to drop casting led to superlattices with decreased order resulting from dendritic growth. Sonication promoted homogeneous superlattice nucleation and growth by providing the energy required to overcome the nucleation energy barrier

1.8 REFERENCES

(1) Brus, L. *J. Phys. Chem.* **1986**, *90*, 2555.

(2) Bäuerlein, E. *Angew. Chem. Int. Ed.* **2003**, *42*, 614.

(3) Dunin-Borkowski, R. E.; McCartney, M. R.; Frankel, R. B.; Bazylinski, D. A.; Pósfai, M.; Buseck, P. R. *Science* **1998**, *282*, 1868.

(4) Frankel, R. B. *Annu. Rev. Biophys. Bioeng.* **1984**, *13*, 85.

(5) Walker, M. W.; Diebel, C. E.; Haugh, C. V.; Pankhurst, P. M.; Montgomery, J. C.; Green, C. R. *Science* **1997**, *390*, 371.

(6) Mann, S.; Sparks, N. H. C.; Walker, M. M.; Kirschvink, J. L. *J. Exp. Biol.* **1988**, *140*, 35.

(7) Kirschvink, J. L.; Kobayashi-Kirschvink, A.; Woodford, B. J. *Proc. Natl. Acad. Sci. USA* **1992**, *89*, 7683.

(8) Schultheiss-Grassi, P. P.; Wessiken, R.; Dobson, J. *Biochem. Biophys. Acta* **1999**, *1426*, 212.

(9) Fuller, M.; Dobson, J.; Wieser, H. G.; Moser, S. *Brain Res. Bull.* **1995**, *36*, 155.

(10) Mulvaney, P. Metal Nanoparticles: Double Layers, Optical Properties, and Electrochemistry. In *Nanoscale Materials in Chemistry*; Klabunde, K. J., Ed.; John Wiley & Sons, Inc.: New York, 2001; pp 121.

(11) Barber, D. J.; Freestone, I. C. *Archaeometry* **1990**, *32*, 33.

(12) Wagner, F. E.; Haslbeck, S.; Stievano, L.; Calogero, S.; Pankhurst, Q. A.; Martinek, K.-P. *Nature* **2000**, *407*, 691.

(13) Ortega-Avilés, M.; San-Germán, C. M.; Mendoza-Anaya, D.; Morales, D.; José-Yacamán, M. *J. Mater. Sci.* **2001**, *36*, 2227.

(14) Friedlander, S. K. *J. Nanopart. Res.* **1999**, *1*, 9.

(15) Faraday, M. *Phil. Trans R. Soc. London* **1857**, *147*, 145.

(16) Williams, D. B.; Carter, C. B. *Transmission Electron Microscopy: A Textbook for Materials Science*; Plenum Press: New York, 1996.

(17) Knoll, M.; Ruska, E. *Z. Physik* **1932**, *78*, 318.

(18) Ruska, E. *Rev. Mod. Phys.* **1987**, *59*, 627.

(19) Turkevich, J.; Hillier, J. *Anal. Chem.* **1949**, *21*, 475.

(20) Binning, G.; Rohrer, H.; Gerber, C.; Weibel, E. *Phys. Rev. Lett.* **1982**, *49*, 57.

(21) Hunter, R. J. *Foundations of Colloid Science*, 2nd ed.; Oxford University Press: New York, 2001.

(22) Berry, C. R. *Phys. Rev.* **1967**, *161*, 611.

(23) Berry, C. R. *Phys. Rev.* **1967**, *153*, 989.

(24) Duonghong, D.; Borgarello, E.; Grätzel, M. *J. Am. Chem. Soc.* **1981**, *103*, 4685.

(25) Rossetti, R.; Brus, L. *J. Phys. Chem.* **1982**, *86*, 4470.

(26) Henglein, A. *Ber. Bunsenges. Phys. Chem.* **1982**, *86*, 301.

(27) Fox, M. A.; Lindig, B.; Chen, C.-C. *J. Am. Chem. Soc.* **1982**, *104*, 5828.

(28) Duonghong, D.; Ramsden, J.; Grätzel, M. *J. Am. Chem. Soc.* **1982**, *104*, 2977.

(29) Moser, J.; Grätzel, M. *J. Am. Chem. Soc.* **1983**, *105*, 6547.

(30) Rossetti, R.; Nakahara, S.; Brus, L. E. *J. Chem. Phys.* **1983**, *79*, 1086.

(31) Ramsden, J. J.; Grätzel, M. *J. Chem. Soc., Faraday Trans. 1* **1984**, *80*, 919.

(32) Fojtik, A.; Weller, H.; Koch, U.; Henglein, A. *Ber. Bunsenges. Phys. Chem.* **1984**, *88*, 969.

(33) Brus, L. E. *J. Chem. Phys.* **1984**, *80*, 4403.

(34) Based on figures from the National Nanotechnology Initiative website, www.nano.gov.

(35) Norris, D. J. Electronic Structure in Semiconductor Nanocrystals. In *Semiconductor and Metal Nanocrystals: Synthesis and Electronic and Optical Properties*; Klimov, V. I., Ed.; Marcel Dekker, Inc.: New York, 2004; Vol. 87; pp 484.

(36) Bawendi, M. G.; Steigerwald, M. L.; Brus, L. E. *Annu. Rev. Phys. Chem.* **1990**, *41*, 477.

(37) Alivisatos, A. P. *Science* **1996**, *271*, 933.

(38) *Nanomaterials: Synthesis, Properties, and Applications*; Edelstein, A. S.; Cammarata, R. C., Eds.; Institute of Physics Publishing: Philadelphia, 2001.

(39) *Semiconductor and Metal Nanocrystals: Synthesis and Electronic and Optical Properties*; Klimov, V. I., Ed.; Marcel Dekker, Inc.: New York, 2004; Vol. 87, pp 484.

(40) *Nanoscale Materials in Chemistry*; Klabunde, K. J., Ed.; John Wiley & Sons, Inc.: New York, 2001.

(41) Hicks, L. D.; Dresselhaus, M. S. *Phys. Rev. B* **1993**, *47*, 16631.

(42) Law, M.; Goldberger, J.; Yang, P. *Annu. Rev. Mater. Res.* **2004**, *34*, 83.

(43) Chen, G. *Int. J. Therm. Sci.* **2000**, *39*, 471.

(44) Shi, L.; Hao, Q.; Yu, C.; Mingo, N.; Kong, X.; Wang, Z. L. *Appl. Phys. Lett.* **2004**, *84*, 2638.

(45) Li, D.; Wu, Y.; Kim, P.; Shi, L.; Yang, P.; Majumdar, A. *Appl. Phys. Lett.* **2003**, *83*, 2934.

(46) Shi, L.; Li, D.; Yu, C.; Jang, W.; Kim, D.; Yao, Z.; Kim, P.; Majumdar, A. *J. Heat Trans.* **2003**, *125*, 881.

(47) Majumdar, A. *Science* **2004**, *303*, 777.

(48) Harman, T. C.; Taylor, P. J.; Walsh, M. P.; LaForge, B. E. *Science* **297**, *297*, 2229.

(49) Venkatasubramanian, R.; Siivola, E.; Colpitts, T.; O'Quinn, B. *Nature* **2001**, *413*, 597.

(50) Colvin, V. L.; Schlamp, M. C.; Alivisatos, A. P. *Nature* **1994**, *370*, 354.

(51) Artemyev, M. V.; Sperling, V.; Woggon, U. *J. Appl. Phys.* **1997**, *81*, 6975.

(52) Coe, S.; Woo, W.-K.; Bawendi, M.; Bulovic, V. *Nature* **2002**, *420*, 800.

(53) Mattoussi, H.; Radzilowski, L. H.; Dabbousi, B. O.; Fogg, D. E.; Schrock, R. R.; Thomas, E. L.; Rubner, M. F.; Bawendi, M. G. *J. Appl. Phys.* **1999**, *86*, 4390.

(54) Muller, R. H.; Keck, C. M. *J. Biotech.* **2003**, *113*, 151.

(55) Sun, B.; Marx, E.; Greenham, N. C. *Nano Lett.* **2003**, *3*, 961.

(56) Huynh, W. U.; Dittmer, J. J.; Libby, W. C.; Whiting, G. L.; Alivisatos, A. P. *Adv. Funct. Mater.* **2003**, *13*, 73.

(57) Huynh, W. U.; Peng, X.; Alivisatos, A. P. *Adv. Mater.* **1999**, *11*, 923.

(58) Plass, R.; Pelet, S.; Krueger, J.; Grätzel, M. *J. Phys. Chem. B* **2002**, *106*, 7578.

(59) Ozkan, M. *Drug Disc. Today* **2004**, *9*, 1065.

(60) Barbé, C.; Bartlett, J.; Kong, L.; Finnie, K.; Lin, H. Q.; Larkin, M.; Calleja, S.; Bush, A.; Calleja, G. *Adv. Mater.* **2004**, *16*, 1959.

(61) Ferry, D. K.; Goodnick, S. M. *Transport in Nanostructures*; Cambridge University Press: USA, 1999; Vol. 6.

(62) Huang, Y.; Duan, X.; Cui, Y.; Lauhon, L. J.; Kim, K.-H.; Lieber, C. M. *Science* **2001**, *294*, 1314.

(63) Duan, X.; Huang, Y.; Lieber, C. M. *Nano Lett.* **2002**, *2*, 487.

(64) McAlpine, M. C.; Friedman, R. S.; Jin, S.; Lin, K.; Wang, W. U.; Lieber, C. M. *Nano Lett.* **2003**, *3*, 1531.

(65) Jin, S.; Whang, D.; McAlpine, M. C.; Friedman, R. S.; Wu, Y.; Lieber, C. M. *Nano Lett.* **2004**, *4*, 915.

(66) Klabunde, K. J.; Mulukutla, R. S. Chemical and Catalytic Aspects of Nanocrystals. In *Nanoscale Materials in Chemistry*; Klabunde, K. J., Ed.; John Wiley & Sons, Inc.: New York, 2001.

(67) Goldstein, A. N.; Echer, C. M.; Alivisatos, A. P. *Science* **1992**, *256*, 1425.

(68) Kolmakov, A.; Moskovits, M. *Annu. Rev. Mater. Res.* **2004**, *34*, 151.

(69) Kong, J.; Franklin, N. R.; Zhou, C.; Chapline, M. G.; Peng, S.; Cho, K.; Dai, H. *Science* **2000**, *287*, 622.

(70) Kolmakov, A.; Zhang, Y.; Cheng, G.; Moskovits, M. *Adv. Mater.* **2003**, *15*, 997.

(71) Arnold, M. S.; Avouris, P.; Pan, Z. W.; Wang, Z. L. *J. Phys. Chem. B* **2003**, *107*, 659.

(72) Cui, Y.; Wei, Q.; Park, H.; Lieber, C. M. *Science* **2001**, *293*, 1289.

(73) Alivisatos, A. P. *J. Phys. Chem.* **1996**, *100*, 13226.

(74) Hu, J.; Li, L.; Yang, W.; Manna, L.; Wang, L.; Alivisatos, A. P. *Science* **2001**, *292*, 2060.

(75) L.Li; Hu, J.; Yang, W.; Alivisatos, A. P. *Nano Lett.* **2001**, *1*, 349.

(76) Kuykendall, T.; Pauzauskie, P. J.; Zhang, Y.; Goldberger, J.; Sirbuly, D.; Denlinger, J.; Yang, P. *Nature Mater.* **2004**, *3*, 524.

(77) Puntes, V. F.; Zanchet, D.; Erdonmez, C. K.; Alivisatos, A. P. *J. Am. Chem. Soc.* **2002**, *124*, 12874.

(78) Narayanan, R.; El-Sayed, M. A. *J. Am. Chem. Soc.* **2004**, *126*, 7194.

(79) Narayanan, R.; El-Sayed, M. A. *J. Phys. Chem. B* **2004**, *108*, 5726.

(80) Narayanan, R.; El-Sayed, M. A. *Nano Lett.* **2004**, *4*, 1343.

(81) Balint, I.; Miyazaki, A.; Aika, K. *Phys. Chem. Chem. Phys.* **2004**, *6*, 2000.

(82) Zhang, B. P.; Binh, N. T.; Wakatsuki, K.; Segawa, Y.; Yamada, Y.; Usami, N.; Kawasaki, M.; Koinuma, H. *J. Phys. Chem. B* **2004**, *108*, 10899.

(83) Wang, Z. L. *Annu. Rev. Phys. Chem.* **2004**, *55*, 159.

(84) Werwa, E.; Seraphin, A. A.; Chiu, L. A.; Zhou, C.; Kolenbrander, K. D. *Appl. Phys. Lett.* **1994**, *64*, 1821.

(85) Morales, A. M.; Lieber, C. M. *Science* **1998**, *279*, 208.

(86) Ingert, D.; Pileni, M. P. *J. Phys. Chem. B* **2003**, *107*, 9618.

(87) Toschev, S. Homogeneous Nucleation. In *Crystal Growth: An Introduction*; Hartman, P., Ed.; American Elsevier: New York, 1973; Vol. 1.

(88) Saunders, A. E.; Sigman, M. B.; Korgel, B. A. *J. Phys. Chem. B* **2004**, *108*, 193.

(89) Saunders, A. E.; Korgel, B. A. *J. Phys. Chem. B* **2004**, *108*, 16732.

(90) Shah, P. S.; Hanrath, T.; Johnston, K. P.; Korgel, B. A. *J. Phys. Chem. B* **2004**, *108*, 9574.

(91) Shah, P. S.; Husain, S.; Johnston, K. P.; Korgel, B. A. *J. Phys. Chem. B* **2002**, *106*, 12178.

(92) Shah, P. S.; Holmes, J. D.; Johnston, K. P.; Korgel, B. A. *J. Phys. Chem. B* **2002**, *106*, 2545.

(93) Dance, I. G.; Choy, A.; Scudder, M. L. *J. Am. Chem. Soc.* **1984**, *106*, 6285.

(94) Spanhel, L.; Haase, M.; Weller, H.; Henglein, A. *J. Am. Chem. Soc.* **1987**, *109*, 5649.

(95) Steigerwald, M. L.; Alivisatos, A. P.; Gibson, J. M.; Harris, T. D.; Kortan, R.; Muller, A. J.; Thayer, A. M.; Duncan, T. M.; Douglass, D. C.; Brus, L. E. *J. Am. Chem. Soc.* **1988**, *110*, 3046.

(96) Murray, C. B.; Norris, D. J.; Bawendi, M. G. *J. Am. Chem. Soc.* **1993**, *115*, 8706.

(97) Murray, C. B.; Kagan, C. R.; Bawendi, M. G. *Annu. Rev. Mater. Sci.* **2000**, *30*, 545.

(98) LaMer, V. K.; Dinegar, R. H. *J. Am. Chem. Soc.* **1950**, *72*, 4847.

(99) Reiss, H. *J. Chem. Phys.* **1951**, *19*, 482.

(100) Micic, O. I.; Curtis, C. J.; Jones, K. M.; Sprague, J. R.; Nozik, A. J. *J. Phys. Chem.* **1994**, *98*, 4966.

(101) Guzelian, A. A.; Banin, U.; Kadavanich, A. V.; Peng, X.; Alivisatos, A. P. *Appl. Phys. Lett.* **1996**, *69*, 1432.

(102) Brust, M.; Walker, M.; Bethell, D.; Schiffrin, D. J.; Whyman, R. *J. Chem. Soc., Chem. Commun.* **1994**, 801.

(103) Brust, M.; Fink, J.; Bethell, D.; Schiffrin, D. J.; Kiely, C. *J. Chem. Soc., Chem. Commun.* **1995**, 1655.

(104) Korgel, B. A.; Fitzmaurice, D. *Adv. Mater.* **1998**, *10*, 661.

(105) Katari, J. E. B.; Colvin, V. L.; Alivisatos, A. P. *J. Phys. Chem.* **1994**, *98*, 4109.

(106) Peng, X.; Wickham, J.; Alivisatos, A. P. *J. Am. Chem. Soc.* **1998**, *120*, 5343.

(107) Sugimoto, T. *Adv. Colloid Interfac. Sci.* **1987**, *28*, 65.

(108) Park, J.; An, K.; Hwang, Y.; Park, J.-G.; Noh, H.-J.; Kim, J.-Y.; Park, J.-H.; Hwang, N.-M.; Hyeon, T. *Nature Mater.* **2004**, *3*, 891.

(109) Wu, Y.; Cui, Y.; Huynh, L.; Barrelet, C. J.; Bell, D. C.; Lieber, C. M. *Nano Lett.* **2004**, *4*, 433.

(110) Ma, D. D. D.; Lee, C. S.; Au, F. C. K.; Tong, S. Y.; Lee, S. T. *Science* **2003**, *299*, 1874.

(111) Kong, X. Y.; Wang, Z. L. *Nano Lett.* **2003**, *3*, 1625.

(112) Ma, C.; Moore, D.; Li, J.; Wang, Z. L. *Adv. Mater.* **2003**, *15*, 228.

(113) Hughes, W. L.; Wang, Z. L. *J. Am. Chem. Soc.* **2004**, *126*, 6703.

(114) Kong, X. Y.; Ding, Y.; Yang, R.; Wang, Z. L. *Science* **2004**, *303*, 1348.

(115) Pan, Z. W.; Dai, Z. R.; Wang, Z. L. *Science* **2001**, *291*, 1947.

(116) Yu, J.-Y.; Chung, S.-W.; Heath, J. R. *J. Phys. Chem. B* **2000**, *104*, 11864.

(117) Ding, Y.; Gao, P. X.; Wang, Z. L. *J. Am. Chem. Soc.* **2004**, *126*, 2066.

(118) Xia, Y.; Yang, P.; Sun, Y.; Wu, Y.; Mayers, B.; Gates, B.; Yin, Y.; Kim, F.; Yan, H. *Adv. Mater.* **2003**, *15*, 353.

(119) Gates, B.; Yin, Y.; Xia, Y. *J. Am. Chem. Soc.* **2000**, *122*, 12582.

(120) Gates, B.; Mayers, B.; Cattle, B.; Xia, Y. *Adv. Funct. Mater.* **2002**, *12*, 219.

(121) Mayers, B.; Xia, Y. *J. Mater. Chem.* **2002**, *12*, 1875.

(122) Puntes, V. F.; Krishnan, K. M.; Alivisatos, A. P. *Science* **2001**, *291*, 2115.

(123) Peng, X.; Manna, L.; Yang, W.; Wickham, J.; Scher, E.; Kadavanich, A.; Alivisatos, A. P. *Nature* **2000**, *404*, 59.

(124) Manna, L.; Scher, E. C.; Alivisatos, A. P. *J. Am. Chem. Soc.* **2000**, *122*, 12700.

(125) Kim, Y.-H.; Jun, Y.-w.; Jun, B.-H.; Lee, S.-M.; Cheon, J. *J. Am. Chem. Soc.* **2002**, *124*, 13656.

(126) Jun, Y.-W.; Casula, M. F.; Sim, J.-H.; Kim, S. Y.; Cheon, J.; Alivisatos, A. P. *J. Am. Chem. Soc.* **2003**, *125*, 15981.

(127) Manna, L.; Scher, E. C.; Alivisatos, A. P. *J. Cluster Sci.* **2002**, *13*, 521.

(128) Manna, L.; Milliron, D. J.; Meisel, A.; Scher, E. C.; Alivisatos, A. P. *Nature Mater.* **2003**, *2*, 382.

(129) Milliron, D. J.; Hughes, S. M.; Cui, Y.; Manna, L.; Li, J.; Wang, L.-W.; Alivisatos, A. P. *Nature* **2004**, *430*, 190.

(130) Peng, X. *Adv. Mater.* **2003**, *15*, 459.

(131) Peng, Z. A.; Peng, X. *J. Am. Chem. Soc.* **2001**, *123*, 1389.

(132) Peng, Z. A.; Peng, X. *J. Am. Chem. Soc.* **2002**, *124*, 3343.

(133) Joo, J.; Na, H. B.; Yu, T.; Yu, J. H.; Kim, Y. W.; Wu, F.; Zhang, J. Z.; Hyeon, T. *J. Am. Chem. Soc.* **2003**, *125*, 11100.

(134) Johnson, C. J.; Dujardin, E.; Davis, S. A.; Murphy, C. J.; Mann, S. *J. Mater. Chem.* **2002**, *12*, 1765.

(135) Busbee, B. D.; Obare, S. O.; Murphy, C. J. *Adv. Mater.* **2003**, *15*, 414.

(136) Jana, N. R.; Gearheart, L.; Murphy, C. J. *Adv. Mater.* **2001**, *13*, 1389.

(137) Jana, N. R.; Gearheart, L.; Murphy, C. J. *J. Phys. Chem. B* **2001**, *105*, 4065.

(138) Sun, Y.; Yin, Y.; Mayers, B. T.; Herricks, T.; Xia, Y. *Chem. Mater.* **2002**, *14*, 4736.

(139) Sun, Y.; Xia, Y. *Adv. Mater.* **2002**, *14*, 833.

(140) Sun, Y.; Gates, B.; Mayers, B.; Xia, Y. *Nano Lett.* **2002**, *2*, 165.

(141) Sun, Y.; Mayers, B.; Herricks, T.; Xia, Y. *Nano Lett.* **2003**, *3*, 955.

(142) Yu, H.; Buhro, W. E. *Adv. Mater.* **2003**, *15*, 416.

(143) Trentler, T. J.; Hickman, K. M.; Goel, S. C.; Viano, A. M.; Gibbons, P. C.; Buhro, W. E. *Science* **1995**, *270*, 1791.

(144) Trentler, T. J.; Goel, S. C.; Hickman, K. M.; Viano, A. M.; Chiang, M. Y.; Beatty, A. M.; Gibbons, P. C.; Buhro, W. E. *J. Am. Chem. Soc.* **1997**, *119*, 2172.

(145) Dingman, S. D.; Rath, N. P.; Gibbons, P. C.; Buhro, W. E. *Angew. Chem. Int. Ed.* **2000**, *39*, 1470.

(146) Markowitz, P. D.; Zach, M. P.; Gikbbons, P. C.; Penner, R. M.; Buhro, W. E. *J. Am. Chem. Soc.* **2001**, *123*, 4502.

(147) Hanrath, T.; Korgel, B. A. *J. Am. Chem. Soc.* **2002**, *124*, 1424.

(148) Davidson, F. M.; Schricker, A. D.; Wiacek, R. J.; Korgel, B. A. *Adv. Mater.* **2004**, *16*, 646.

(149) Lu, X.; Hanrath, T.; Johnston, K. P.; Korgel, B. A. *Nano Lett.* **2003**, *3*, 93.

(150) Holmes, J. D.; Johnston, K. P.; Doty, R. C.; Korgel, B. A. *Science* **2000**, *287*, 1471.

(151) Hanrath, T.; Korgel, B. A. *Adv. Mater.* **2003**, *15*, 437.

(152) Connolly, S.; Fullam, S.; Korgel, B.; Fitzmaurice, D. *J. Am. Chem. Soc.* **1998**, *120*, 2969.

(153) Korgel, B. A.; Fitzmaurice, D. *Phys. Rev. B* **1999**, *59*, 14191.

(154) Hostetler, M. J.; Stokes, J. J.; Murray, R. W. *Langmuir* **1996**, *12*, 3604.

(155) Luedtke, W. D.; Landman, U. *J. Phys. Chem.* **1996**, *100*, 13323.

(156) Doty, R. C.; Yu, H.; Shih, K.; Korgel, B. A. *J. Phys. Chem. B* **2001**, *105*, 8291.

(157) Collier, C. P.; Saykally, R. J.; Shiang, J. J.; Henrichs, S. E.; Heath, J. R. *Science* **1997**, *277*, 1978.

(158) Parthasarathy, R.; Lin, X.-M.; Jaeger, H. M. *Phys. Rev. Lett.* **2001**, *87*, 186807.

(159) Levin, I.; Ott, E. *J. Am. Chem. Soc.* **1932**, *54*, 828.

(160) Raman, C. V.; Jayaraman, A. *Proc. Indian Acad. Sci.* **1953**, *38A*, 343.

(161) Copisarow, A. C.; Copisarow, M. J. *Nature* **1946**, *157*, 768.

(162) Darragh, P. J.; Gaskin, A. J.; Terrell, B. C.; Sanders, J. V. *Nature* **1966**, *209*, 13.

(163) Sanders, J. V. *Nature* **1964**, *204*, 1151.

(164) Alder, J.; Hoover, W. G.; Young, D. A. *J. Chem. Phys.* **1968**, *49*, 3688.

(165) Pusey, P. N.; Poon, W. C. K.; Ilett, S. M.; Bartlett, P. *J. Phys.: Condens. Matter* **1994**, *6*, A29.

(166) Pusey, P. N.; Megen, W. v. *Nature* **1986**, *320*, 340.

(167) Ackerson, B. J.; Schatzel, K. *Phys. Rev. E* **1995**, *52*, 6448.

(168) Auer, S.; Frenkel, D. *Nature* **2001**, *409*, 1020.

(169) Asherie, N.; Lomakin, A.; Benedek, G. B. *Phys. Rev. Lett.* **1996**, *77*, 4832.

(170) Dixit, N. M.; Zukoski, C. F. *Phys. Rev. E* **2001**, *64*, 041604.

(171) Alder, B. J.; Wainwright, T. E. *J. Chem. Phys.* **1957**, *27*, 1208.

(172) Frenkel, D. *Phys. World* **1993**, *6*, 24.

(173) Ackerson, B. J. *Nature* **1993**, *365*, 11.

(174) Turkevich, J.; Stevenson, P. C.; Hillier, J. *Disc. Faraday Soc.* **1951**, *11*, 55.

(175) Schmid, G.; Lehnert, A. *Angew. Chem. Int. Ed. Engl.* **1989**, *28*, 780.

(176) Bentzon, M. D.; Wonterghem, J. v.; Morup, S.; Tholen, A.; Koch, C. J. W. *Phil. Mag. B* **1989**, *60*, 169.

(177) Ohara, P. C.; Leff, D. V.; Heath, J. R.; Gelbart, W. M. *Phys. Rev. Lett.* **1995**, *75*, 3466.

(178) Hamaker, H. C. *Physica IV* **1937**, *10*, 1058.

(179) Korgel, B. A.; Fullam, S.; Connolly, S.; Fitzmaurice, D. *J. Phys. Chem. B* **1998**, *102*, 8379.

(180) Luedtke, W. D.; Landman, U. *J. Phys. Chem. B* **1998**, *102*, 6566.

(181) Whetten, R. L.; Shafigullin, M. N.; Khoury, J. T.; Schaaff, T. G.; Vezmar, I.; Alvarez, M. M.; Wilkinson, A. *Acc. Chem. Res.* **1999**, *32*, 397.

(182) Giersig, M.; Mulvaney, P. *Langmuir* **1993**, *9*, 3408.

(183) Giersig, M.; Mulvaney, P. *J. Phys. Chem.* **1993**, *97*, 6334.

(184) Wang, Z. L.; Harfenist, I. V.; Whetten, R. L.; Bentley, J.; Evans, N. D. *J. Phys. Chem. B* **1998**, *102*, 3068.

(185) Harfenist, S. A.; Wang, Z. L.; Alvarez, M. M.; Vezmar, I.; Whetten, R. L. *J. Phys. Chem.* **1996**, *100*, 13904.

(186) Wang, Z. L. *Adv. Mater.* **1998**, *10*, 13.

(187) Wang, Z. L.; Harfenist, S. A.; Vezmar, I.; Whetten, R. L.; Bentley, J.; Evans, N. D.; Alexander, K. B. *Adv. Mater.* **1998**, *10*, 808.

(188) Sellers, H.; Ulman, A.; Shnidman, Y.; Eilers, J. E. *J. Am. Chem. Soc.* **1993**, *115*, 9389.

(189) Walczak, M. M.; Chung, C.; Stole, S. M.; Widrig, C. A.; Porter, M. D. *J. Am. Chem. Soc.* **1991**, *113*, 2370.

(190) Bain, C. D.; Whitesides, G. M. *J. Am. Chem. Soc.* **1989**, *111*, 7164.

(191) Wang, Z. L. *Mater. Char.* **1999**, *42*, 101.

(192) Korgel, B. A.; Fitzmaurice, D. *Phys. Rev. Lett.* **1998**, *80*, 3531.

(193) Harfenist, S. A.; Wang, Z. L.; Whetten, R. l.; Vezmar, I.; Alvarez, M. M. *Adv. Mater.* **1997**, *9*, 817.

(194) Lin, X. M.; Jaeger, H. M.; Sorensen, C. M.; Klabunde, K. J. *J. Phys. Chem. B* **2001**, *105*, 3353.

(195) Murray, C. B.; Kagan, C. R.; Bawendi, M. G. *Science* **1995**, *270*, 1335.

(196) Talapin, D. V.; Shevchenko, E. V.; Kornowski, A.; Gaponik, N.; Haase, M.; Rogach, A. L.; Weller, H. *Adv. Mater.* **2001**, *13*, 1868.

Chapter 2: Solventless Synthesis of Monodisperse Cu_2S Nanoplatelets[†‡]

2.1 INTRODUCTION

The physical properties of inorganic nanostructures fundamentally relate to their chemical composition, size, crystal structure, surface chemistry and shape. The ability to synthetically tune these material parameters provides the opportunity to study and understand the relationship between chemical, structural and quantum effects that occur uniquely at the nanoscale. Solution-phase synthetic approaches have been applied with a high degree of success to produce a variety of different nanocrystal materials, with very controllable size and size distributions in many cases.[1] Due to the importance of dimensionality on the properties of nanoscale materials, there has been a significant effort in identifying routes to controlling shape using these colloidal synthetic methods. In these methods, inorganic particles are controllably precipitated from molecular precursors in the presence of organic ligands. The ligands adsorb to the nanocrystal surface and control growth by providing steric stabilization and preventing aggregation. The adsorbed ligands can change the growth kinetics and surface energies of different crystal faces, which can ultimately lead to anisotropic growth of low symmetry nanostructures, such as nanorods, nanodisks, and nanowires.[2,3] The internal crystallinity also influences the nanocrystal shape, as

---

[†] The contents of this chapter appear in *J. Am. Chem. Soc*. **2003**, 125, 16050.

[‡] XRD data is from *J. Am. Chem. Soc*. **2003**, 125, 5638.

different crystal planes exhibit significantly different surface energies: even nanocrystals with "spherical" morphologies typically exhibit faceted geometries such as truncated icosahedrons that reduce exposure of high energy crystal planes.[4] Materials with anisotropic crystal structure, such as hexagonal materials, are particularly predisposed to anisotropic growth, as the {001} planes (those perpendicular to the c-axis) exhibit significantly different surface energy relative to the {100} and {110} crystal planes. This anisotropy has been exploited to form a variety of aspherical structures including cubes, rods, platelets, and wires from materials such as Ag,[5] Au,[5,6] $BaWO_4$,[7] CdSe,[3] Co,[2] Cu,[8] GaN,[9] GaP,[10] InP,[11] Ni,[12] NiO,[13] Se,[14] and Si.[15]

Cu_2S nanoplatelets were produced by the solventless thermolysis of a molecular copper alkylthiolate precursor.[16] Nanoplatelets (4 nm by 12 nm) with very monodisperse size and shape can be produced using this method and strands of self-assembled nanoplatelets can be formed that extend micrometers in length. The hexagonally faceted platelets form with the c-axis of the crystal structure orthogonal to the two elongated growth axes. The platelets are oriented on end and therefore appear to be rod-like in two-dimensional TEM images. This crystallographic orientation is unlike the majority of nanorod materials reported to date where growth is favored along the c-axis.[3,6,10,11,14] The hcp-Co nanodisks in Ref. 2 provide a notable exception to those cases. The Cu_2S nanodisks evolve into faceted platelets as a result of limited growth in the <001> direction. The growth mechanism and underlying factors that determine the morphology of Cu_2S

nanodisks are discussed based on the combined importance of face-sensitive surface energy and *reactivity* on the nanostructure morphology.

2.2 EXPERIMENTAL

All chemicals were used as supplied from Aldrich Chemical Co. Water was doubly distilled and deionized. Cu_2S nanocrystals were obtained by the thermolysis of a copper thiolate-derived precursor. In a typical preparation, 32 mL of an aqueous copper (II) nitrate solution (0.21 g $Cu(NO_3)_2 \cdot xH_2O$) is combined with 25 mL $CHCl_3$ containing 0.08 to 0.21 g sodium octanoate ($NaOOC(CH_2)_6CH_3$), to form a two-phase solution with a clear aqueous phase and a blue organic phase. The sodium octanoate serves as a phase transfer catalyst for the Cu^{2+} ions. After 20 min of vigorous stirring, the aqueous phase appears clear, at which point 240 µL dodecanethiol ($C_{12}H_{25}SH$) is added. The organic phase changes color to a hue that ranges from blue-green to pale yellow depending on the initial amount of sodium octanoate used. After stirring for 10 min, the aqueous phase is discarded. The organic solvent is then evaporated to give a waxy solid. The waxy solid precursor material is heated in air for times ranging from 10 to 180 min at temperatures ranging from 140 to 200ºC. After heating, the solid appears brown to black and consists of nanocrystals that redisperse in chloroform. The nanocrystals are precipitated in excess ethanol to remove residual impurities prior to characterization. The yield for the reaction is typically 10 to 20%.

In an alternate preparation, Cu_2S nanodisks are synthesized using tetraoctylammonium bromide (0.18 g $[CH_3(CH_2)_7]_4NBr$ in 25 mL $CHCl_3$), instead of sodium octanoate, as the phase transfer catalyst. Tetraoctylammonium bromide does not transfer the copper ions to the organic phase as efficiently as sodium octanoate and the aqueous layer remains blue after stirring for 20 min, however, a sufficient amount of Cu^{2+} ions transfers to successfully produce Cu_2S nanocrystals. 240 μL dodecanethiol ($C_{12}H_{25}SH$) is added. The mixture is stirred for another 20 min before separating the organic and aqueous phases. Evaporation of the organic solvent gives a waxy solid that serves as the precursor material. Nanocrystals are formed by heating in air with subsequent purification as described above for the nanocrystals synthesized in the presence of octanoate.

The nanocrystals were characterized with transmission electron microscopy (TEM), scanning electron microscopy (SEM), X-ray diffraction (XRD), Fourier transform infrared (FTIR) spectroscopy, and differential scanning calorimetry (DSC). High resolution TEM images were obtained using a JEOL 2010F TEM equipped with a field emission gun operating at a 200 kV accelerating voltage. Images were acquired digitally using a Gatan multipole scanning CCD camera with imaging software system. TEM images were also in some cases obtained using a Philips 208 TEM with 80 kV accelerating voltage. TEM samples were prepared by drop casting nanocrystals dispersed in chloroform onto a 200 mesh carbon coated copper TEM grid purchased from Electron Microscopy Sciences. SEM samples were prepared by drop casting nanocrystals from dispersions on glassy carbon substrates approximately 75 x 75 mm and 1 mm thick. Images were taken on a LEO 1530 SEM equipped with a GEMINI field emission column with a thermal field emitter operating at a 1 kV accelerating voltage. Images were digitally acquired using an Inlens detector and LEO 32 software system. XRD was obtained from nanoplatelets drop cast from chloroform onto quartz (0001) substrates using a Bruker-Nonius D8 Advance Theta-2Theta powder diffractometer with Cu Kα radiation, Bruker Sol-X Si(Li) solid state detector, and a rotating stage. XRD patterns were collected over an 8 to 12 hr period with a 0.02° angle increment at a rate of 12° / min. FTIR spectra were obtained on an Infinity Gold (Thermo Mattson, Model 960M0019) spectrometer. Samples were prepared by depositing thin films of nanocrystals from solution onto a silicon substrate. DSC samples were prepared by depositing unreacted copper alkylthiolate precursor into an aluminum sample boat. Samples were run on a Perkin-Elmer DSC 7.

2.3 RESULTS

2.3.1 Synthesis

The reaction temperature and time affect the size and shape of the Cu_2S nanocrystals. The TEM images shown in Figure 2.1 illustrate how the size and shape evolve with increased reaction time. In Figures 2.1A-D, TEM images of Cu_2S nanocrystals synthesized at 155ºC reveal the shape evolution from small spherical particles into flat platelets with increased reaction time. After 30 min (Figure 2.1A), the nanocrystals are small spheres with 3.2 nm diameter ($\sigma = \pm$ 19.0% for 400 particles counted). After 60 min (Figure 2.1B), disk-like particles start to form, and typically are observed within fields of smaller spheres. The disk diameter increases to 3.6 nm (σ = ± 21.3% for 400 particles counted). At longer reaction times, the disk-like particles tend to stack together into extended chains (Figure 2.1C and 2.1D). The particle size increases to 4.5 nm (σ = ± 26.6% for 400 particles counted) after 120 min and 5.6 nm (σ = ± 28.0% for 400 particles counted) after 150 min. Larger disks exhibit increased faceting and orient on the substrate either on end in chains of stacked particles or flat on the substrate. Larger diameter platelets have a higher tendency to lie flat on the substrate relative to smaller disks as seen by the larger isolated particles in Figure 2.1D.

A high yield of monodisperse nanodisks that self-assemble into chains of stacked disks could be produced over a range of temperatures from 148 to 200° C (Figure 2.2). The reaction temperature increases the growth rate but does not qualitatively affect the morphological evolution of the nanocrystals from spheres to nanodisks to faceted nanoplatelets with reaction time. A high yield of nanodisks could be obtained at a range of reaction temperatures by quenching the reaction at shorter time at higher temperature. Figure 2.2 shows examples of monodisperse nanodisks formed at 148°C (140 min), 165°C (90 min), 180°C (30 min) and 200°C (15 min). Increased temperature enhances the rate of C-S bond thermolysis of dodecanethiol, which speeds the overall growth rate by increasing S monomer availability to the growing nanocrystals. Increased temperature also increases precursor mass transfer to the nanocrystal surface.

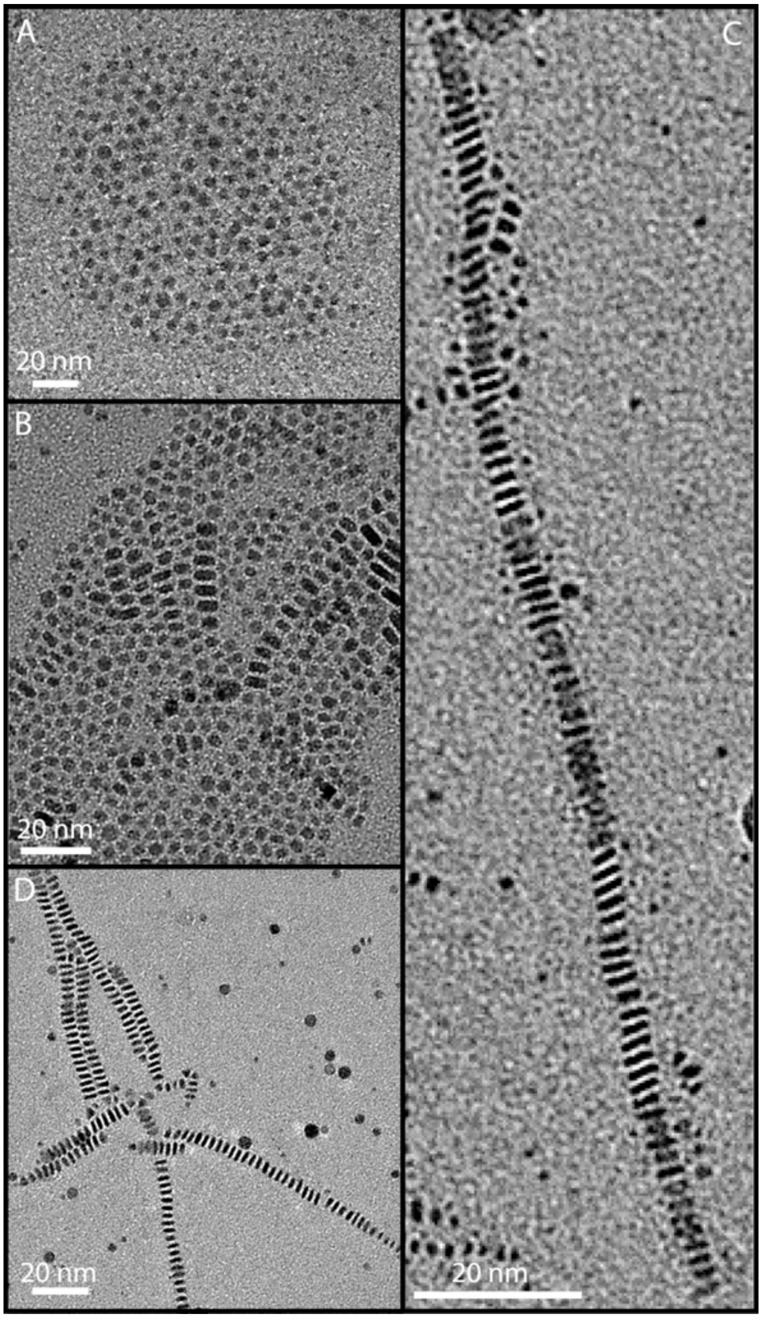

Figure 2.1: TEM images of Cu_2S nanocrystals and nanoplatelets formed with different reaction times at 155°C ((A) 30 min, (B) 60 min, (C) 120 min, (D) 150 min).

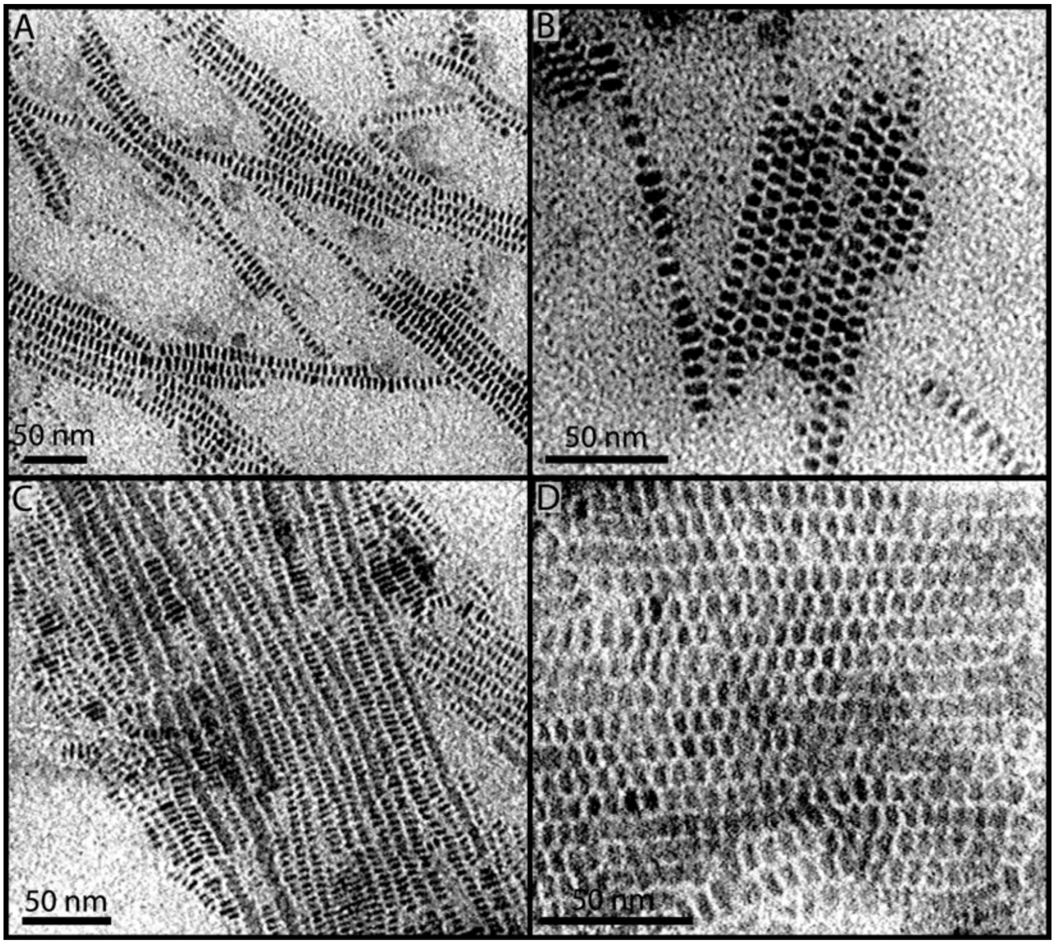

Figure 2.2: TEM images of self-assembled arrays of Cu_2S nanodisks synthesized at different temperature and time: (A) 148º C, 140 min; (B) 165º C, 90 min; (C) 180º C, 30 min; (D) 200º C, 15 min.

SEM imaging (Figure 2.3) revealed that nanodisks deposited onto a substrate from concentrated dispersions form 3D colloidal crystals. Monodisperse nanocrystals (Figure 2.3A-C) form well ordered crystals exhibiting parallel alignment of chains of stacked nanodisks with lengths up to a few microns. Figure 2.3D is an SEM image showing the entire colloidal crystal demonstrating their typical shape and size. The long range 1D and 3D ordering observed in these formations appears to result from attraction other than just asymmetric van der Waals attraction. One possibility is that the nanocrystals are ferroelectric as observed in bulk hexagonal Cu_2S with the individual nanocrystal dipole-dipole moments aligning with respect to one another.[17,18]

2.3.2 Disk Morphology

TEM tilting experiments clearly reveal the platelet morphology of the Cu_2S nanocrystals. Figure 2.4 shows a series of TEM images of a chain of Cu_2S nanodisks stacked side by side taken after horizontal tilting by +15.0º, 0.0º, and -14.7º. The outlined regions highlight disks that appear rod-like when the beam is oriented down the flat axis of the disks, and then overlap at off-axis angles. The nanocrystals would not overlap with tilting if they were cylindrical rods because the short axis diameter would not vary with viewing angle. Notice that the apparent overlap between neighboring platelets is large for those with diameters greater than 20 nm, but significantly less for those under 20 nm. The sample holder on the JEOL 2010F TEM is constrained to a tilt range of ± 15º, which limits the ability to identify the disk-like morphology of the nanocrystals as the size decreases. The morphology of particles with diameter smaller than approximately 15 nm is difficult to differentiate by tilt experiments using low resolution TEM, due to the absence of clear overlap between neighboring particles and only minimal change in particle width or interparticle spacing with tilting. However, as discussed below, sample tilting combined with high resolution TEM imaging of the lattice planes provides an effective way to characterize the nanocrystal morphology.

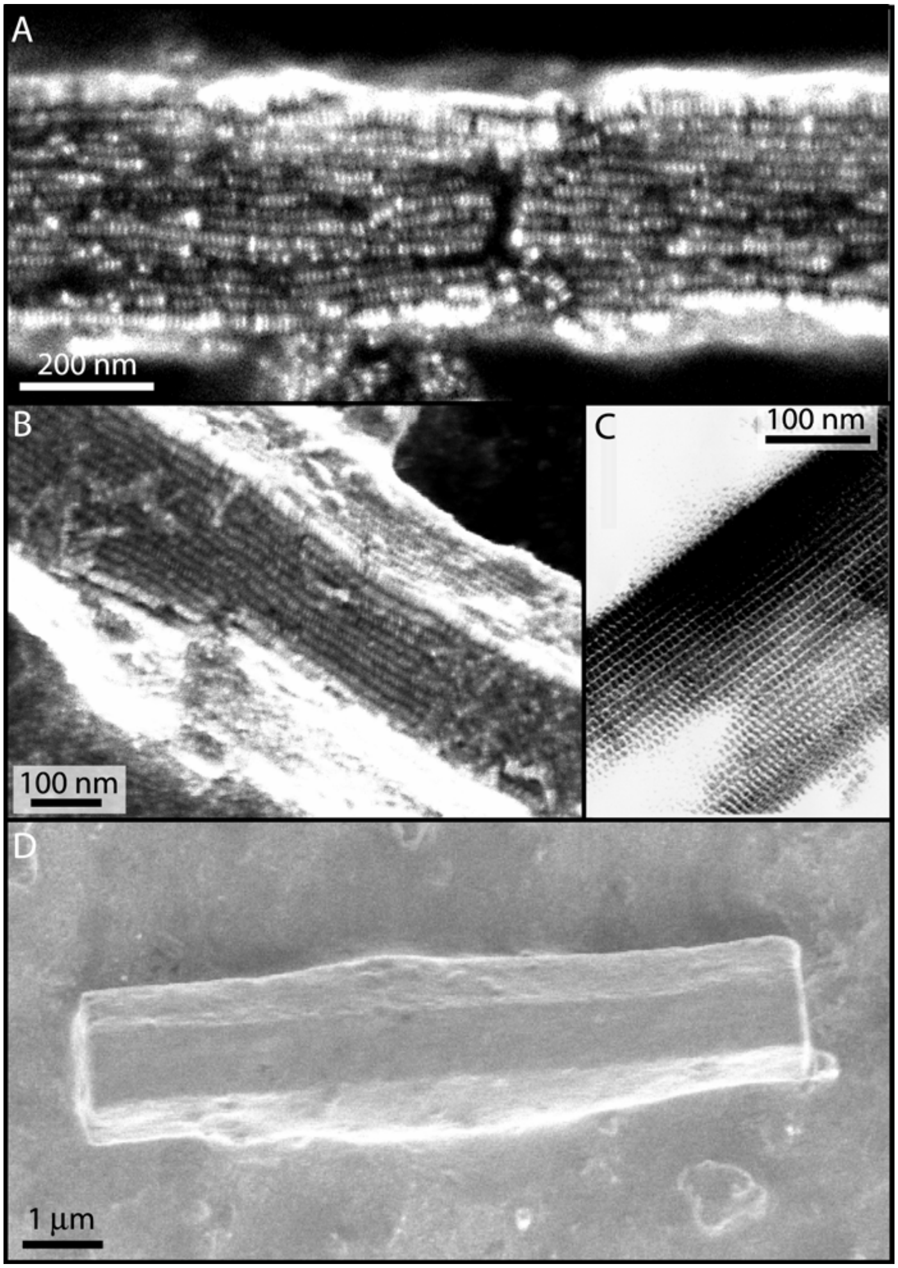

Figure 2.3: SEM images (A, B, D) and TEM image (C) of self-assembled three dimensional colloidal crystals of Cu_2S nanodisks formed via deposition of monodisperse nanodisks from concentrated dispersions.

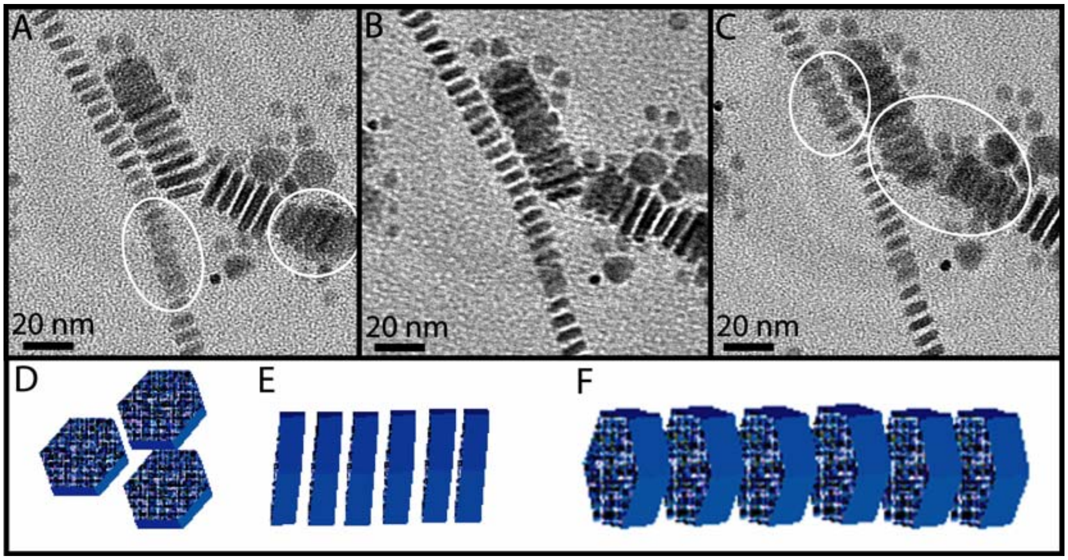

Figure 2.4: TEM images of stacked nanoplatelets tilted at (A) +15.0º, (B) 0.0º, and (C) -14.7º. The circled regions highlight platelets tilted through the plane of their [001] zone axis. When observing the platelets off-axis, the platelets appear to overlap. Schematic of nanoplatelets oriented (D) parallel to the substrate lying on their major facet, (E) oriented perpendicular to the substrate into a one dimensional array resembling a rod-like morphology, and (F) tilted with respect to the substrate demonstrating the overlap of each particle when imaged with TEM.

2.3.3 Crystallographic Orientation of Nanoplatelets.

The XRD pattern in Figure 2.5 reveals that the Cu_2S nanocrystals have the hexagonal (high chalcocite) crystal structure. This is the high temperature crystal phase of bulk Cu_2S, which undergoes a phase transition at 105ºC from monoclinic (low chalcocite) to hexagonal.[19] The hexagonal structure is thermodynamically favored at the synthetic temperatures, and remains metastable in the nanodisks at room temperature. A similar structural metastability has been observed in much larger monoclinic (low chalcocite) Cu_2S nanowires grown at room temperature by flowing H_2S over copper foil.[20] The monoclinic Cu_2S nanowires transform to hexagonal crystal structure when heated above approximately 100°C.[21] Upon cooling, the nanowires do not structurally relax back to monoclinic until reaching 75°C. Structural metastability has also been observed in nanocrystals of CdSe[3] and Si[22] below their pressure-induced structural phase transitions, and altogether unique phase behavior in nanostructures is not uncommon, as in the case of Co.[23]

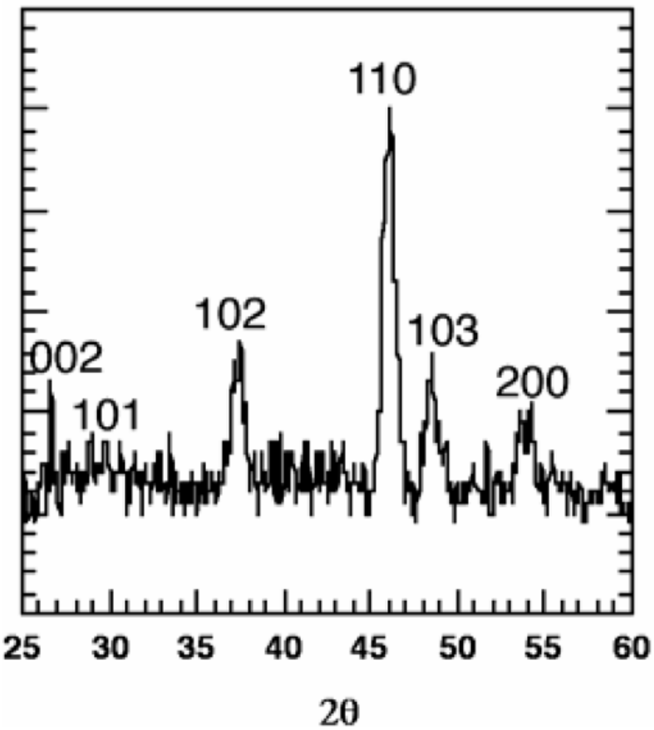

Figure 2.5: XRD pattern for Cu_2S nanoplatlets demonstrating hexagonal (high chalcocite) crystal structure.

A detailed analysis of HRTEM images of the Cu_2S nanodisks was performed to determine the crystallographic orientation. Two primary disk orientations on the substrate—disks resting on their side in stacked chains of particles and disks lying flat on the substrate—were studied. Lattice imaging with of many particles with different orientations reveal the disks to be single crystals with the [001] direction oriented in the direction of the short axis. Figures 2.6 and 2.7 show examples of typical HRTEM images of two disks with different orientations on the substrate. Figure 2.6 shows a faceted Cu_2S platelet resting on its face. The 2.0 Å lattice spacing between the (110) lattice planes are visible. The fast Fourier transform (FFT) of the HRTEM image gives a hexagonal array of spots located 3.4 Å from the center spot. These spots are characteristic of the {100} family of planes of hexagonal Cu_2S. The outer hexagonal array of spots located 2.0 Å from the center point corresponds to the {110} family of hexagonal planes. The observed intensities of the {100} reflections are weak compared to the {110} reflections, which is consistent with the selection rules for the hexagonal crystal structure.[24] The 30° rotation of the outer array of spots relative to the inner array from the {100} planes matches the diffraction pattern expected for an hexagonal lattice with the electron beam incident to the [001] direction.[25] This direction is parallel to the c-axis of the Cu_2S crystal structure, indicating that the {001} family of planes are oriented parallel to the substrate in this nanodisk. All of the faceted platelets imaged lying on their face (9 of 9) exhibited this crystallographic orientation.

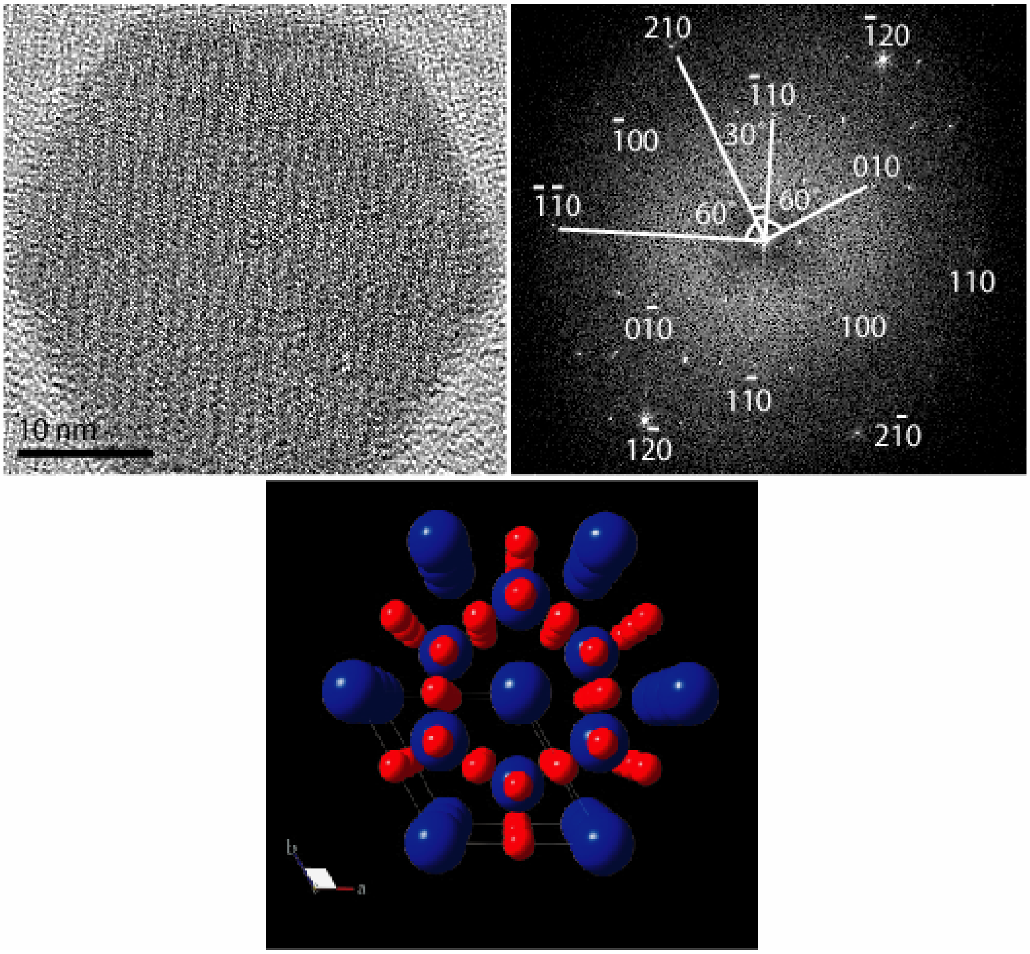

Figure 2.6: (Top, Left) HRTEM image of a hexagonal platelet lying flat on the substrate with the electron beam incident from the [001] direction. (Bottom, Middle) Corresponding crystallographic model of the Cu_2S high chalcocite structure when viewed from the same direction as the imaged nanocrystal. (Top, Right) FFT of the imaged nanocrystal demonstrating crystal orientation.

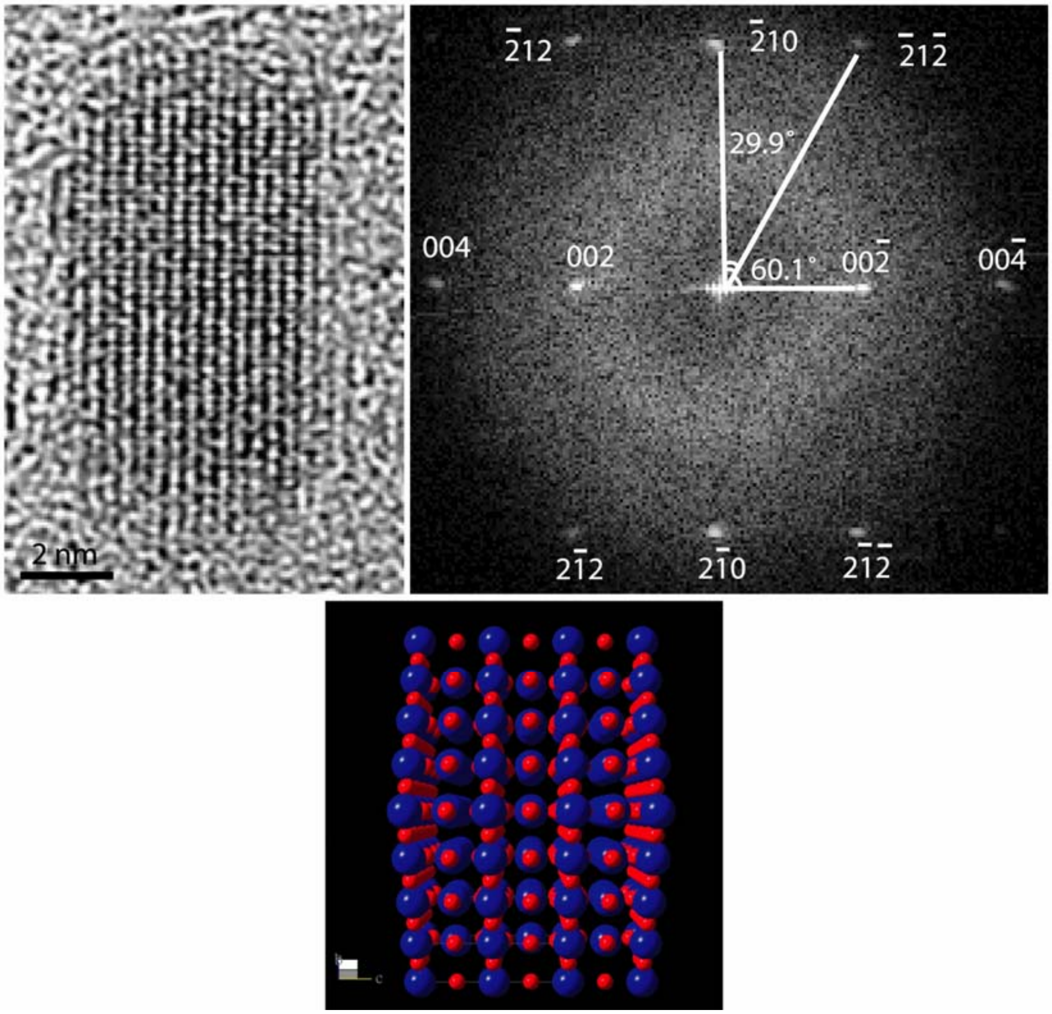

Figure 2.7: (Top, Left) HRTEM image of a hexagonal platelet standing on end perpendicular to the substrate with the electron beam incident to the [010] direction. (Bottom, Middle) Corresponding crystallographic model of the hexagonal Cu_2S structure when viewed from the same direction as the imaged nanocrystal showing orientation of the c-axis of the crystal in the short growth direction. (Top, Right) FFT of the imaged nanocrystal demonstrating crystal orientation.

Figure 2.7 shows an HRTEM image of a nanoplatelet oriented perpendicular to the substrate. The (002) planes appear to reside parallel to the long axis of the platelet with the (110) planes along the short axis. Analysis of the FFT of the image in Figure 2.6 helps confirm these assignments. Bright reflections in the FFT corresponding to a 3.4 Å lattice spacing are consistent with the {002} family of planes. These spots are rotated 90° relative to the {110} reflections with lattice spacing 2.0 Å. The reflections corresponding to the {112} family of planes complete the rectangular array of spots with a lattice spacing of 1.7 Å. These reflections are 29.9° from the {110} reflections and 60.1° from the {002} reflections. The reflections for the hexagonal {001} and {003} planes are forbidden and do not appear in the FFT pattern. The FFT corresponds to the standard indexed diffraction pattern of an hexagonal crystal with the incident electron beam oriented in the [010] direction except for two deviations.[25] First, the angles between the {112} reflections and the {002} and {110} reflections are 57.8° and 32.2° for the standard diffraction pattern of a hexagonal crystal. This corresponds to a 2.3° shift of from the standard pattern. Second, the ratios of lengths between the (-212) and (002) and the (-210) and (002) reflections are larger for the Cu_2S pattern than the standard hexagonal pattern. These variations result from the slight elongation of the c-axis observed in the Cu_2S high chalcocite crystal structure. A determination of the angles between these planes for the high chalcocite structure matches exactly the measured values from the FFT. The incident electron beam is oriented perpendicular to the c-axis, exactly 90° relative to the direction of the beam used to image the platelet in Figure 2.6. The FFT of the Cu_2S nanodisk in Figure 2.7 confirms that the (002) planes reside parallel to the long axis of the platelet with the (110) planes along the short axis.

Again, the c-axis of the hexagonal crystal structure is parallel to the short growth direction of the platelet.

The majority of nanodisks imaged on their side, such as the one in Figure 2.7, reveal a crystallographic orientation rotated exactly 90° from platelets lying on their face. A cylindrical rod would not exhibit a preferred lattice orientation in the tilt experiments. The fact that the (002) lattice planes of nanocrystals with diameter smaller than 15 nm are normal to the slow growth direction of stacked particles provides evidence of platelet morphology; however, HRTEM can provide more conclusive evidence by determining if the [010] zone axis is within the tilt range of the sample holder (±15º) for the majority of nanocrystals. When the beam is oriented down the [010] zone axis, both the (002) and (110) planes become visible. Figure 2.8 shows HRTEM images of two nanodisks at three different tilt angles. In Figure 2.8A, the (002) lattice fringes are visible along the long axis of the particle on the left. After tilting the sample -0.6° in the x-direction (approximately horizontal to the image) and +6.1°. in the y-direction (approximately vertical to the image) (Figure 2.8B), the particle on the left reveals the (110) fringes parallel to the short axis and the particle on the right exhibits both the (002) fringes along the long axis and the (110) fringes along the short axis. Tilting an additional -5.4° in the x-direction eliminates the lattice fringes. A small variation in tilt angle of only a few degrees was necessary to find the [010] zone axis in each particle. The preferential alignment of the [010] direction orthogonal to the substrate provides confirmation that the smaller rod-like particles are indeed nanodisks.

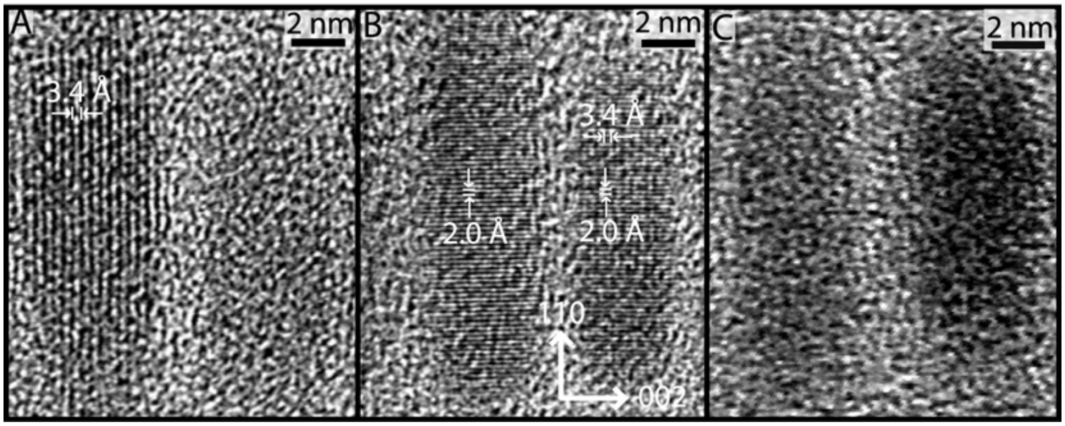

Figure 2.8: HRTEM images of two nanoplatelets oriented perpendicular to the substrate tilted (A) 0.0° in the x and y directions, (B) -0.6° in the x-direction (approximately horizontal to the image) and +6.1° in the y-direction (approximately vertical to the image), and (C) tilted an additional 5.4° in the x-direction. Images illustrate how the (002) planes (3.4 Å lattice spacing) are oriented perpendicular to the short axis of the nanocrystals with the {110} planes (2.0 Å lattice spacing) oriented parallel. (C) demonstrates how planes are not observed with continued tilting in the x-direction.

Visualization of the hexagonal Cu_2S crystal structure using the "Balls and Sticks" software package helps illustrate the relationship between the crystallographic orientation and the favored growth direction of the nanodisks. The high chalcocite structure has the $P6_3/mmc$ space group with a primitive hexagonal unit cell, a = 3.89 Å and c = 6.88 Å. Buerger and Wuensch modeled the XRD patterns of bulk high chalcocite and determined the location of S atoms at the hexagonal sites (S′ at 0 0 0 and S′′ at 0.333 0.667 0.25). The Cu atoms are located at a fraction of three interstitial locations (Cu′ in 2b at 0 0 0.25, Cu′′ in 4f at 0.333 0.667 0.578, Cu′′′ in 6g at 0 0.5 0).[19] Each primitive hexagonal cell contains 4 S atoms and 8 Cu atoms with each Cu atom having a total of 12 lattice locations which they occupy at a ratio of 1.24 : 1.63 : 1.13 for each of the 3 possible groups of sites.[19] The Cu atoms in high chalcocite have been described as being disordered with rapid diffusion between possible interstitial locations.[26,27] The atomic models in Figures 2.6 and 2.7 showing the Cu and S atoms as viewed from the [001] and [010] directions, respectively, are consistent with the measured FFT patterns. Therefore, the faceted disk morphology results from growth favored in the <100> directions.

2.3.4 Reaction Mechanism and Role of Capping Ligand.

A mixture of octanoate and dodecanethiol is used to synthesize the Cu_2S nanodisks. Clearly, dodecanethiol provides the sulfur source to the growing nanocrystals; however, what role does dodecanethiol play in terms of controlling particle growth? Octanoate serves as the phase transfer catalyst to solubilize copper cations in the organic solvent, but what role does octanoate play during the synthesis? As discussed below, we found with the aid of FTIR spectroscopy that octanoate serves as the primary capping ligand that controls nanocrystal growth with dodecanethiol providing little steric stabilization.

When tetraoctylammonium bromide (TOAB) was used in place of sodium octanoate as the phase transfer catalyst, the Cu_2S nanodisks exhibited the same morphology, but the disk size was much larger, as shown in Figure 2.9. In addition, the disks exhibited less “rounding” of the crystal facets, and in some cases, accelerated <110> growth with respect to the {100} crystal facets appears to have given rise to convex curvature of the platelet facets. These disks exhibited the high chalcocite Cu_2S crystal structure, which was verified by indexing FFT patterns of HRTEM images with lattice resolution.

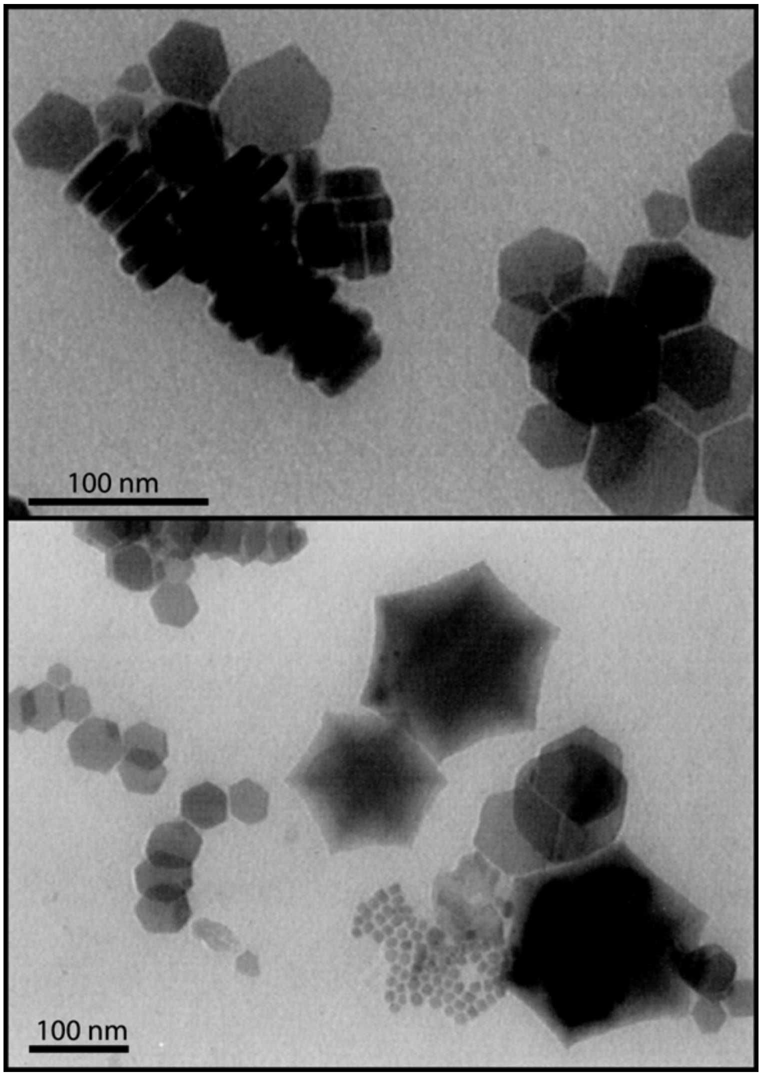

Figure 2.9: TEM images of typical Cu_2S nanocrystals formed by replacing sodium octanoate with tetraoctylammonium bromide as the phase transfer catalyst.

Figure 2.10 compares FTIR spectra for pure sodium octanoate, and nanocrystals synthesized in the presence of sodium octanoate and tetraoctylammonium bromide (TOAB). The characteristic methyl and methylene stretches appear at 2962, 2924, 2872, and 2853 cm^{-1} in the FTIR spectra of octanoate, octanoate-capped nanodisks, and disks synthesized with TOAB. The FTIR spectra in Figures 2.10A and 2.10B, both exhibit bands at 1570 and 1710 cm^{-1} characteristic of C-O stretching in the carboxylate ion, and prominent bands at 1378 and 1463 cm^{-1} corresponding to C-H bending frequencies. Nanodisks formed without sodium octanoate do not have absorption bands at 1570 and 1710 cm^{-1}. The TOAB-synthesized nanodisks did show prominent C-H bond bending bands at 1342 and 1469 cm^{-1} with a small peak at 1378 cm^{-1} that match those of both neat 98% 1-dodecanethiol and TOAB.[28] The nanodisks synthesized in the presence of TOAB are coated with either dodecanethiol, TOAB, or a combination of the two as the capping ligand. Regardless of the actual ligand capping these nanocrystals, the adsorption to the particles is significantly weaker based on the increased particle size observed when synthesizing particles with TOAB under similar reaction conditions. In contrast, disks synthesized with sodium octanoate exhibit the C-O stretching modes and increased absorption in the C-H bending band located at 1378 cm^{-1} relative to 1342 cm^{-1} particles formed with TOAB, showing that octanoate serves as the primary capping ligand during nanodisk growth.

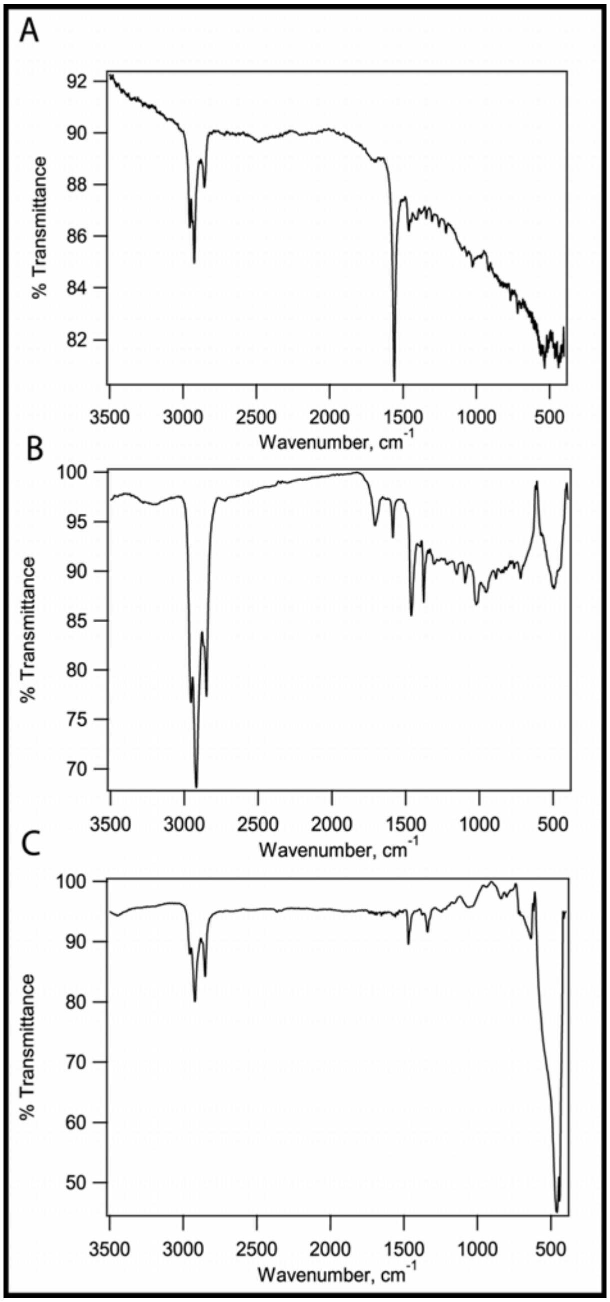

Figure 2.10: FTIR spectra of (A) sodium octanoate, (B) Cu_2S nanocrystals formed with sodium octanoate as the phase transfer catalyst, and (C) Cu_2S nanocrystals formed with tetraoctylammonium bromide as the phase transfer catalyst.

DSC was used to examine the decomposition of copper alkylthiolate precursor used in the synthesis. Figure 2.11 shows the DSC curve of initially unreacted precursor as it is heated from 25 to 225ºC. A broad peak from 43 to 78ºC appears showing the melting of the precursor from its initial waxy state to a viscous fluid. The sharp peak at 113.5ºC indicates decomposition of the copper alkylthiolate precursor as the C-S bond is cleaved to form Cu_2S. Two small peaks shown in the inset of Figure 2.11 at 214.5 and 218.5ºC correspond to the slightly elevated boiling points for 1-dodecene and dodecane (normal b.p. of 213 and 216ºC) confirming that the dodecanethiol C-S bond is cleaved and no further decomposition of the organic chain occurs.

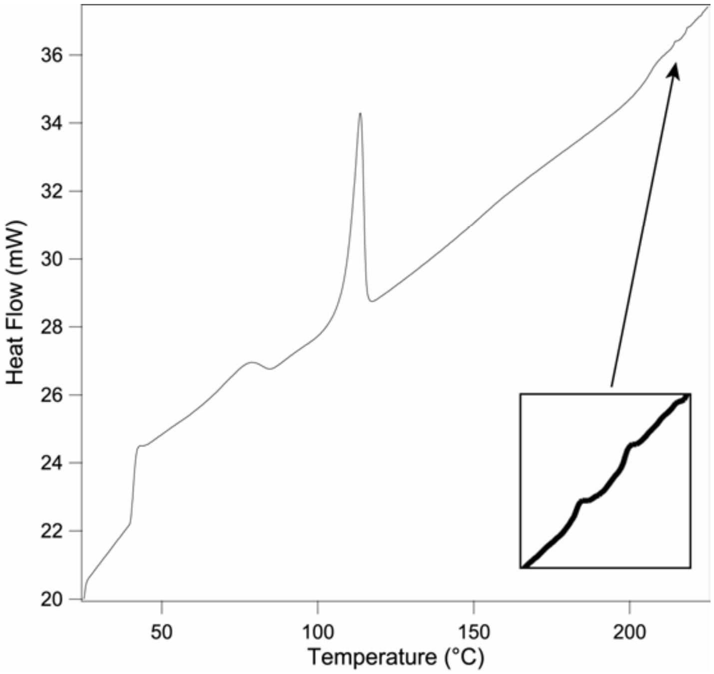

Figure 2.11: DSC curve for heating initially unreacted copper thiolate precursor from 25 to 225ºC.

2.4 DISCUSSION

The octanoate serves as the capping ligand that stabilizes nanodisk size and shape. This is consistent with observed chemisorption of alkylated carboxylic acids on Cu (100) surfaces.[29] Although dodecanethiol and/or TOAB can serve to a limited extent as a capping ligand, as confirmed by FTIR of nanodisks synthesized using TOAB, C-S bond cleavage is what gives rise to particle growth and therefore cannot serve as a chemically inert passivant. Octanoate slows particle growth by reducing monomer accessibility to the particle surface. The nanocrystal morphology, however, appears to be independent of the chemical nature of the capping ligand, which is different than CdSe and Co where the capping ligand chemistry is critical to nanodisk and nanorod formation.[2,3]

In the thermodynamic limit, the face-dependent surface energies dictate particle shape and faceting. Matysina determined that hexagonal metals with c/a ratios greater than the ideal hexagonal values (i.e., $c/a > 1.633$) have (101) and (100) surface energies approximately 1.5 times larger than those for the (001) facets.[30] Hexagonal Cu_2S has a c/a ratio of 1.697 and should exhibit higher surface energies on the (101) and (100) lattice planes. The formation of large (001) crystal facets limits exposure of these higher energy surfaces, but to an extent much greater than expected from these thermodynamic considerations. In other words, nanodisk growth is more anisotropic than expected based on surface energy considerations: for example, the surface to volume ratio is 0.49 for a hexagonal platelet with sides 15 nm long and a 6 nm thickness versus 0.26 for a sphere of equivalent total volume. Likewise, the growth of hexagonal prisms does not resemble expectations for rapid, kinetically controlled growth similar to what occurs along the c-axis in monoclinic Cu_2S nanowires or CdSe nanorods.[3,21]

The reaction kinetics of dodecanethiol thermolysis appear to largely determine the nanodisk shape. Pure dodecanethiol (boiling point is 266 to 283ºC) is chemically stable over all the reaction temperatures examined, yet provides S monomer through S-C bond thermolysis. Kühnle et al. and Vollmer et al. investigated dodecanethiol adsorption on Cu(110) and Cu(100) surfaces and found that the S-C bond cleaves at temperatures greater than 127ºC to form monolayers of adsorbed sulfur.[31,32] Laibinis et al. detected increased S concentrations on Cu thin films after exposure to alkanethiols of varying chain lengths in isooctane solutions, indicating the formation of thin layers of Cu_2S at the Cu film interface.[33]

Studies of alkanethiol adsorption on Cu(111) surfaces revealed that the outermost Cu atomic layers reconstruct into a pseudo-(100) layer.[34-36] Thiolate adsorption on Cu(110) and Cu(100) surfaces does not give rise to a surface reconstruction.[31,32] Apparently, the Cu(111) surface reconstructs because thiol adsorption on the Cu(100) surface is much more energetically favorable and actually reorients the (111) planes.[35] On the pseudo-(100) plane, the S atoms lie on the four-fold hollow sites located between Cu atoms with a lateral expansion of 3.5% x 15% with respect to a true Cu (100) lattice plane.[35] This surface reconstruction is consistent with the tendency of sulfur to form chemically stable four-fold coordination with Cu.[37,38] Interestingly, the copper atoms in the {100} planes of Cu_2S exhibit a square lattice with sites available for four-fold coordination to adsorbed sulfur (Figure 2.12A). In fact, the Cu sublattice is expanded enough to accomodate S atoms within the lattice plane. The {001} planes do not exhibit this four-fold symmetry. Based on the crystallographic orientation of the nanodisks, the Cu_2S preferentially grows in the <100> directions as opposed to the <001>. This growth direction provides faces with the four fold surface sites that promote S adsorption and incorporation to form the next layer of Cu_2S. In comparison, the {001} planes (Figure 2.12B) are the most atomically dense structures with S atoms lying in six-fold sites, and are expected to kinetically inhibit S addition.

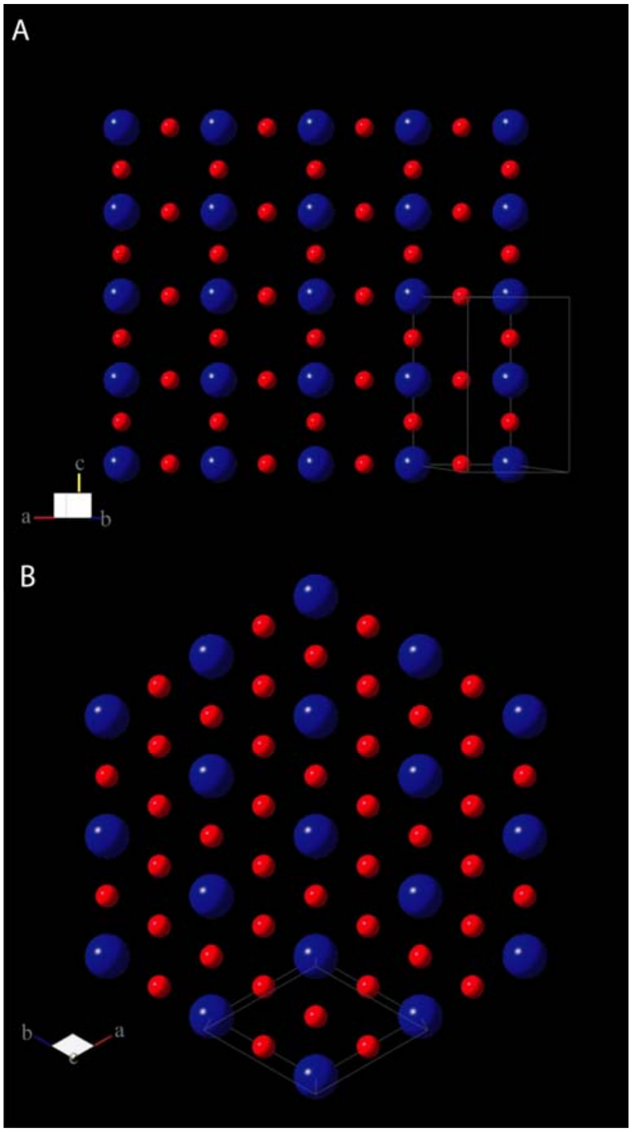

Figure 2.12: Crystallographic model showing the most atomically dense layers of atoms for the {100} planes (A) and {001} planes (B) of the hexagonal Cu_2S structure.

2.5 CONCLUSIONS

In the solventless Cu_2S nanodisk synthesis, sodium octanoate functions as both the phase transfer catalyst and the capping ligand. The hexagonal (high chalcocite) nanodisks are faceted platelets with the c-axis oriented perpendicular to the faster growing {100} planes. Nanodisk growth is limited in the [001] direction and predominantly occurs along the six energetically equivalent {100} directions to form hexagonal prisms. The nanodisk shape appears to relate to the preferred adsorption and cleavage of dodecanethiol on {100} facets compared to the {001} as expected based on alkanethiol adsorption studies demonstrating preferential S adsorption at four-fold coordinating Cu surface sites. Anisotropic control of crystal morphology based on face-sensitive surface reactivity offers an interesting potential avenue for controlling nanostructures with different shape.

2.6 REFERENCES

(1) Murray, C. B.; Kagan, C. R.; Bawendi, M. G. *Annu. Rev. Mater. Sci.* **2000**, *30*, 545.

(2) Puntes, V. F.; Zanchet, D.; Erdonmez, C. K.; Alivisatos, A. P. *J. Am. Chem. Soc.* **2002**, *124*, 12874.

(3) Peng, X.; Manna, L.; Yang, W.; Wickham, J.; Scher, E.; Kadavanich, A.; Alivisatos, A. P. *Nature* **2000**, *404*, 59.

(4) Korgel, B. A.; Fullam, S.; Connolly, S.; Fitzmaurice, D. *J. Phys. Chem. B* **1998**, *102*, 8379.

(5) Sun, Y.; Xia, Y. *Science* **2002**, *298*, 2176.

(6) Nikoobakht, B.; El-Sayed, M. A. *Chem. Mater.* **2003**, *15*, 1957.

(7) Kwan, S.; Kim, F.; Akana, J.; Yang, P. *Chem. Commun.* **2001**, *5*, 447.

(8) Liu, Z.; Bando, Y. *Adv. Mater.* **2003**, *15*, 303.

(9) Bae, S. Y.; Seo, H. W.; Park, J.; Yang, H.; Kim, H.; Kim, S. *Appl. Phys. Lett.* **2003**, *82*, 4564.

(10) Kim, Y.-H.; Jun, Y.-w.; Jun, B.-H.; Lee, S.-M.; Cheon, J. *J. Am. Chem. Soc.* **2002**, *124*, 13656.

(11) Ahrenkiel, S. P.; Micic, O. I.; Miedaner, A.; Curtis, C. J.; Nedeljkovic, J. M.; Nozik, A. J. *Nano Lett.* **2003**, *3*, 833.

(12) Cordente, N.; Respaud, M.; Senocq, F.; Casanove, M.-J.; Amiens, C.; Chaudret, B. *Nano Lett.* **2001**, *1*, 565.

(13) Wang, W.; Liu, Y.; Xu, C.; Zheng, C.; Wang, G. *Chem. Phys. Lett.* **2002**, *362*, 119.

(14) Gates, B.; Mayers, B.; Cattle, B.; Xia, Y. *Adv. Funct. Mater.* **2002**, *12*, 219.

(15) Holmes, J. D.; Johnston, K. P.; Doty, R. C.; Korgel, B. A. *Science* **2000**, *287*, 1471.

(16) Larsen, T. H.; Sigman, M.; Ghezelbash, A.; Doty, R. C.; Korgel, B. A. *J. Am. Chem. Soc.* **2003**, *125*, 5638.

(17) Bieniulis, M. Z.; Corry, C. E.; Hoskins, E. R. *Geophys. Res. Lett.* **1987**, *14*, 135.

(18) Corry, C. E. *Appl. Geophys.* **1994**, *32*, 55.

(19) Buerger, M. J.; Wuensch, B. J. *Science* **1963**, *141*, 276.

(20) Wang, S.; Yang, S.; Dai, Z. R.; Wang, Z. L. *Phys. Chem. Chem. Phys.* **2001**, *3*, 3750.

(21) Wang, S.; Guo, L.; Wen, X.; Yang, S.; Zhao, J.; Liu, J.; Wu, Z. *Mater. Chem. Phys.* **2002**, *75*, 32.

(22) Tolbert, S. H.; Herhold, A. B.; Brus, L. E.; Alivisatos, A. P. *Phys. Rev. Lett.* **1996**, *76*, 4384.

(23) Dinega, D. P.; Bawendi, M. G. *Angew. Chem. Int. Ed.* **1999**, *38*, 1788.

(24) The minimum intensity, $|F|^2 = f^2$, is expected for the {100} reflections since the Miller indices match h+2k = 3m+1 and l is even, where F is the structure factor for the unit-cell equivalents of the scattering amplitude f(T) and m is an integer. Maximum intensity, $|F|^2 = 4f^2$, is expected for the {110} reflections with Miller indices following h+2k = 3m and l being even.

(25) Williams, D. B.; Carter, C. B. *Transmission Electron Microscopy: A Textbook for Materials Science*; Plenum Press: New York, 1996.

(26) Buerger, M. J. *Anais Acad. Brasil. Cienc.* **1949**, *21*, 261.

(27) Jensen, M. L. Ph.D. Thesis, M.I.T., 1951.

(28) *The Aldrich Library of FT-IR Spectra*, 2nd ed.; Sigma-Aldrich, 1997; Vol. 1.

(29) Dubois, L. H.; Zegarski, B. R.; Nuzzo, R. G. *Langmuir* **1986**, *2*, 412.

(30) Matysina, Z. A. *Mater. Chem. Phys.* **1999**, *60*, 70.

(31) Kuhnle, A.; Vollmer, S.; Linderoth, T. R.; Witte, G.; Woll, C.; Besenbacher, F. *Langmuir* **2002**, *18*, 5558.

(32) Vollmer, S.; Witte, G.; Woll, C. *Langmuir* **2001**, *17*, 7560.

(33) Laibinis, P. E.; Whitesides, G. M.; Allara, D. L.; Tao, Y.-T.; Parikh, A. N.; Nuzzo, R. G. *J. Am. Chem. Soc.* **1991**, *113*, 7152.

(34) Imanishi, A.; Isawa, K.; Matsui, F.; Tsuduki, T.; Yokoyama, T.; Kondoh, H.; Kitajima, Y.; Ohta, T. *Surf. Sci.* **1998**, *407*, 282.

(35) Driver, S. M.; Woodruff, D. P. *Surf. Sci.* **2001**, *479*, 1.

(36) Driver, S. M.; Woodruff, D. P. *Langmuir* **2000**, *16*, 6693.

(37) Foss, M.; Feidenhans'l, R.; Nielsen, M.; Findeisen, E.; Buslaps, T.; Johnson, R. L.; Besenbacher, F. *Surf. Sci.* **1997**, *388*, 5.

(38) Jackson, G. J.; Driver, S. M.; Woodruff, D. P.; Cowie, B. C. C.; Jones, R. G. *Surf. Sci.* **2000**, *453*, 183.

Chapter 3: Solventless Synthesis of Bi_2S_3 (Bismuthinite) Nanorods, Nanowires, and Nanofabric*

3.1 INTRODUCTION

General synthetic approaches for sterically-stabilized nanocrystals with tunable composition, size, and shape are being developed to produce high quality nanomaterials for fundamental studies and practical applications. Solution-phase, ligand-assisted arrested precipitation has been effective for many types of solids, including those with metallic, covalent, and ionic chemical bonding.[1] Size (and shape) distribution control remains the primary challenge in these syntheses as frequent interparticle collisions can lead to aggregative growth resulting in broad log-normal size distributions and significant concentrations of crystallographic defects in the particle cores.[2-5] Nanocrystal arrested precipitation in the *absence of solvent* has been explored, thus eliminating interparticle diffusion and collisions during the growth process, which in principle should promote diffusion-limited particle growth and narrow size and shape distributions. Using this solventless approach, size- and shape-monodisperse metal sulfide nanocrystals—Cu_2S and NiS nanorods, nanodisks and nanoprisms—have indeed been produced by thermally decomposing metal alkylthiolate precursors in the presence of octanoate.[6-8]

---

* The contents of this chapter have been accepted for publication in *Chemistry of Materials*.

This chapter discusses the solventless synthesis of crystalline *high aspect ratio* Bi_2S_3 nanowires from a bismuth (Bi) alkylthiolate precursor and further shows that the nanowire aspect ratio can be decreased significantly by increasing the relative availability of sulfur in the reaction. Several techniques have previously been reported for synthesizing elongated Bi_2S_3 nanocrystals including solvothermal[9-12] and hydrothermal[13-15] decomposition, microwave irradiation,[16] crystallization of amorphous colloids,[17] chemical vapor deposition,[11,18] and sonochemical methods,[19] but the solventless technique offers the significant advantage of simultaneously forming highly crystalline rods or wires with well defined surfaces and small average diameters (10.7 nm for nanorods and 26.0 nm for nanowires). Bi_2S_3 is a photoconductive, direct band gap (Eg = 1.3 eV) semiconductor,[20,21] with numerous potential applications ranging from photovoltaics[20,22,23] to sensors[20] to thermoelectrics.[24,25]

3.2 EXPERIMENTAL

All chemicals were used as received from Aldrich Chemical Co. Water was doubly distilled and deionized.

3.2.1 Nanowire Synthesis

36 mL of 10.9 mM bismuth nitrate ($Bi(NO_3)_3$) [0.19 g] is mixed with 25 mL chloroform ($CHCl_3$) with 0.42 g of sodium octanoate ($NaOOC(CH_2)_6CH_3$). In aqueous solutions, bismuth nitrate dissociates into ionic species ranging from $Bi(NO_3)^{2+}$ to $Bi(NO_3)_4^-$.[26] Negatively charged octanoate serves as a phase transfer catalyst for $Bi(NO_3)_{3-n}^{n+}$ ions, solvating them in the organic phase. 300 μL of

dodecanethiol ($C_{12}H_{25}SH$) is added, resulting in a bright yellow organic phase. The thiol forms a stronger complex with the Bi cations and the color change results from the charge transfer complex formed as the thiol displaces the octanoate. Following 20 to 60 minutes of stirring, the organic phase is separated and then evaporated to leave a bright yellow waxy precursor material. The Bi_2S_3 precursor is heated for 1 hr at 225°C in air to produce a brownish/black solid composed of nanowires. At these temperatures, the sulfur-carbon bond cleaves to form a crystalline metal sulfide product. The product is dispersed in chloroform and centrifuged at 7000 rpm for 10 minutes to remove molecular byproducts from the reaction. The nanowire yield is ~20% based on number of moles of Bi converted to Bi_2S_3.

3.2.2 Nanorod Synthesis

36 mL of 12.0 mM $Bi(NO_3)_3$ (0.21 g) is combined with a dispersion of 0.20 g $NaOOC(CH_2)_6CH_3$ in 25 mL $CHCl_3$. After 10 minutes of vigorous stirring, 0.18 g of elemental sulfur (S) is added. The mixture is stirred for 60 minutes with the organic phase becoming a faint yellow color. The organic phase is separated and dried on a rotary evaporator to leave a bright yellow waxy solid. 240 μL dodecanethiol is then added dropwise to the solid. One hour later, the waxy precursor material appears as a dark red material: the thiol diffuses into the solid and changes the color of the material. The precursor is heated for 1 hr at 160°C to produce a black solid containing nanorods. The product is redispersed in chloroform and precipitated by adding excess ethanol to remove unwanted

molecular byproducts. The nanorod yield is ~33% based on number of moles of Bi converted to Bi_2S_3.

3.2.3 Characterization

Transmission electron microscopy (TEM), scanning electron microscopy (SEM), X-ray diffraction (XRD), and selective area electron diffraction (SAED) were used to characterize the nanocrystals. Low to intermediate resolution TEM images were obtained digitally using a Philips 208 TEM operating at 80 kV accelerating voltage with an AMT Advantage HR model CCD camera. High resolution TEM and SAED were performed using a JEOL 2010F TEM equipped with a field emission gun operating at 200 kV accelerating voltage. Images were acquired digitally on a Gatan multipole scanning CCD camera. Electron diffraction patterns were taken using a 10 μm diffraction aperture. All TEM samples were prepared by drop casting nanocrystals from chloroform onto 200 mesh carbon film coated Cu grids (Ladd Research) or 200 mesh lacey carbon coated Cu grids (Electron Microscopy Sciences). SEM was performed on nanowire samples using a LEO 1530 field emission gun SEM operating at 1 to 3 kV accelerating voltage with digital image acquisition using an Inlens detector and LEO 32 software system. SEM images were obtained from nanorods and nanowires drop cast onto glassy carbon substrates (1 x 1 cm and 1 mm thick) from chloroform using a LEO 1530 field emission gun SEM at 1 to 3 kV accelerating voltage. Images were acquired digitally by an Inlens detector equipped with a LEO 32 software system. XRD was obtained from nanowires and nanorods drop cast from chloroform onto quartz (0001) substrates using a

Bruker-Nonius D8 Advance Theta-2Theta powder diffractometer with Cu Kα radiation, Bruker Sol-X Si(Li) solid state detector, and a rotating stage. XRD patterns were collected over an 8 to 12 hr period with a 0.02° angle increment at a rate of 12° / min.

3.3 RESULTS AND DISCUSSION

3.3.1 Control of Nanocrystal Aspect Ratio

Figure 3.1 shows TEM and SEM images of nanowires produced in this reaction. The nanowires are ~25 nm in diameter with the majority exceeding 5 μm in length. The aspect ratio is greater than 100 and nanowires as long as 70 μm can be observed. In the solventless reaction environment, the hydrocarbon chains from the octanoate and the decomposing thiolate confine nanocrystal growth to localized reaction volumes that do not mix to an appreciable extent, much like what occurs in confining media like polymers, glasses and zeolites. In the solventless media, however, the host material does not exhibit well-defined "pores" and rearranges around the precipitating material as it degrades during the reaction. The organic species adsorbs relatively strongly to the surface of the nanowires, providing dispersibility in organic solvents such as chloroform and hexane and nanometer-scale separation between neighboring wires. In fact, Bi_2S_3 nanowires appear to form as close-packed bundles, like those shown in Figures 3.1C-3.1E, with wires separated by an intervening organic layer.

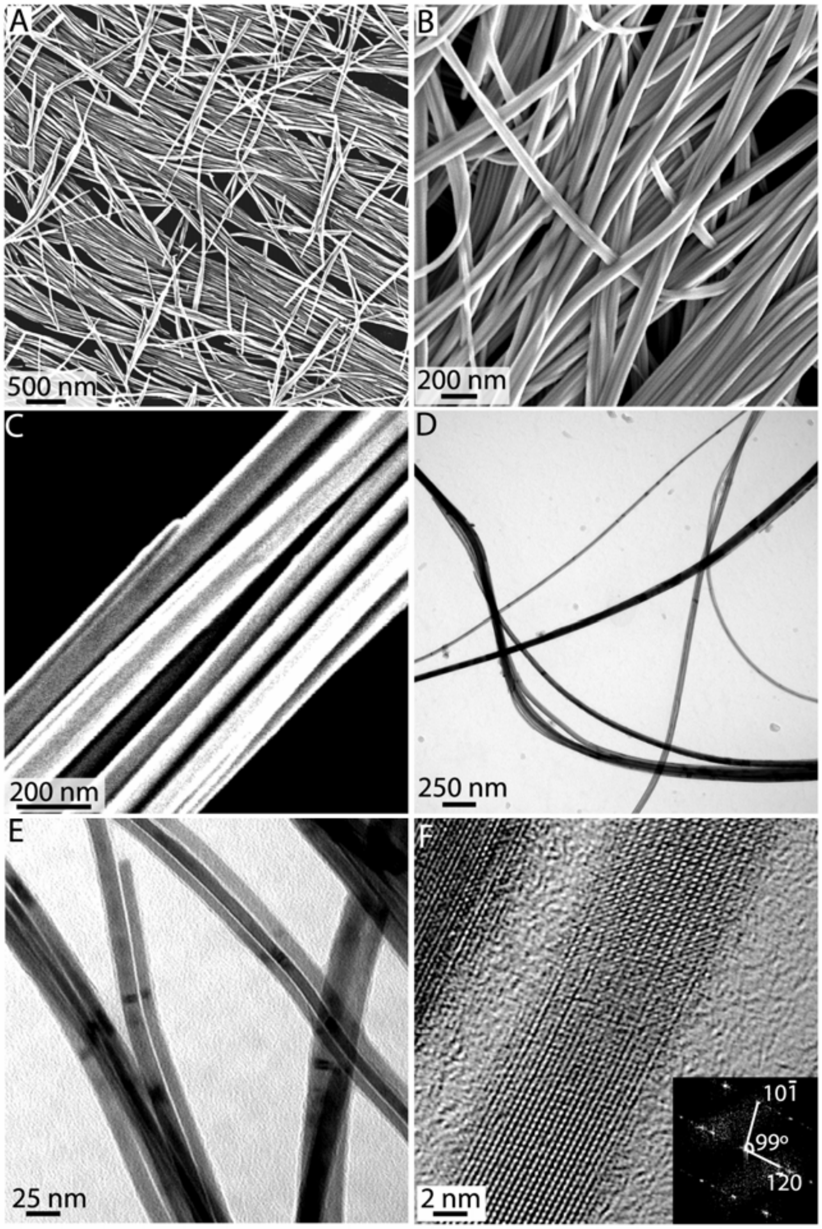

Figure 3.1: (A, B, C) SEM and (D, E) low resolution TEM images of Bi_2S_3 nanowires. The wires range from 0.5 μm up to 70 μm long, with the majority of wires longer than 5 μm. The average diameter was 26.0 nm ($\sigma = \pm$ 17.4 nm for 200 wires counted). (F) High resolution TEM image of an 8 nm diameter nanowire; (Inset) FFT of the TEM image revealing that the nanowire growth direction is [002].

The addition of elemental sulfur to the solventless reaction of the Bi alkylthiolate and octanoate mixture produces shorter aspect ratio nanorods. The highest quality product is obtained at significantly reduced reaction temperatures of ~160^{o}C, with nanorods that are on average ~10 nm in diameter and ~70 nm long, as shown in the TEM images in Figure 3.2. The nanorods readily disperse in organic solvents, such as chloroform and hexane, indicating that their surfaces are terminated with organic ligands.

3.3.2 Crystallographic Structure and Orientation

Both the nanowires and nanorods are composed of orthorhombic Bi_2S_3 (bismuthinite, JCPDS file #17-0320). The nanorod XRD patterns (Figure 3.3B) show no significant deviation in relative peak intensities from that of bulk bismuthinite. However, the diffraction patterns for the nanowires (Figure 3.3A) exhibit higher (101) peak intensity and decreased intensity of the merged (130)/(310) peaks. The relatively large differences in peak intensities indicate that the material is composed of aspherical crystalline domains that are elongated in a preferred crystallographic orientation.

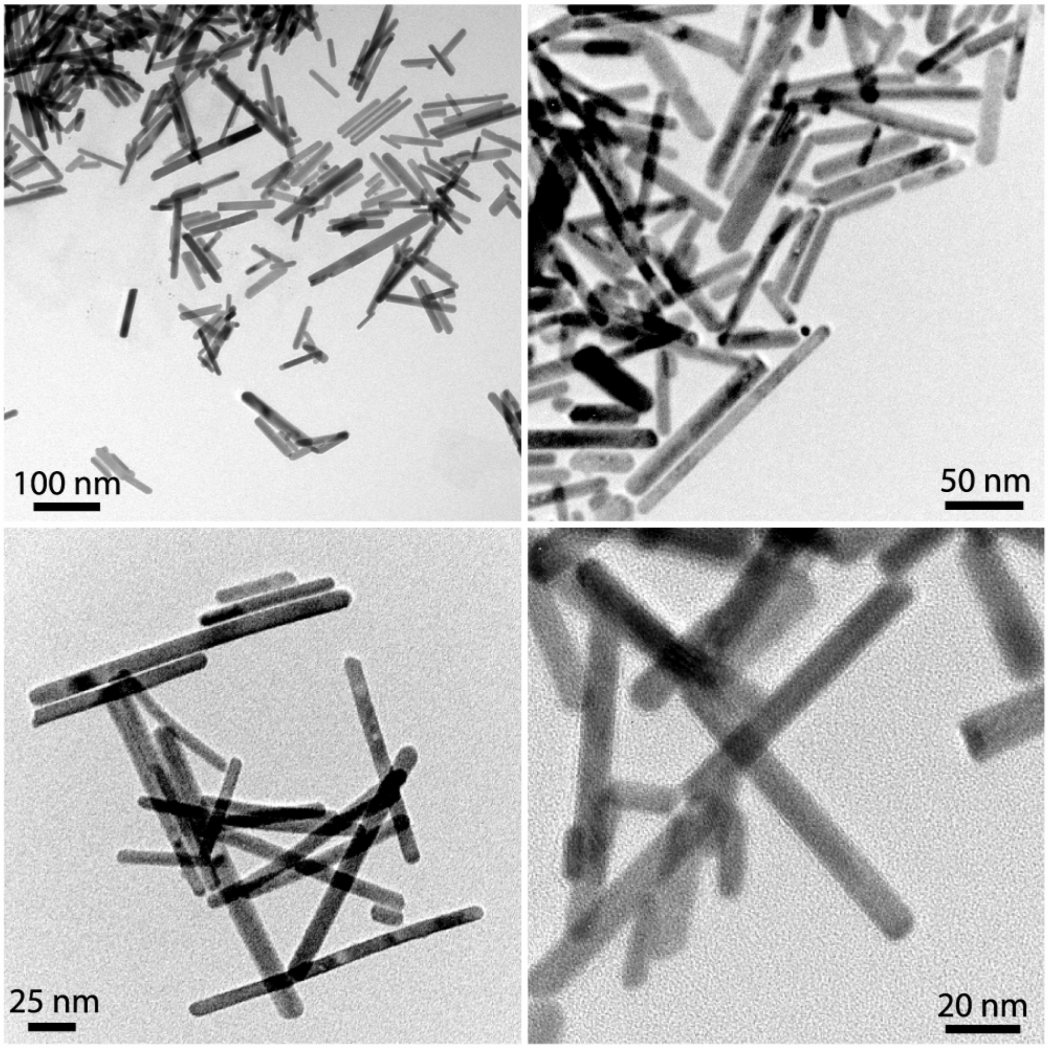

Figure 3.2: TEM images of Bi_2S_3 nanorods with an aspect ratio of ~7: average length and diameter of 73.6 nm (σ = ± 38.8 nm for 200 rods counted) and 10.7 nm (σ = ± 3.2 nm for 200 rods counted).

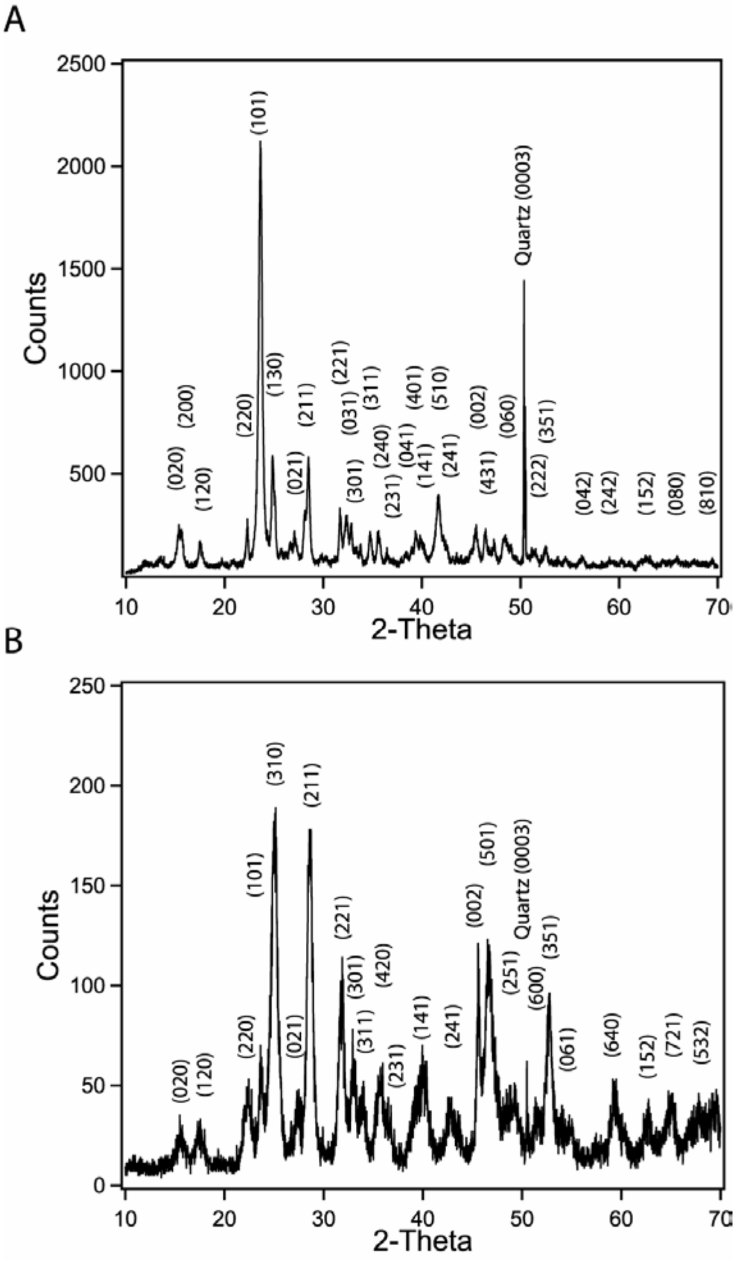

Figure 3.3: XRD obtained from Bi_2S_3 (A) nanowires and (B) nanorods. Both exhibit orthorhombic Bi_2S_3 crystal structure (bismuthinite, JCPDS file #17-0320).

Fast Fourier transforms (FFTs) of HRTEM images and selected area electron diffraction (SAED) patterns reveal that the nanowires extend preferentially in the [002] direction. For example, the FFT of the 8 nm diameter nanowire in Figure 3.1F is consistent with a nanowire elongated in the [002] direction with an electron beam incident along the [212] zone axis. To help interpret many of the FFT and SAED patterns, electron diffraction (ED) patterns were simulated with the JEMS software package using the appropriate lattice cell dimensions (11.149 x 11.304 x 3.981 Å) for orthorhombic Bi_2S_3 with the *Pbnm* (62) space group with Bi and S atomic coordinates listed in Wyckoff.[27] Figure 3.4 shows examples of experimental SAED patterns compared to simulated diffraction patterns. Both nanowires in Figure 3.4 are elongated in the [002] direction. The nanowire in Figure 3.4A is oriented with its [120] zone axis perpendicular to the substrate, and as a result the {001} and $\{2\bar{1}0\}$ reflections appear in the SAED pattern parallel and perpendicular, respectively, to the [002] direction (the long axis of the nanowire), with the $(2\bar{1}\bar{1})$ reflection occurring at 52° from the $\{2\bar{1}0\}$ reflection. The nanowire in Figure 3.4D is oriented with its [121] zone axis perpendicular to the substrate. Therefore, the $\{2\bar{1}0\}$ reflections appear across the width of the wire and the $\{10\bar{1}\}$ and $\{\bar{1}1\bar{1}\}$ reflections appear at 73° and 115° from the $\{2\bar{1}0\}$ reflections. The {002} family of planes is oriented at 90° from the $[2\bar{1}0]$ direction (i.e., perpendicular to the growth direction) and 19.5° from the $[10\bar{1}]$ direction, consistent with a nanowire elongated in [002] direction. Note that no lattice reflections appear in the SAED pattern parallel to the long axis because of the particular crystallographic zone axis parallel to the incident electron beam. Of the 64 nanowires examined by SAED and/or FFT, all 64 were extended in the [002] direction.

It is worth noting a few unexpected features in the experimental diffraction patterns, as in Figure 3.4B, that result from the small size of the sample: (1) the kinematically forbidden (001) and $(00\overline{1})$ reflections appear and (2) numerous faint reflections appear, representing non-integer fractions of the allowed reflections. These additional reflections are most likely due to breaks in crystal lattice symmetry such as monatomic steps and kinks along the nanocrystal surface.[28-30]

The Bi_2S_3 nanorods are also oriented with their long axes in the [002] direction. See for example, two representative nanorods in Figure 3.5 with their FFTs and the simulated ED patterns. The rod in Figure 3.5A is oriented on its [120] zone axis and as a result the {210} family of lattice reflections appears at 90° to the [002] growth direction. In Figure 3.5D, the electron beam is incident down the [110] zone axis of this nanorod and therefore the $\{\overline{1}10\}$ reflections occur across the short axis of the wire, perpendicular to the [002] direction. All of the nanorods examined by HRTEM (26 of 26) were elongated in the [002] direction.

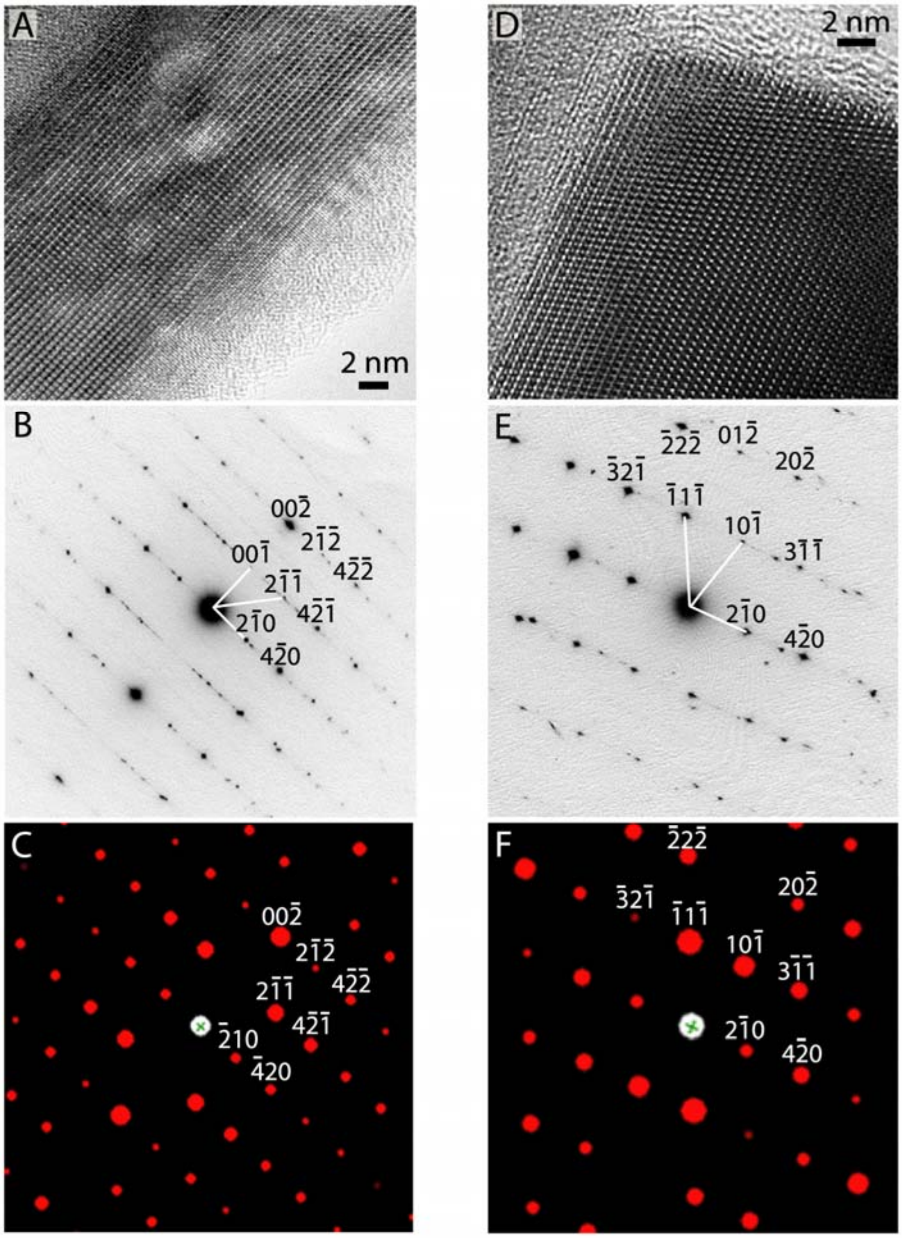

Figure 3.4: (A,D) HRTEM images of Bi_2S_3 nanowires with (B,E) SAED patterns obtained from the imaged area. The ED patterns match (C,F) electron diffraction patterns simulated with the electron beam oriented along the [120] and [121] zone axes, respectively, with the nanowires elongated in the [002] direction.

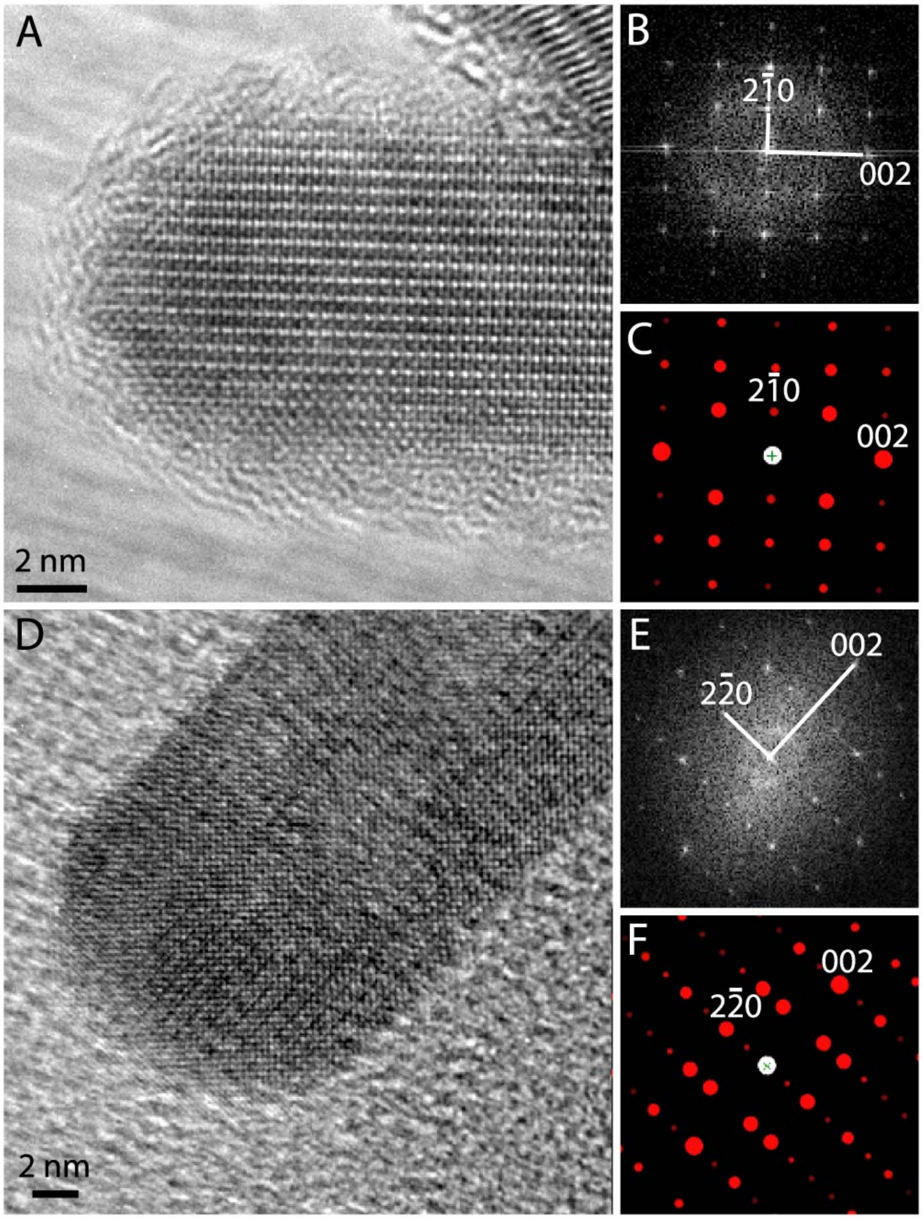

Figure 3.5: (A,D) HRTEM images and (B,E) corresponding FFTs of two Bi_2S_3 nanorods. (C,F) The ED patterns simulated for rods elongated in the [002] direction with the electron beam incident along the [120] and [110] zone axes, respectively, match the FFTs and confirm the crystallographic orientation and growth direction of the nanorod.

The addition of elemental sulfur to the reaction environment changes the nanocrystal growth kinetics significantly and "quenches" nanowire elongation. The sulfur-carbon bond in free dodecanethiol is relatively stable and will not break at 160°C unless complexed with Bi. Therefore, the only way to increase the sulfur-to-bismuth ratio in the reaction is to add an independent sulfur source, i.e., elemental sulfur. The addition of free sulfur increases the rate of Bi_2S_3 formation, the thermodynamic driving force for nucleation,[31] and depletes the available Bi needed to extend the nanostructures to very long aspect ratios. Dodecanethiol plays an important role in nanorod formation, as poorly formed agglomerated particles resulted when it was not added to the reaction; however, it is the addition of free sulfur to the reaction that prevents nanowires from growing with very long aspect ratios, terminating growth to produce rods.

3.3.3 Formation of Nanofabric

Higher reaction temperatures (240°C) also change the nanowire growth kinetics, resulting in different nanomaterial morphologies. At these higher synthetic temperatures, fabric-like structures form as an interlocking square lattice of interwoven nanowires exhibiting an extremely high degree of orientational order (Figure 3.6). The yield of these matted structures is relatively low (estimated at $< 1\%$ of total nanocrystal mass); however, they occur reproducibly in all reactions. Furthermore, reactions at 225°C rarely produced these kinds of structures. The fabrics typically consist of two interpenetrating layers of crossed nanowires as shown in Figure 3.6B and 3.6C that cover an area of $\sim 10\ \mu m^2$. Thicker fabrics with multiple layers of crossed nanowires could also be observed

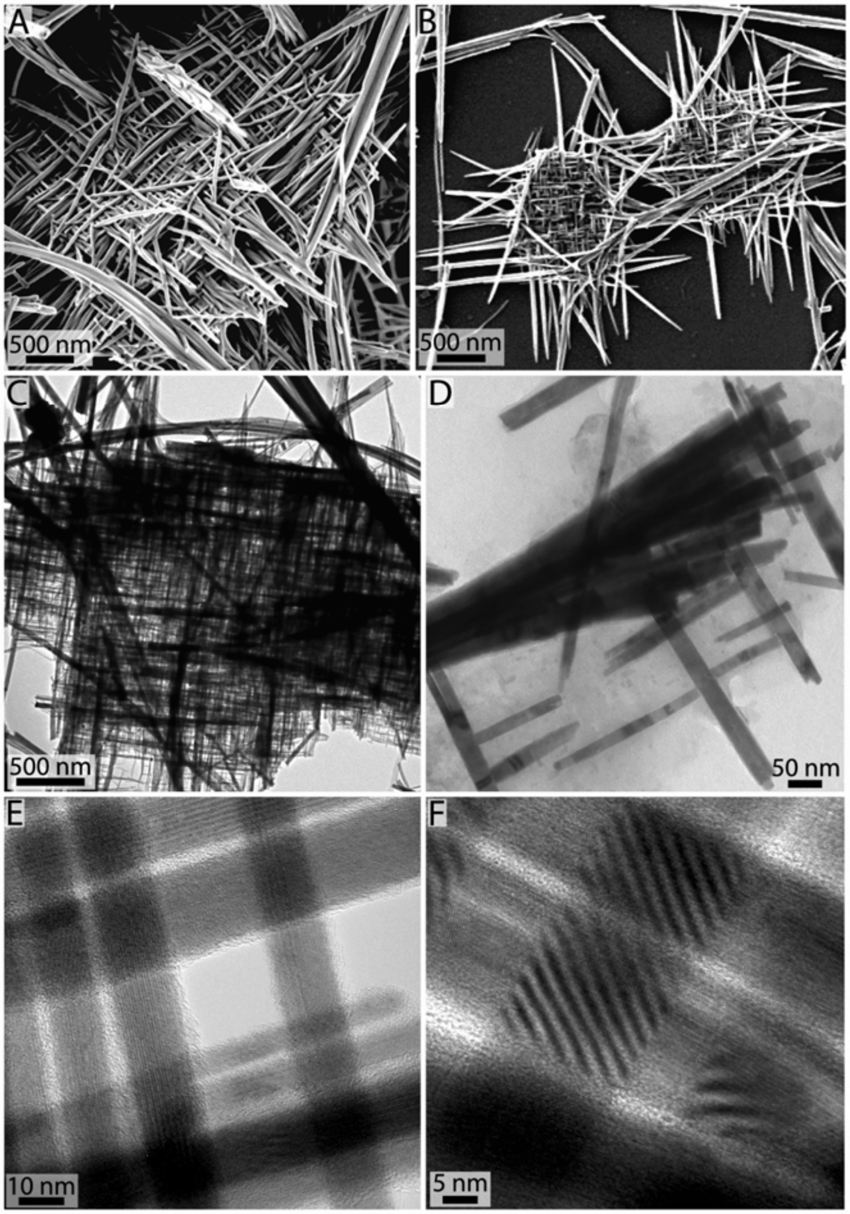

Figure 3.6: (A) and (B) SEM images of Bi_2S_3 nanofabric. (C) Low resolution TEM image of nanofabric illustrating a high degree of order throughout the fabric over micron length scales. (D) Area of fabric in its initial stages of formation showing the nucleation of new wires at 90° relative to preexisting ones. (E) Intermediate and (F) HRTEM images showing areas of densely ordered nanowires forming the inner mesh of the fabric.

(Figure 3.6A). The nanowires in the fabric are densely packed with wire to wire separations as small as one nanometer (as in Figure 3.6E), and they exhibit a very high degree of perpendicular orientational order with very few misaligned nanowires. The nanowire fabrics form as a result of the epitaxial nucleation and growth of wires on wires that occurs at these temperatures.

In the fabrics, the nanowires exhibit crystallographic registry between crossed and parallel wires. As shown in Figure 3.6D, nanowires are found to grow from the surface of existing wires. Unlike hexagonally branched Bi_2S_3 snowflakelike structures observed by Lu et al. and Wang et al. in their hydrothermal synthesis, the Bi_2S_3 structures formed in the solventless environment exhibit perpendicular branching.[32,33] The "symmetry-breaking" results from the asymmetric Bi_2S_3 crystal structure and the epitaxial registry between crystallographic planes of crossed nanowires. FFTs of high resolution TEM images (as in Figure 3.7A) of regions of crossed nanowires reveal two identical overlapping diffraction patterns oriented at exactly 90° with respect to one other. In order for this to occur, all of the wires in the image must be oriented with the same zone axis along the direction of the electron beam, in this case the [110] zone axis, with the same growth direction. The elongation of the nanowires in the [002] direction is revealed in the two {002} spots (1.99 Å spacing) in the FFT oriented perpendicular to each other. The $\{\bar{1}10\}$ lattice reflections from each nanowire in the FFT are oriented at an angle of 90° from one another as depicted schematically in Figure 3.7E. With the electron beam incident along the [110] zone axis, the $\{2\bar{2}\bar{1}\}$ and $\{\bar{2}2\bar{1}\}$ sets of lattice reflections appear at 45°

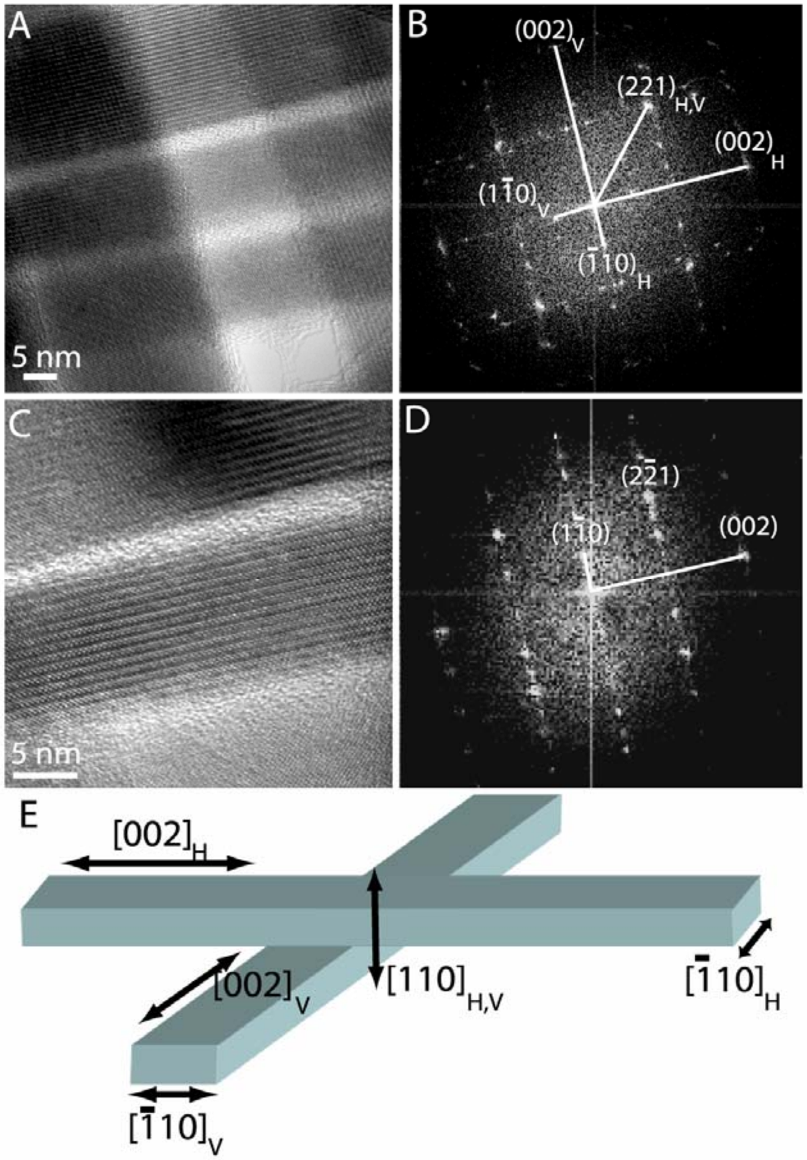

Figure 3.7: (A) HRTEM image and (B) corresponding FFT of the image reveals the precise crystallographic registry between crossed nanowires in the fabric. The FFT shows the overlapping patterns of the crossed nanowires—the FFTs match simulated electron diffraction from the [110] zone axis (For example, see Figure 3.1F). (C) Magnified HRTEM image of the three horizontally oriented nanowires imaged in (A); (D) the FFT of the imaged region containing all three nanowires shows that all three wires are crystallographically oriented with respect to their [110] zone axes.

from the $\{\bar{1}10\}$ and {002} lattice reflections, and therefore, with the nanowires perpendicularly oriented, the $\{2\bar{2}\bar{1}\}$ and $\{\bar{2}2\bar{1}\}$ diffraction spots overlap exactly in the FFT. The parallel nanowires also exhibit crystallographic registry indicating that they originated from the surface of the same nanowire. Figure 3.7C shows a magnified image of the three parallel wires in Figure 3.7A. The FFT of the image shows spots as expected from a single perfect crystal with the beam incident along the [110] zone axis. The extent of crystallographic registry between crossed nanowires in the fabric results from the heterogeneous seeding of nanowires and their "epitaxial" growth.

The crossed nanowire growth appears to originate from a lattice defect, as Moiré fringes (Figure 3.6F) at the crossed nanowire junctions reveal that the two nanowires do not exhibit the same crystallographic orientation.[34,35] The nanowires in the fabric are all elongated in the [002] direction and are oriented with their [110] zone axes perpendicular to the substrate. At the nanowire junction, both of the crossed nanowires are oriented with their {110} lattice planes parallel to the substrate (perpendicular to the [110] direction). A rotation of the orthorhombic Bi_2S_3 crystal lattice by 90° around the [110] direction produces two interfacing crystal domains with a small amount of lattice mismatch. The {220} and {440} lattice spacings (3.967 Å and 1.985 Å) running parallel to the growth direction are very close to the {001} and {002} lattice spacings (3.981 Å and 1.990 Å) perpendicular to the growth direction. Furthermore, the $\{2\bar{2}\bar{1}\}$ and $\{\bar{2}2\bar{1}\}$ sets of lattice planes oriented at 45° from the $\{\bar{1}10\}$ and {002} lattice reflections have no lattice mismatch for orthogonally oriented wires. Therefore, despite the difference in crystallographic orientation the crossed nanowires exhibit minimal lattice distortion at their junction and heterogeneous growth of crossed nanowires is favored in this system at high synthetic temperatures.

3.4 CONCLUSIONS

The synthesis of high aspect ratio orthorhombic Bi_2S_3 (bismuthinite) nanowires by Bi alkylthiolate thermolysis shows that the solventless approach to nanomaterials precipitation has the potential for producing a wide range of morphologies, from spherical particles, disks, rods, prisms, and wires. The asymmetric nanocrystal shape reflects the asymmetric crystal structure of the solid, and differences in crystal growth kinetics as a function of crystallographic orientation have been found to be important in the solventless environment. The addition of "free" chemical species, such as elemental sulfur, into the reaction mixture can be used to change the growth kinetics and provides a potential route for obtaining general shape tunability in the solventless environment.

3.5 REFERENCES

(1) For a recent review, see *Semiconductor and Metal Nanocrystals: Synthesis and Electronic Properties*; Klimov, V.I., Ed.; Marcel Dekker: New York, **2004**.

(2) Peng, Z. A.; Peng, X. *J. Am. Chem. Soc.* **2002**, *124*, 3343.

(3) Peng, X. *Adv. Mater.* **2003**, *15*, 459.

(4) LaMer, V. K.; Dinegar, R. H. *J. Am. Chem. Soc.* **1950**, *72*, 4847.

(5) Sugimoto, T. *Chem. Eng. Technol.* **2003**, *26*, 313.

(6) Larsen, T. H.; Sigman, M.; Ghezelbash, A.; Doty, R. C.; Korgel, B. A. *J. Am. Chem. Soc.* **2003**, *125*, 5638.

(7) Sigman, M. B.; Ghezelbash, A.; Hanrath, T.; Saunders, A. E.; Lee, F.; Korgel, B. A. *J. Am. Chem. Soc.* **2003**, *125*, 16050.

(8) Ghezelbash, A.; Sigman, M. B.; Korgel, B. A. *Nano Lett.* **2004**, *4*, 537.

(9) Wang, D.; Shao, M.; Yu, D.; Li, G.; Qian, Y. *J. Cryst. Growth* **2002**, *243*, 331.

(10) Liu, Z.; Peng, S.; Xie, Q.; Hu, Z.; Yang, Y.; Zhang, S.; Qian, Y. *Adv. Mater.* **2003**, *15*, 936.

(11) Koh, Y. W.; Lai, C. S.; Du, A. Y.; Tiekink, E. R. T.; Loh, K. P. *Chem. Mater.* **2003**, *15*, 4544.

(12) Yu, S.; Qian, Y.; Shu, L.; Xie, Y.; Yang, L.; Wang, C. *Mater. Lett.* **1998**, *35*, 116.

(13) Zhang, W.; Yang, Z.; Huang, X.; Zhang, S.; Yu, W.; Qian, Y.; Jia, Y.; Zhou, G.; Chen, L. *Solid State Commun.* **2001**, *119*, 143.

(14) Shao, M.; Zhang, W.; Wu, Z.; Ni, Y. *J. Cryst. Growth* **2004**, *265*, 318.

(15) Zhang, H.; Ji, Y.; ma, X.; Xu, J.; Yang, D. *Nanotechnology* **2003**, *14*, 974.

(16) Liao, X.-H.; Wang, H.; Zhu, J.-J.; Chen, H.-Y. *Mater. Res. Bull.* **2001**, *36*, 2339.

(17) Cao, X.; Li, L.; Xie, Y. *J. Coll. Inter. Sci.* **2004**, *273*, 175.

(18) Ye, C.; Meng, G.; Jiang, Z.; Wang, Y.; Wang, G.; Zhang, L. *J. Am. Chem. Soc.* **2002**, *124*.

(19) Wang, H.; Zhu, J.-J.; Zhu, J.-M.; Chen, H.-Y. *J. Phys. Chem. B* **2002**, *106*, 3848.

(20) Grigas, J.; Talik, E.; Lazauskas, V. *Phys. Stat. Sol. (b)* **2002**, *232*, 220.

(21) Black, J.; Conwell, E. M.; Seigle, L.; Spencer, C. W. *J. Phys. Chem. Solids 2* **1957**, *2*, 240.

(22) Suarez, R.; Nair, P. K.; Kamat, P. V. *Langmuir* **1998**, *14*, 3236.

(23) Mane, R. S.; Sankapal, B. R.; Lokhande, C. D. *Mater. Chem. Phys.* **1999**, *60*, 158.

(24) Chen, B.; Uher, C. *Chem. Mater.* **1997**, *9*, 1655.

(25) Cantarero, A.; Martinez-Pastor, J.; Segura, A. *Phys. Rev. B* **1987**, *35*, 9586.

(26) Cotton, F. A.; Wilkinson, G. *Advanced Inorganic Chemistry*, 3rd ed.; John Wiley & Sons: New York, 1972.

(27) Wyckoff, R. W. G. *Crystal Structures: Inorganic Compounds*, 2nd ed.; Interscience Publishers: New York, 1964; Vol. 2nd.

(28) Gibson, J. M.; Lanzerotti, M. Y.; Elser, V. *Appl. Phys. Lett.* **1989**, *55*, 1394.

(29) Lynch, D. F. *Acta Cryst.* **1971**, *A27*, 399.

(30) Castaño, V.; Gómez, A.; Yacaman, M. J. *Surf. Sci.* **1984**, *146*, L587.

(31) Toschev, S. Homogeneous Nucleation. In *Crystal Growth: An Introduction*; Hartman, P., Ed.; American Elsevier: New York, 1973; Vol. 1.

(32) Lu, Q.; Gao, F.; Komameni, S. *J. Am. Chem. Soc.* **2004**, *126*, 54.

(33) Wang, D.; Shao, M.; Yu, D.; Yu, W.; Qian, Y. *J. Cryst. Growth* **2003**, *254*, 487.

(34) Williams, D. B.; Carter, C. B. *Transmission Electron Microscopy: A Textbook for Materials Science*; Plenum Press: New York, 1996.

(35) Based on the measured spacing, d_M of 24.3 Å between Moiré fringes in Figure 3.6F, the mismatch between the {002} lattice planes along the

length of one wire and the {440} lattice planes across the width of the second indicates a rotational shift between the two crystal lattices of the wires of 2.3° (i.e. wires are 87.7° apart) as determined by the following equation $d_M = (d_1 d_2) / ((d_1-d_2)^2 + d_1 d_2 ß^2)^{1/2}$ for Moiré fringes with both translational and rotational mismatch with d_1 and d_2 being the spacing between the two sets of planes and ß being the degree of rotation between the two sets of planes. This calculated rotation between crystal lattices is comparable to the measured value of 87° between the actual wires in Figure 3.6F. Bulk values of 1.99 Å for the {002} planes and 1.985 Å for the {440} planes were used in the calculation to represent the translational mismatch between lattice fringes of the two crossing wires.

Chapter 4: Strongly Birefringent $Pb_3O_2Cl_2$ Nanobelts Synthesized by a Solventless Approach[*]

4.1 INTRODUCTION

Materials with anisotropic crystal structure exhibit a variety of physical properties that depend strongly on crystallographic direction, such as the refractive index (i.e., birefringent materials),[1-4] the permanent dipole moment in ferroelectrics,[5-7] the coercivity in ferromagnets,[8,9] and carrier mobilities in ionic conductors.[10-13] In nanomaterials, this orientational dependence can be enhanced by producing structures with non-spherical shape elongated along a preferred crystal axis.[14] It turns out that many nanomaterials with anisotropic crystal structures will form non-spherical structures due to significant differences in the growth kinetics of each crystal face.[14,15] The study and development of synthesis techniques that utilize surface energy differences between individual lattice planes are essential to both the understanding of shape control mechanisms and the resulting effect of that shape on the physical properties of nanocrystalline materials. In particular, a variety of colloidal synthetic routes have proven to be a productive means of forming nanocrystals with anisotropic shapes. These techniques include thermal decomposition, the use of surfactants that selectively

---

[*] The contents of this chapter to be submitted to *Angew. Chem. Int. Ed.*

adsorb to specific lattice planes directing crystal growth,[16-21] vapor or solution-liquid-solid growth,[22-24] and template directed growth.[14,25,26]

Cu_2S nanodisks, Bi_2S_3 nanorods and nanowires, and NiS nanorods have been produced via the solventless thermolysis of metal alkylthiolate precursors.[27-29] This chapter reports the solventless synthesis of $Pb_3O_2Cl_2$ nanobelts using a lead chloride ($PbCl^-$)-octanoate derived precursor. The synthesis demonstrates the extension of this solventless nanomaterials technique to form a non-sulfide material with a ternary atomic composition. Similar to the Bi_2S_3 system, the nanobelts exhibit aspect ratios significantly larger than expected from previous materials formed using this solventless technique. The orthorhombic crystal structure of these belts is highly birefringent as shown by their ability to polarize light. This property offers the possibility for use as components in optical devices and provides a test system for examining the properties of birefringent materials with spatial dimensions significantly less than the wavelength of visible light.

4.2 EXPERIMENTAL

All chemicals were used as supplied from Aldrich Chemical Co. Water was distilled and deionized.

4.2.1 Nanobelt Synthesis

$Pb_3O_2Cl_2$ nanobelts are obtained by thermolysis of a lead chloride ($PbCl^-$) octanoate-derived precursor in the absence of solvent similar to previous work for Cu_2S and NiS by our group.[27,29] In a typical preparation, lead (II) chloride (0.20 g $PbCl_2$) is added to 32 mL of DI water. Due to the low solubility of lead (II) chloride in water, sonication is needed to form a slightly cloudy, aqueous dispersion. 25 mL of chloroform ($CHCl_3$) with 0.17 g sodium octanoate ($NaOOC(CH_2)_6CH_3$) is added to the aqueous $PbCl_2$ solution forming two phases. In aqueous solutions, $PbCl_2$ dissociates to form $PbCl^+$.[30] Sodium octanoate serves as a phase transfer catalyst and complexes with lead (II) chloride ion to form a clear to slightly cloudy solution in the organic phase. After stirring for ~20 minutes, the aqueous phase is separated and discarded. Ethylenediamine ($C_2H_8N_2$, 500 μL) is then added to the organic solution. Following 10 min of stirring, the organic solvent is evaporated on a rotary evaporator to obtain an opaque gel which serves as the starting material for the nanowires. Nanoribbons were obtained by heating the precursor in air or under nitrogen for 60 min at 190ºC. Upon heating, the solid darkens becoming gray in color. The material obtained after the reaction can be redispersed in chloroform with mild sonication. To remove reaction by products, the nanobelts are precipitated in excess ethanol. Purified nanobelts appear as a powder that is white in color. Typical yields for the synthesis are 30%.

4.2.2 Characterization

The nanoribbons were characterized using transmission electron microscopy (TEM), X-ray diffraction (XRD), electron diffraction (ED), scanning electron microscopy (SEM), and optical microscopy. High resolution TEM and ED patterns was performed on samples drop cast from chloroform on 200 mesh lacey carbon coated Cu grids (Electron Microscopy Sciences) using a JEOL 2010F TEM equipped with a field emission gun operating at 200 kV accelerating voltage. Images were acquired digitally on a Gatan multipole scanning CCD camera. TEM images were also in some cases obtained using a Philips 208 TEM with 80 kV accelerating voltage. SEM was performed on a LEO 1530 field emission gun SEM operating at 1 kV accelerating voltage with digital image acquisition using an Inlens detector and LEO 32 software system. Samples were prepared for SEM by drop casting from chloroform on glassy carbon substrates approximately 1 x 1 cm and 1 mm thick. XRD was performed using a Bruker-Nonius D8 Advance Theta-2Theta powder diffractometer with Cu Kα radiation and a Bruker Sol-X Si(Li) solid state detector. XRD samples were prepared by drop casting nanowires from chloroform onto a quartz (001) substrate. XRD patterns were collected for rotating samples over an 8 hr period with a 0.02° angle increment at a rate of 12° / min.

The birefringent properties of the wires were examined on a Carl Zeiss Axioskop 2MAT optical microscope equipped with 50X and 100X objective lenses, polarization filters, and a halogen light source. The microscope was operated in transmission mode with images digitally acquired using an AxioCam MRc5 CCD camera. A Red 1 compensator and a Brace-Köhler compensator with 656 nm band interference filter were used to measure birefringence values for the nanobelts. Samples were examined while exposed to air (n = 1.00) and immersed in glycerin (n = 1.47) under a glass cover slip with no differences noted between measurements. Nanobelt thickness was determined using a Digital Instruments Dimension 3100 atomic force microscope (AFM) operating in tapping mode.

4.3 RESULTS AND DISCUSSION

4.3.1 Nanobelt Formation and Morphology

Figure 4.1 shows TEM images of $Pb_3O_2Cl_2$ nanobelts. The nanobelt precursor is formed using sodium octanoate as a phase transfer catalyst to transport ($PbCl^-$) ions from an aqueous phase into chloroform. Ethylenediamine is added to the organic layer to inhibit particulate growth prior to solvent removal via evaporation. The precursor is heated in an oven at 190º C for 1 hour forming single-crystalline nanobelts with very regular surface structure that is redispersible in chloroform. SEM images (Figure 4.2) show the rectangular prism or belt-like morphology of the nanostructures.

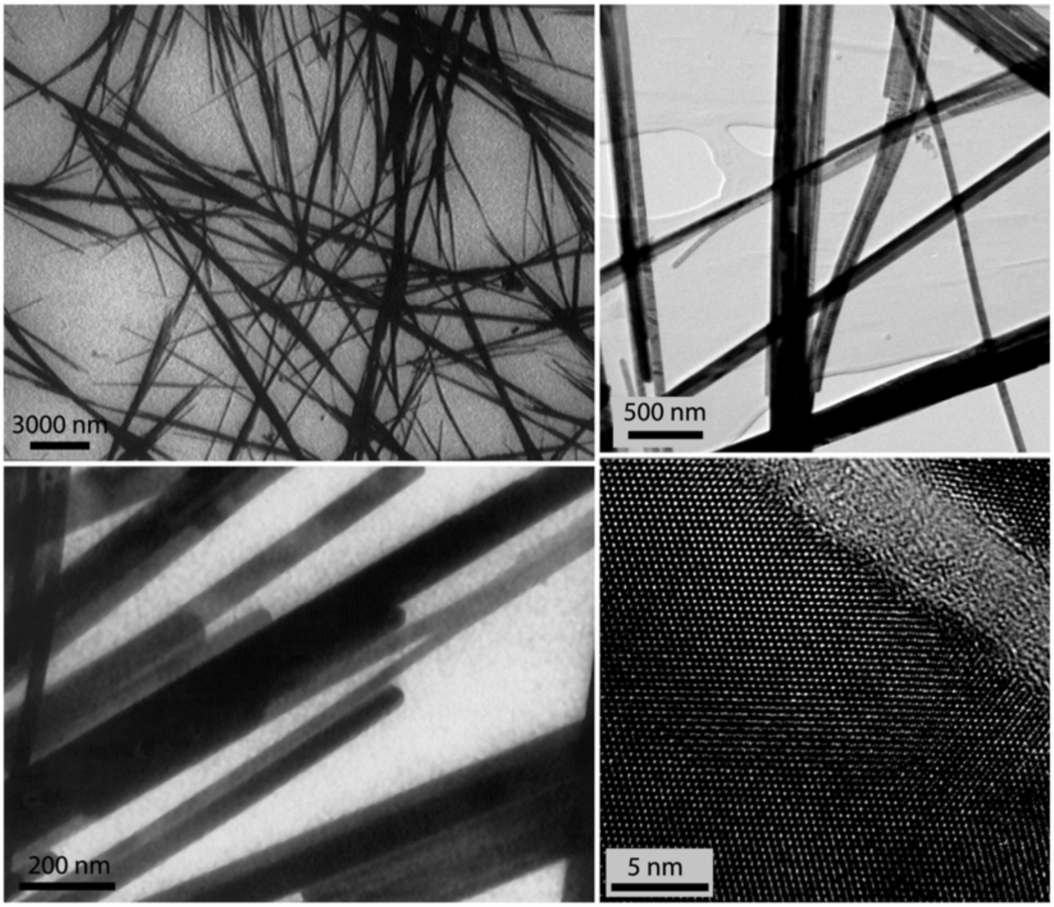

Figure 4.1: TEM images of highly crystalline $Pb_3O_2Cl_2$ nanobelts formed via solventless thermolysis technique.

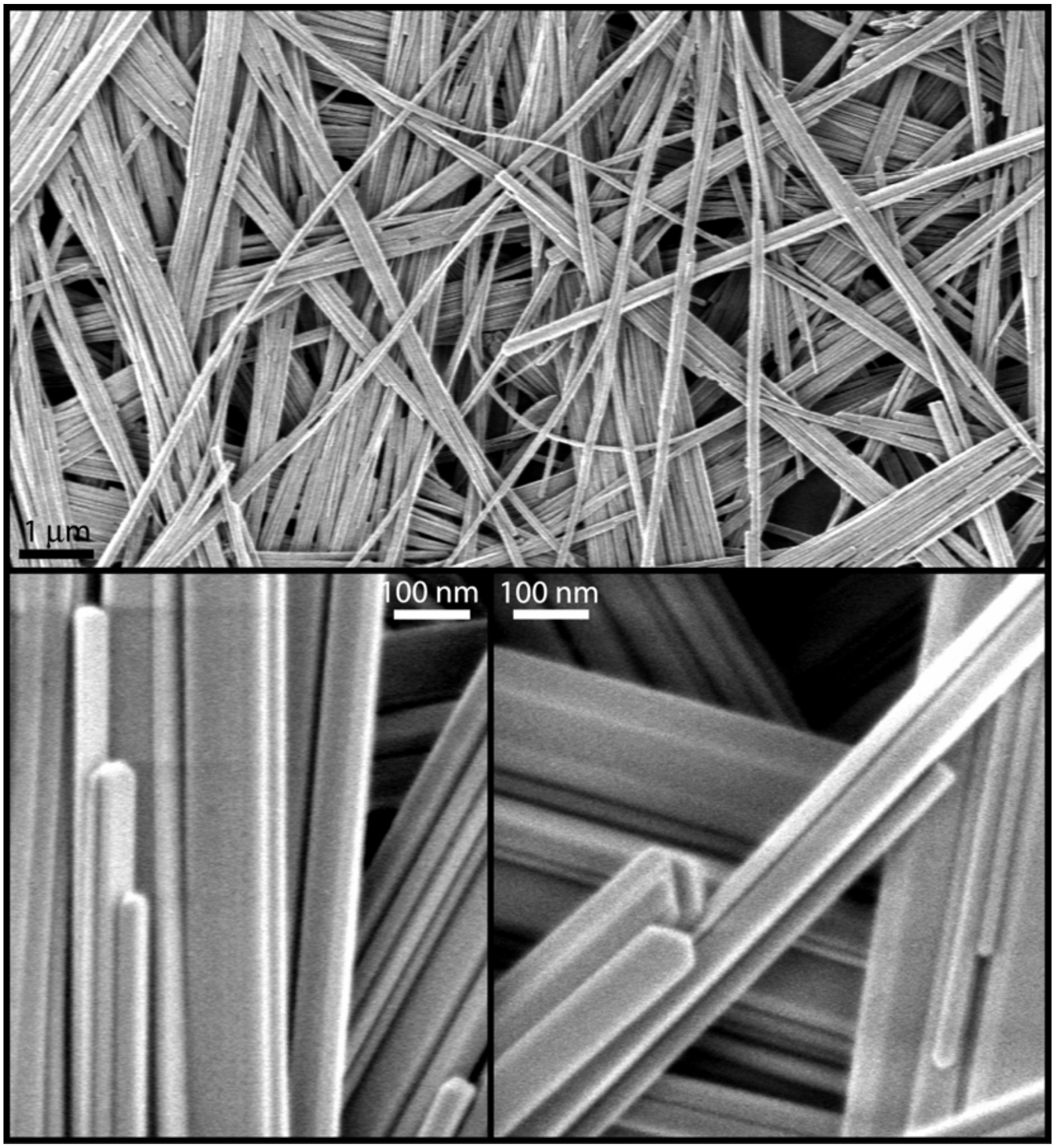

Figure 4.2: SEM images of $Pb_3O_2Cl_2$ nanobelts deposited on a glassy carbon substrate illustrating belt-like morphology and tendency to align into bundles of belts.

Individual nanobelts are much greater than 4 μm in length often extending up to 20 μm. The belt widths ranged from 29 to 170 nm with a log normal average of 61.6 nm (See Appendix B for histogram and log normal distribution). The belt thickness fits a normal distribution with an average value of 23.3 nm ($\sigma = \pm 26\%$). SEM images also show that the nanobelts tend to bundle together, particularly when deposited from concentrated dispersions.

4.3.2 Crystallographic Orientaton

The XRD pattern in Figure 4.3 reveals that the nanobelts consist of $Pb_3O_2Cl_2$ with an orthorhombic crystal structure (mendipite).

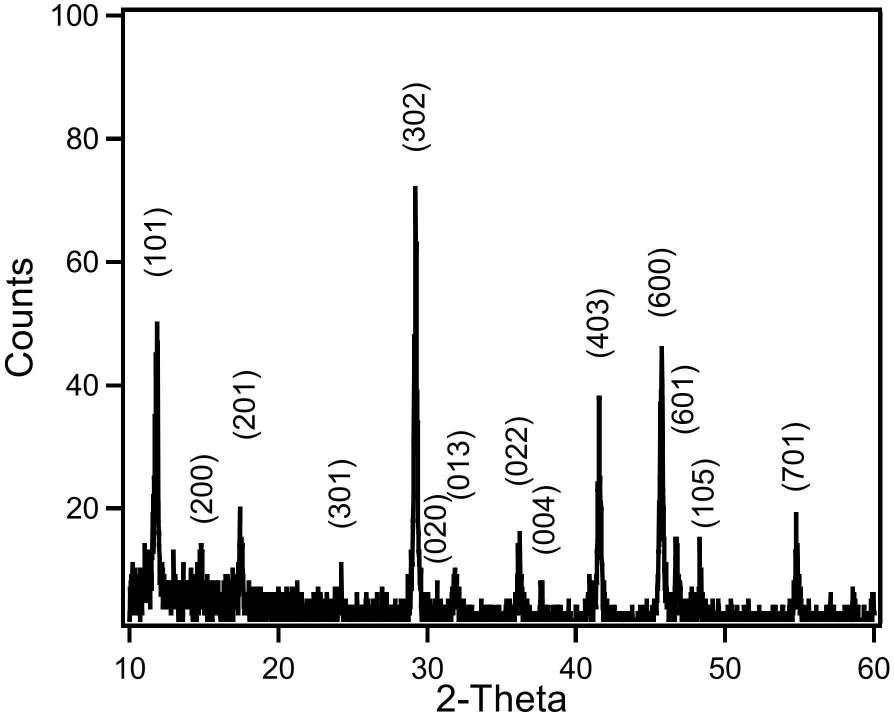

Figure 4.3: XRD pattern of the nanobelts exhibiting the orthorhombic $Pb_3O_2Cl_2$ (mendipite) structure.

The (200) and (600) peak intensities are enhanced relative to the bulk XRD pattern for mendipite (PDF file number 25-0448), and the peak intensity for the (020) and (013) planes are decreased significantly compared to the bulk. Notably, the strong reflections typically observed for the (211), (112), (311), (113), and (033) planes are absent, indicating that the belt alignment on the substrate prevents the orientation of certain planes to those needed for diffraction.

The relationship between crystallographic orientation and nanobelt morphology was examined by HRTEM and electron diffraction. Figure 4.4A and 4.4B show HRTEM and ED from a nanobelt. Since the crystal structure of $Pb_3O_2Cl_2$ is relatively complicated, the zone axis orientation, and the growth direction were determined by simulating the measured electron diffraction pattern using the JEMS simulation package. The simulations were performed using cell dimensions of 11.879 x 5.809 x 9.511 Å for the orthorhombic mendipite structure and Pb, O, and Cl atomic positions as determined by Krivovichev and Burns and Norén et al.[31,32] The simulated ED pattern for a nanobelt is shown in Figure 4.4C. It reveals that the belt is oriented with the beam penetrating the thickness of the belt down the [001] zone axis. The {020} lattice reflections appear along the growth direction of the wire and lie exactly 90˚ from the zone axis. The {020} lattice planes measure 3.00 Å from the experimental ED pattern versus 2.90 Å for the bulk XRD pattern.

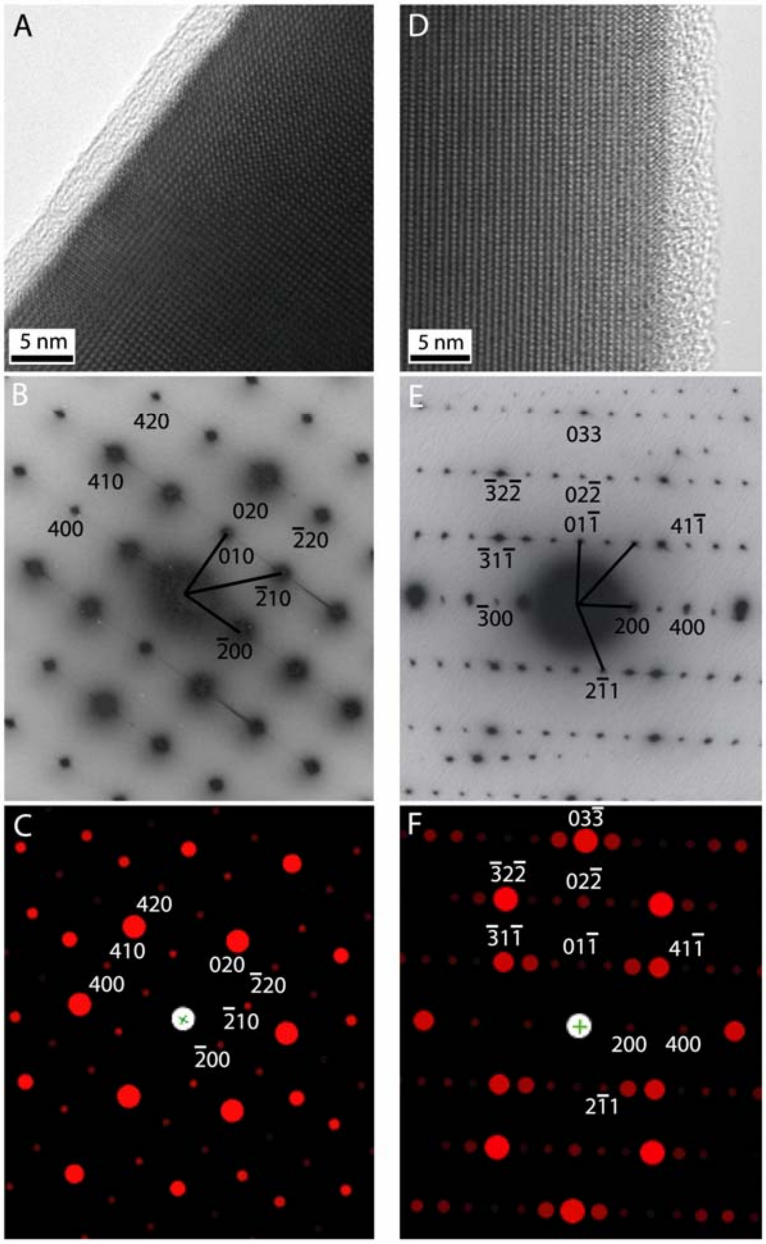

Figure 4.4: (A) HRTEM image, (B) selective area electron diffraction pattern, and (C) simulated electron diffraction pattern for $Pb_3O_2Cl_2$ nanobelt oriented along the [001] zone axis with a [010] growth direction. (D) HRTEM image, (E) selective area electron diffraction pattern, and (F) simulated electron diffraction pattern for $Pb_3O_2Cl_2$ nanobelt oriented along the [011] zone axis with a [013] growth direction.

The (010) and (030) lattice planes are forbidden in the bulk; however, these reflections appear in the ED pattern obtained for the nanoribbons. Reflections due to multiple diffraction events would appear in the simulated ED pattern since the JEMS simulation package utilizes dynamical diffraction theory. These reflections do not appear in the simulations. Instead, the appearance of the forbidden reflections is more likely due to kinematic breaks in crystal lattice symmetry such as monatomic steps along the nanocrystal surface.[33-35] Reflections for the (200) lattice plane at 6.21 Å and (400) lattice plane at 3.08 Å are present 90° from the {020} reflections and are also exactly 90° from the [001] zone axis. The orientation of the {020} and {200} reflections with respect to the [001] zone axis indicate that this belt grows in the [010] direction with the width and thickness of the belt oriented in the [100] and [001] directions, respectively. This belt morphology is illustrated by the atomic model in Figure 4.5. The [010] growth direction was observed in 90% of the belts examined (18 out of 20 belts).

Figures 4.4D-F show the TEM and corresponding experimental and simulated ED patterns for a nanobelt that did not grow in the [010] direction. This belt is oriented with the electron beam incident down the [011] zone axis. The lattice spacings for the {011} and {200} reflections measure 4.95 and 5.91 Å, in agreement with the simulated values of 5.02 and 5.98 Å. The $(0\bar{1}1)$ and $(01\bar{1})$ reflections are oriented along the growth direction of the belt; however, the angle between the [011] zone axis and the $(01\bar{1})$ lattice plane is 62.8°, indicating that neither the $[0\bar{1}1]$ or $[01\bar{1}]$ is the growth direction. The closest possible growth direction evident from the ED pattern is the [013] direction, as indicated by the fact that the $(01\bar{3})$ and $(0\bar{1}3)$ lattice planes are oriented 87.3° and 92.7° from the [011] zone axis. The {200} planes are oriented across the width of the wire, with the [200] direction exactly 90° from the [011] zone axis (oriented across the belt thickness) and the [013] direction that is oriented down the length of the belt. Therefore, ED reveals that these belts exhibit {013} lattice planes down the wire length, {011} planes across the width, and {200} planes across the thickness. Again, forbidden reflections appear in the ED pattern; this time for the (300) and (500) lattice planes. The two orientations discussed in Figure 4.4 are the only two orientations observed by single nanowire ED or HRTEM FFT on 20 different wires. Each crystallographic orientation is consistent with a rectangular prism or belt-like morphology.

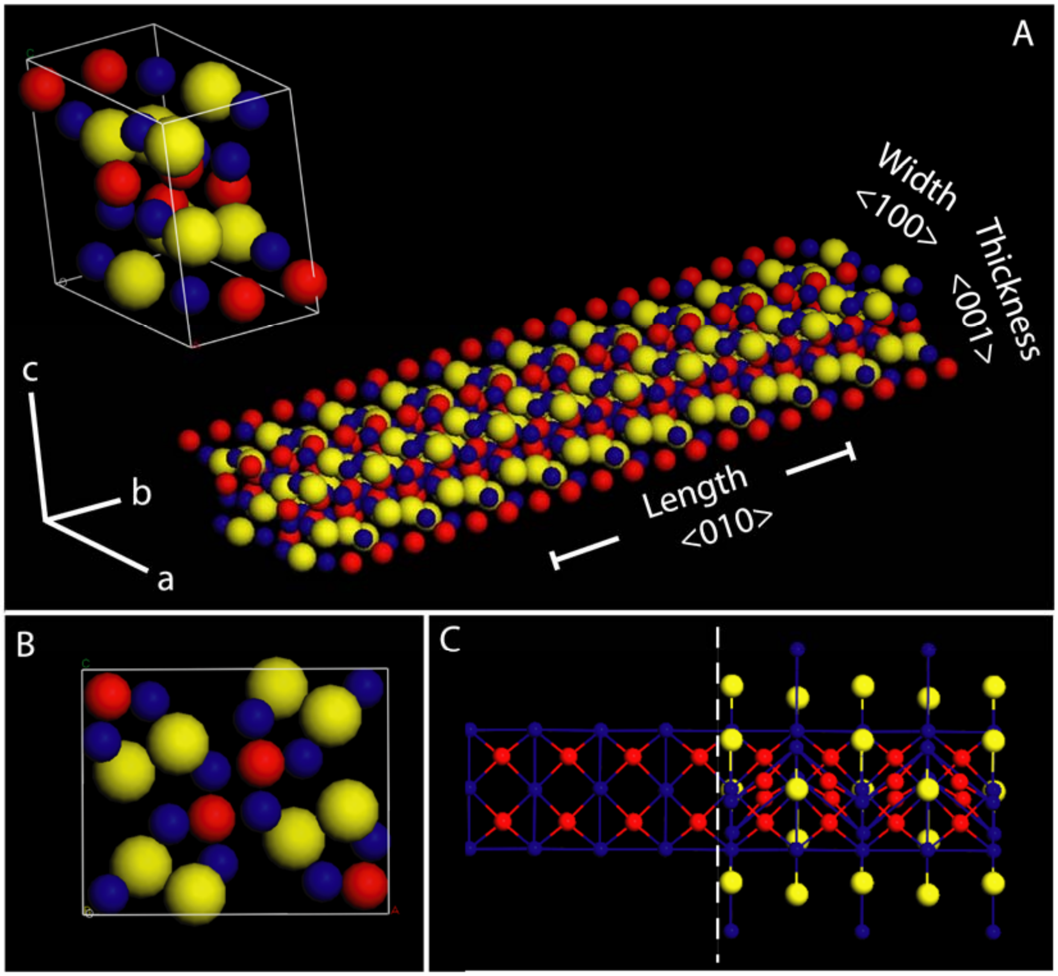

Figure 4.5: (A) Crystallographic model produced using the Materials Studio software package showing the orthorhombic $Pb_3O_2Cl_2$ unit cell (with Pb^{+2} ions (blue), O^{-2} ions (red), and Cl^{-} ions (yellow)) and a nanobelt. The nanobelt demonstrates the growth direction and surface planes observed for the majority (90%) of analyzed nanobelts. (B) Unit cell oriented along the [010] zone axis illustrating the linked OPb_4 tetrahedra. (C) Belt oriented down the $[\bar{1}01]$ zone axis showing the chains of OPb_4 tetrahedra down the length of the nanobelt. For clarity, the peripheral atoms to the left of the dashed line are removed. The full unit cell is shown to the left of the dashed line.

As shown in the unit cell in Figure 4.5A, mendipite has an orthorhombic crystal structure with $a \neq b \neq c$. When viewed from the [010] direction (Figure 4.5B), two linked (OPb_4) tetrahedra are located at the center of the unit cell with oxygen and chlorine anions shielded from one another by Pb^{+2} cations.[31] The linked tetrahedra repeat down the length of the nanobelt forming chains in the [010] direction as shown when the belt is viewed down the $[\bar{1}01]$ zone axis, as in Figure 4.5C. These chains of tetrahedra coincide with the observed growth direction of the nanobelts suggesting that their formation is responsible for their anisotropic morphology. Although several groups have reported the use of bidentate ligands as a template promoting nanowire and nanorod growth, ethylenediamine does not have this effect on the $Pb_3O_2Cl_2$ nanobelts.[36-39] Syntheses without ethylenediamine resulted in wire formation with the same growth direction as those formed in its presence (See Appendix B). The only observed effect is that ethylenediamine inhibits the formation of smaller nanocrystals and other particulates in addition to the nanobelts. In addition, the role of octanoate was examined by altering the optimum synthesis conditions. $Pb_3O_2Cl_2$ nanobelts were formed regardless of whether the sample was heated in air or under a nitrogen environment. $Pb_3O_2Cl_2$ nanobelts were also formed by adding $PbCl_2$ directly to sodium octanoate in chloroform eliminating the use of DI water in the synthesis. This experiment was used as a test case to examine the results of adding $PbCl_2$ directly to chloroform without the use of sodium octanoate. Synthesis without the use of sodium octanoate did not form nanobelts suggesting that octanoate serves as the oxygen source for their formation via O-C bond cleavage. These results are similar to those previously reported in the formation of Cu_2S where dodecanethiol was used as the sulfur source,[28] indicating the importance of the reaction mechanism in the control of anisotropic nanocrystal growth.

4.3.3 Birefringent Properties

The nanobelt anisotropy leads to physical properties that depend strongly on the crystallographic direction. For example, $Pb_3O_2Cl_2$ is strongly birefringent. Birefringence results from differences in the velocity of light propagation along different crystal axes due to variations in the interaction strength between the electric field of the incident light waves and the outermost electrons of the atoms in the crystal lattice.[4] The induced dipole moment **p**, formed within a single atom depends on its polarizability α, and the electric field strength **E**:

$$\boldsymbol{p} = \alpha \boldsymbol{E} \tag{1}$$

In a single case like an ideal gas, the polarizability relates to the refractive index n, of the material via the following relation:

$$n^2 = 1 + \frac{N\alpha}{\varepsilon_o} \tag{2}$$

where N is the number density of atoms and ε_o is the permittivity of free space. The cumulative effect of the polarizabilities of individual atom in the crystal and the anisotropic symmetry of the atoms in the lattice result in a refractive index that depends on the orientation of the crystal lattice with respect to incident light. This difference in refractive index alters light in two ways. First, a single ray of light splits into two traveling waves at different velocities and typically different angles with respect to each other through the crystal. Second, the two rays of light are polarized at an angle 90° from one another. Due to its anisotropy in all three crystallographic directions, mendipite is a biaxial crystal with bulk refractive indices of 2.24 for propagation along the a-axis of the unit cell, 2.31 for the b-axis, and 2.27 for the c-axis with a maximum difference in refractive index or birefringence of 0.07.

In order to observe the birefringence of nanocrystal superstructures, a group of stringent criteria must be satisfied. These include the synthesis of nanocrystals with an anisotropic crystal lattice, the consistent orientation of that crystal lattice with respect to the particular nanocrystal shape (for the case of $Pb_3O_2Cl_2$, the majority of nanobelts must have the same growth direction), and alignment of the individual nanocrystals into ordered thin films that exhibit local domains which polarize light collectively. The birefringent properties of the nanobelts were examined using an optical microscope equipped with crossed polarizers. In particular, thin films of nanobelts were deposited onto glass substrates, and their ability to polarize incident light was examined. Optical images of an area of a dried nanobelt thin film are shown without and with crossed polarizers (polarizing and analyzing filter oriented 90° to one other) in Figures 4.6A and B. These materials exhibit strong birefringence. Individual domains exhibiting wire alignment with the same polarization extend from 12 to 37 μm in length and 3 to 10 μm in width indicating significant local order within the film similar to that observed with SEM imaging. Figure 4.6C and D are images of the nanobelts dispersed in chloroform without and with polarizers.

Again, the nanobelts demonstrate a significant degree of order with local domains aligning in the flow fields of the evaporating solvent over length scales tens of microns in length and width.

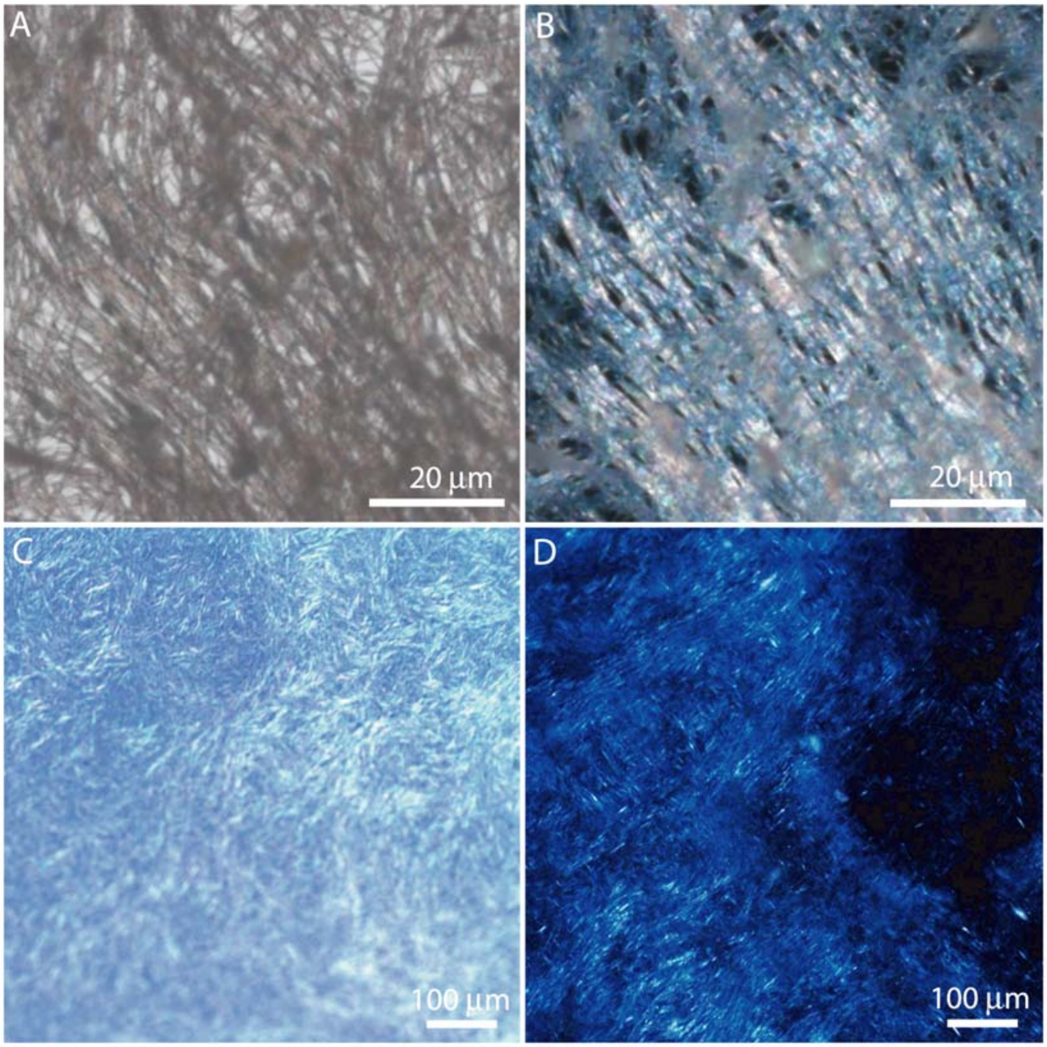

Figure 4.6: Optical microscope images of $Pb_3O_2Cl_2$ nanobelt thin films imaged (A) without and (B) with crossed polarizers. Similar structures are observed for nanobelts imaged while dispersed in a droplet of chloroform as observed (C) without and (D) with crossed polarizers.

For orthorhombic materials, the three directions that a ray of light is allowed to vibrate within the crystal structure coincides with the a, b, and c crystallographic axes.[4] Since the dimensions of the individual nanobelts are confined to these axes, transmitted light should be polarized in those directions; i.e. down the length in the [010] direction and across the width in the [100] direction of the belts. To confirm this relationship, crossed polarizers were rotated horizontally relative to small bundles of belts on a glass substrate (Figure 4.7A-D). Figure 4.7A shows two small bundles of nanobelts exhibiting strong birefringence when viewed with the polarizer oriented at 0° and the analyzer at 90° relative to the image. In this configuration, the belts are oriented with two of their allowable vibration directions for light oriented at 45° and 135° relative to the polarizer. This results in a maximum brightness because incident light is split into two components that vibrate in the 45° and 135° directions which sum vectorially to give a maximum intensity of polarized light projected onto the analyzer axis at 90°.[40] Figure 4.7B shows the same belts when imaged with the polarizer and analyzer rotated 45° relative to their initial position in Figure 4.7A. With this configuration, the belts appear dark due to the allowable vibration directions for light being oriented parallel and perpendicular to the polarizing filter. The darkness occurs because the polarized light passes unaltered through the nanobelts transmitting light with no vectorial polarization in the direction of the analyzing filter (90° from the polarizer). Figure 4.7C shows the belts imaged when the polarizer and analyzer are at an intermediate position of intensity (rotated 60° relative to their initial position) resulting from a decrease in the magnitude of the vectorial sum of polarization projected toward the direction of the analyzer. The intensity of polarized light transmitted through the belts continues to increase as the angle of the polarizer is increased until it reaches a second maximum at 90° as shown in Figure 4.7D. Since the majority of nanobelts shown via TEM and SEM are oriented with the thickness (averaging ~23 nm) of the belt lying flat on the substrate, this dimension is the most likely direction through which incident light is transmitted through the nanobelt.

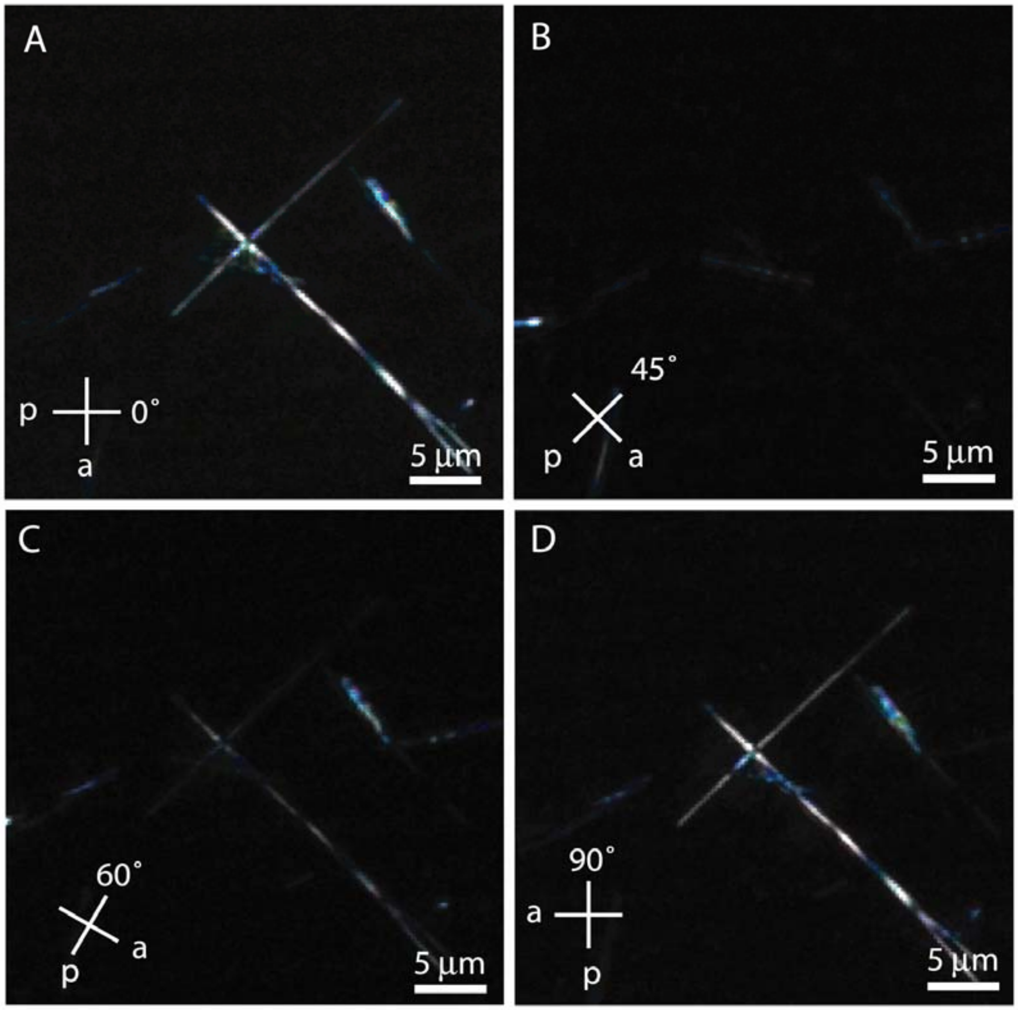

Figure 4.7: Series of optical microscope images of two thin bundles of $Pb_3O_2Cl_2$ nanobelts < 400 nm in width imaged through crossed polarizers oriented horizontally with respect to the sample as designated by the small white cross in the bottom left corner. (A) Polarizing filter (p) oriented at 0° and analyzing filter (a) oriented at 90°. (B) Polarizing filter at 45° and analyzing filter at 135°. (C) Polarizing filter at 60° and analyzing filter at 150°. (D) Polarizing filter at 90° and analyzing filter at 180°.

Interference colors were used to estimate the difference in refractive index between the [010] and [100] crystallographic directions of the nanobelts. The optical microscope image in Figure 4.8A shows a nanobelt between crossed polarizers with a Red 1 compensator oriented at 45° (NE-SW direction) between the sample and the analyzer. The compensator is itself a birefringent material that adds an optical path difference (OPD) of 550 nm to the two incident rays of polarized light. When the highest refractive index ([010] direction) of the nanobelt is oriented perpendicular to that of the compensator as in Figure 4.8A, the OPD from the nanobelt and the compensator subtract leaving a reddish-orange color corresponding to a total OPD of ~450 nm as determined from a Michel Lévy chart.[41] The OPD due to the nanobelt is therefore ~100 nm. Figure 4.8B shows the same nanobelt rotated so that its largest refractive index is oriented parallel to the compensator. For this case, the OPD due to the nanobelt adds to the compensator resulting in a blue color. The cumulative OPD from the Michel Lévy chart is ~650 nm again indicating that the OPD of the nanobelt is ~100 nm. Non-contact AFM reveals that the thickness d, of the nanobelt imaged in Figure 4.8A and B is 68 nm. From these measurements, the birefringence of the nanobelt is calculated to be ~1.5 as determined from Equation 3:

$$\Delta = d(n_s - n_f) \tag{3}$$

where Δ is the optical path difference or retardation, n_s is the refractive index of the slow direction (largest value), n_f is the refractive index of the fast direction (lowest value), and $(n_s - n_f)$ is the birefringence. This value is 20 times larger than the bulk birefringence value of 0.07 for mendipite. For comparison, two of the most strongly known natural birefringent minerals, calcite and rutile, have maximum birefringence values of 0.154 and 0.287.[42]

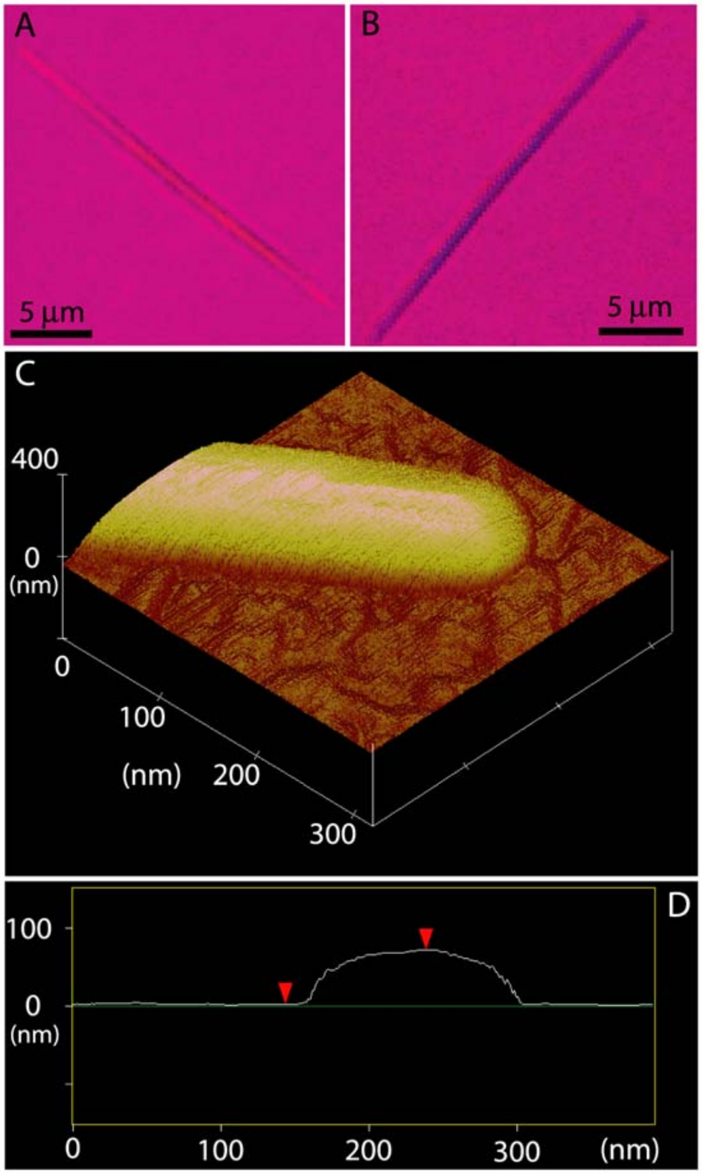

Figure 4.8: (A) Nanobelt imaged through crossed polarizers with a Red 1 compensator oriented perpendicular to the length of the belt. (B) Same nanobelt rotated 90° with respect to the orientation of the compensator demonstrating change in interference colors. (C) 3D AFM (tapping mode) image and (D) cross sectional height profile of the nanobelt imaged in (A) and (B). Dimensions of imaged nanobelt are 68 nm in thickness and 130 nm in width.

Since the use of interference colors is an approximate technique requiring the somewhat subjective selection of colors from a chart, the Brace-Köhler method was employed as a second technique to measure the birefringence of the nanobelts. A λ/20 Brace-Köhler compensator was inserted between the sample and the analyzing polarizer at 135° (NW-SE direction). This position is referred to as 0° with regard to the orientation of the direction of maximum refractive index of the mica prism within its rotary holder. Monochromatic light was used by inserting a 656 nm band pass filter resulting in a maximum measurable OPD of up to 32.8 nm. Nanobelts including the one shown in Figure 4.8 were oriented with the length of the belt ([010] direction) at 45° (NE-SW direction) relative to the crossed polarizers. When viewed in the microscope, the nanobelt was dark. Rotation of the Brace-Köhler compensator through the full range of 360° revealed maxima in transmitted light at 90° and 270° and only one additional minima at 180°. The existence of two minima versus the expected four indicates that the measuring range of 32.8 nm has been exceeded for the compensator. Therefore, the OPD of the nanobelts is greater than 32.8 nm. For the nanobelt shown in Figure 4.8, this corresponds to a birefringence of at least 0.48. The amount of light transmitted at 0° and 180° is an indicator of the degree that a material exceeds the measuring range of the compensator. Because the nanobelts are completely dark at 0° and 180°, the true value of the birefringence for the belts is believed to be closer to the minimum value of 0.48 determined using the Brace-Köhler method than the value of 1.5 determined from interference colors.

The largest reported birefringence value found in the literature is 0.43 for the polymer poly(ethylene 2,6-naphthalene-dicarboxylate),[43] although values up to 0.79 have been extrapolated from experimental results for 100% crystalline PEN.[44] The largest value for an inorganic material is ~0.3 for oriented nanostructured porous Si.[45] Interestingly, bulk Si exhibits almost no birefringence due to an isotropic crystal structure, but the oriented alignment of porous nanowires does due to what was suggested to be purely dielectric effects. The maximum birefringence for porous Si was found for the largest size (10 to 50 nm in diameter) wires examined, while smaller sizes (2 to 8 nm) exhibited decreased values less than 0.1. Determination of the reason for the observed increase in birefringence for the $Pb_3O_2Cl_2$ nanobelts is currently in progress, but the anisotropic shape of the belts appears to be a significant factor.

4.4 CONCLUSIONS

In conclusion, $Pb_3O_2Cl_2$ nanobelts with controlled crystallographic orientation were synthesized using a solventless thermolysis technique. Individual belts are greater than 4 μm in length, with a log mean average width of 61.6 nm, and a mean thickness of 23.3 nm. XRD confirmed that the nanobelts consist of mendipite with an orthorhombic crystal structure. HRTEM imaging and electron diffraction analysis were used to determine that growth primarily occurs in the [010] direction, with the width in the [100] direction and the thickness in the [001] direction. The birefringence of the nanobelts was determined to be greater than 0.48 as determined by the Brace-Köhler method.

The observed birefringence of these nanobelts provides a platform for studying the effects of anisotropic crystal structures of materials with length scales smaller than the wavelength of visible light. It also offers the possibility for interesting applications including the possible formation of small scale birefringent polarizers with the development of suitable techniques for ordering the particles over longer length scales.

4.5 REFERENCES

(1) Heer, W. A. d.; Bacsa, W. S.; Châtelain, A.; Gerfin, T.; Humphrey-Baker, R.; Forro, L.; Ugarte, D. *Science* **1995**, *268*, 845.

(2) Lemaire, B. J.; Davidson, P.; Ferré, J.; Jamet, J. P.; Panine, P.; Dozov, I.; Jolivet, J. P. *Phys. Rev. Lett.* **2002**, *88*, 125507.

(3) Kovalev, D.; Polisski, G.; Diener, J.; Heckler, H.; Künzner, N.; Timoshenko, V. Y.; Koch, F. *Appl. Phys. Lett.* **2001**, *78*, 916.

(4) Hartshorne, N. H.; Stuart, A. *Crystals and the Polarising Microscope*; Edward Arnold Ltd.: London, 1960.

(5) Sasaki, T.; Katsuragi, A.; Mochizuki, O.; Nakazawa, Y. *J. Phys. Chem. B* **2003**, *107*, 7659.

(6) Glinchuk, M. D.; Morozovskaya, A. N. *Phys. Stat. Sol. (b)* **2003**, *238*, 81.

(7) Kim, H.-W.; Lee, H.-S.; Kim, J.-D. *Liq. Cryst.* **2002**, *29*, 413.

(8) Diehl, M. R.; Yu, J.-Y.; Heath, J. R.; Held, G. A.; Doyle, H.; Sun, S.; Murray, C. B. *J. Phys. Chem. B* **2001**, *105*, 7913.

(9) Jun, Y.-W.; Jung, Y.-Y.; Cheon, J. *J. Am. Chem. Soc.* **2002**, *124*, 615.

(10) Nassary, M. M.; Gerges, M. K.; Shaban, H. T.; Salwa, A. S. *Physica B* **2003**, *337*, 130.

(11) Hasenöhrl, S.; Novák, J.; Kúdela, R.; Betko, J.; Morvic, M.; Fedor, J. *J. Cryst. Growth* **2003**, *248*, 369.

(12) Niitsu, G. T.; Nagata, H.; Rodrigues, A. C. *J. Appl. Phys.* **2004**, *95*, 3116.

(13) Rodrigues, V.; Fuhrer, T.; Ugarte, D. *Phys. Rev. Lett.* **2000**, *85*, 4124.

(14) Xia, Y.; Yang, P.; Sun, Y.; Wu, Y.; Mayers, B.; Gates, B.; Yin, Y.; Kim, F.; Yan, H. *Adv. Mater.* **2003**, *15*, 353.

(15) Lee, S.-M.; Cho, S.-N.; Cheon, J. *Adv. Mater.* **2003**, *15*, 441.

(16) Puntes, V. F.; Zanchet, D.; Erdonmez, C. K.; Alivisatos, A. P. *J. Am. Chem. Soc.* **2002**, *124*, 12874.

(17) Jun, Y.-W.; Casula, M. F.; Sim, J.-H.; Kim, S. Y.; Cheon, J.; Alivisatos, A. P. *J. Am. Chem. Soc.* **2003**, *125*, 15981.

(18) Manna, L.; Scher, E. C.; Alivisatos, A. P. *J. Am. Chem. Soc.* **2000**, *122*, 12700.

(19) Lu, Q.; Gao, F.; Komameni, S. *J. Am. Chem. Soc.* **2004**, *126*, 54.

(20) Messer, B.; Song, J. H.; Huang, M.; Wu, Y.; Kim, F.; Yang, P. *Adv. Mater.* **2000**, *12*, 1526.

(21) Gates, B.; Mayers, B.; Cattle, B.; Xia, Y. *Adv. Funct. Mater.* **2002**, *12*, 219.

(22) Duan, X.; Lieber, C. M. *J. Am. Chem. Soc.* **2000**, *122*, 188.

(23) Hanrath, T.; Korgel, B. A. *J. Am. Chem. Soc.* **2002**, *124*, 1424.

(24) Holmes, J. D.; Johnston, K. P.; Doty, R. C.; Korgel, B. A. *Science* **2000**, *287*, 1471.

(25) Han, W.; Fan, S.; Li, Q.; Hu, Y. *Science* **1997**, *277*, 1287.

(26) Penner, R. M. *J. Phys. Chem. B* **2002**, *106*, 3339.

(27) Larsen, T. H.; Sigman, M.; Ghezelbash, A.; Doty, R. C.; Korgel, B. A. *J. Am. Chem. Soc.* **2003**, *125*, 5638.

(28) Sigman, M. B.; Ghezelbash, A.; Hanrath, T.; Saunders, A. E.; Lee, F.; Korgel, B. A. *J. Am. Chem. Soc.* **2003**, *125*, 16050.

(29) Ghezelbash, A.; Sigman, M. B.; Korgel, B. A. *Nano Lett.* **2004**, *4*, 537.

(30) Cotton, F. A.; Wilkinson, G. *Advanced Inorganic Chemistry*, Third ed.; John Wiley & Sons: New York, 1972.

(31) Krivovichev, S. V.; Burns, P. C. *Eur. J. Mineral.* **2001**, *13*, 801.

(32) Noren, L.; Tan, E. S. Q.; Withers, R. L.; Sterns, M.; Rundlof, H. *Mater. Res. Bull.* **2002**, *37*, 1431.

(33) Gibson, J. M.; Lanzerotti, M. Y.; Elser, V. *Appl. Phys. Lett.* **1989**, *55*, 1394.

(34) Lynch, D. F. *Acta Cryst.* **1971**, *A27*, 399.

(35) Castaño, V.; Gómez, A.; Yacaman, M. J. *Surf. Sci.* **1984**, *146*, L587.

(36) Deng, Z.-X.; Wang, C.; Sun, X.-M.; Li, Y.-D. *Inorg. Chem.* **2002**, *41*, 869.

(37) Deng, Z.-X.; Li, L.; Li, Y. *Inorg. Chem.* **2003**, *42*, 2331.

(38) Fan, W.; Sun, S.; Song, X.; Zhang, W.; Yu, H.; Tan, X.; Cao, G. *J. Solid State Chem.* **2004**, *177*, 2329.

(39) Gao, F.; Lu, Q.; Zhao, D. *Chem. Lett.* **2002**, *7*, 732.

(40) A review of the effects of crossed polarizers on birefringent crystals is located at http://www.olympusmicro.com/primer/java/polarizedlight/crystal/index.html.

(41) Neese, W. D. *Introduction to Optical Mineralogy*; Oxford University Press: New York, 1986.

(42) Physical property data for minerals are located at www.mindat.org.

(43) Hamza, A. A.; Sokkar, T. Z. N.; El-Bakary, M. A. *J. Opt. A: Pure Appl. Opt.* **2001**, *3*, 421.

(44) Cakmak, M.; Kim, J. C. *J. Appl. Polym. Sci.* **1997**, *64*, 729.

(45) Kunzner, N.; Kovalev, D.; Diener, J.; Gross, E.; Timoshenko, V. Y.; Polisski, G.; Koch, F. *Opt. Lett.* **2001**, *26*, 1265.

Chapter 5: Metal Nanocrystal Superlattice Nucleation and Growth*

5.1 INTRODUCTION

Small angle X-ray scattering has revealed that size-monodisperse ($\sigma \lesssim \pm 10\%$) organic monolayer-coated silver nanocrystals spontaneously self-assemble into superlattice thin films when drop cast from concentrated dispersions.[1-3] Superlattice crystallization is a thermodynamically driven process, with the lattice structure depending primarily on the size distribution and interparticle interactions.[2-5] For crystallization to occur during the time allowed by solvent evaporation, the energetic barrier to superlattice nucleation must be overcome and the nanocrystals must have enough diffusional freedom to reorient into their lowest energy lattice positions after condensing from solution. This appears to be the case for monodisperse nanocrystals drop cast from good solvents.

High resolution scanning electron microscopy (HRSEM) was utilized to image superlattice thin films deposited from various solvents and conditions to examine the underlying crystallization kinetics of nanocrystal organization. Deposition of nanocrystals by evaporating a good solvent leads to heterogeneous superlattice nucleation and thin film growth on the $(111)_s$ plane. Significant

---

* The contents of this chapter appear in *Langmuir* **2004**, 20, 978.

differences in superlattice morphology are observed with deposition from different solvents, such as toluene, hexane and chloroform and it appears that subtle differences in interparticle attraction lead to significant differences in superlattice nucleation and growth kinetics. The addition of antisolvent increases interparticle attraction, but does not lead to homogeneous superlattice nucleation during the evaporative drying process, only to the deposition of thin films of spatially disordered nanocrystal films. However, an input of energy by sonication during evaporative drying does promote homogeneous superlattice nucleation during the drop casting process.

5.2 EXPERIMENTAL

Dodecanethiol-stabilized gold and silver nanocrystals were produced by arrested precipitation.[4,6] All chemicals were used as supplied from Aldrich Chemical Co.

5.2.1 Gold Nanocrystal Synthesis

An aqueous gold tetrachloroaurate solution (0.38 g $HAuCl_4{\bullet}3H_2O$ in 36 mL D-H_2O) is combined with an organic solution of the phase transfer catalyst, tetraoctylammonium bromide (2.7 g $[CH_3(CH_2)_7]_4NBr$ in 24.5 mL toluene). The mixture is stirred for approximately one hour before discarding the aqueous phase. The organic solution containing the metal ion/surfactant molecules is then combined with an aqueous solution of the reducing agent, sodium borohydride (0.5 g $NaBH_4$ in 30 mL D-H_2O). After stirring for 4 to 12 hours, the aqueous phase is discarded. 240 μL of dodecanethiol ($C_{12}H_{25}SH$) is then added to the nanocrystal dispersion.

5.2.2 Silver Nanocrystal Synthesis

An aqueous solution of silver ions (0.19 g $AgNO_3$ in 36 mL D-H_2O) was added to an organic solution containing a phase transfer catalyst, tetraoctylammonium bromide (2.7 g $[CH_3(CH_2)_7]_4NBr$ in 24.5 mL chloroform). The mixture is stirred for approximately one hour before discarding the aqueous phase. 240 μL of dodecanethiol ($CH_3(CH_2)_{11}SH$) is added to the organic phase and stirred for five to ten minutes before mixing with an aqueous solution of the reducing agent, sodium borohydride (0.5 g $NaBH_4$ in 30 mL D-H_2O). The two-phase mixture is stirred for 4 to 12 hours before collecting the organic phase for nanocrystal purification.

5.2.3 Post-Synthesis Preparation

After synthesizing the gold and silver nanocrystals, ethanol is added as an antisolvent to precipitate the hydrophobic nanocrystals. The particles are isolated from the supernatant by centrifugation. After this cleaning step to remove residual phase transfer catalyst and other reaction byproducts, the nanocrystal size distribution is narrowed (<10% polydispersity) by size selective precipitation using ethanol/chloroform as the solvent/antisolvent pair.[4,7] The nanocrystals used for this study ranged from 5 to 7 nm in diameter, as determined by transmission electron microscopy (TEM) and small angle X-ray scattering (SAXS).

5.2.4 Nanocrystal Thin Film Formation

Nanocrystal films at least 25 monolayers thick were formed by drop casting from relatively concentrated dispersions on glassy carbon substrates approximately 75 x 75 mm and 1 mm thick. Between eight to twelve drops of solution was added to the substrate, allowing each drop to partially evaporate in order to maintain a small deposition area—a circular region about 10 mm in diameter. Four different deposition solvents were used, n-hexane, ethanol, chloroform and toluene.

5.2.5 High Resolution Scanning Electron Microscopy (HRSEM)

HRSEM images were acquired on a LEO 1530 SEM equipped with a GEMINI field emission column with a thermal field emitter operating at a 1 kV accelerating voltage. Images were digitally acquired using an Inlens detector and LEO 32 software system.

5.3 RESULTS

5.3.1 Superlattice Crystallographic Orientation and Gross Morphology

Figure 5.1 shows a face centered cubic (fcc) superlattice of C_{12}-monolayer coated silver nanocrystals on a glassy carbon substrate formed by drop casting from a concentrated chloroform nanocrystal dispersion. The HRSEM image provides resolution of individual particles separated by 1.5 nm by the organic passivating molecules. The superlattice orients with the $(111)_s$ plane parallel to the substrate. In a few instances, the $(110)_s$ plane was observed parallel to the surface; however, this crystallographic orientation was always associated with a major local defect in the superlattice. The inset in Figure 5.1 magnifies a $(110)_s$ vicinal facet showing spatial registry between close-packed nanocrystal layers spanning several monolayers in thickness in the $[111]_s$ direction. The angle between the $(111)_s$ and the $(110)_s$ planes was estimated from the two dimensional image to be 154° in agreement with the designation of fcc packing versus hexagonal close packing (hcp). Superlattices of both Au and Ag nanocrystals in the size range 5 to 7 nm diameter deposited from hexane, chloroform and toluene generally form fcc superlattices oriented with the fcc $(111)_s$ plane parallel to the substrate, although the gross morphology of the films depended greatly on the solvent.

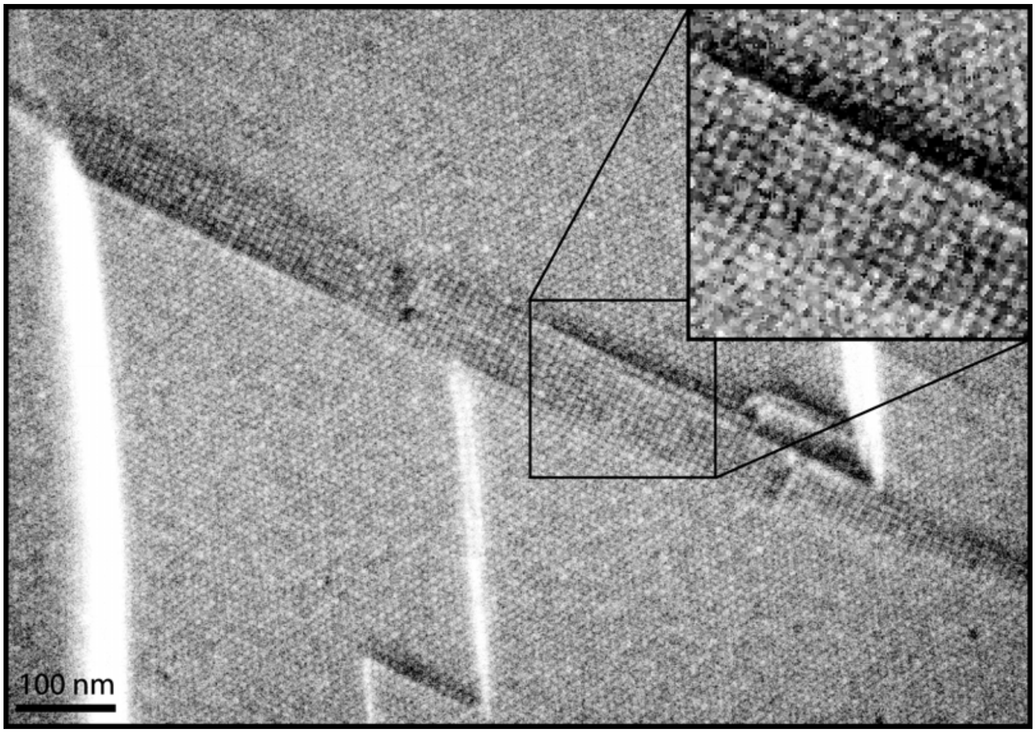

Figure 5.1: HRSEM image of the surface of a silver nanocrystal superlattice film deposited from chloroform. The nanocrystals 7.2 ± 0.6 nm in diameter. The inset highlights the change in superlattice orientation from the $(111)_s$ surface to the $(110)_s$ surface.

Figure 5.2 shows HRSEM images of gold nanocrystal superlattice thin films formed by drop casting from hexane (Figs. 5.2A-5.2C) and chloroform (Figs. 5.2D-5.2F). Gold nanocrystals exhibit superlattice morphologies similar to the silver nanocrystals. The films in Figure 5.2 were prepared using the same

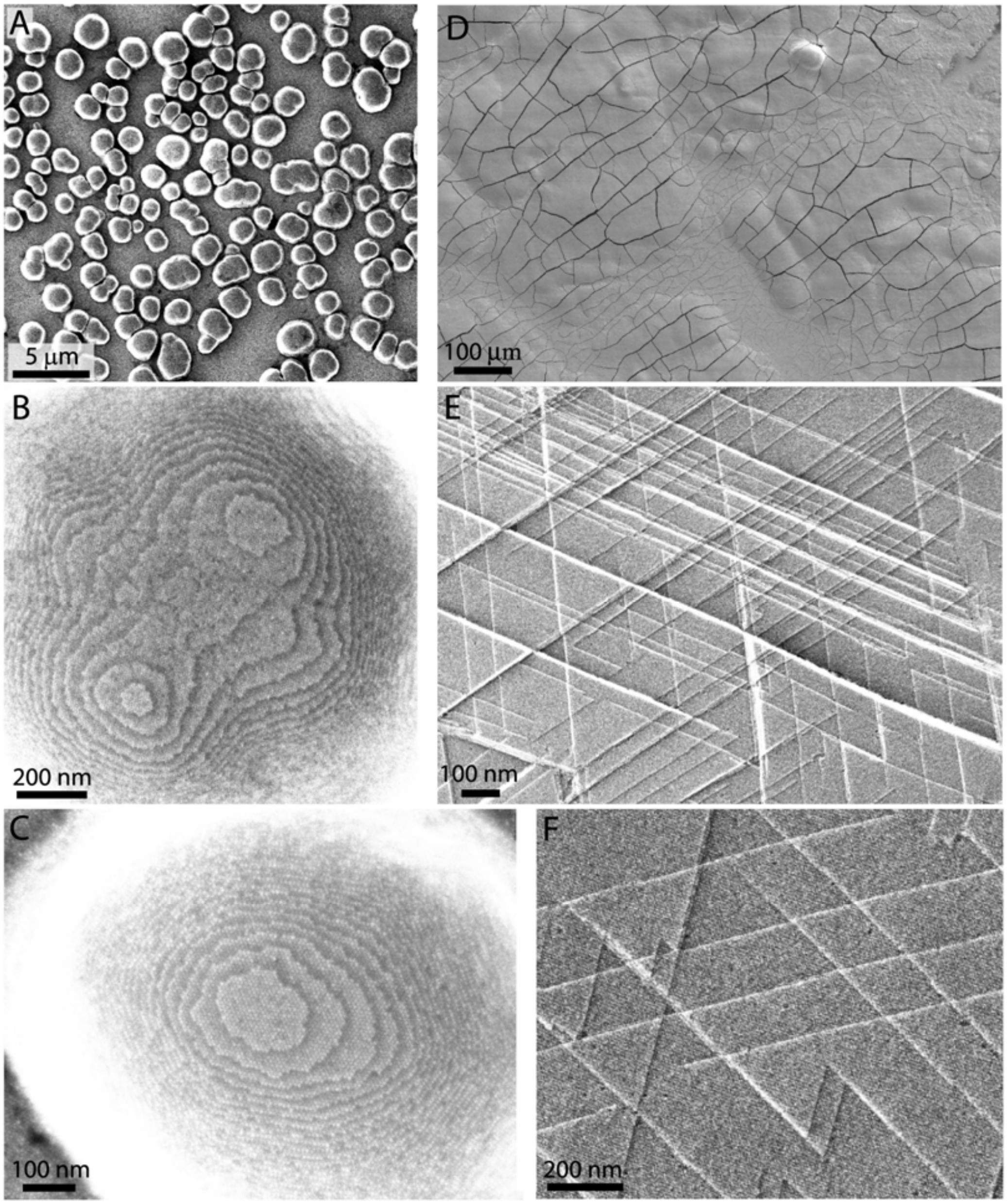

Figure 5.2: HRSEM images of gold nanocrystals deposited on a glassy carbon substrate by drop casting from (A-C) hexane and (D-F) chloroform. All of the films were formed from the same nanocrystal preparation and size selective precipitation.

size selective precipitation fraction of gold nanocrystals (particle diameter 6.3±0.6 nm). Even though both chloroform and hexane are expected to be good solvents (with $\chi \approx 0$), the film morphologies differ signficantly. Hexane deposition produces rough films on a microscopic length scale and the particles deposit as mounds (Figure 5.2A). Chloroform produces microscopically smooth films, varying in thickness by only a couple of monolayers (Fig. 5.2D-5.2F).

The nanocrystal mounds formed by drop casting from hexane typically range from 0.5 to 3 μm in diameter.[8] There is spatial registry between the nanocrystal layers throughout the entire structure with the particles forming an fcc superlattice with the $(111)_s$ lattice plane parallel to the substrate (Figures 5.2B and 5.2C). Figure 5.3A shows a nucleating cluster at the top of the mound. The underlying superlattice plane determines the spatial position and interparticle separation of the nanocrystals in the nucleating cluster. The superlattice nucleates heterogeneously and the $(111)_s$ plane grows radially. As the next layer nucleates, the underlying layers continue to spread from the nucleation site independent of the superlattice crystallographic direction. An isolated 2D nucleation cluster tops the majority of the mounds (Fig. 5.2B), however there are two nucleation sites on top of approximately 20% of the mounds (8 of 36 imaged) (Fig. 5.2C). In mounds with two nucleation sites, the underlying superlattice crystallographic plane is spatially ordered without a dislocation or defect separating the two crystal domains in most cases. This morphology is similar to that observed in liquid phase epitaxy experiments for supersaturation levels high enough to produce 2D nucleation.[9]

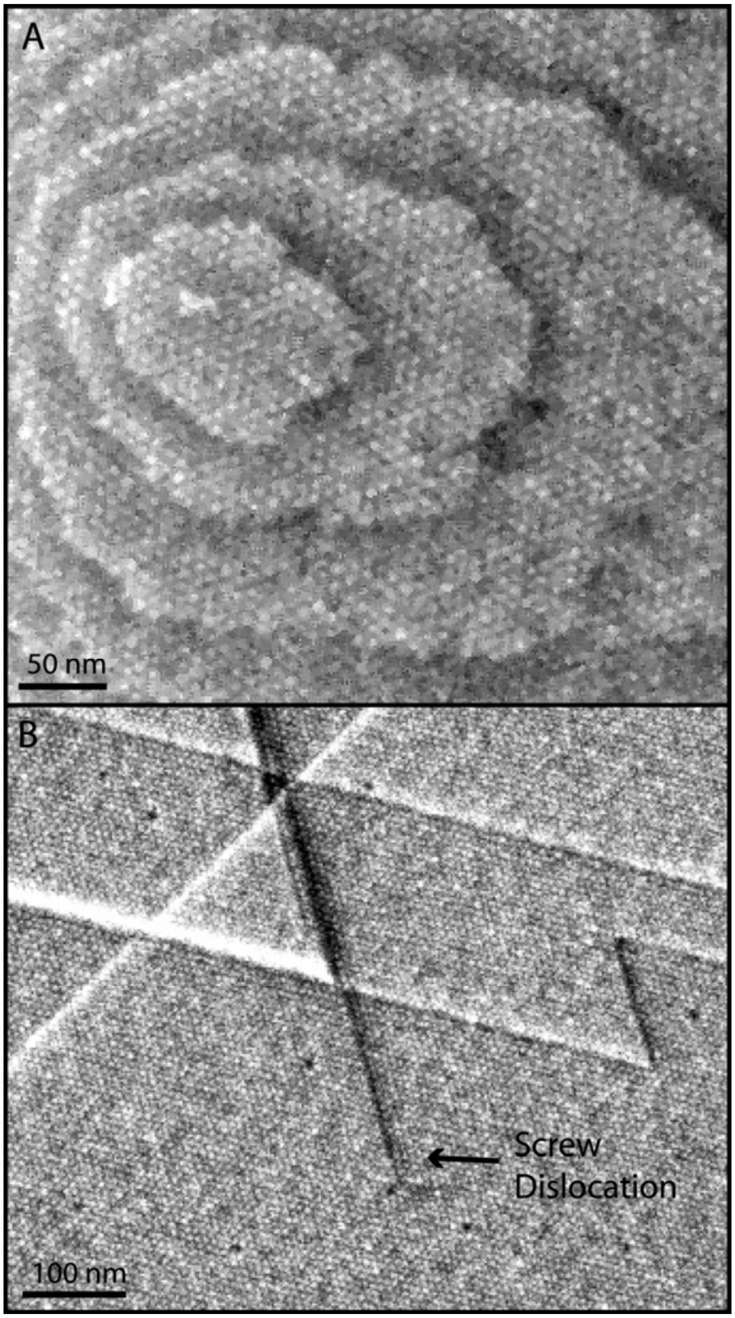

Figure 5.3: (A) HRSEM image of gold nanocrystals drop cast from hexane and (B) chloroform. Kinks result from screw dislocations and the thin film grows preferentially along the $[110]_s$ direction when deposited from chloroform.

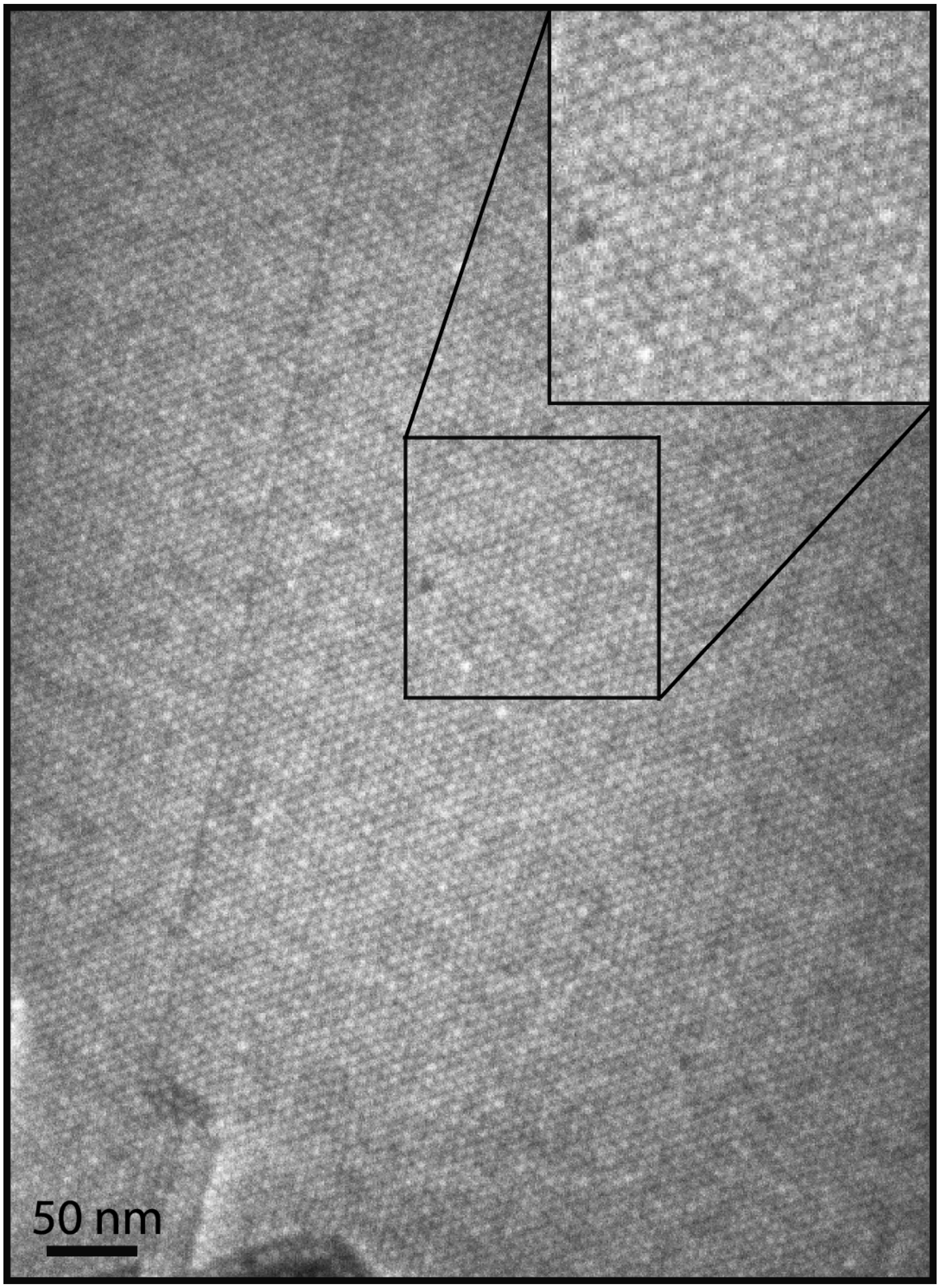

Figure 5.4: HRSEM image of Au nanocrystals drop cast from chloroform demonstrating the ability to create local areas of thin film with no variation in height.

In contrast, nanocrystal thin films deposited from chloroform vary in thickness by only a few monolayers (Figures 5.2D-5.2F). Areas of superlattice film with no variation in height have been formed from chloroform over length scales on the order of several hundred nanometers as shown in Figure 5.4. The fcc superlattice orients with the $(111)_s$ plane parallel to the substrate with the surface exhibiting overlapping triangles (Figures 5.2E and 5.2F), indicating that crystallization occurs primarily along the $[110]_s$ growth direction. This growth morphology initiates from kinks developed from screw locations in the film (Figure 5.3B). Similar thin film morphologies have been observed in liquid phase epitaxy.[9] Macroscopic cracks form in the film (Figure 5.2D) as residual solvent evaporates from the superlattice. It appears that this final drying stage occurs after superlattice crystallization, as triangular growth features can be found split by the cracks.

5.3.2 Nanocrystal Deposition from a Poor Solvent

Nanocrystals deposited from dispersions containing a significant amount of miscible polar solvent (9:1 v:v hexane:ethanol) exhibited morphologies that varied significantly across the substrate. Ordered superlattices were not observed and the majority of the substrate was covered with extended dendritic structures as shown in Figure 5.5A. At this antisolvent concentration, the interparticle attraction should be on the order of the thermal energy kT, where k is Boltzmann's constant and T is temperature. Nonetheless, the dendritic growth morphology is characteristic of high supersaturation with low particle mobility after adsorption and negligible desorption during the drying process. Homogeneous superlattice nucleation and growth under these conditions of relatively large interparticle attraction (~*kT*) in the ethanol/hexane solution was not observed during the rapid drying under ambient conditions.

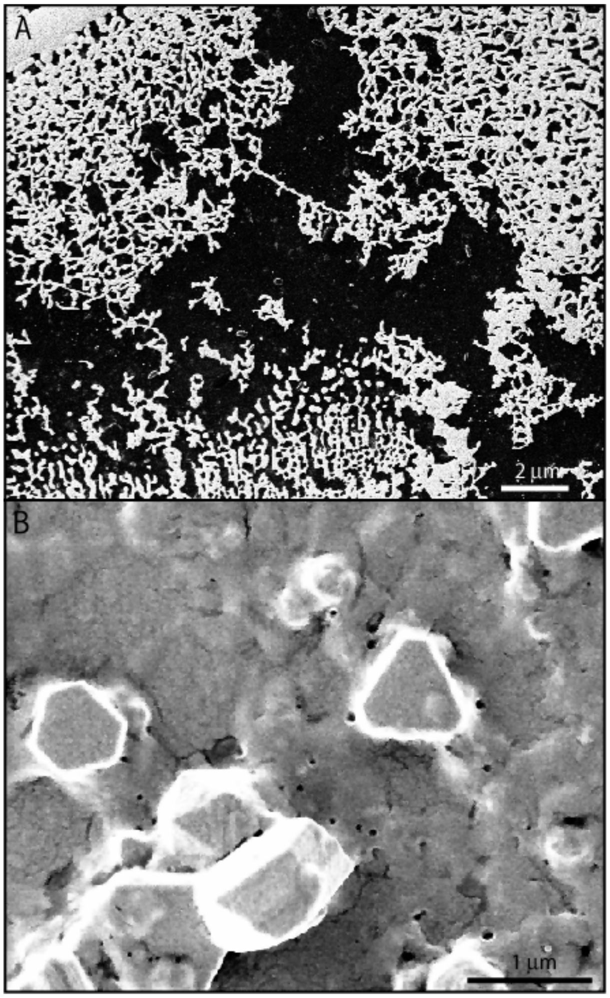

Figure 5.5: HRSEM image of gold nanocrystals deposited from 1:9 EtOH:hexane (A) without and (B) with sonication. Without sonication the films exhibit non-uniform roughness with significant areas of dendritic growth. Sonication leads to the formation of homogeneously nucleated nanocrystal superlattice crystallites that have settled on the substrate.

Sonicating the dispersions in the process of drop casting induced homogeneous nucleation and growth of nanocrystal superlattice crystals (Figure 5.5B). Homogeneous superlattice nucleation and growth was never found from dispersions in good solvents, such as hexane and toluene, even with sonication. The superlattice crystallites formed in hexane/ethanol (9:1 v:v) exhibit various faceted shapes, including hexagonal, triangular, and truncated triangular prisms, and on a few occasions octahedrons. HRSEM images shown in Figure 5.6 with individual nanocrystal resolution confirmed that these colloidal crystals are composed of nanocrystals that have not fused together. On the time scales of drop casting (tens of seconds), homogeneous superlattice nucleation did not occur without sonication, even with increased solvent polarity. Interparticle attraction is not the only requirement for homogeneous superlattice nucleation and growth; the kinetics of the process also play an important role. Homogeneous superlattice crystallization generally requires slow solvent evaporation: For example, Murray, et al. use a mixture of low volatility octane/octanol solvent to crystallize CdSe nanocrystals[10] and Shevchenko et al. reported homogeneous FePt nanocrystal nucleation and growth via the gradual addition of an anti-solvent through a buffer solution.[11] Sonication promotes superlattice nucleation and speeds the crystallization process.

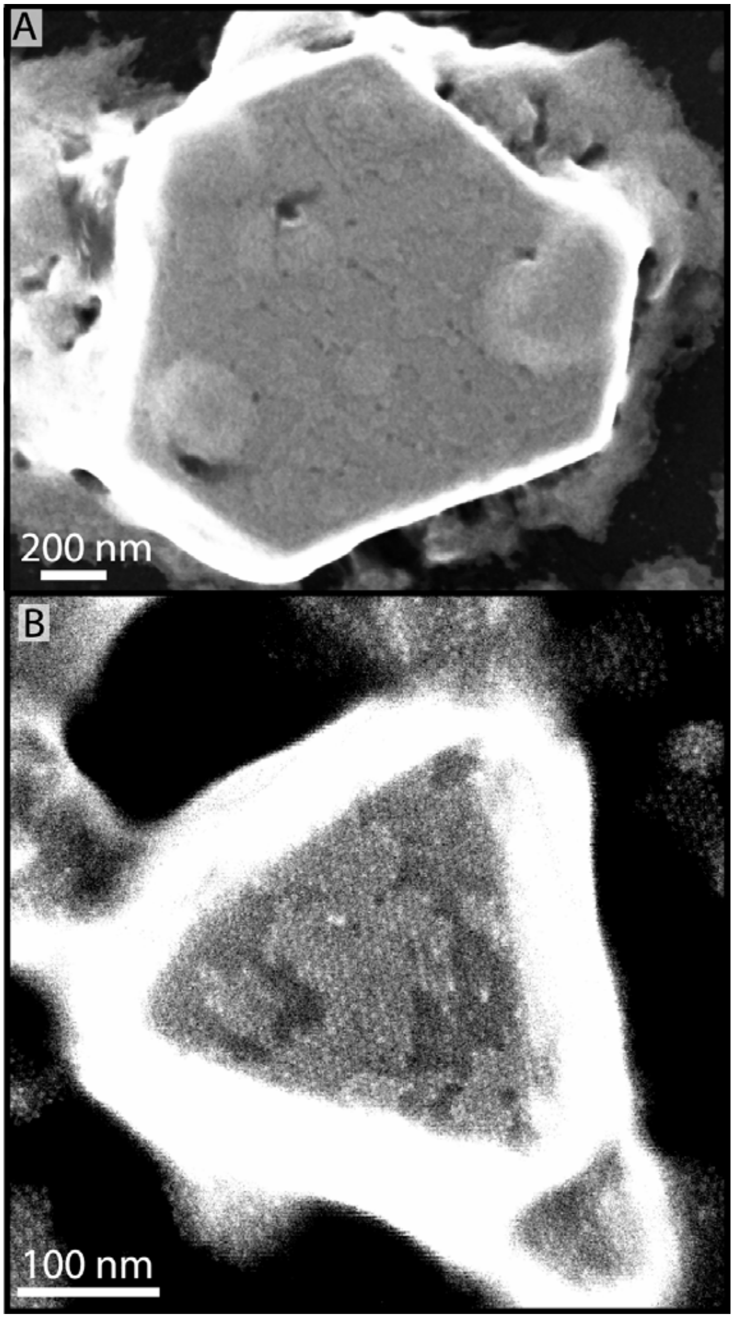

Figure 5.6: HRSEM image of complete colloidal crystals formed from individual nanocrystals as demonstrated by the individual nanocrystal resolution in (B). Colloidal crystals formed a variety of shapes including (A) truncated triangular prism and (B) triangular prism.

5.3.3 Effect of Substrate Temperature on Superlattice Crystallization

Figures 5.7A and 5.7B show gold nanocrystal films deposited from toluene at room temperature and 40° C. The deposition temperature affects the superlattice morphology. Films deposited at room temperature from toluene exhibit mound densities (related to the nucleation frequency) greater than in films deposited from hexane. Higher deposition temperatures (40^{o}C) produced flatter films. The mound density relates to the nucleation frequency and higher thermal energy appears to decrease the interparticle attractions, leading to lower concentrations of nuclei and enhanced particle-substrate wetting. The nanocrystal films deposited from toluene at 40^{o}C, however, exhibit many more superlattice defects than those deposited from chloroform at room temperature, perhaps due to the effect of higher temperature on defect formation.

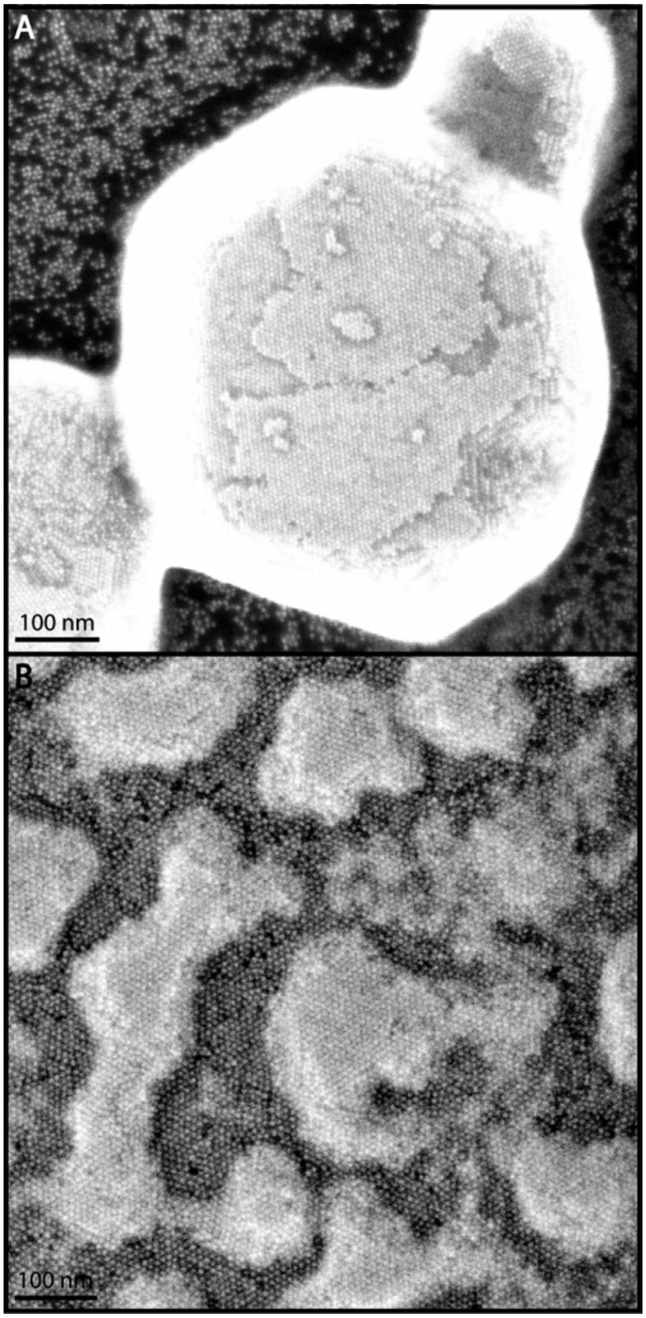

Figure 5.7: HRSEM image of gold nanocrystals deposited from toluene at (A) room temperature and (B) 40˚ C. At room temperature, the particles exhibit mounds; whereas, at higher temperature the particles form a flatter film with locally disordered structure.

5.4 DISCUSSION

5.4.1 Superlattice Crystallization and Comparison to Classical Crystallization Theory

Nanocrystal superlattices can nucleate either heterogeneously on a substrate, or homogeneously in solution. When the polar solvent composition is high—above the dispersibility limit—homogeneous crystallization can occur. However, the activation energy barrier for homogeneous nucleation is significant and occurs only when the solvent evaporation rate is slow relative to the nucleation rate, with time scales on the order of several hours. The nucleation barrier can also be overcome with energetic input by sonication. The activation barrier for heterogeneous nucleation appears to be relatively low, as superlattices grow epitaxially on the $(111)_s$ plane during drop casting.

Once nucleation occurs, a nanocrystal incorporates into the superlattice through a series of elementary steps: (1) bulk particle diffusion from solution to the substrate, (2) adsorption, (3) surface diffusion, and (4) incorporation into the growing crystal. The particle may also desorb from the surface prior to incorporating into the lattice. The crystal surface morphology depends on the rate-limiting step in the process. Deposition limited by bulk diffusion leads to rough films with local disorder. This occurs when the interparticle attractions are strong. For example, nanocrystals deposited from poor solvents (i.e., ethanol/hexane ratios greater than approximately 1:20) often exhibit dendritic or spherulitic structures resulting from sticking coefficients close to one with negligible surface mobility.

When crystallization is limited by surface diffusion, superlattices tend to have relatively smooth surfaces with long-range packing order.[12] For example, particles deposited from chloroform give smooth films with triangular patterns due to preferential growth along the $[110]_s$ direction. Different solvents, however, produce superlattices with varying morphology and roughness. For instance, nanocrystal superlattices deposited from hexane form isotropic mounds, indicating a relative enhancement in $[111]_s$ directed crystallization. Both hexane and chloroform are good solvents for dodecane ($\chi \approx 0$), however, the Hamaker constant is approximately 20% higher for both Ag and Au in hexane relative to chloroform due to the lower dielectric screening in hexane (see Appendix C for calculations).[13] These differences in interparticle attraction appear to give rise to significant differences in surface mobility and (heterogeneous) nucleation rates.

Figure 5.8 shows a schematic and an HRSEM image of kinks, steps, and terraces on the surface of a nanocrystal superlattice.[14] According to classical crystallization theory, adparticles tend to incorporate at kink sites as they provide the greatest number of nearest neighbors to maximize attractive forces.[14] At a kink, a nanocrystal can form 9 bonds with neighboring particles; whereas, a step edge can only accomodate 8 bonds, and a terrace only 6.[12,15] Crystallization depends on the relationship between the mean kink separation and the surface diffusion length.[14] For instance, superlattices deposited from hexane and chloroform exhibit morphologies that typify the crystallization limits of slow and rapid surface diffusion, respectively.

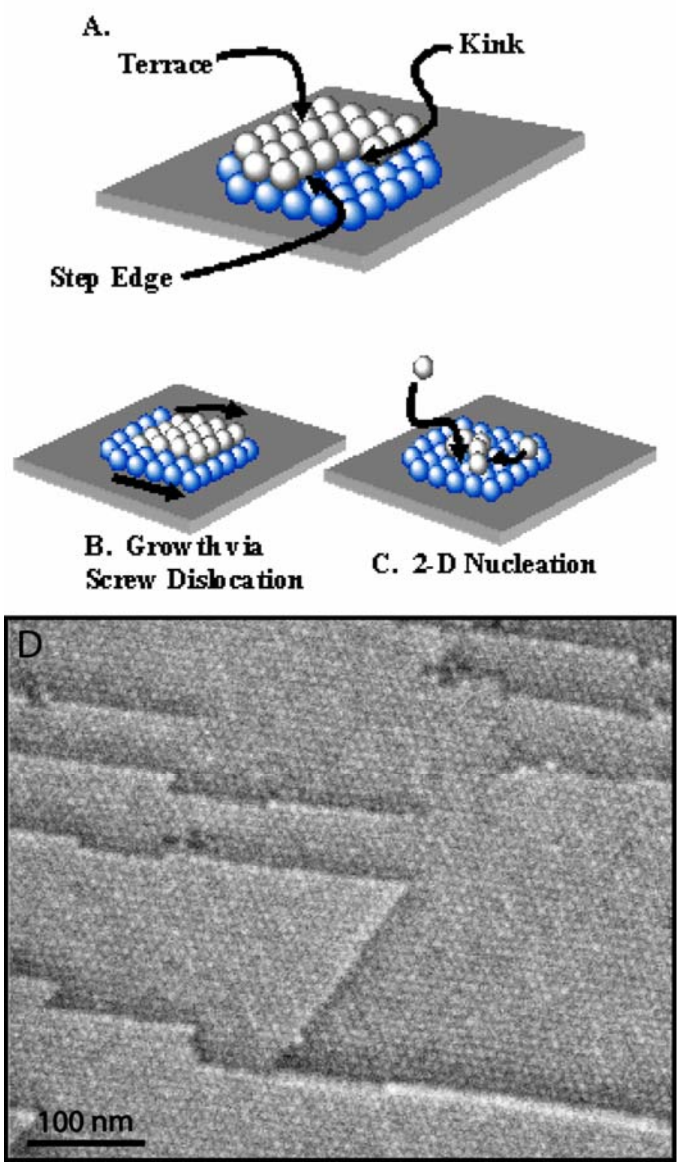

Figure 5.8: (A) Kink-step model for crystal growth. (B) Crystal growth occurring by the formation of kinks via dislocation processes. Nanocrystal superlattices were observed with these morphologies when drop cast from chloroform. (C) Crystal growth occurring through the formation of kinks by repeated 2D nucleation, as observed for thin films deposited from hexane. (D) HRSEM image of silver nanocrystals (diameter of 7.2 ± 0.6 nm) drop cast from chloroform. The nanocrystal superlattice film grows heterogeneously and the preferred growth direction of steps along the $[110]_s$ direction is apparent.

The surface mobility depends strongly on the particle location. Nanocrystals can diffuse on a terrace surface until colliding with a step and then diffuse laterally along a step until reaching a kink. When diffusion lengths are long, the resulting films are flat with a preferred crystallographic growth direction since the particles can reach a step edge and ultimately a kink before colliding with another nanocrystal.[16] Nanocrystals deposited from chloroform exhibit flat films with a low kink density along step edges. Growth proceeds heteroepitaxially along the $[110]_s$ direction leading to the characteristic triangular patterns that result when the surface diffusion lengths exceed half the separation distance between successive steps, yet are less than the average kink spacing along the step edges.[17] From the estimation criteria proposed by Bennema,[17] the characteristic surface diffusion lengths are on the order of 10 nanocrystal diameters or approximately 60 nm. The crystal facets with the densest packing (i.e., $(111)_s$) have the lowest surface free energy and therefore, the slowest growth rate relative to other crystallographic directions.[18] The lateral surface diffusional flux promotes the thermodynamically favored growth parallel to the substrate (in the $[110]_s$ direction) while limiting growth in the $[111]_s$ direction.[19]

It is worth noting that the superlattices formed from chloroform exhibit a large number of screw dislocations that appear to be primary contributors to kink formation (Figure 5.3B and 5.8D). This indicates that crystallization is occurring at relatively low supersaturation.[20] Higher supersaturation increases nucleation rates, leads to higher kink density and promotes crystallization in the $[111]_s$ direction.[12] It appears that superlattices deposited from hexane form at higher supersaturation with much shorter surface diffusion lengths, as growth is relatively isotropic. Slower surface diffusion results in a higher nucleation density as adsorbed nanocrystals do not efficiently reach the step edge before colliding with other adsorbed particles.[19] Figure 5.3A shows a nucleation event consisting of an epitaxial planar cluster of four nanocrystals. The layer subsequently grows epitaxially from the nucleus to form another terrace. Nanocrystals continue to adsorb and diffuse until reaching the step edge. The isotropic radial growth of the (111)s planes results in a very high kink density along the terrace edges and short surface diffusion lengths.

It appears that the difference between superlattices deposited from hexane and chloroform relates to differences in supersaturation in the two solvents. Higher supersaturation enhances nucleation and crystallization in the $[111]_s$ direction, giving rise to isotropic superlattice growth, as illustrated in Figure 5.3A.[20] Deposition from chloroform results in $[110]_s$ directed crystallization characteristic of long surface diffusion lengths relative to kink density, characteristic of low supersaturation. Supersaturation in the solvents relates to the interparticle attractions. The apparently lower supersaturation in chloroform is consistent with a lower Hamaker constant in chloroform relative to hexane due to the lower dielectric screening in hexane.

5.5 CONCLUSIONS

Gold and silver nanocrystal superlattices were formed by drop casting from concentrated dispersions in hexane, chloroform and toluene. In all cases, the nanocrystals nucleate heterogeneously with the $(111)_s$ crystallographic plane normal to the substrate. The gross morphology of the films, however, differed significantly depending on the solvent. Nanocrystals deposited from hexane formed mound-like structures and rough films. The mounds consisted of lattice planes forming concentric circles with high kink density, indicating that the surface diffusion lengths were small relative to the step-to-step separation. Nanocrystals deposited from chloroform formed flat films with triangular features with a very low kink density due to preferential crystallization along the $[110]_s$ direction. Based on the kink density and preferred crystallographic growth direction, the surface diffusion length in chloroform appears to significantly exceed that in hexane. This appears to be related to a predicted 20% difference in Hamaker constants between the particles in the two media.

Substrate temperature and solvent polarity also affect the superlattice film morphology. Higher temperature led to smoother films, apparently due to decreased interparticle attraction. Deposition from a poor solvent (i.e., ethanol/hexane mixtures) led to dendritic and spherulitic growth morphologies and in very polar environments, to homogeneous particle aggregation. Sonication under conditions of poor solvation promoted homogeneous superlattice nucleation and growth by providing the energy required to overcome the nucleation energy barrier.

5.6 REFERENCES

(1) Connolly, S.; Fullam, S.; Korgel, B.; Fitzmaurice, D. *J. Am. Chem. Soc.* **1998**, *120*, 2969.

(2) Korgel, B. A.; Fitzmaurice, D. *Phys. Rev. Lett.* **1998**, *80*, 3531.

(3) Korgel, B. A.; Fitzmaurice, D. *Phys. Rev. B* **1999**, *59*, 14191.

(4) Korgel, B. A.; Fullam, S.; Connolly, S.; Fitzmaurice, D. *J. Phys. Chem. B* **1998**, *102*, 8379.

(5) Ge, G.; Brus, L. *J. Phys. Chem. B* **2000**, *104*, 9573.

(6) Brust, M.; Walker, M.; Bethell, D.; Schiffrin, D. J.; Whyman, R. *J. Chem. Soc., Chem. Commun.* **1994**, 801.

(7) Murray, C. B.; Norris, D. J.; Bawendi, M. G. *J. Am. Chem. Soc.* **1993**, *115*, 8706.

(8) Mounds reaching sizes larger than 3 μm were not observed due to contact with neighboring mounds. At this size most mounds begin to connect to nearest neighbors forming irregular bunches of what was initially several different mounds.

(9) Bauser, E. Atomic Mechanisms in Semiconductor Liquid Phase Epitaxy. In *Handbook of Crystal Growth 3b: Thin Films and Epitaxy*; Hurle, D. T. J., Ed.; Elsevier: Amsterdam, 1994; pp 880.

(10) Murray, C. B.; Kagan, C. R.; Bawendi, M. G. *Science* **1995**, *270*, 1335.

(11) Shevchenko, E.; Talapin, D.; Kornowski, A.; Wiekhorst, F.; Kotzler, J.; Haase, M.; Rogach, A.; Weller, H. *Adv. Mater.* **2002**, *14*, 287.

(12) Sangwal, K. *Progress in Crystal Growth and Characterization* **1998**, *36*, 163.

(13) The Hamaker constant for both Ag and Au nanocrystals is ~20% higher in hexane than chloroform. However, the Hamaker constant for Ag nanocrystals is 18% lower in magnitude than Au in both solvents.

(14) Burton, W. K.; Cabrera, N.; Frank, F. C. *Phil. Trans. R. Soc. London Ser. A* **1951**, *243*, 299.

(15) Bond energies for individual nanocrystals attaching to a kink, step, and terrace site of the colloidal crystal were determined from the potential

wells located in The Supplemental Information. For gold nanocrystals in hexane, incorporation into a kink site is 2.178/kT or 0.056 eV, versus 1.815/kT or 0.047 eV for a step, and 1.089/kT or 0.028 eV for a terrace. For gold in chloroform, bonding is 0.048 eV for a kink, 0.040 eV for a step, 0.024 eV for a terrace site.

(16) Scheel, H. J. Historical Introduction. In *Handbook of Crystal Growth 1a: Thermodynamics and Kinetics*; Hurle, D. T. J., Ed.; Elsevier: Amsterdam, 1993; pp 3.

(17) Bennema, P. *J. Cryst. Growth* **1969**, *5*, 29.

(18) Hunter, R. J. *Foundations of Colloid Science*, 2nd ed.; Oxford University Press: New York, 2001.

(19) Vidali, G. Epitaxial Growth of Nanoparticles: Mechanistic Comparisons of Physical and Chemical Processes. In *Nanoparticles in Solids and Solutions*; Dekany, I., Ed.; Kluwer Academic Publishers: Dordrecht, 1996; Vol. 18; pp 17.

(20) Sunagawa, I. Growth of Crystals in Nature. In *Materials Science of the Earth's Interior*; Sunagawa, I., Ed.; D. Reidel Publishing Company: Dordrecht, 1984; pp 63.

Chapter 6: Conclusions and Recommendations

6.1 CONCLUSIONS

6.1.1 Solventless Synthesis

A novel, generic synthesis technique was developed utilizing the solventless thermal decomposition of molecular precursors to form metal sulfide and oxy-chloride nanocrystals. In particular, this technique has been utilized to form Cu_2S, Bi_2S_3, $Pb_3O_2Cl_2$, and NiS[1] nanocrystals. The technique offers the advantage of limiting aggregative growth that typically results from increased interparticle collisions that occur in solvent. In addition, this technique provides a platform for studying factors controlling the growth of anisotropically shaped nanocrystals.

6.1.2 Solventless Synthesis of Copper (I) Sulfide

Cu_2S nanocrystals with disk-like morphologies were synthesized by the solventless thermolysis of a copper alkylthiolate molecular precursor. The nanodisks ranged from circular to hexagonal prisms from 3 to 150 nm in diameter and 3 to 12 nm in thickness depending on the growth conditions. HRTEM revealed the high chalcocite (hexagonal) crystal structure oriented with the c-axis ([001] direction) orthogonal to the favored growth direction. This disk morphology is thermodynamically favored as it allows the extension of the higher energy {100} and {110} surfaces with respect to the {001} planes. The hexagonal prism morphology also appears to relate to increased C-S bond cleavage of adsorbed dodecanethiol along the more energetic {100} facets relative to {001} facets. Monodisperse Cu_2S nanodisks self-assemble into ribbons of stacked platelets. This solventless approach provides a new technique to synthesize anisotropic metal chalcogenide nanostructures with shapes that depend on both the face-sensitive thermodynamic surface energy and the surface reactivity.

6.1.3 Solventless Synthesis of Bismuth (III) Sulfide

Orthorhombic Bi_2S_3 (bismuthinite) nanorods and nanowires are synthesized by the solventless thermolysis of bismuth alkylthiolate precursors. Reactions carried in air at ~225°C in the presence of a capping ligand species, octanoate, produce high aspect ratio (>100) nanowires. Lower aspect ratio nanowires (~7) are produced by the same approach with the addition of elemental sulfur at lower reaction temperature (~160°C). Both the nanowires and nanorods are oriented with their long axes in the [002] crystallographic direction. Higher reaction temperatures (~250°C) produce crossed nanowire networks, or fabrics, with highly oriented growth as a result of heterogeneous nanowire nucleation and epitaxial elongation off the surface of existing wires.

6.1.4 Solventless Synthesis of Lead Oxy-Chloride (Mendipite)

$Pb_3O_2Cl_2$ nanobelts were synthesized in the absence of solvent via the thermal decomposition of a $PbCl^+$-octanoate derived molecular precursor. Individual nanobelts with an orthorhombic (mendipite) crystal structure were greater than 4 μm in length, with a log mean average width of 61.6 nm, and a mean thickness of 23.3 nm. The anisotropic belt-like shape grows in the [010] direction with the [100] direction occurring across the width, and the [001] direction across the thickness. The growth direction appears to result from the elongation of double chains of (OPb_4) tetrahedra present in the mendipite crystal structure. The specific orientation between nanocrystal shape and crystal structure provides an ideal means of studying the birefringent properties of nanocrystals. In particular, the birefringence of the nanobelts was determined to be approximately a magnitude larger than the bulk value of 0.07 for mendipite.

6.1.5 Self-Assembly of Metallic Nanocrystals

Thin films of dodecanethiol-passivated Au and Ag nanocrystals drop cast from different solvents were examined by HRSEM. C_{12}-coated Au and Ag nanocrystals, 5 to 7 nm in diameter, form face-centered cubic (fcc) superlattices oriented with the $(111)_s$ planes parallel to the substrate when deposited from good solvents, such as hexane, chloroform and toluene. The gross morphology of the films depended on the solvent: hexane produced rough superlattice films; whereas, chloroform deposited smooth films. The difference in interparticle attraction—which is approximately 20% higher in hexane—appears to give rise to the difference in film morphology. Addition of a poor solvent to the dispersion prior to drop casting led to superlattices with decreased order. Although the superlattices always orient with $(111)_s$ as the basal plane on the substrate, superlattices deposited from chloroform grow preferentially in the $[110]_s$ direction, whereas hexane deposits superlattices that grow primarily in the $[111]_s$ direction.

6.2 RECOMMENDATIONS FOR FUTURE WORK

6.2.1 Solventless Synthesis

Several routes are available for the continued study of nanocrystal synthesis using the developed solventless technique. In addition to the nanocrystals mentioned in Chapters 2-4, several other materials were produced in nanocrystalline form, albeit their size is significantly larger than desired (~100 nm). Figure 6.1 shows SEM/TEM images and the corresponding XRD patterns for (A,B) PbS, (C,D) Cu_2O, and (E,F) Bi nanoparticles (See Appendix D for synthesis conditions). These systems were not studied in detail, but they demonstrate the possibility for expanding this technique to include the formation and study of metallic and oxide nanomaterials.

Studies comparing the size, dispersity, and shape of nanocrystals produced using the solventless technique relative to comparable solution phase methods would also be of interest. The molecular precursors formed for the solventless technique may be dissolved and subsequently reacted in high boiling point solvents such as dioctylether or TOP/TOPO. Comparative studies of the particles produced in solvent can then be performed in order to verify the effects of the solventless environment on nanocrystal growth. In addition, the shape of the particles formed in solution is of interest. The highly anisotropic wires and belts produced for Bi_2S_3 and $Pb_3O_2Cl_2$ are not usually observed in solution syntheses without using multiple injections or seed particles as in the solution-liquid-solid technique.

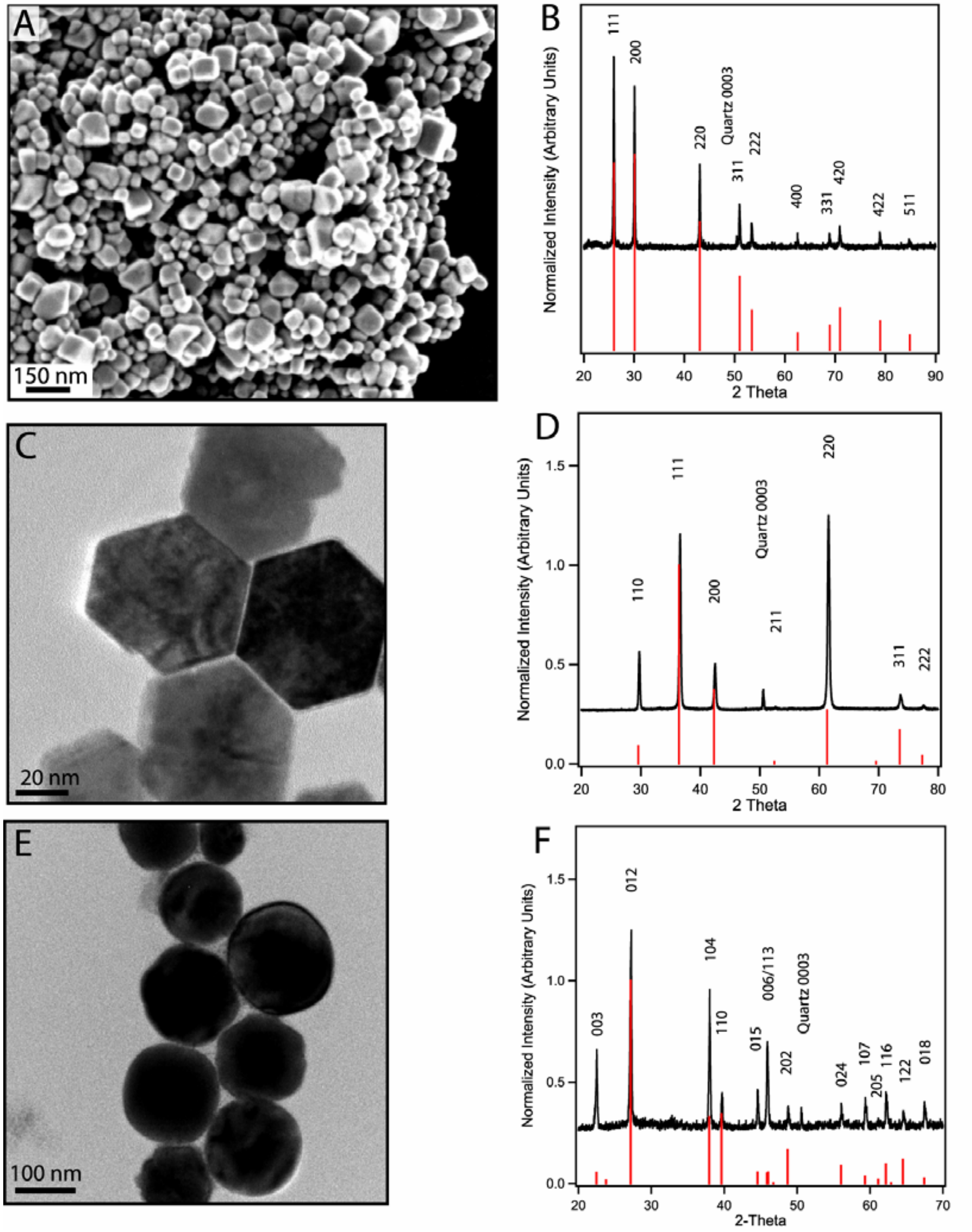

Figure 6.1: (A) SEM image and (B) XRD pattern of PbS crystals formed using solventless technique. (C) TEM image and (D) XRD pattern of Cu$_2$O nanocrystals. (E) TEM image and (F) XRD pattern of Bi nanocrystals.

Finding suitable alternative capping ligands would also be beneficial for the Bi_2S_3 and to a somewhat lesser extent the $Pb_3O_2Cl_2$ syntheses. Both of these systems have a strong tendency to bundle together when drop cast from solution. Longer chained ligands may improve the ability to isolate individual wires or belts to further study their physical properties. In particular, a study of the heat and electron transport properties would be of interest with respect to the expected thermoelectric properties of Bi_2S_3 nanowires. Improved capping would also enable the study and development of methods suitable for aligning wires and belts into superlattices. Organized arrays of $Pb_3O_2Cl_2$ nanobelts would be particularly useful for utilizing their high birefringence in small scale optical components.

6.2.2 Single Step Nanocrystal Coatings

Initial studies demonstrate that the solventless synthesis is particularly well suited for developing methods of growing nanocrystals directly onto a substrate in a single step. Figure 6.2 consists of SEM images taken of (A,B) Cu_2S nanoplatelets and Bi_2S_3 (C) nanorods and (D) nanowires formed by spreading the precursor material directly onto a glassy carbon substrate. The substrates were then heated at the same temperatures as the usual methods of formation. The images in Figure 6.2 are of the as produced nanocrystals. No purification step was taken to remove residual by-products that are largely removed via vaporization during the heating step. Homogeneity of these films is a significant problem, but improved methods would be of considerable interest for applications such as coatings or catalysts. One possibility for improving homogeneity would be to spray concentrated precursor solution onto the surface prior to heating. In addition, the effect of substrate material on nanocrystal growth may be examined. For example, Kuykendall et al. studied the effect of single crystal substrates on the growth direction and cross sectional shape of GaN nanowires formed using a metal-organic chemical vapor deposition technique.[2] This type of precise control over crystal growth is not necessarily expected using the solventless precursor, but substrate composition may encourage improved nucleation and growth of aligned rod- or wire-like nanocrystals similar to those shown in Figure 6C.

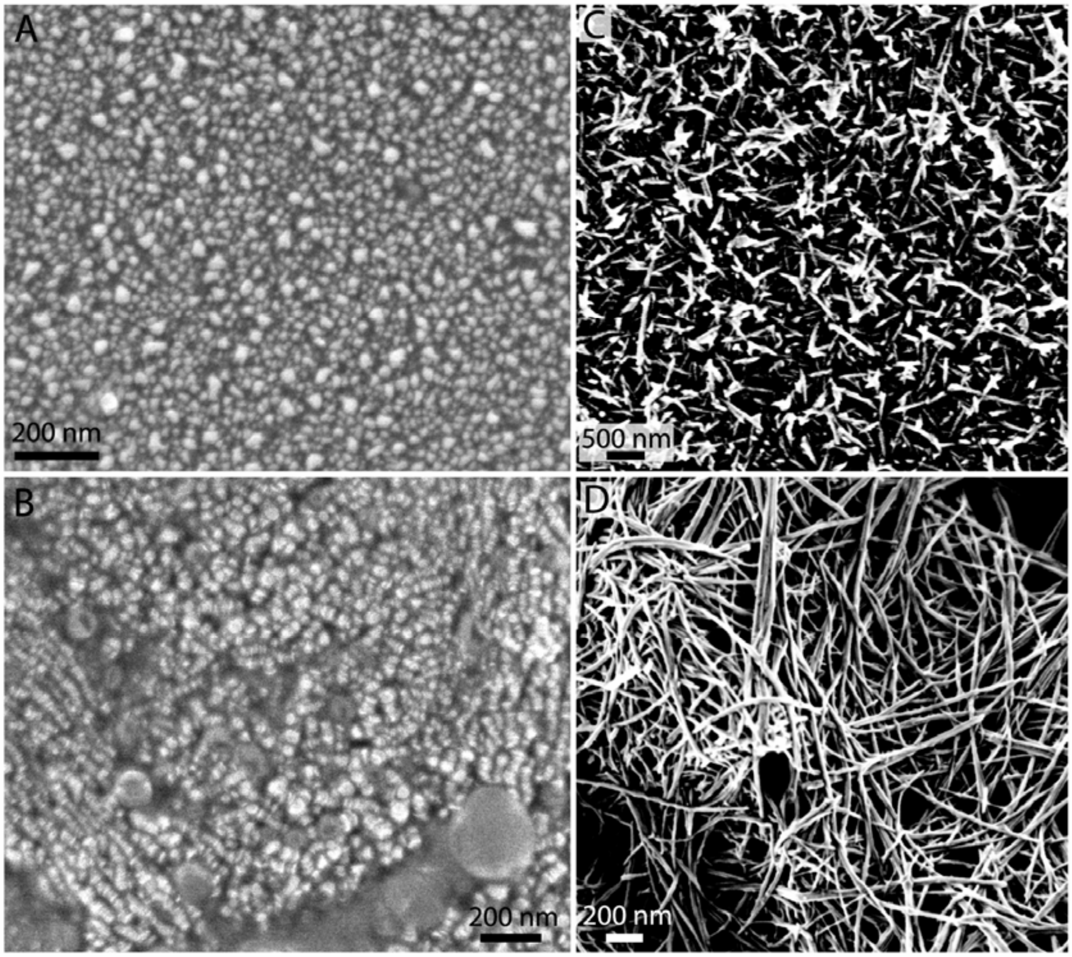

Figure 6.2: (A) SEM image of Cu_2S nanoplatelets formed from reacting molecular precursor directly on a glassy carbon substrate. (B) SEM image showing local ordering of Cu_2S nanodisks as grown without purification. (C) and (D) SEM images of Bi_2S_3 nanorods and nanowires formed from reacting molecular precursor on glassy carbon substrate.

6.2.3 Self-Assembly of Nanocrystals

The study of self-assembled metallic nanocrystals in Chapter 5 focused on the effect of interparticle core-core attraction on the observed thin film morphology, but additional factors also have a significant effect on thin film formation. In particular, ligand surface coverage has been identified using SAXS as a critical factor relative to both the strength of interparticle attraction experienced between nanocrystals in solution as well as the degree of steric repulsion that they provide.[3] Unfortunately, the use of SAXS to study nanocrystal interactions in chloroform is not possible due to the absorption of X-rays by the solvent. Solvents such as toluene, hexane, and low concentration solutions of ethanol would be suitable though for performing a systematic SAXS and SEM study of three dimensional thin film formation. The examination of factors such as ligand length, surface coverage, and ligand functionality would provide insight into the magnitude and effect of ligand-solvent and ligand-ligand interactions on nanocrystal self-assembly and morphology. In addition, substrate-nanocrystal interactions have been identified as a factor affecting the wetting of nanocrystal thin films on substrate.[4] Comparison of thin films detailed in Chapter 5 with depositions on conductive substrates suitable for SEM imaging, such as HOPG or metallic films evaporated onto glassy carbon would provide a route for further study of substrate effects on superlattice formation. Ultimately, the goals of these studies would be to better understand how to form long range, flat films suitable for device applications such as LEDs or photovoltaic cells.

6.3 REFERENCES

(1) Ghezelbash, A.; Sigman, M. B.; Korgel, B. A. *Nano Lett.* **2004**, *4*, 537.

(2) Kuykendall, T.; Pauzauskie, P. J.; Zhang, Y.; Goldberger, J.; Sirbuly, D.; Denlinger, J.; Yang, P. *Nature Mater.* **2004**, *3*, 524.

(3) Saunders, A. E.; Korgel, B. A. *J. Phys. Chem. B* **2004**, *108*, 16732.

(4) Korgel, B. A.; Fitzmaurice, D. *Phys. Rev. Lett.* **1998**, *80*, 3531.

Appendix A

A.1 ADDITIONAL IMAGES: SOLVENTLESS SYNTHESIS

Figures A.1-3 consist of additional images and data taken of the nanocrystals discussed in Chapters 2-4. Figure A.4 shows polarized optical microscopy images of drying droplets of chloroform with Bi_2S_3 and $Pb_3O_2Cl_2$ nanowires undergoing Marangoni convective flow. Figures A.5-7 are images of Bi_2S_3 nanowires that demonstrated interesting, but currently irreproducible, assembly/formation.

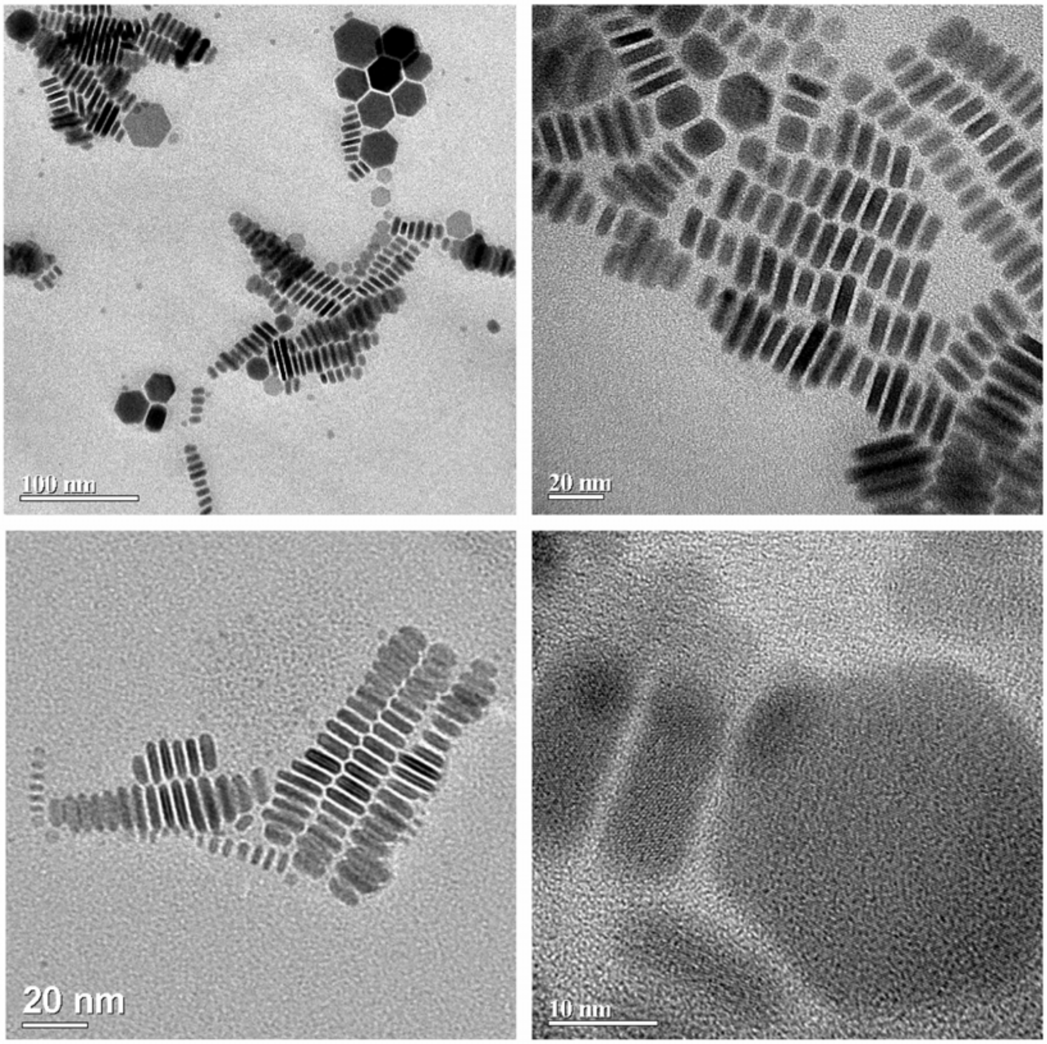

Figure A.1: TEM images of Cu_2S nanoplatelets demonstrating both of the typical orientations discussed in Chapter 2.

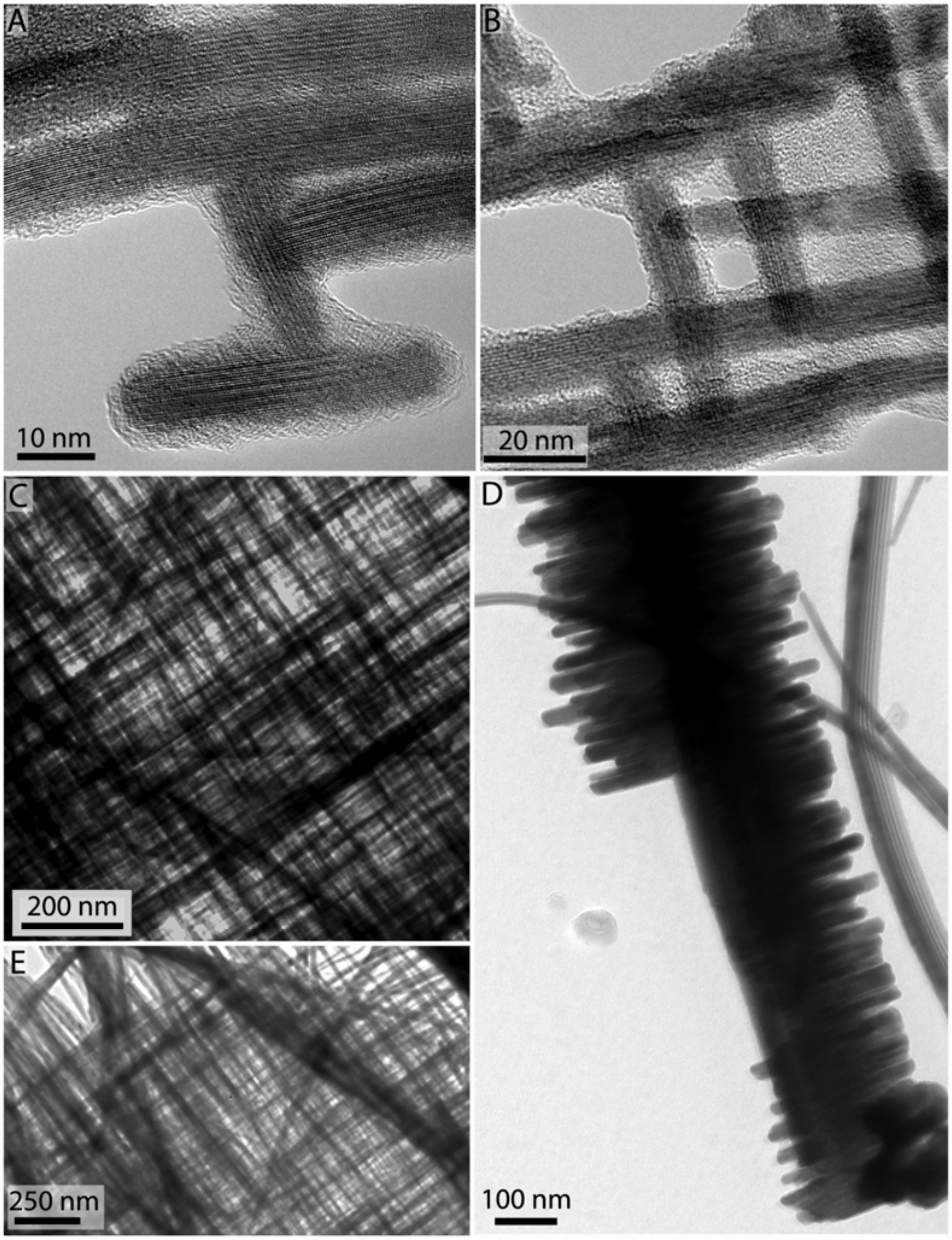

Figure A.2: (A,B) HRTEM images of Bi_2S_3 nanofabric (see Chapter 3) demonstrating oriented alignment. (C,E) Lower resolution images show ordering over larger length scales. (D) Small section of wires nucleating at 90° to one another.

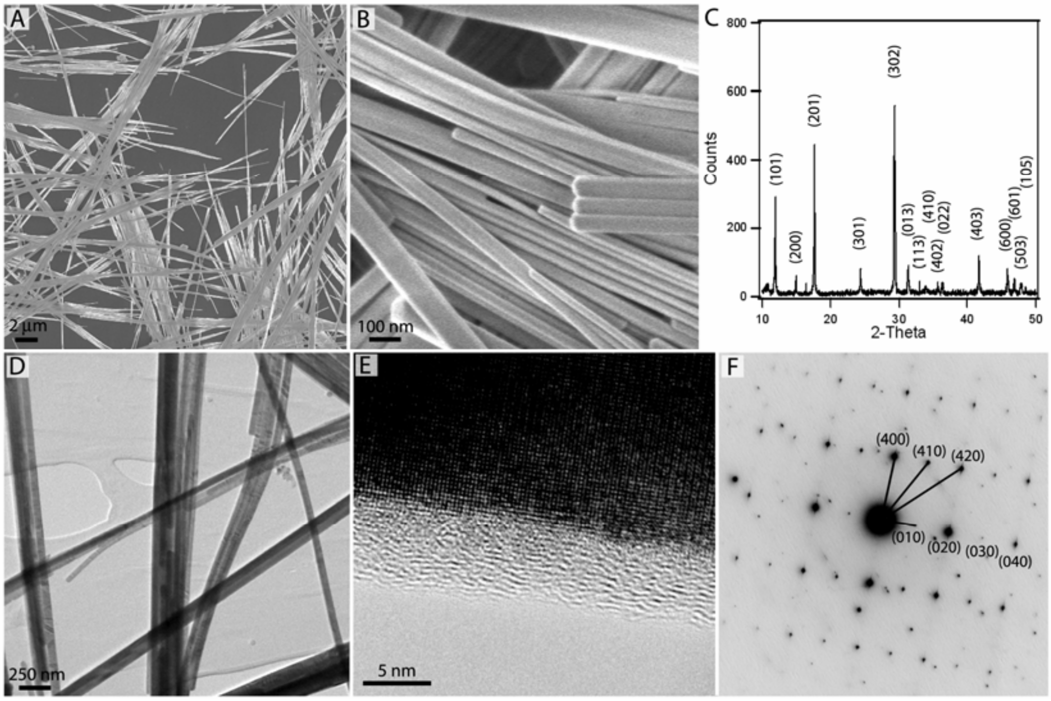

Figure A.3: (A,B) SEM images of $Pb_3O_2Cl_2$ nanobelts discussed in Chapter 4. (C) Additional XRD pattern of the nanobelts showing orthorhombic (mendipite) crystal structure. (D) Low and (E) high resolution TEM images of nanobelts. (F) Electron diffraction pattern corresponding to the belt in (E) oriented with respect to the [001] zone axis showing growth in the [010] direction.

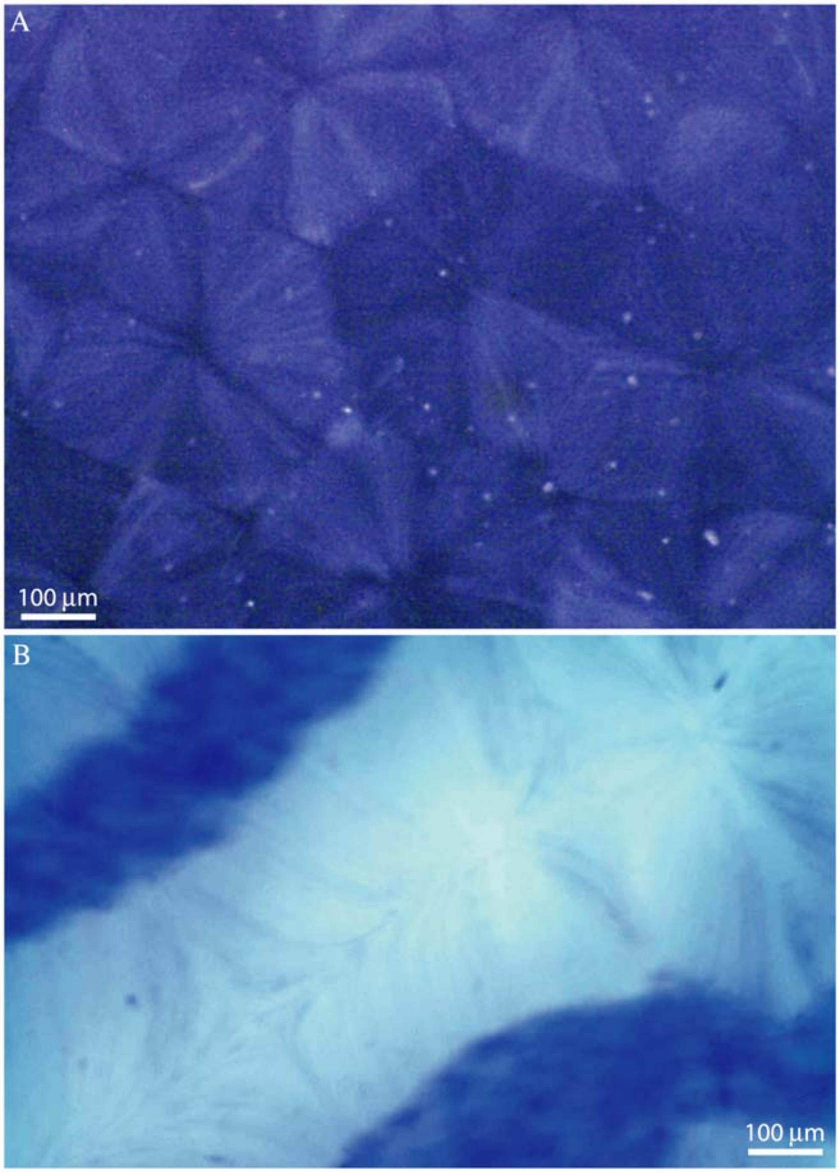

Figure A.4: Optical microscopy images taken through crossed polarizers of (A) Bi_2S_3 and (B) $Pb_3O_2Cl_2$ nanowires in a drying droplet of chloroform undergoing convective Marangoni flow. The birefringent wires and belts form “contrails” when imaged with millisecond exposure times showing their flow patterns. The wires (A) show ordered cells with a significant number of pentagons as well as the expected hexagons. The belts (B) tend to form bands undergoing Marangoni flow interspersed with what appeared to be relatively stable areas of fluid.

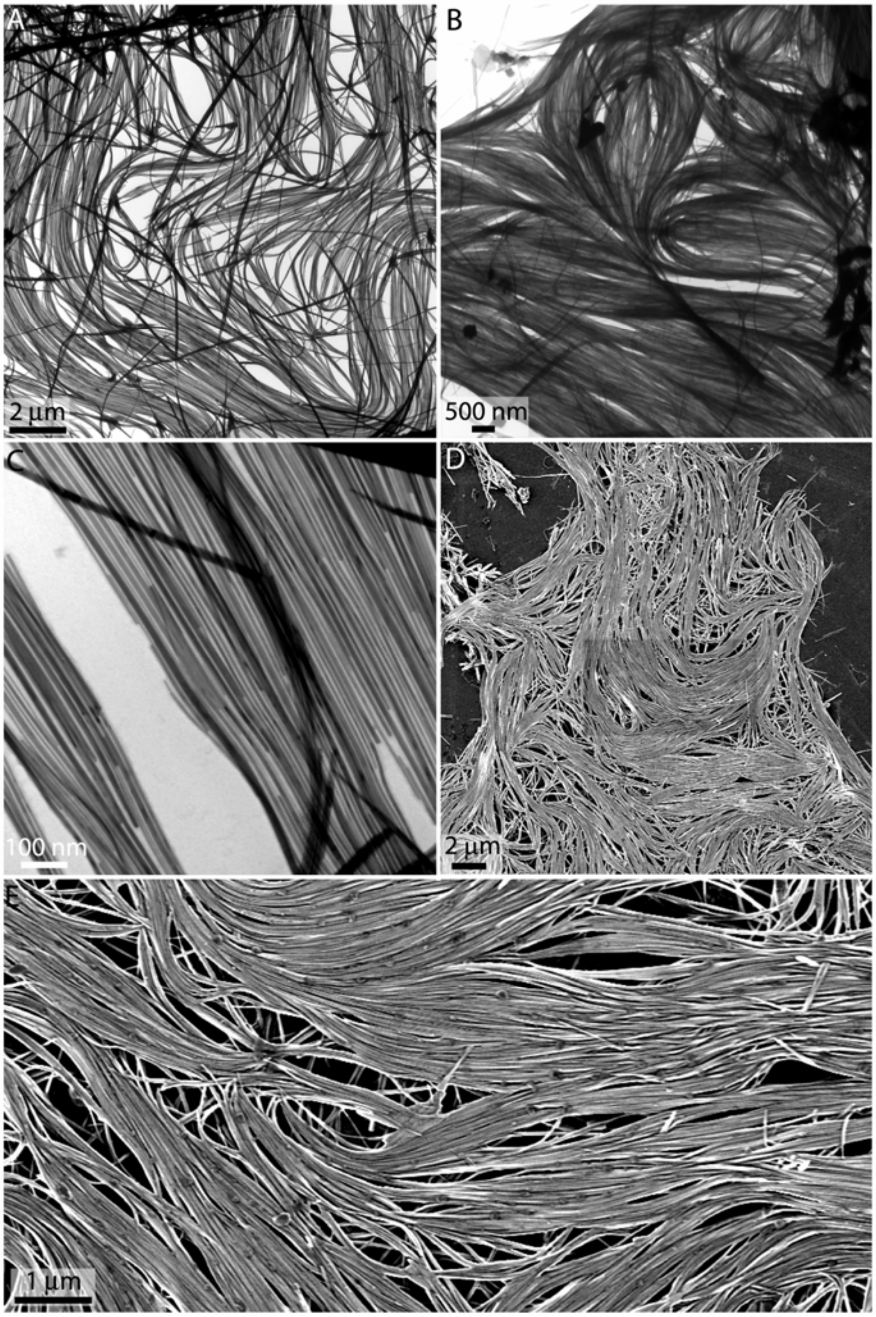

Figure A.5: (A,B,C) TEM and (D,E) SEM images of Bi_2S_3 nanowire "spaghetti" formed during a typical nanowire synthesis.

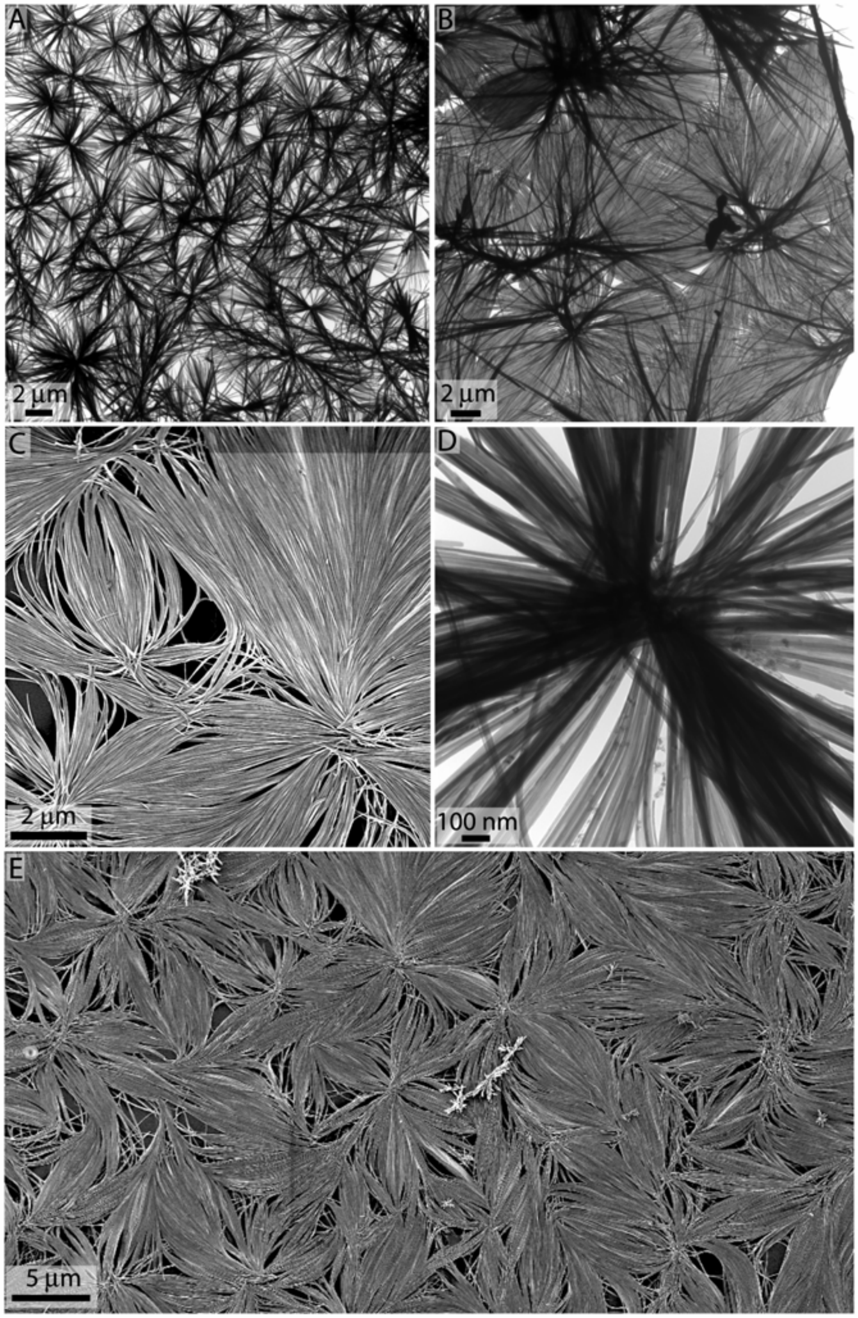

Figure A.6: (A,B,D) TEM and (C,E) SEM images of Bi_2S_3 nanowire “starbursts” or “flowers” formed during a typical nanowire synthesis.

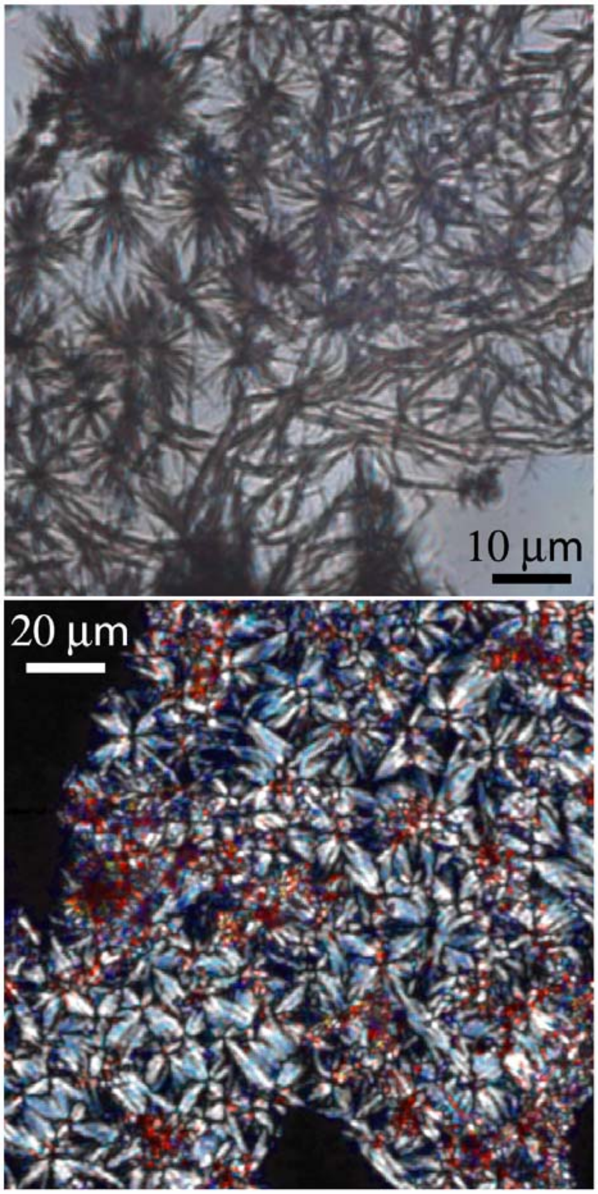

Figure A.7: Optical microscopy images (top) without crossed polarizers and (bottom) with crossed polarizers of the Bi_2S_3 “flowers” shown in Figure A.6 deposited as a dry film on a glass slide. The “flowers” show maximum intensity of polarized light (bottom) in the 45° and 135° directions relative to the polarizing and analyzing filters at 0° and 90°. The variation in interference colors results from differing thickness of material.

A.2 ADDITIONAL IMAGES: SELF-ASSEMBLY

Figures A.8 and A.9 are additional images of self-assembled Au nanocrystal superlattices formed by drop casting particles from solutions of chloroform and hexane as discussed in Chapter 5. Figures A.10 and A.11 show some of the interesting orientations obtained by suspending a glassy carbon substrate vertically in a solution of Au nanocrystals in hexane. The solvent was allowed to slowly evaporate down the length of the substrate overnight depositing nanocrystals on the substrate as the solvent level decreased. The resulting sample was inhomogeneous, but resulted in areas of highly ordered superlattices. This process is described as “evaporative casting” of nanocrystals from solution.

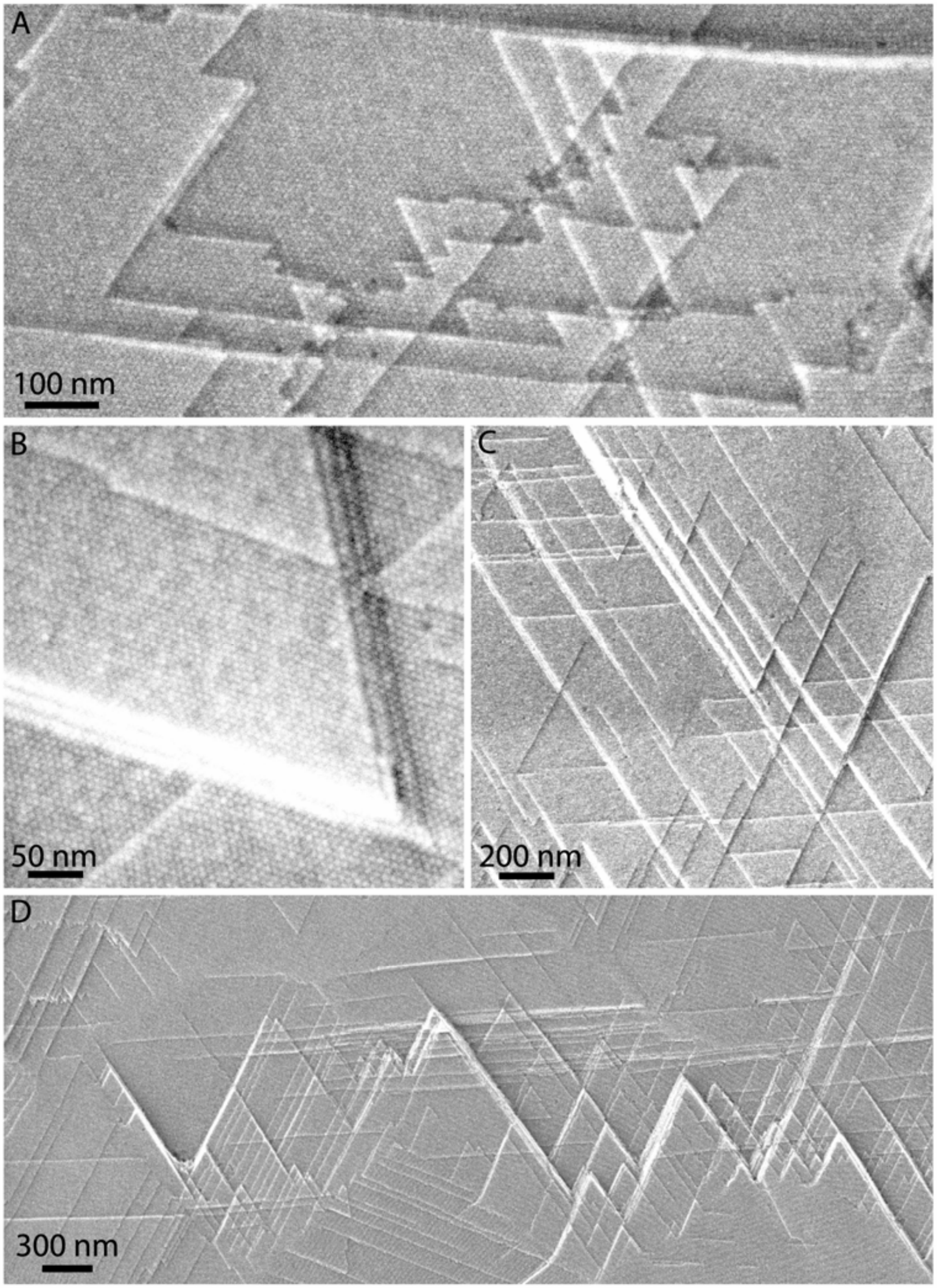

Figure A.8: SEM images of Au nanocrystal superlattices deposited from chloroform.

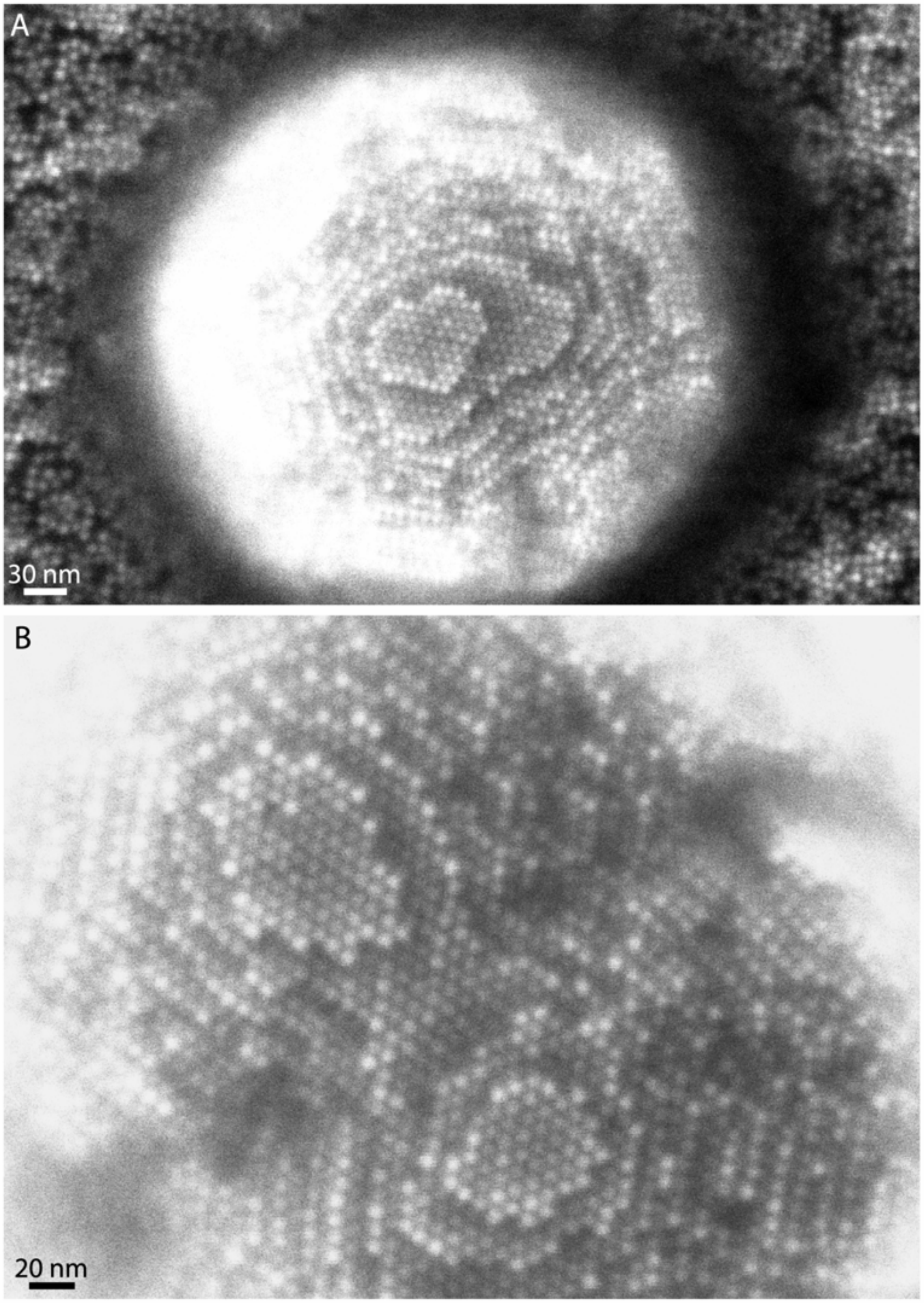

Figure A.9: SEM images of Au nanocrystal superlattices deposited from hexane.

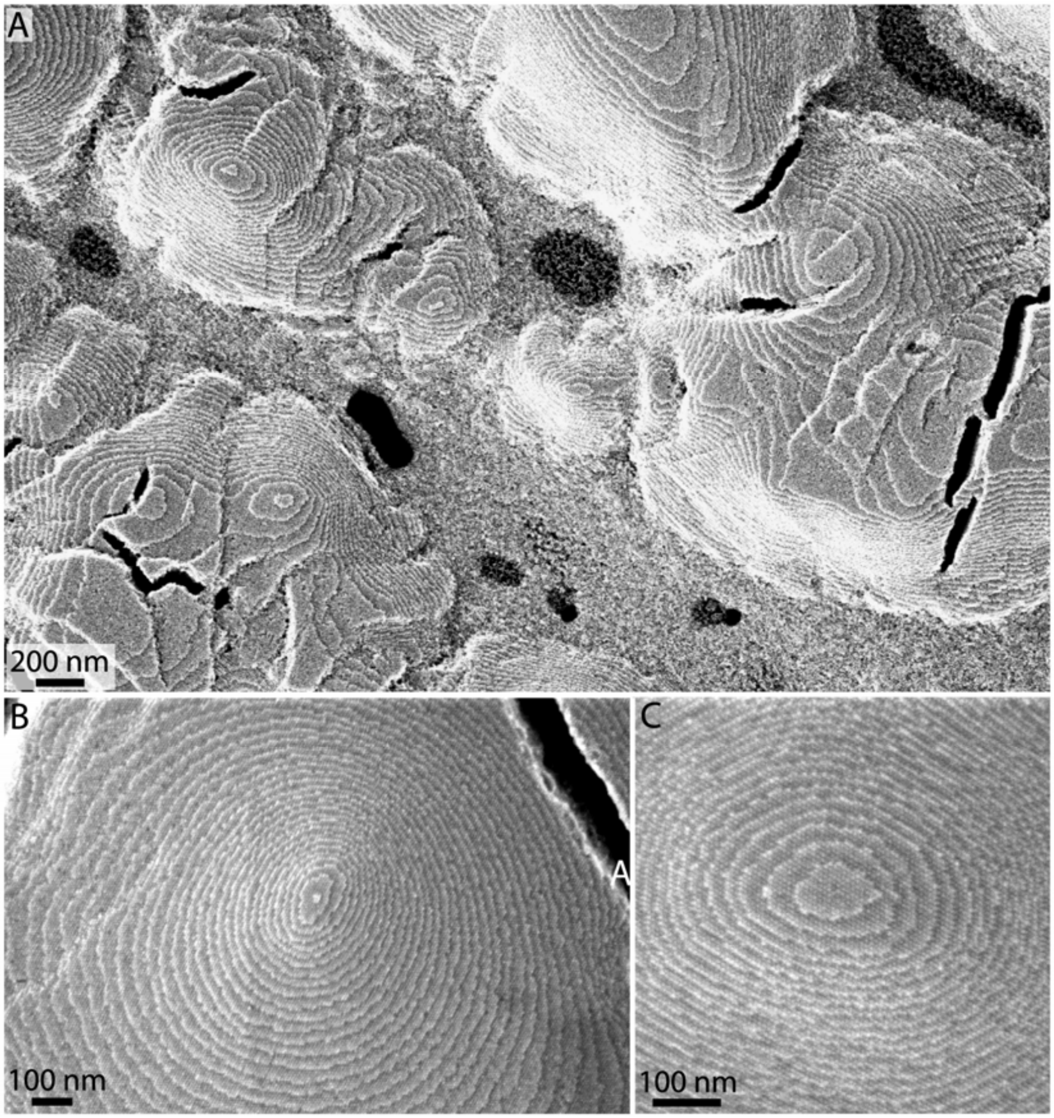

Figure A.10: SEM images of mounds of Au nanocrystals formed via evaporative casting of nanocrystals from hexane.

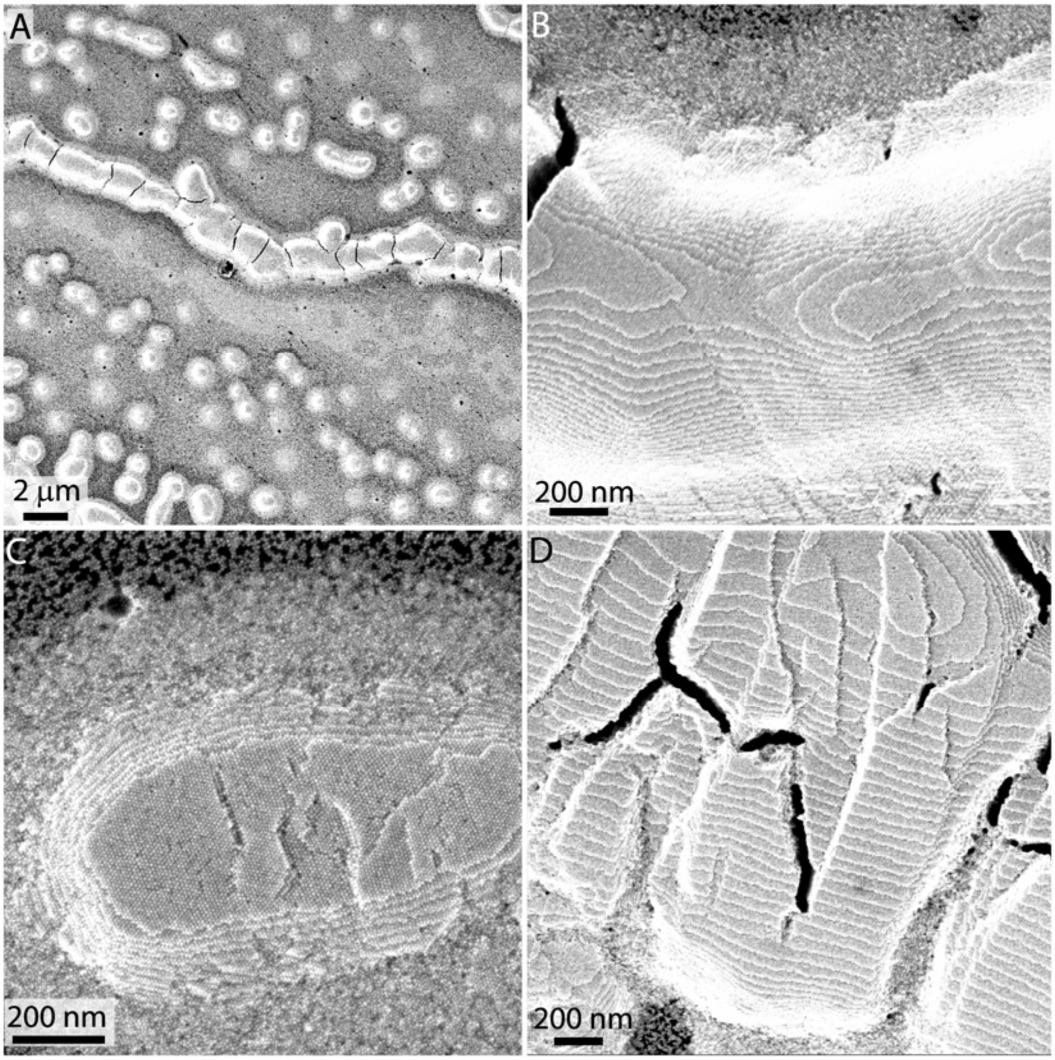

Figure A.11: SEM images of Au nanocrystals deposited by evaporative casting of particles from hexane showing the formation of linear ridges of particles accumulated and deposited at the solvent-air interface.

A.3 SEM IMAGES OF INVERSE OPAL NANOCRYSTAL SUPERLATTICE FILMS

Figures A.12 and A.13 are images of inverse opal nanocrystal superlattice films formed by drop casting fluorooctyl methacrylate-thiol (FOMA-SH) capped Au nanocrystals from 1,1,2 trichlorotrifluoroethane (Freon-113) in a humid environment as described by Shah et al. and Saunders et al.[1,2] During evaporation, water droplets condense at the evaporating Freon interface and are stabilized by the nanocrystals in solution. The water droplets serve as a template for the ordered formations observed in these images.

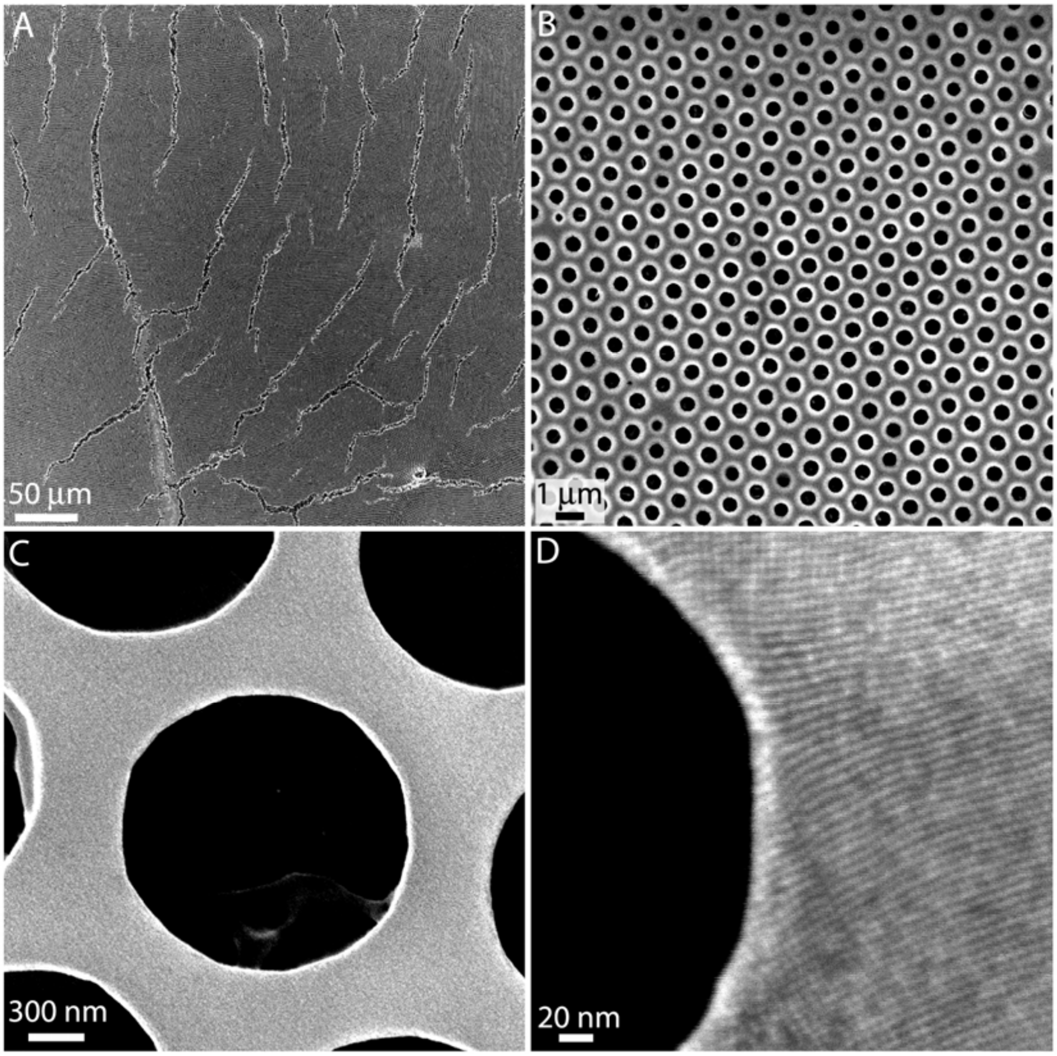

Figure A.12: (A,B,C) SEM images of hexagonally ordered holes within Au nanocrystal thin films over varying length scales. (D) HRSEM image of Au nanocrystal superlattice illustrating orientation of individual nanocrystals within the film.

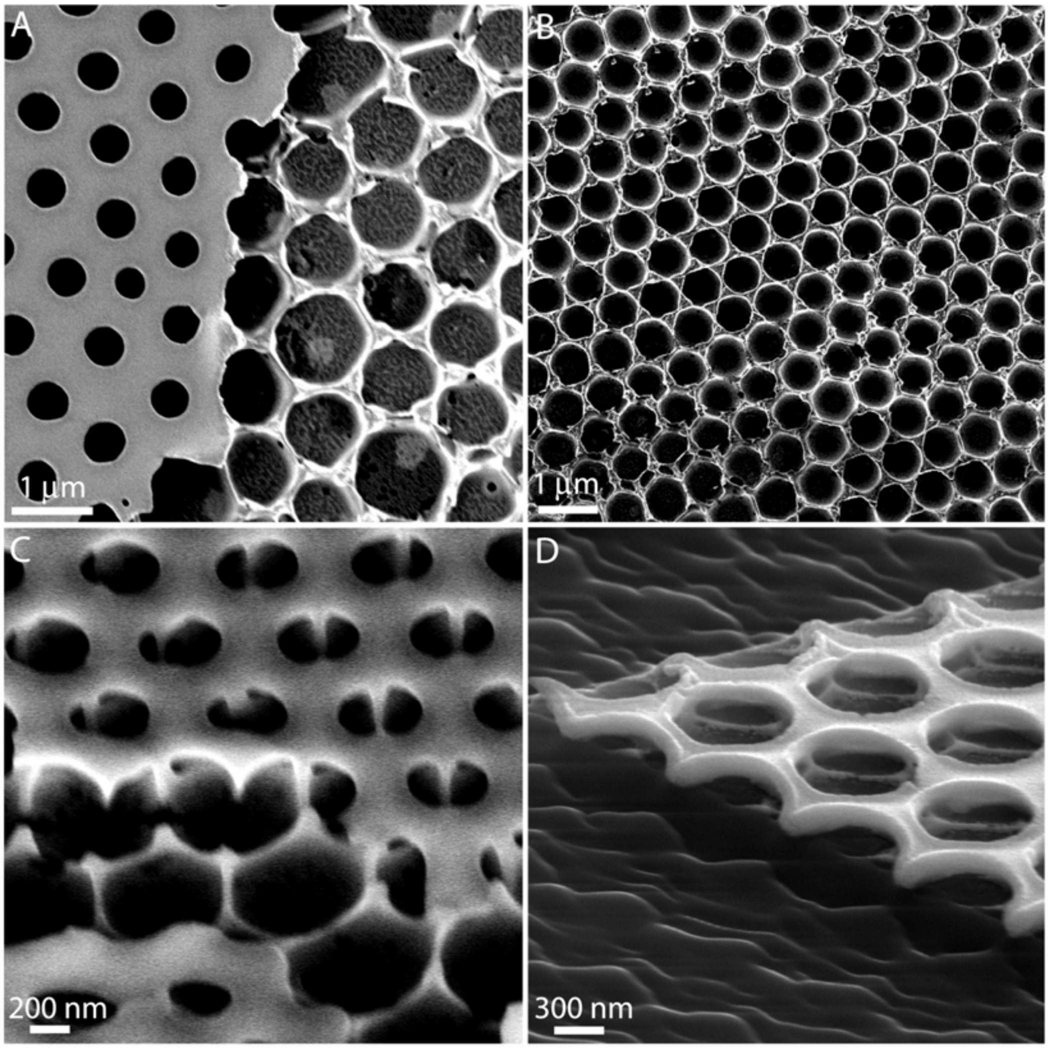

Figure A.13: (A) SEM image of macroporous nanocrystal film with half of the top layer of nanocrystals removed by placing tape gently on the surface and lifting off. (B) Entire section of film with the top layer of crystals removed using tape showing the ordered underlayer. (C) SEM image tilted at 45° showing the pillared structure between individual holes in the thin film. (D) SEM image tilted at 60° showing nanocrystal film cut into a triangular section using e-beam lithography.

A.4 AFM AND MFM IMAGING

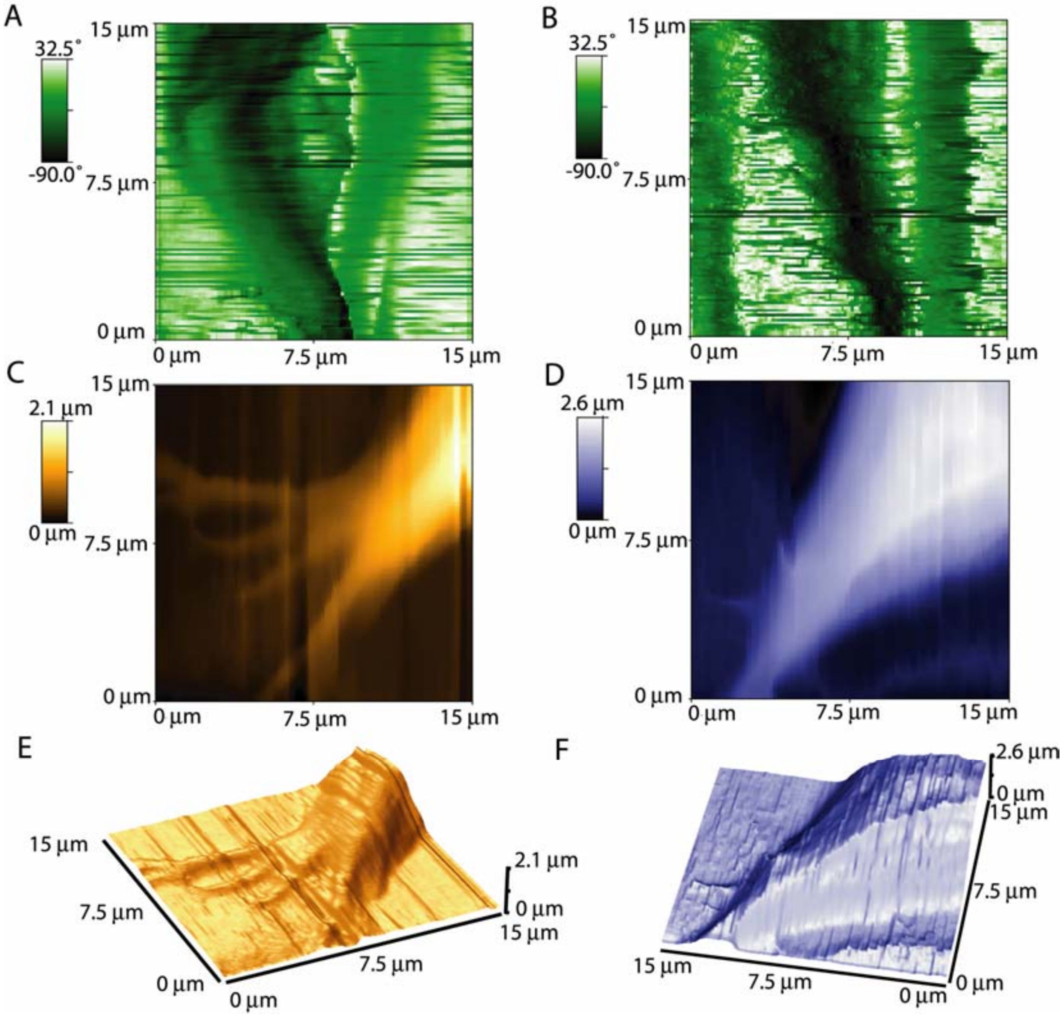

Figure A.14: Contact AFM images scanned in liquid of nerve cells grown on a glass substrate using a tip coated with polystyrene to prevent cell puncture. (A,B) Portions of two nerve cells shaded to give 3D appearance. (C,E) Raw image and 3D image of a nerve cell with dendrites. (D,F) Raw image and 3D image of nerve cell body.

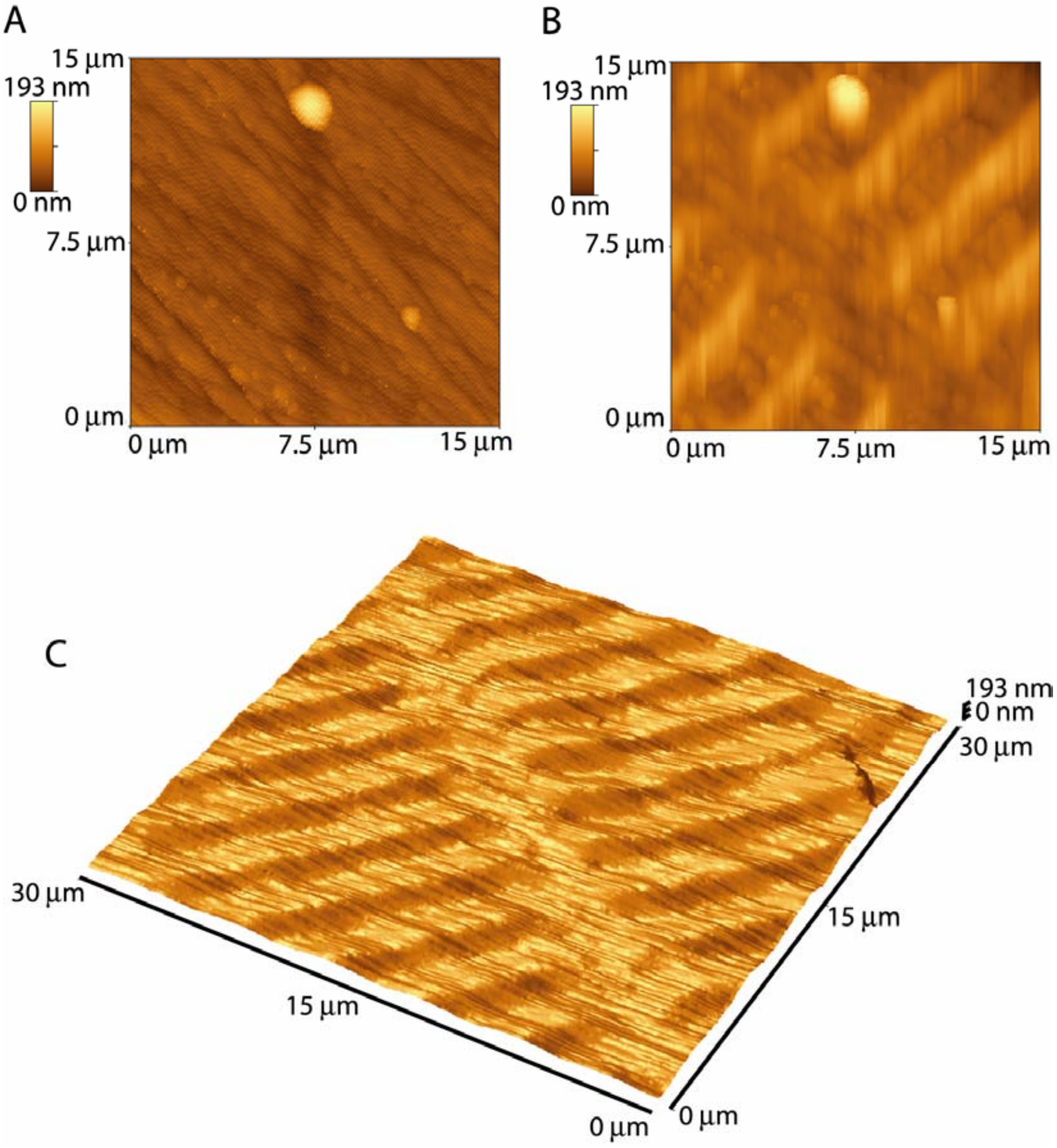

Figure A.15: Magnetic force microscopy (MFM) images of a section of typical data storage material illustrating the transition from short range van der Waals forces to longer range magnetic forces as the height of the magnetized MFM tip is successively pulled away from the sample surface. (A) Surface topography appears when operating under typical non-contact scanning conditions (tip closest to substrate) resulting from the dominant short range van der Waals force between the MFM tip and the substrate. (B) At an intermediate tip height, the image begins to show magnetic domains in addition to surface topography. (C) 3D construction showing only the spatial variation of magnetic forces at the final (largest separation between tip and sample) scanning conditions.

A.5 BIBLIOGRAPHY

(1) Saunders, A. E.; Shah, P. S.; Sigman, M. B.; Hanrath, T.; Hwang, H. S.; Lim, K. T.; Johnston, K. P.; Korgel, B. A. *Nano Lett.* **2004**, *4*, 1943.

(2) Shah, P. S.; Sigman, M. B.; Stowell, C. A.; Lim, K. T.; Johnston, K. P.; Korgel, B. A. *Adv. Mater.* **2003**, *15*, 971.

Appendix B

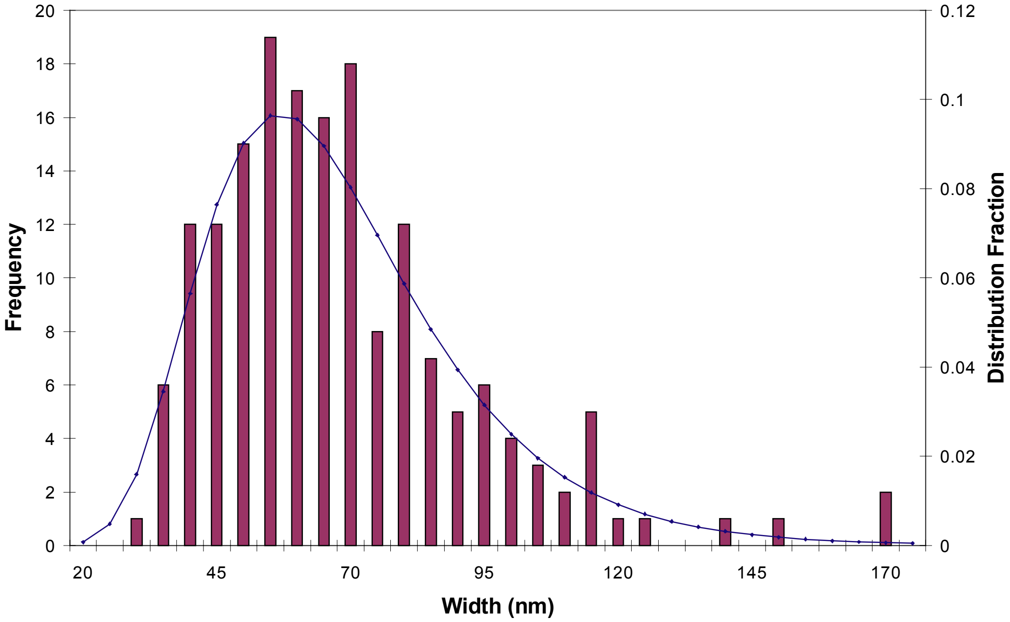

Figure B.1: Histogram of $Pb_3O_2Cl_2$ nanobelt width demonstrating log normal size distribution.

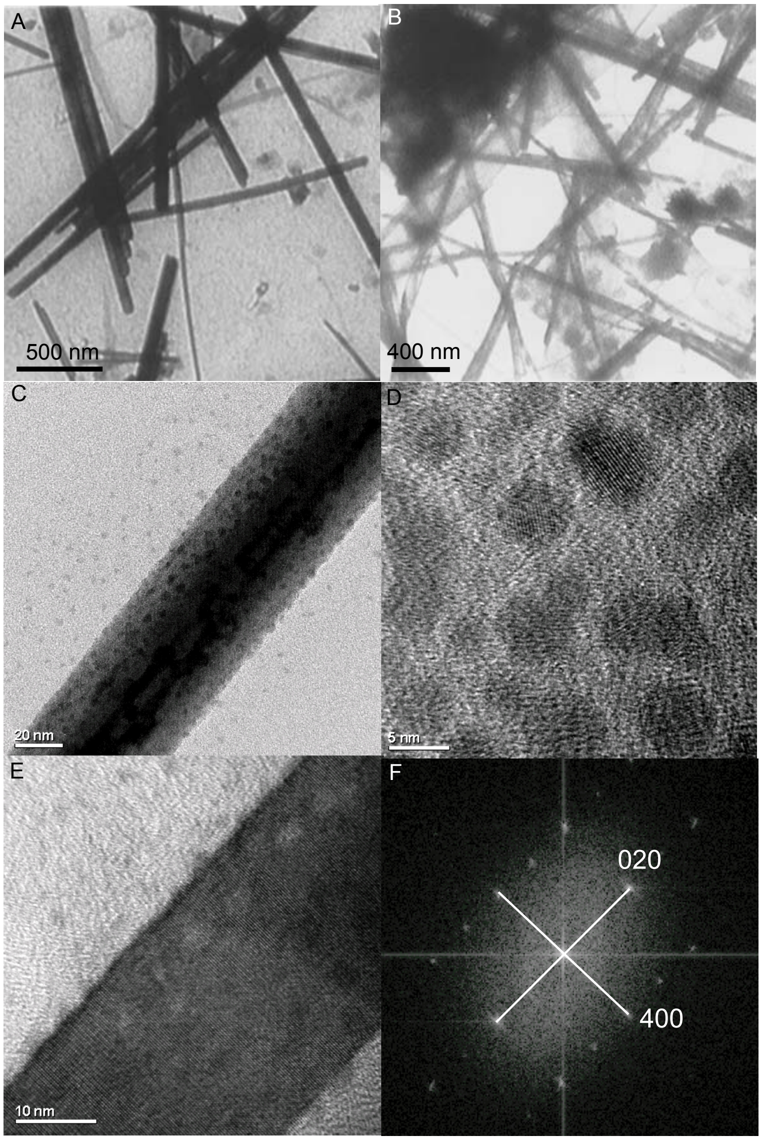

Figure B.2: (A) and (B) low resolution TEM images of $Pb_3O_2Cl_2$ nanobelts formed without the use of ethylenediamine in the synthesis. (C) and (D) TEM images showing increased formation of small nanocrystals in addition to nanobelt formation. (E) HRTEM image of nanobelt formed without ethylenediamine indicating that these belts grow in the [010] direction as shown via the FFT in (F).

Appendix C

C.1 CALCULATION OF THE INTERPARTICLE INTERACTION ENERGY.

The interaction energy between two gold nanocrystals is calculated following the procedures outlined in Shah et al.[90] The total interaction energy Φ_{total}, between C_{12}-monolayer coated gold and silver nanocrystals dispersed in hexane and chloroform includes the core-core van der Waals attraction Φ_{vdW}, and the repulsive forces from the organic capping ligands that includes an osmotic and elastic term (Φ_{osm} and Φ_{elas}):[91,296]

(1)
$$\Phi_{total} = \Phi_{vdW} + \Phi_{osm} + \Phi_{elas}$$

Φ_{vdW} depends on the particle radius R, and the center-to-center separation d:

(2)
$$\Phi_{vdW} = -\frac{A_{121}}{6}\left[\frac{2R^2}{d^2 - 4R^2} + \frac{2R^2}{d^2} + \ln\left(\frac{d^2 - 4R^2}{d^2}\right)\right]$$

The Hamaker constant A_{121}, for the metal nanocrystals (subscript 1) interacting across the solvent (subscript 2) was estimated from the Hamaker constants for metal and solvent interacting across vacuum A_{11} and A_{22}, respectively:[297]

(3) $$A_{121} \approx \left(\sqrt{A_{11}} - \sqrt{A_{22}}\right)^2$$

.

The literature value of A_{11}= 2.83 eV for gold and 2.48 eV for silver was used.[298] A_{22} was estimated for hexane, toluene, or chloroform using a simplified form of Lifshitz theory:

(4) $$A_{22} = \frac{3}{4}k_B T\left(\frac{\varepsilon_2 - 1}{\varepsilon_2 + 1}\right)^2 + \frac{3h\nu_e}{16\sqrt{2}}\frac{\left(n_2^2 - 1\right)^2}{\left(n_2^2 + 1\right)^{3/2}}$$

where ε is the dielectric constant and n the refractive index, k_B is Boltzmann's constant, h is Planck's constant, T is temperature, and ν_e is the maximum electronic ultraviolet adsorption frequency (taken to be 3×10^{15} s^{-1}). Due to weaker charge screening by hexane relative to chloroform and toluene, the Hamaker constant is 18% higher for gold in hexane (A_{121} = 1.36 eV) than in chloroform (A_{121} = 1.16 eV). The Hamaker constant for silver is 20% higher in hexane (A_{121} = 1.13 eV) than in chloroform (A_{121} = 0.94 eV). The osmotic and elatic repulsive energies, Φ_{osm} and Φ_{elas} were determined using expressions developed by Vincent, et al.[296]

(5) $$\Phi_{osm} = \frac{4\pi R k_B T\phi^2}{\upsilon_{solv}}\left(\frac{1}{2} - \chi\right)\left(l - \frac{d - 2R}{2}\right)^2 \qquad \text{for } l < d - 2R < 2l$$

(6) $$\Phi_{osm} = \frac{4\pi R k_B T\phi^2}{\upsilon_{solv}}\left(\frac{1}{2} - \chi\right)\left[l^2\left(\frac{d - 2R}{2l} - \frac{1}{4} - \ln\left(\frac{d - 2R}{l}\right)\right)\right] \qquad \text{for } d - 2R < l$$

$$(7)\ \Phi_{elas} = \frac{2\pi R k_B T l^2 \phi \rho}{MW_2}\left\{ x \ln\left[x\left(\frac{3-x}{2}\right)^2 \right] - 6\ln\left(\frac{3-x}{2}\right) + 3(1-x) \right\} \text{ for } x = \frac{d-2R}{l}$$

where ν_{solv} is the solvent molecular volume, φ, *l*, and ρ are the the volume fraction profile, the length and the density of the adsorbed organic ligands, and MW_2 is the molecular weight of the metal. The Flory-Huggins interaction parameter χ, between the solvent and dodecane was taken as 0 for the good solvents (i.e., pure hexane, chloroform and toluene) and were calculated for the mixtures with ethanol.

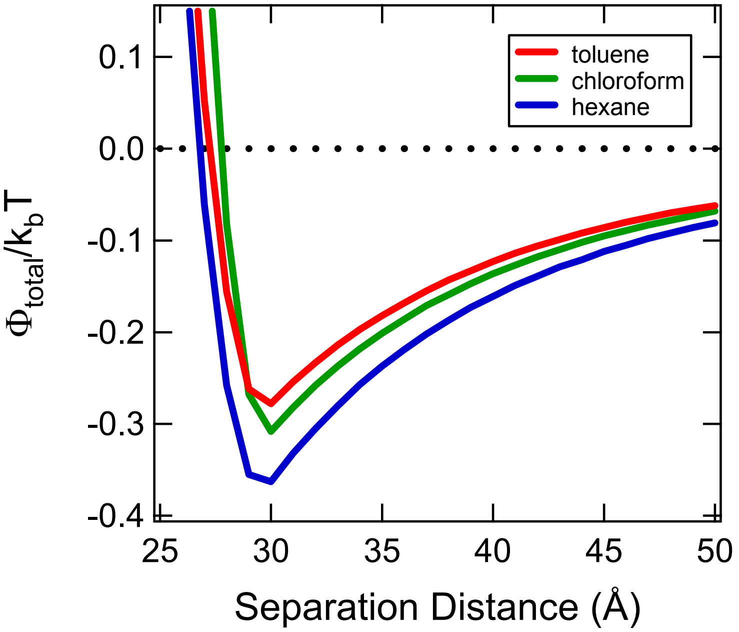

Figure C.1: Interparticle interaction energy as a function of interparticle separation for two gold nanocrystals in hexane, toluene, and chloroform. For these calculations, the nanoparticle diameter was 6.3 nm with a capping ligand chain length of 1.5 nm corresponding to the length of dodecane. The χ values for all solvents were set to zero.

C.2 EFFECT OF SOLVENT ON NANOCRYSTAL SOLUBILITY

In order to examine the effect of solvent conditions on the equilibrium between thiol adsorbed on the nanocrystal surface versus free thiol in solution, 1.8 ± 0.1 mg of dry C_{12} capped Au nanocrystals were dispersed in 7.2 mL of chloroform and hexane. Absorption spectra were obtained on a Cary-Varian 500 SCAN UV-Vis-NIR spectrophotometer by placing the solutions in quartz sample cells with a 1.0 cm optical length. The concentration was adjusted until both solutions had an optical absorption density of 0.365 at the maximum of the plasmon absorption peak at 515 nm. Final concentrations were 0.0268 mg/mL Au nanocrystals in chloroform and 0.0283 mg/mL Au nanocrystals in hexane. UV-vis absorption spectra were recorded periodically for ~1150 min. The change in nanocrystal solubility was estimated based on relative change in absorption intensity over time using Beer's law:

$$A = \varepsilon bc \tag{1}$$

where A is the optical absorption intensity, ε is the molar absorptivity, b is the optical length of the sample cell, and c is the concentration of the solution. The molar absorptivity was determined from the initial solutions to be 13.5 cm^2/mg for Au nanocrystals in chloroform and 12.6 cm^2/mg in hexane. Figure C2 shows the resulting decrease in the optical absorption spectra for (A) Au nanocrystals in chloroform (1 at 0 min, 2 at 65 min, 3 at 130 min, 4 at 265 min, and 5 at 1140 min) and (B) Au nanocrystals in hexane (1 at 0 min, 2 at 78 min, 3 at 127 min, 4 at 228 min, and 5 at 1140 min).

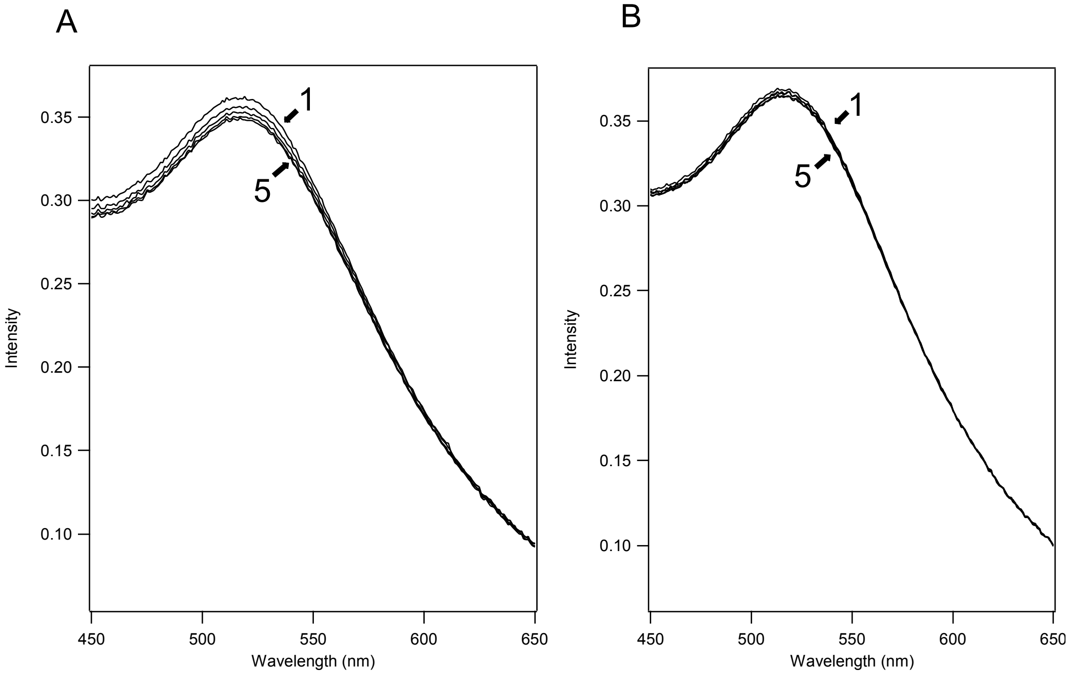

Figure C.2: Change in absorbance of Au nanocrystals dispersed in (A) chloroform and (B) hexane over time from (1) 0 min to (5) 1140 min.

Based on the change in absorption from 0 to 1140 min, the concentration of Au nanocrystals in chloroform decreased by 3.6% versus 1.3% for Au nanocrystals in hexane. This observed difference between the two solvents indicates that the thiol ligands tend to desorb at a slightly increased rate in chloroform than hexane. Comparing the change in concentration from 0 to 30 min, the concentration of Au nanocrystals in chloroform decreased by 0.5% versus 0.2% for Au nanocrystals in hexane. For shorter time scales (more comparable to the time scales used during the thin film depositions), the decrease in concentration due to thiol equilibria is significantly smaller and is not believed to contribute significantly to the observed differences in thin film formation that occurred during this experimentation.

C.3 REFERENCES

(1) Shah, P. S.; Husain, S.; Johnston, K. P.; Korgel, B. A. *J. Phys. Chem. B* **2002**, *106*, 12178.

(2) Vincent, B.; Edwards, J.; Emmett, S.; Jones, A. *Colloids Surf.* **1986**, *18*, 261.

(3) Shah, P. S.; Holmes, J. D.; Johnston, K. P.; Korgel, B. A. *J. Phys. Chem. B* **2002**, *106*, 2545.

(4) Israelachvili, J. *Intermolecular and Surface Forces*, 2nd ed.; Academic Press: New York, 1992.

(5) Bargeman, D.; Vader, F. v. V. *J. Electroanal. Chem.* **1971**, *37*, 45.

Appendix D

PbS nanocrystals were synthesized by the thermolysis of a lead thiolate-derived precursor. 32 mL of an aqueous lead (II) chloride solution (0.21 g $PbCl_2$) was combined with 25 mL $CHCl_3$ containing 0.18 g of sodium octanoate ($NaOOC(CH_2)_6CH_3$), to form a two-phase solution. After 20 min of vigorous stirring, 240 μL dodecanethiol ($C_{12}H_{25}SH$) was added. The organic phase changed to a pale yellow color. After stirring for 10 min, the aqueous phase was discarded. The organic solvent was evaporated to give a waxy solid. The waxy solid precursor material was heated in air for 180 min at 180ºC. The resulting solid was black and consisted of nanocubes that redispersed in chloroform. The nanocrystals were precipitated in excess ethanol to remove residual impurities prior to characterization by TEM and XRD.

Cu_2O nanocrystals were synthesized by adding 0.10 g of $Cu(NO_3)_2$ and 0.10 g $Pb(NO_3)_2$ to 32 mL DI water. 25 mL of $CHCl_3$ containing 0.18 g of sodium octanoate ($NaOOC(CH_2)_6CH_3$) was added to form a two-phase solution. After stirring for ~30 min, the aqueous phase was discarded. The organic solvent was evaporated to give a waxy solid. The solid precursor material was heated under vacuum for 90 min at 210ºC. The resulting solid was black and consisted of nanoplatelets that redispersed in chloroform. The nanocrystals were precipitated in excess ethanol to remove residual impurities prior to characterization by TEM and XRD.

Bi nanocrystals were synthesized by adding 0.222 g of bismuth acetate [$Bi(C_2H_3O_2)_3$] to 32 mL DI water. 25 mL of $CHCl_3$ containing 0.18 g of sodium octanoate ($NaOOC(CH_2)_6CH_3$) was added to form a two-phase solution. After 20 min of vigorous stirring, 480 μL dodecanethiol ($C_{12}H_{25}SH$) was added. After stirring for ~20 min, the aqueous phase was discarded. The organic solvent was evaporated to give a waxy solid. The solid precursor material was heated in air for 60 min at 160ºC. The resulting solid was black and consisted of large spherical nanocrystals that redispersed in chloroform. The nanocrystals were precipitated in excess ethanol to remove residual impurities prior to characterization by TEM and XRD.

Bibliography

Ackerson, B. J.; Schatzel, K. *Phys. Rev. E* **1995**, *52*, 6448.

Ackerson, B. J. *Nature* **1993**, *365*, 11.

Ahrenkiel, S. P.; Micic, O. I.; Miedaner, A.; Curtis, C. J.; Nedeljkovic, J. M.; Nozik, A. J. *Nano Lett.* **2003**, *3*, 833.

Alder, B. J.; Wainwright, T. E. *J. Chem. Phys.* **1957**, *27*, 1208.

Alder, J.; Hoover, W. G.; Young, D. A. *J. Chem. Phys.* **1968**, *49*, 3688.

The Aldrich Library of FT-IR Spectra, 2nd ed.; Sigma-Aldrich, 1997; Vol. 1.

Alivisatos, A. P. *J. Phys. Chem.* **1996**, *100*, 13226.

Alivisatos, A. P. *Science* **1996**, *271*, 933.

Arnold, M. S.; Avouris, P.; Pan, Z. W.; Wang, Z. L. *J. Phys. Chem. B* **2003**, *107*, 659.

Artemyev, M. V.; Sperling, V.; Woggon, U. *J. Appl. Phys.* **1997**, *81*, 6975.

Asherie, N.; Lomakin, A.; Benedek, G. B. *Phys. Rev. Lett.* **1996**, *77*, 4832.

Auer, S.; Frenkel, D. *Nature* **2001**, *409*, 1020.

Bae, S. Y.; Seo, H. W.; Park, J.; Yang, H.; Kim, H.; Kim, S. *Appl. Phys. Lett.* **2003**, *82*, 4564.

Bain, C. D.; Whitesides, G. M. *J. Am. Chem. Soc.* **1989**, *111*, 7164.

Balint, I.; Miyazaki, A.; Aika, K. *Phys. Chem. Chem. Phys.* **2004**, *6*, 2000.

Barbé, C.; Bartlett, J.; Kong, L.; Finnie, K.; Lin, H. Q.; Larkin, M.; Calleja, S.; Bush, A.; Calleja, G. *Adv. Mater.* **2004**, *16*, 1959.

Barber, D. J.; Freestone, I. C. *Archaeometry* **1990**, *32*, 33.

Bargeman, D.; Vader, F. v. V. *J. Electroanal. Chem.* **1971**, *37*, 45.

Bäuerlein, E. *Angew. Chem. Int. Ed.* **2003**, *42*, 614.

Bauser, E. Atomic Mechanisms in Semiconductor Liquid Phase Epitaxy. In *Handbook of Crystal Growth 3b: Thin Films and Epitaxy*; Hurle, D. T. J., Ed.; Elsevier: Amsterdam, 1994; pp 880.

Bawendi, M. G.; Steigerwald, M. L.; Brus, L. E. *Annu. Rev. Phys. Chem.* **1990**, *41*, 477.

Bennema, P. *J. Cryst. Growth* **1969**, *5*, 29.

Bentzon, M. D.; Wonterghem, J. v.; Morup, S.; Tholen, A.; Koch, C. J. W. *Phil. Mag. B* **1989**, *60*, 169.

Berry, C. R. *Phys. Rev.* **1967**, *153*, 989.

Berry, C. R. *Phys. Rev.* **1967**, *161*, 611.

Bieniulis, M. Z.; Corry, C. E.; Hoskins, E. R. *Geophys. Res. Lett.* **1987**, *14*, 135.

Binning, G.; Rohrer, H.; Gerber, C.; Weibel, E. *Phys. Rev. Lett.* **1982**, *49*, 57.

Black, J.; Conwell, E. M.; Seigle, L.; Spencer, C. W. *J. Phys. Chem. Solids 2* **1957**, *2*, 240.

Brus, L. *J. Phys. Chem.* **1986**, *90*, 2555.

Brus, L. E. *J. Chem. Phys.* **1984**, *80*, 4403.

Brust, M.; Fink, J.; Bethell, D.; Schiffrin, D. J.; Kiely, C. *J. Chem. Soc., Chem. Commun.* **1995**, 1655.

Brust, M.; Walker, M.; Bethell, D.; Schiffrin, D. J.; Whyman, R. *J. Chem. Soc., Chem. Commun.* **1994**, 801.

Buerger, M. J.; Wuensch, B. J. *Science* **1963**, *141*, 276.

Buerger, M. J. *Anais Acad. Brasil. Cienc.* **1949**, *21*, 261.

Burton, W. K.; Cabrera, N.; Frank, F. C. *Phil. Trans R. Soc. London Ser. A* **1951**, *243*, 299.

Busbee, B. D.; Obare, S. O.; Murphy, C. J. *Adv. Mater.* **2003**, *15*, 414.

Cakmak, M.; Kim, J. C. *J. Appl. Polym. Sci.* **1997**, *64*, 729.

Cantarero, A.; Martinez-Pastor, J.; Segura, A. *Phys. Rev. B* **1987**, *35*, 9586.

Cao, X.; Li, L.; Xie, Y. *J. Coll. Inter. Sci.* **2004**, *273*, 175.

Castaño, V.; Gómez, A.; Yacaman, M. J. *Surf. Sci.* **1984**, *146*, L587.

Chen, B.; Uher, C. *Chem. Mater.* **1997**, *9*, 1655.

Chen, G. *Int. J. Therm. Sci.* **2000**, *39*, 471.

Coe, S.; Woo, W.-K.; Bawendi, M.; Bulovic, V. *Nature* **2002**, *420*, 800.

Collier, C. P.; Saykally, R. J.; Shiang, J. J.; Henrichs, S. E.; Heath, J. R. *Science* **1997**, *277*, 1978.

Colvin, V. L.; Schlamp, M. C.; Alivisatos, A. P. *Nature* **1994**, *370*, 354.

Connolly, S.; Fullam, S.; Korgel, B.; Fitzmaurice, D. *J. Am. Chem. Soc.* **1998**, *120*, 2969.

Copisarow, A. C.; Copisarow, M. J. *Nature* **1946**, *157*, 768.

Cordente, N.; Respaud, M.; Senocq, F.; Casanove, M.-J.; Amiens, C.; Chaudret, B. *Nano Lett.* **2001**, *1*, 565.

Corry, C. E. *Appl. Geophys.* **1994**, *32*, 55.

Cotton, F. A.; Wilkinson, G. *Advanced Inorganic Chemistry*, Third ed.; John Wiley & Sons: New York, 1972.

Cui, Y.; Wei, Q.; Park, H.; Lieber, C. M. *Science* **2001**, *293*, 1289.

Dance, I. G.; Choy, A.; Scudder, M. L. *J. Am. Chem. Soc.* **1984**, *106*, 6285.

Darragh, P. J.; Gaskin, A. J.; Terrell, B. C.; Sanders, J. V. *Nature* **1966**, *209*, 13.

Davidson, F. M.; Schricker, A. D.; Wiacek, R. J.; Korgel, B. A. *Adv. Mater.* **2004**, *16*, 646.

Deng, Z.-X.; Li, L.; Li, Y. *Inorg. Chem.* **2003**, *42*, 2331.

Deng, Z.-X.; Wang, C.; Sun, X.-M.; Li, Y.-D. *Inorg. Chem.* **2002**, *41*, 869.

Diehl, M. R.; Yu, J.-Y.; Heath, J. R.; Held, G. A.; Doyle, H.; Sun, S.; Murray, C. B. *J. Phys. Chem. B* **2001**, *105*, 7913.

Dinega, D. P.; Bawendi, M. G. *Angew. Chem. Int. Ed.* **1999**, *38*, 1788.

Ding, Y.; Gao, P. X.; Wang, Z. L. *J. Am. Chem. Soc.* **2004**, *126*, 2066.

Dingman, S. D.; Rath, N. P.; Gibbons, P. C.; Buhro, W. E. *Angew. Chem. Int. Ed.* **2000**, *39*, 1470.

Dixit, N. M.; Zukoski, C. F. *Phys. Rev. E* **2001**, *64*, 041604.

Doty, R. C.; Yu, H.; Shih, K.; Korgel, B. A. *J. Phys. Chem. B* **2001**, *105*, 8291.

Driver, S. M.; Woodruff, D. P. *Surf. Sci.* **2001**, *479*, 1.

Driver, S. M.; Woodruff, D. P. *Langmuir* **2000**, *16*, 6693.

Duan, X.; Huang, Y.; Lieber, C. M. *Nano Lett.* **2002**, *2*, 487.

Duan, X.; Lieber, C. M. *J. Am. Chem. Soc.* **2000**, *122*, 188.

Dubois, L. H.; Zegarski, B. R.; Nuzzo, R. G. *Langmuir* **1986**, *2*, 412.

Dunin-Borkowski, R. E.; McCartney, M. R.; Frankel, R. B.; Bazylinski, D. A.; Pósfai, M.; Buseck, P. R. *Science* **1998**, *282*, 1868.

Duonghong, D.; Ramsden, J.; Grätzel, M. *J. Am. Chem. Soc.* **1982**, *104*, 2977.

Duonghong, D.; Borgarello, E.; Grätzel, M. *J. Am. Chem. Soc.* **1981**, *103*, 4685.

Fan, W.; Sun, S.; Song, X.; Zhang, W.; Yu, H.; Tan, X.; Cao, G. *J. Solid State Chem.* **2004**, *177*, 2329.

Faraday, M. *Phil. Trans. R. Soc. London* **1857**, *147*, 145.

Ferry, D. K.; Goodnick, S. M. *Transport in Nanostructures*; Cambridge University Press: USA, 1999; Vol. 6.

Fojtik, A.; Weller, H.; Koch, U.; Henglein, A. *Ber. Bunsenges. Phys. Chem.* **1984**, *88*, 969.

Foss, M.; Feidenhans'l, R.; Nielsen, M.; Findeisen, E.; Buslaps, T.; Johnson, R. L.; Besenbacher, F. *Surf. Sci.* **1997**, *388*, 5.

Fox, M. A.; Lindig, B.; Chen, C.-C. *J. Am. Chem. Soc.* **1982**, *104*, 5828.

Frankel, R. B. *Annu. Rev. Biophys. Bioeng.* **1984**, *13*, 85.

Frenkel, D. *Phys. World* **1993**, *6*, 24.

Friedlander, S. K. *J. Nanopart. Res.* **1999**, *1*, 9.

Fuller, M.; Dobson, J.; Wieser, H. G.; Moser, S. *Brain Res. Bull.* **1995**, *36*, 155.

Gao, F.; Lu, Q.; Zhao, D. *Chem. Lett.* **2002**, *7*, 732.

Gates, B.; Mayers, B.; Cattle, B.; Xia, Y. *Adv. Funct. Mater.* **2002**, *12*, 219.

Gates, B.; Yin, Y.; Xia, Y. *J. Am. Chem. Soc.* **2000**, *122*, 12582.

Ge, G.; Brus, L. *J. Phys. Chem. B* **2000**, *104*, 9573.

Ghezelbash, A.; Sigman, M. B.; Korgel, B. A. *Nano Lett.* **2004**, *4*, 537.

Gibson, J. M.; Lanzerotti, M. Y.; Elser, V. *Appl. Phys. Lett.* **1989**, *55*, 1394.

Giersig, M.; Mulvaney, P. *J. Phys. Chem.* **1993**, *97*, 6334.

Giersig, M.; Mulvaney, P. *Langmuir* **1993**, *9*, 3408.

Glinchuk, M. D.; Morozovskaya, A. N. *Phys. Stat. Sol. (b)* **2003**, *238*, 81.

Goldstein, A. N.; Echer, C. M.; Alivisatos, A. P. *Science* **1992**, *256*, 1425.

Grigas, J.; Talik, E.; Lazauskas, V. *Phys. Stat. Sol. (b)* **2002**, *232*, 220.

Guzelian, A. A.; Banin, U.; Kadavanich, A. V.; Peng, X.; Alivisatos, A. P. *Appl. Phys. Lett.* **1996**, *69*, 1432.

Hamaker, H. C. *Physica IV* **1937**, *10*, 1058.

Hamza, A. A.; Sokkar, T. Z. N.; El-Bakary, M. A. *J. Opt. A: Pure Appl. Opt.* **2001**, *3*, 421.

Han, W.; Fan, S.; Li, Q.; Hu, Y. *Science* **1997**, *277*, 1287.

Hanrath, T.; Korgel, B. A. *Adv. Mater.* **2003**, *15*, 437.

Hanrath, T.; Korgel, B. A. *J. Am. Chem. Soc.* **2002**, *124*, 1424.

Harfenist, S. A.; Wang, Z. L.; Whetten, R. l.; Vezmar, I.; Alvarez, M. M. *Adv. Mater.* **1997**, *9*, 817.

Harfenist, S. A.; Wang, Z. L.; Alvarez, M. M.; Vezmar, I.; Whetten, R. L. *J. Phys. Chem.* **1996**, *100*, 13904.

Harman, T. C.; Taylor, P. J.; Walsh, M. P.; LaForge, B. E. *Science* **297**, *297*, 2229.

Hartshorne, N. H.; Stuart, A. *Crystals and the Polarising Microscope*; Edward Arnold Ltd.: London, 1960.

Hasenöhrl, S.; Novák, J.; Kúdela, R.; Betko, J.; Morvic, M.; Fedor, J. *J. Cryst. Growth* **2003**, *248*, 369.

Heer, W. A. d.; Bacsa, W. S.; Châtelain, A.; Gerfin, T.; Humphrey-Baker, R.; Forro, L.; Ugarte, D. *Science* **1995**, *268*, 845.

Henglein, A. *Ber. Bunsenges. Phys. Chem.* **1982**, *86*, 301.

Hicks, L. D.; Dresselhaus, M. S. *Phys. Rev. B* **1993**, *47*, 16631.

Holmes, J. D.; Johnston, K. P.; Doty, R. C.; Korgel, B. A. *Science* **2000**, *287*, 1471.

Hostetler, M. J.; Stokes, J. J.; Murray, R. W. *Langmuir* **1996**, *12*, 3604.

Hu, J.; Li, L.; Yang, W.; Manna, L.; Wang, L.; Alivisatos, A. P. *Science* **2001**, *292*, 2060.

Huang, Y.; Duan, X.; Cui, Y.; Lauhon, L. J.; Kim, K.-H.; Lieber, C. M. *Science* **2001**, *294*, 1314.

Hughes, W. L.; Wang, Z. L. *J. Am. Chem. Soc.* **2004**, *126*, 6703.

Hunter, R. J. *Foundations of Colloid Science*, 2nd ed.; Oxford University Press: New York, 2001.

Huynh, W. U.; Dittmer, J. J.; Libby, W. C.; Whiting, G. L.; Alivisatos, A. P. *Adv. Funct. Mater.* **2003**, *13*, 73.

Huynh, W. U.; Peng, X.; Alivisatos, A. P. *Adv. Mater.* **1999**, *11*, 923.

Imanishi, A.; Isawa, K.; Matsui, F.; Tsuduki, T.; Yokoyama, T.; Kondoh, H.; Kitajima, Y.; Ohta, T. *Surf. Sci.* **1998**, *407*, 282.

Ingert, D.; Pileni, M. P. *J. Phys. Chem. B* **2003**, *107*, 9618.

Israelachvili, J. *Intermolecular and Surface Forces*, 2nd ed.; Academic Press: New York, 1992.

Jackson, G. J.; Driver, S. M.; Woodruff, D. P.; Cowie, B. C. C.; Jones, R. G. *Surf. Sci.* **2000**, *453*, 183.

Jana, N. R.; Gearheart, L.; Murphy, C. J. *Adv. Mater.* **2001**, *13*, 1389.

Jana, N. R.; Gearheart, L.; Murphy, C. J. *J. Phys. Chem. B* **2001**, *105*, 4065.

Jensen, M. L. Ph.D. Thesis, M.I.T., 1951.

Jin, S.; Whang, D.; McAlpine, M. C.; Friedman, R. S.; Wu, Y.; Lieber, C. M. *Nano Lett.* **2004**, *4*, 915.

Johnson, C. J.; Dujardin, E.; Davis, S. A.; Murphy, C. J.; Mann, S. *J. Mater. Chem.* **2002**, *12*, 1765.

Joo, J.; Na, H. B.; Yu, T.; Yu, J. H.; Kim, Y. W.; Wu, F.; Zhang, J. Z.; Hyeon, T. *J. Am. Chem. Soc.* **2003**, *125*, 11100.

Jun, Y.-W.; Casula, M. F.; Sim, J.-H.; Kim, S. Y.; Cheon, J.; Alivisatos, A. P. *J. Am. Chem. Soc.* **2003**, *125*, 15981.

Jun, Y.-W.; Jung, Y.-Y.; Cheon, J. *J. Am. Chem. Soc.* **2002**, *124*, 615.

Katari, J. E. B.; Colvin, V. L.; Alivisatos, A. P. *J. Phys. Chem.* **1994**, *98*, 4109.

Kim, H.-W.; Lee, H.-S.; Kim, J.-D. *Liq. Cryst.* **2002**, *29*, 413.

Kim, Y.-H.; Jun, Y.-w.; Jun, B.-H.; Lee, S.-M.; Cheon, J. *J. Am. Chem. Soc.* **2002**, *124*, 13656.

Kirschvink, J. L.; Kobayashi-Kirschvink, A.; Woodford, B. J. *Proc. Natl. Acad. Sci. USA* **1992**, *89*, 7683.

Klabunde, K. J.; Mulukutla, R. S. Chemical and Catalytic Aspects of Nanocrystals. In *Nanoscale Materials in Chemistry*; Klabunde, K. J., Ed.; John Wiley & Sons, Inc.: New York, 2001.

Knoll, M.; Ruska, E. *Z. Physik* **1932**, *78*, 318.

Koh Y. W.; Lai, C. S.; Du, A. Y.; Tiekink, E. R. T.; Loh, K. P. *Chem. Mater.* **2003**, *15*, 4544.

Kolmakov, A.; Moskovits, M. *Annu. Rev. Mater. Res.* **2004**, *34*, 151.

Kolmakov, A.; Zhang, Y.; Cheng, G.; Moskovits, M. *Adv. Mater.* **2003**, *15*, 997.

Kong, J.; Franklin, N. R.; Zhou, C.; Chapline, M. G.; Peng, S.; Cho, K.; Dai, H. *Science* **2000**, *287*, 622.

Kong, X. Y.; Ding, Y.; Yang, R.; Wang, Z. L. *Science* **2004**, *303*, 1348.

Kong, X. Y.; Wang, Z. L. *Nano Lett.* **2003**, *3*, 1625.

Korgel, B. A.; Fitzmaurice, D. *Phys. Rev. B* **1999**, *59*, 14191.

Korgel, B. A.; Fitzmaurice, D. *Adv. Mater.* **1998**, *10*, 661.

Korgel, B. A.; Fullam, S.; Connolly, S.; Fitzmaurice, D. *J. Phys. Chem. B* **1998**, *102*, 8379.

Korgel, B. A.; Fitzmaurice, D. *Phys. Rev. Lett.* **1998**, *80*, 3531.

Kovalev, D.; Polisski, G.; Diener, J.; Heckler, H.; Künzner, N.; Timoshenko, V. Y.; Koch, F. *Appl. Phys. Lett.* **2001**, *78*, 916.

Krivovichev, S. V.; Burns, P. C. *Eur. J. Mineral.* **2001**, *13*, 801.

Kuhnle, A.; Vollmer, S.; Linderoth, T. R.; Witte, G.; Woll, C.; Besenbacher, F. *Langmuir* **2002**, *18*, 5558.

Kunzner, N.; Kovalev, D.; Diener, J.; Gross, E.; Timoshenko, V. Y.; Polisski, G.; Koch, F. *Optics Letters* **2001**, *26*, 1265.

Kuykendall, T.; Pauzauskie, P. J.; Zhang, Y.; Goldberger, J.; Sirbuly, D.; Denlinger, J.; Yang, P. *Nature Mater.* **2004**, *3*, 524.

Kwan, S.; Kim, F.; Akana, J.; Yang, P. *Chem. Commun.* **2001**, *5*, 447.

Laibinis, P. E.; Whitesides, G. M.; Allara, D. L.; Tao, Y.-T.; Parikh, A. N.; Nuzzo, R. G. *J. Am. Chem. Soc.* **1991**, *113*, 7152.

LaMer, V. K.; Dinegar, R. H. *J. Am. Chem. Soc.* **1950**, *72*, 4847.

Larsen, T. H.; Sigman, M.; Ghezelbash, A.; Doty, R. C.; Korgel, B. A. *J. Am. Chem. Soc.* **2003**, *125*, 5638.

Law, M.; Goldberger, J.; Yang, P. *Annu. Rev. Mater. Res.* **2004**, *34*, 83.

Lee, S.-M.; Cho, S.-N.; Cheon, J. *Adv. Mater.* **2003**, *15*, 441.

Lemaire, B. J.; Davidson, P.; Ferré, J.; Jamet, J. P.; Panine, P.; Dozov, I.; Jolivet, J. P. *Phys. Rev. Lett.* **2002**, *88*, 125507.

Levin, I.; Ott, E. *J. Am. Chem. Soc.* **1932**, *54*, 828.

Li, D.; Wu, Y.; Kim, P.; Shi, L.; Yang, P.; Majumdar, A. *Appl. Phys. Lett.* **2003**, *83*, 2934.

Li, L.; Hu, J.; Yang, W.; Alivisatos, A. P. *Nano Lett.* **2001**, *1*, 349.

Liao, X.-H.; Wang, H.; Zhu, J.-J.; Chen, H.-Y. *Mater. Res. Bull.* **2001**, *36*, 2339.

Lin, X. M.; Jaeger, H. M.; Sorensen, C. M.; Klabunde, K. J. *J. Phys. Chem. B* **2001**, *105*, 3353.

Liu, Z.; Bando, Y. *Adv. Mater.* **2003**, *15*, 303.

Liu, Z.; Peng, S.; Xie, Q.; Hu, Z.; Yang, Y.; Zhang, S.; Qian, Y. *Adv. Mater.* **2003**, *15*, 936.

Lu, Q.; Gao, F.; Komameni, S. *J. Am. Chem. Soc.* **2004**, *126*, 54.

Lu, X.; Hanrath, T.; Johnston, K. P.; Korgel, B. A. *Nano Lett.* **2003**, *3*, 93.

Luedtke, W. D.; Landman, U. *J. Phys. Chem. B* **1998**, *102*, 6566.

Luedtke, W. D.; Landman, U. *J. Phys. Chem.* **1996**, *100*, 13323.

Lynch, D. F. *Acta Cryst.* **1971**, *A27*, 399.

Ma, C.; Moore, D.; Li, J.; Wang, Z. L. *Adv. Mater.* **2003**, *15*, 228.

Ma, D. D. D.; Lee, C. S.; Au, F. C. K.; Tong, S. Y.; Lee, S. T. *Science* **2003**, *299*, 1874.

Majumdar, A. *Science* **2004**, *303*, 777.

Mane, R. S.; Sankapal, B. R.; Lokhande, C. D. *Mater. Chem. Phys.* **1999**, *60*, 158.

Mann, S.; Sparks, N. H. C.; Walker, M. M.; Kirschvink, J. L. *J. Exp. Biol.* **1988**, *140*, 35.

Manna, L.; Milliron, D. J.; Meisel, A.; Scher, E. C.; Alivisatos, A. P. *Nature Mater.* **2003**, *2*, 382.

Manna, L.; Scher, E. C.; Alivisatos, A. P. *J. Cluster Sci.* **2002**, *13*, 521.

Manna, L.; Scher, E. C.; Alivisatos, A. P. *J. Am. Chem. Soc.* **2000**, *122*, 12700.

Markowitz, P. D.; Zach, M. P.; Gikbbons, P. C.; Penner, R. M.; Buhro, W. E. *J. Am. Chem. Soc.* **2001**, *123*, 4502.

Mattoussi, H.; Radzilowski, L. H.; Dabbousi, B. O.; Fogg, D. E.; Schrock, R. R.; Thomas, E. L.; Rubner, M. F.; Bawendi, M. G. *J. Appl. Phys.* **1999**, *86*, 4390.

Matysina, Z. A. *Mater. Chem. Phys.* **1999**, *60*, 70.

Mayers, B.; Xia, Y. *J. Mater. Chem.* **2002**, *12*, 1875.

McAlpine, M. C.; Friedman, R. S.; Jin, S.; Lin, K.; Wang, W. U.; Lieber, C. M. *Nano Lett.* **2003**, *3*, 1531.

Messer, B.; Song, J. H.; Huang, M.; Wu, Y.; Kim, F.; Yang, P. *Adv. Mater.* **2000**, *12*, 1526.

Micic, O. I.; Curtis, C. J.; Jones, K. M.; Sprague, J. R.; Nozik, A. J. *J. Phys. Chem.* **1994**, *98*, 4966.

Milliron, D. J.; Hughes, S. M.; Cui, Y.; Manna, L.; Li, J.; Wang, L.-W.; Alivisatos, A. P. *Nature* **2004**, *430*, 190.

Morales, A. M.; Lieber, C. M. *Science* **1998**, *279*, 208.

Moser, J.; Grätzel, M. *J. Am. Chem. Soc.* **1983**, *105*, 6547.

Muller, R. H.; Keck, C. M. *J. Biotech.* **2003**, *113*, 151.

Mulvaney, P. Metal Nanoparticles: Double Layers, Optical Properties, and Electrochemistry. In *Nanoscale Materials in Chemistry*; Klabunde, K. J., Ed.; John Wiley & Sons, Inc.: New York, 2001; pp 121.

Murray, C. B.; Kagan, C. R.; Bawendi, M. G. *Annu. Rev. Mater. Sci.* **2000**, *30*, 545.

Murray, C. B.; Kagan, C. R.; Bawendi, M. G. *Science* **1995**, *270*, 1335.

Murray, C. B.; Norris, D. J.; Bawendi, M. G. *J. Am. Chem. Soc.* **1993**, *115*, 8706.

Nanomaterials: Synthesis, Properties, and Applications; Edelstein, A. S.; Cammarata, R. C., Eds.; Institute of Physics Publishing: Philadelphia, 2001.

Nanoscale Materials in Chemistry; Klabunde, K. J., Ed.; John Wiley & Sons, Inc.: New York, 2001.

Narayanan, R.; El-Sayed, M. A. *J. Am. Chem. Soc.* **2004**, *126*, 7194.

Narayanan, R.; El-Sayed, M. A. *J. Phys. Chem. B* **2004**, *108*, 5726.

Narayanan, R.; El-Sayed, M. A. *Nano Lett.* **2004**, *4*, 1343.

Nassary, M. M.; Gerges, M. K.; Shaban, H. T.; Salwa, A. S. *Physica B* **2003**, *337*, 130.

Niitsu, G. T.; Nagata, H.; Rodrigues, A. C. *J. Appl. Phys.* **2004**, *95*, 3116.

Nikoobakht, B.; El-Sayed, M. A. *Chem. Mater.* **2003**, *15*, 1957.

Noren, L.; Tan, E. S. Q.; Withers, R. L.; Sterns, M.; Rundlof, H. *Mater. Res. Bull.* **2002**, *37*, 1431.

Norris, D. J. Electronic Structure in Semiconductor Nanocrystals. In *Semiconductor and Metal Nanocrystals: Synthesis and Electronic and Optical Properties*; Klimov, V. I., Ed.; Marcel Dekker, Inc.: New York, 2004; Vol. 87; pp 484.

Ohara, P. C.; Leff, D. V.; Heath, J. R.; Gelbart, W. M. *Phys. Rev. Lett.* **1995**, *75*, 3466.

Ortega-Avilés, M.; San-Germán, C. M.; Mendoza-Anaya, D.; Morales, D.; José-Yacamán, M. *J. Mater. Sci.* **2001**, *36*, 2227.

Ozkan, M. *Drug Disc. Today* **2004**, *9*, 1065.

Pan, Z. W.; Dai, Z. R.; Wang, Z. L. *Science* **2001**, *291*, 1947.

Park, J.; An, K.; Hwang, Y.; Park, J.-G.; Noh, H.-J.; Kim, J.-Y.; Park, J.-H.; Hwang, N.-M.; Hyeon, T. *Nature Mater.* **2004**, *3*, 891.

Parthasarathy, R.; Lin, X.-M.; Jaeger, H. M. *Phys. Rev. Lett.* **2001**, *87*, 186807.

Peng, X. *Adv. Mater.* **2003**, *15*, 459.

Peng, X.; Manna, L.; Yang, W.; Wickham, J.; Scher, E.; Kadavanich, A.; Alivisatos, A. P. *Nature* **2000**, *404*, 59.

Peng, X.; Wickham, J.; Alivisatos, A. P. *J. Am. Chem. Soc.* **1998**, *120*, 5343.

Peng, Z. A.; Peng, X. *J. Am. Chem. Soc.* **2002**, *124*, 3343.

Peng, Z. A.; Peng, X. *J. Am. Chem. Soc.* **2001**, *123*, 1389.

Penner, R. M. *J. Phys. Chem. B* **2002**, *106*, 3339.

Plass, R.; Pelet, S.; Krueger, J.; Grätzel, M. *J. Phys. Chem. B* **2002**, *106*, 7578.

Puntes, V. F.; Krishnan, K. M.; Alivisatos, A. P. *Science* **2001**, *291*, 2115.

Puntes, V. F.; Zanchet, D.; Erdonmez, C. K.; Alivisatos, A. P. *J. Am. Chem. Soc.* **2002**, *124*, 12874.

Pusey, P. N.; Poon, W. C. K.; Ilett, S. M.; Bartlett, P. *J. Phys.: Condens. Matter* **1994**, *6*, A29.

Pusey, P. N.; Megen, W. v. *Nature* **1986**, *320*, 340.

Raman, C. V.; Jayaraman, A. *Proc. Indian Acad. Sci.* **1953**, *38A*, 343.

Ramsden, J. J.; Grätzel, M. *J. Chem. Soc., Faraday Trans. 1* **1984**, *80*, 919.

Reiss, H. *J. Chem. Phys.* **1951**, *19*, 482.

Rodrigues, V.; Fuhrer, T.; Ugarte, D. *Phys. Rev. Lett.* **2000**, *85*, 4124.

Rossetti, R.; Nakahara, S.; Brus, L. E. *J. Chem. Phys.* **1983**, *79*, 1086.

Rossetti, R.; Brus, L. *J. Phys. Chem.* **1982**, *86*, 4470.

Ruska, E. *Rev. Mod. Phys.* **1987**, *59*, 627.

Sanders, J. V. *Nature* **1964**, *204*, 1151.

Sangwal, K. *Progress in Crystal Growth and Characterization* **1998**, *36*, 163.

Sasaki, T.; Katsuragi, A.; Mochizuki, O.; Nakazawa, Y. *J. Phys. Chem. B* **2003**, *107*, 7659.

Saunders, A. E.; Shah, P. S.; Sigman, M. B.; Hanrath, T.; Hwang, H. S.; Lim, K. T.; Johnston, K. P.; Korgel, B. A. *Nano Lett.* **2004**, *4*, 1943.

Saunders, A. E.; Korgel, B. A. *J. Phys. Chem. B* **2004**, *108*, 16732.

Saunders, A. E.; Sigman, M. B.; Korgel, B. A. *J. Phys. Chem. B* **2004**, *108*, 193.

Scheel, H. J. Historical Introduction. In *Handbook of Crystal Growth 1a: Thermodynamics and Kinetics*; Hurle, D. T. J., Ed.; Elsevier: Amsterdam, 1993; pp 3.

Schmid, G.; Lehnert, A. *Angew. Chem. Int. Ed. Engl.* **1989**, *28*, 780.

Schultheiss-Grassi, P. P.; Wessiken, R.; Dobson, J. *Biochem. Biophys. Acta* **1999**, *1426*, 212.

Sellers, H.; Ulman, A.; Shnidman, Y.; Eilers, J. E. *J. Am. Chem. Soc.* **1993**, *115*, 9389.

Semiconductor and Metal Nanocrystals: Synthesis and Electronic Properties; Klimov, V.I., Ed.; Marcel Dekker: New York, **2004**.

Shah, P. S.; Sigman, M. B.; Stowell, C. A.; Lim, K. T.; Johnston, K. P.; Korgel, B. A. *Adv. Mater.* **2003**, *15*, 971.

Shah, P. S.; Hanrath, T.; Johnston, K. P.; Korgel, B. A. *J. Phys. Chem. B* **2004**, *108*, 9574.

Shah, P. S.; Holmes, J. D.; Johnston, K. P.; Korgel, B. A. *J. Phys. Chem. B* **2002**, *106*, 2545.

Shah, P. S.; Husain, S.; Johnston, K. P.; Korgel, B. A. *J. Phys. Chem. B* **2002**, *106*, 12178.

Shao, M.; Zhang, W.; Wu, Z.; Ni, Y. *J. Cryst. Growth* **2004**, *265*, 318.

Shevchenko, E.; Talapin, D.; Kornowski, A.; Wiekhorst, F.; Kotzler, J.; Haase, M.; Rogach, A.; Weller, H. *Adv. Mater.* **2002**, *14*, 287.

Shi, L.; Hao, Q.; Yu, C.; Mingo, N.; Kong, X.; Wang, Z. L. *Appl. Phys. Lett.* **2004**, *84*, 2638.

Shi, L.; Li, D.; Yu, C.; Jang, W.; Kim, D.; Yao, Z.; Kim, P.; Majumdar, A. *J. Heat Trans.* **2003**, *125*, 881.

Sigman, M. B.; Ghezelbash, A.; Hanrath, T.; Saunders, A. E.; Lee, F.; Korgel, B. A. *J. Am. Chem. Soc.* **2003**, *125*, 16050.

Sigman, M. B.; Saunders, A. E.; Korgel, B. A. *Langmuir* **2004**, *20*, 978.

Spanhel, L.; Haase, M.; Weller, H.; Henglein, A. *J. Am. Chem. Soc.* **1987**, *109*, 5649.

Steigerwald, M. L.; Alivisatos, A. P.; Gibson, J. M.; Harris, T. D.; Kortan, R.; Muller, A. J.; Thayer, A. M.; Duncan, T. M.; Douglass, D. C.; Brus, L. E. *J. Am. Chem. Soc.* **1988**, *110*, 3046.

Suarez, R.; Nair, P. K.; Kamat, P. V. *Langmuir* **1998**, *14*, 3236.

Sugimoto, T. *Chem. Eng. Technol.* **2003**, *26*, 313.

Sugimoto, T. *Adv. Colloid Interfac. Sci.* **1987**, *28*, 65.

Sun, B.; Marx, E.; Greenham, N. C. *Nano Lett.* **2003**, *3*, 961.

Sun, Y.; Mayers, B.; Herricks, T.; Xia, Y. *Nano Lett.* **2003**, *3*, 955.

Sun, Y.; Xia, Y. *Adv. Mater.* **2002**, *14*, 833.

Sun, Y.; Yin, Y.; Mayers, B. T.; Herricks, T.; Xia, Y. *Chem. Mater.* **2002**, *14*, 4736.

Sun, Y.; Gates, B.; Mayers, B.; Xia, Y. *Nano Lett.* **2002**, *2*, 165.

Sun, Y.; Xia, Y. *Science* **2002**, *298*, 2176.

Sunagawa, I. Growth of Crystals in Nature. In *Materials Science of the Earth's Interior*; Sunagawa, I., Ed.; D. Reidel Publishing Company: Dordrecht, 1984; pp 63.

Talapin, D. V.; Shevchenko, E. V.; Kornowski, A.; Gaponik, N.; Haase, M.; Rogach, A. L.; Weller, H. *Adv. Mater.* **2001**, *13*, 1868.

Tolbert, S. H.; Herhold, A. B.; Brus, L. E.; Alivisatos, A. P. *Phys. Rev. Lett.* **1996**, *76*, 4384.

Toschev, S. Homogeneous Nucleation. In *Crystal Growth: An Introduction*; Hartman, P., Ed.; American Elsevier: New York, 1973; Vol. 1.

Trentler, T. J.; Goel, S. C.; Hickman, K. M.; Viano, A. M.; Chiang, M. Y.; Beatty, A. M.; Gibbons, P. C.; Buhro, W. E. *J. Am. Chem. Soc.* **1997**, *119*, 2172.

Trentler, T. J.; Hickman, K. M.; Goel, S. C.; Viano, A. M.; Gibbons, P. C.; Buhro, W. E. *Science* **1995**, *270*, 1791.

Turkevich, J.; Stevenson, P. C.; Hillier, J. *Disc. Faraday Soc.* **1951**, *11*, 55.

Turkevich, J.; Hillier, J. *Anal. Chem.* **1949**, *21*, 475.

Venkatasubramanian, R.; Siivola, E.; Colpitts, T.; O'Quinn, B. *Nature* **2001**, *413*, 597.

Vidali, G. Epitaxial Growth of Nanoparticles: Mechanistic Comparisons of Physical and Chemical Processes. In *Nanoparticles in Solids and Solutions*; Dekany, I., Ed.; Kluwer Academic Publishers: Dordrecht, 1996; Vol. 18; pp 17.

Vincent, B.; Edwards, J.; Emmett, S.; Jones, A. *Colloids Surf.* **1986**, *18*, 261.

Vollmer, S.; Witte, G.; Woll, C. *Langmuir* **2001**, *17*, 7560.

Wagner, F. E.; Haslbeck, S.; Stievano, L.; Calogero, S.; Pankhurst, Q. A.; Martinek, K.-P. *Nature* **2000**, *407*, 691.

Walczak, M. M.; Chung, C.; Stole, S. M.; Widrig, C. A.; Porter, M. D. *J. Am. Chem. Soc.* **1991**, *113*, 2370.

Walker, M. W.; Diebel, C. E.; Haugh, C. V.; Pankhurst, P. M.; Montgomery, J. C.; Green, C. R. *Science* **1997**, *390*, 371.

Wang, D.; Shao, M.; Yu, D.; Yu, W.; Qian, Y. *J. Cryst. Growth* **2003**, *254*, 487.

Wang, D.; Shao, M.; Yu, D.; Li, G.; Qian, Y. *J. Cryst. Growth* **2002**, *243*, 331.

Wang, H.; Zhu, J.-J.; Zhu, J.-M.; Chen, H.-Y. *J. Phys. Chem. B* **2002**, *106*, 3848.

Wang, S.; Guo, L.; Wen, X.; Yang, S.; Zhao, J.; Liu, J.; Wu, Z. *Mater. Chem. Phys.* **2002**, *75*, 32.

Wang, S.; Yang, S.; Dai, Z. R.; Wang, Z. L. *Phys. Chem. Chem. Phys.* **2001**, *3*, 3750.

Wang, W.; Liu, Y.; Xu, C.; Zheng, C.; Wang, G. *Chem. Phys. Lett.* **2002**, *362*, 119.

Wang, Z. L. *Annu. Rev. Phys. Chem.* **2004**, *55*, 159.

Wang, Z. L. *Mater. Char.* **1999**, *42*, 101.

Wang, Z. L. *Adv. Mater.* **1998**, *10*, 13.

Wang, Z. L.; Harfenist, S. A.; Vezmar, I.; Whetten, R. L.; Bentley, J.; Evans, N. D.; Alexander, K. B. *Adv. Mater.* **1998**, *10*, 808.

Wang, Z. L.; Harfenist, I. V.; Whetten, R. L.; Bentley, J.; Evans, N. D. *J. Phys. Chem. B* **1998**, *102*, 3068.

Werwa, E.; Seraphin, A. A.; Chiu, L. A.; Zhou, C.; Kolenbrander, K. D. *Appl. Phys. Lett.* **1994**, *64*, 1821.

Whetten, R. L.; Shafigullin, M. N.; Khoury, J. T.; Schaaff, T. G.; Vezmar, I.; Alvarez, M. M.; Wilkinson, A. *Acc. Chem. Res.* **1999**, *32*, 397.

Williams, D. B.; Carter, C. B. *Transmission Electron Microscopy: A Textbook for Materials Science*; Plenum Press: New York, 1996.

Wu, Y.; Cui, Y.; Huynh, L.; Barrelet, C. J.; Bell, D. C.; Lieber, C. M. *Nano Lett.* **2004**, *4*, 433.

Wyckoff, R. W. G. *Crystal Structures: Inorganic Compounds*, 2 ed.; Interscience Publishers: New York, 1964; Vol. 2.

Xia, Y.; Yang, P.; Sun, Y.; Wu, Y.; Mayers, B.; Gates, B.; Yin, Y.; Kim, F.; Yan, H. *Adv. Mater.* **2003**, *15*, 353.

Ye, C.; Meng, G.; Jiang, Z.; Wang, Y.; Wang, G.; Zhang, L. *J. Am. Chem. Soc.* **2002**, *124*.

Yu, H.; Buhro, W. E. *Adv. Mater.* **2003**, *15*, 416.

Yu, J.-Y.; Chung, S.-W.; Heath, J. R. *J. Phys. Chem. B* **2000**, *104*, 11864.

Yu, S.; Qian, Y.; Shu, L.; Xie, Y.; Yang, L.; Wang, C. *Mater. Lett.* **1998**, *35*, 116.

Zhang, B. P.; Binh, N. T.; Wakatsuki, K.; Segawa, Y.; Yamada, Y.; Usami, N.; Kawasaki, M.; Koinuma, H. *J. Phys. Chem. B* **2004**, *108*, 10899.

Zhang, H.; Ji, Y.; Ma, X.; Xu, J.; Yang, D. *Nanotechnology* **2003**, *14*, 974.

Zhang, W.; Yang, Z.; Huang, X.; Zhang, S.; Yu, W.; Qian, Y.; Jia, Y.; Zhou, G.; Chen, L. *Solid State Commun.* **2001**, *119*, 143.

Vita

Michael Barron Sigman, Jr., the son of Mrs. Catharine C. Sigman and Dr. Michael B. Sigman and the elder brother of Mary Bess Horton, was born in Athens, Georgia on December 13, 1973. After graduating from Newton County High School in June of 1992, he attended the University of Florida at Gainesville. He transferred to the Georgia Institute of Technology in March of 1994. Michael graduated with Highest Honor with a Bachelor of Chemical Engineering degree in December of 1996. He married Stacey Leigh McCart on May 3, 1997. He worked in the pharmaceutical industry as a process engineer for Merck & Co., Inc. at their Flint River Plant in Albany, Georgia until July of 2000. In August of 2000, he entered graduate school at the University of Texas at Austin in the Department of Chemical Engineering and pursued his Ph.D. under the advisement of Dr. Brian A. Korgel. Michael and Stacey were blessed with their son, Michael Garrett Sigman, on June 20, 2003.

Permanent address: 10020 City Pond Road
Covington, GA 30014

This dissertation was typed by the author.